

# **BULETINUL INSTITUTULUI POLITEHNIC DIN IAȘI**

**Publicat de  
UNIVERSITATEA TEHNICĂ "GH.ASACHI", IAȘI**

**Tomul LII (LVI)**

**Fasc. 1**

**Secția  
ȘTIINȚA ȘI INGINERIA MATERIALELOR**

**2006**

**President of the Editorial Board of Bulletin of the Polytechnic Institute**

**Prof. univ. dr. eng Nicolae Badea, Technical University “Gh. Asachi” Iași, Romania**  
Rector of Technical University “Gh. Asachi” of Iasi

**Editor-in-Chief of Bulletin of the Polytechnic Institute**

**Prof. univ. dr. eng Ion Giurma, Technical University “Gh. Asachi” Iași, Romania**  
Vice-Rector of Technical University “Gh. Asachi” of Iasi

**Managing Editor of Bulletin of the Polytechnic Institute**

**Prof. univ. dr. eng. Dan Gălușcă, Technical University “Gh. Asachi” Iași, Romania**  
Dean of the Faculty of Materials Science and Engineering

**Managing Editor of the *MATERIALS SCIENCE AND ENGINEERING***

**Assoc. prof. dr. eng. Iulian Ioniță, Technical University “Gh. Asachi” Iași, Romania**  
Scientific secretary of the Faculty of Materials Science and Engineering

**Editorial Board of the Section *MATERIALS SCIENCE AND ENGINEERING***

**Prof.univ.dr.eng. Yuri A. Burennikov, Vinnitsia State Technical University, Ukraine**

**Prof.univ.dr.eng. Borivoje Miškovič, Yugoslav Association of Metallurgical Engineers,  
Belgrad, Serbia-Montenegro**

**Prof.univ.dr.eng. Paolo Nanni, Universita degli Studi da Genova, Italy**

**Prof.univ.dr.eng. Strul Moisa, Ben-Gurion University of the Negev, Beer-Sheva, Israel**

**Prof.univ.dr.eng. Corneliu Munteanu, Technical University “Gh. Asachi” Iași,  
Romania**

**Prof.univ.dr.eng. Vasile Cojocaru-Filipiuc, Technical University “Gh. Asachi” Iași,  
Romania**

**Prof.univ.dr.eng. Constantin Baciu, Technical University “Gh. Asachi” Iași, Romania**

**Prof.univ.dr.eng. Luchian Zaharia, Technical University “Gh. Asachi” Iași, Romania**

**Prof.univ.dr.eng. Ioan Carcea, Technical University “Gh. Asachi” Iași, Romania**

**Prof.univ.dr.eng. Adrian Dima, Technical University “Gh. Asachi” Iași, Romania**

**Prof.univ.dr.eng. Ioan Alexandru, Technical University “Gh. Asachi” Iași, Romania**

**Assoc.prof.dr.eng. Leandru Gheorghe Bujoreanu, Technical University “Gh. Asachi”  
Iași, Romania**

**Assoc. prof.dr. eng. Ioan Rusu, Technical University “Gh. Asachi” Iași, Romania**

**Assoc. prof.dr. eng. Gheorghe Bădărău, Technical University “Gh. Asachi” Iași,  
Romania**

**Assoc. prof.dr. eng. Petrică Vizureanu, Technical University “Gh. Asachi” Iași,  
Romania**

**Editorial Secretary of the *MATERIALS SCIENCE AND ENGINEERING***

**Assoc.prof.dr.eng. Gheorghe Bădărău, Technical University “Gh. Asachi” Iași,  
Romania**

**MATERIALS SCIENCE AND ENGINEERING**

<b>CONTENTS</b>		
1	ROMEO CHELARIU, D.M. GORDIN, T. GLORIAN, IOAN CARCEA, COSTEL ROMAN - THE INFLUENCE OF SOME THERMAL TREATMENT PARAMETERS ON STRUCTURE AND MICROHARDNESS OF SOME TITANIUM ALLOYS	1
2	MIHAI ALEXANDRU, ADRIAN DIMA, GHEORGHE BADARAU PETRICA VIZUREANU, NECULAI SCANTEIANU and DOINA HINCU - THEORETICAL AND EXPERIMENTAL CONSIDERATIONS CONCERNING THE DETERMINATION OF THE OPTIMUM OF THE COLD ROLLING FORCE	9
3	MIHAI ALEXANDRU - THEORETICAL AND EXPERIMENTAL CONTRIBUTIONS CONCERNING THE OPTIMIZATION OF THE ROLLING PARAMETERS	15
4	MIHAI ALEXANDRU, GHEORGHE BADARAU, PETRICA VIZUREANU, ALINA-ADRIANA MINEA, ROMICA MANEA and CONSTANTIN ALEXANDRU - MODERNIZATION TRENDS IN THE COLD ROLLING OF THE RAIL GUARD PROFILE TYPE A	21
5	GH. T. POP and LILIANA VERESTIUC - RESEARCHES CONCERNING PROCESSING BIOACTIVE MATERIALS	27
6	ADRIAN ALEXANDRU, SORIN IACOB STRUGARU, IOAN ALEXANDRU, LAURENTIU CIOBANU and SORIN TANASUCA - COMPUTERIZED QUANTITATIVE MICROGRAPHICAL ANALYSIS OF DEPOSED LAYERS BY ELECTRICAL DISCHARGE IN PULSE ON AN HIGH ALLOYED TOOLS STEEL	35
7	BAHRIN V. and HABA C. G - CONSIDERATIONS REGARDING THE MODEL REFERENCE CONTROL SYSTEM FOR SPEED CONTROL OF DC MOTOR	41
8	GELU BARBU - STUDY CONCERNING THE INFLUENCE OF VIBRATIONS ON THE COMPOSITION AND HARDNESS OF AN INGOT	47
9	GELU BARBU- THE CONNOTATIONS ON HARDNESS AT DYNAMIC CAST PIECES	53
10	LIDIA BENE, PIER LUIGI BONORA and FRANÇOIS WENGER - NANOSTRUCTURED COMPOSITE COATING Ni-SiC OBTAINED BY ELECTRODEPOSITION	59
11	VASILE BULANCEA, ȘTEFAN LĂCĂTUȘU and IOAN ALEXANDRU - THE USES AND CLASSIFICATION OF BIOMATERIALS	69
12	VASILE BULANCEA, IOAN ALEXANDRU, ADRIAN ALEXANDRU and DORIN CONDURACHE - CRYOGENIC TREATMENTS APPLIED TO STEELS	75
13	DORU CANTEMIR, LEONARDO BERTINI, MARCO BEGHINI, and PAUL DORU BÂRSĂNESCU - EXPERIMENTAL DETERMINATION OF PERFORATED PLATES HOLES DISTORTION DUE TO MULTIPASS WELDING	81
14	HORIA CHIRIAC, ANCA-EUGENIA MOGA, CARMEN GHERASIM and DUMITRU-DANIEL HEREA - SYNTHESIS AND MAGNETIC PROPERTIES OF Ni AND Ni-Fe NANOPARTICLES FOR BIOMEDICAL APPLICATIONS	87
15	HORIA CHIRIAC and DUMITRU-DANIEL HEREA - POLYMER-COATED MAGNETIC MICROPARTICLES AS MARKERS FOR MAGNETIC BIOSENSORS	93

16	VASILE COJOCARU-FILIPCIUC - POINT OF VIEW GIVEN SPHEROIDIZING OF GRAPHITE	99
17	IOAN DAMIAN, VIOREL PALEU and SPIRIDON CREȚU - EXPERIMENTAL DATA ACQUISITION FOR BALL BEARING FRICTION TORQUE MEASURING	109
18	ADRIAN DIMA, ALINA ADRIANA MINEA and IULIA MARGARETA DIMA - HEAT PROCESS OPTIMIZATION IN INDUSTRIAL FURNACES	113
19	ADRIAN DIMA, IULIA MARGARETA DIMA and ALINA MINEA - STUDIES CONCERNING THE ENHANCING OF THE MECHANICAL CHARACTERISTICS OF THE ALUMINUM CAST ALLOYS BY HEAT TREATMENTS	117
20	MARIANA LATU - CURRENT IN A 1D CIRCULAR WIRE	121
21	VASILE MANOLE and IOAN ALEXANDRU - NUMERICAL AND EXPERIMENTAL CONTRIBUTION ABOUT THE ELECTRICAL RESISTANCE OF STEELS COVERED WITH DIFFERENT KIND OF METALIC LAYERS	127
22	VASILE MANOLE and IOAN ALEXANDRU - THEORETICAL ASPECTS ABOUT PHYSICAL PROCESSES OF TWO METALS CONTACT	135
23	FLORIN MUNTEANU, MIHAI GAFIȚANU and PAUL BOTEZ - UHMWPE ACETABULAR CUP WEAR BY VISCO-ELASTO-PLASTIC DEFORMATION	143
24	POPO RODION - REJECTION POTENTIALLY DEFECTIVE KMOS CJ.	151
25	NASTACA TIMOFTE and BOGDAN NICOLAU - THE STUDY OF THE SANDS OF CĂPUȘ (CLUJ COUNTY) WITH THE VIEW TO USING IN FOUNDRIES	157
26	URSE MARIA, CHIRIAC HORIA, GRIGORAS MARIAN and MOGA ANCA-EUGENIA - COMPARATIVE STUDY ON MICROSTRUCTURAL AND MAGNETIC PROPERTIES OF FePt AND Fe/FePt THIN FILMS	163
27	CRISTINA PRISACARIU, PAUL C. BUCKLEY and VICTOR ADRIAN PRISACARIU - PARTICULAR ASPECTS ON THE DEFORMATION AND FRACTURE OF NOVEL DIBENZYL POLYURETHANE ELASTOMERS OF VARIABLE CRYSTALLINITY	169
28	STEFAN GRIGORAS and CRISTEL STIRBU - TUBING AND CASING THREAD JOINT. THEORETICAL RESEARCH AND EXPERIMENTAL TESTS	177
29	CRISTEL STIRBU and STEFAN GRIGORAS - TECHNICAL SOLUTIONS FOR TUBING AND CASING THREADED JOINTS	183
30	LEANDRU-GHEORGHE BUJOREANU, VASILE DIA, VIORICA DAVID, CORNELIU MUNTEANU and FLORIN MAXIM - TEMPERING EFFECTS ON THE MICROSTRUCTURE AND TENSILE BEHAVIOUR OF A Cu-Zn-Al SHAPE MEMORY ALLOY	191
31	FLORIN DIACONESCU, IOAN ALEXANDRU et IOAN CARCEADES - RECHESCHES CONCERNANT L'INFLUENCE DE LA TEMPÉRATURE DE CHAUFFAGE PRÉALABLE DE LA COQUILLE SUR LES PROPRIÉTÉS MÉCANIQUES D'UN BRONZE ANTIFRICTION COULÉ PAR CENTRIFUGATION	195
32	FLORIN DIACONESCU et ROMEU CHELARIU - DES RECHERCHES CONCERNANT L'INFLUENCE DE LA TEMPÉRATURE DE CHAUFFAGE PRÉALABLE SUR LA DISTRIBUTION DU Pb DANS LES PIÈCES COULÉES PAR CENTRIFUGATION EN BRONZE CuPb10Sn10	201
33	FLORIN DIACONESCU et ROMEU CHELARIU - DES RECHERCHES CONCERNANT L'INFLUENCE DE LA ROTATION DE LA COQUILLE SUR LA DISTRIBUTION DU Pb DANS LES PIÈCES COULÉES PAR CENTRIFUGATION EN BRONZE CuPb10Sn10	207
34	DIACONESCU FLORIN, ALEXANDRU IOAN et CARCEA IOAN - DES RECHERCHES CONCERNANT L'INFLUENCE DE LA ROTATION DE LA COQUILLE SUR LES PROPRIÉTÉS MÉCANIQUES D'UN BRONZE COULÉ PAR CENTRIFUGATION	211

35	FLORIN BRÎNZĂ, CRISTIAN PÎRGHIE, NICOLAE SULIȚANU – A SUITABLE METHOD FOR OBTAINING FUNCTIONAL POLYMER-METAL COMPOSITED MATERIALS BY ELECTRODEPOSITION	217
36	MIHAI GRAMATICU AND SILVIU GABRIEL STROE – HARDENING OPTIMIZING BY INDUCTION OF REVOLUTION SAMPLES	221
37	MIHAI MIHALCUT, PAUL-DORU BARSANESCU and CONSTANTIN BITCA – FATIGUE UNDER MULTIAXIAL STRESSES OF SOME STEELS	229
38	PETRU MOLDOVAN, GABRIELA POPESCU, IOANA APOSTOLESCU, MARIANA ZSIGMOND – MODIFICATION AND GRAIN REFINING OF MULTIFUNCTIONAL MATERIALS IN Al-Si-Mg SYSTEM BY ADDITION OF Sr, Ti AND B	235
39	ROMANIȚA TEODORESCU, MARIA GHEORGHE – THE TECHNOLOGY FOR HEAVY METALS FROM ELECTROPLATING SLUDGE VALORIFICATION, FOR ENVIRONMENT DEPOLLUTION	241
40	MIRELA SOHACIU, AVRAM NICOLAE – PROCESSING EXAMPLE FOR SUSTAINABLE DEVELOPMENT CONCEPTON METALLURGICAL FIELD LEVEL	249
41	DOINA RĂDUCANU, TOM SAVU, MIHAI TÂRCOLEA, IONEL NEGULESCU, ION CINCA, VASILE DĂNUȚ COJOCARU – SOLUTIONS FOR A DATA ACQUISITION SYSTEM IN MATERIAL SCIENCE	255

**ȘTIINȚA ȘI INGINERIA MATERIALELOR**

<b>CUPRINS</b>		
1	ROMEO CHELARIU, D.M. GORDIN, T. GLORIANȚ, IOAN CARCEA și COSTEL ROMAN - INFLUENȚA TRATAMENTULUI TERMIC ASUPRA STRUCTURII ALIAJULUI Ti6Al4V	1
2	MIHAI ALEXANDRU, ADRIAN DIMA, GHEORGHE BADARAU PETRICA VIZUREANU, NECULAI SCANTEIANU și DOINA HINCU - INFLUENȚA TRATAMENTULUI TERMIC ASUPRA STRUCTURII ALIAJULUI Ti6Al4V	9
3	MIHAI ALEXANDRU - CONTRIBUȚII TEORETICE ȘI EXPERIMENTALE PRIVIND OPTIMIZAREA PARAMETRILOR PROCESULUI DE LAMINARE	15
4	MIHAI ALEXANDRU, GHEORGHE BADARAU, PETRICA VIZUREANU, ALINA-ADRIANA MINEA, ROMICA MANEA și CONSTANTIN ALEXANDRU - TENDINȚE DE MODERNIZARE ÎN LAMINAREA LA RECE A PROFILELOR PARAPET TIP A	21
5	GH. T. POP și LILIANA VERESTIUC - CERCETĂRI PRIVIND PROCESAREA DE NOI MATERIALE BIOACTIVE	27
6	ADRIAN ALEXANDRU, SORIN IACOB STRUGARU, IOAN ALEXANDRU, LAURENTIU CIOBANU și SORIN TANASUCA - ANALIZA MICROGRAFICĂ CANTITATIVĂ COMPUTERIZATĂ A STRATURILOR DEPUSE PRIN DESCĂRCĂRI ELECTRICE ÎN IMPULS PE UN OȚEL BOGAT ALIAT DE SCULE	35
7	BAHRIN V. și HABA C. G - CONSIDERAȚII PRIVIND SISTEMUL DE CONTROL AL MODELULUI DE REFERINȚĂ PENTRU CONTROLUL VITEZEI UNUI MOTOR CC	41
8	GELU BARBU – STUDII REFERITOARE LA INFLUENȚA VIBRAȚIILOR ASUPRA COMPOZIȚIEI ȘI DURITĂȚII LINGOURILOR	47
9	GELU BARBU – CONOTAȚII ASUPRA DURITĂȚII LA PIESELE TURNATE DINAMIC	53
10	LIDIA BENEĂ, PIER LUIGI BONORA și FRANÇOIS WENGER - INVELISURI DIN Ni-SiC COMPOZITE NANOSTRUCTURATE OBTINUTE PRIN ELECTRODEPUNERE	59
11	VASILE BULANCEA, ȘTEFAN LĂCĂTUȘU și IOAN ALEXANDRU - UTILIZAREA ȘI CLASIFICAREA BIOMATERIALELOR	69
12	VASILE BULANCEA, IOAN ALEXANDRU, ADRIAN ALEXANDRU și DORIN CONDURACHE - TRATAMENTUL CRIOGENIC APLICAT OȚELURILOR	75
13	DORU CANTEMIR, LEONARDO BERTINI, MARCO BEGHINI și PAUL DORU BÂRSĂNESCU - DETERMINAREA EXPERIMENTALĂ A OVALIZĂRII GAURILOR UNOR PLACI PERFORATE SUDATE MULTISTRAT	81
14	HORIA CHIRIAC, ANCA-EUGENIA MOGA, CARMEN GHERASIM și DUMITRU-DANIEL HEREA - SINTEZA ȘI PROPRIETĂȚILE MAGNETICE ALE NANOPARTICULELOR DE Ni ȘI Ni-Fe PENTRU APLICAȚII BIOMEDICALE	87
15	HORIA CHIRIAC și DUMITRU-DANIEL HEREA - MICROPARTICULE MAGNETICE ACOPERITE CU POLIMER CA MARCHERI ÎN BIOSENZORI	93

16	VASILE COJOCARU-FILIPCIUC - PUNCT DE VEDERE PRIVIND NODULIZAREA GRAFITULUI	99
17	IOAN DAMIAN, VIOREL PALEU și SPIRIDON CREȚU - ACHIZIȚIE DE DATE EXPERIMENTALE PENTRU MĂSURAREA MOMENTULUI DE FRECARE DIN RULMENȚII CU BILE	109
18	ADRIAN DIMA, ALINA ADRIANA MINEA și IULIA MARGARETA DIMA - OPTIMIZAREA PROCESELOR DE INCALZIRE IN CUPTOARELE INDUSTRIALE	113
19	ADRIAN DIMA, IULIA MARGARETA DIMA și ALINA MINEA - STUDII PRIVIND CRESTEREA CARACTERISTICILOR MECANICE ALE ALIAJELOR TURNATE DIN ALUMINIUPRIN TRATAMENTE TERMICE	117
20	MARIANA LATU - CURENTUL INTR-UN FIR CIRCULAR 1D	121
21	VASILE MANOLE și IOAN ALEXANDRU - CONTRIBUȚII NUMERICE și EXPERIMENTALE ASUPRA REZISTIVITĂȚII ELECTRICE A OȚELURILOR ACOPERITE CU DIVERSE TIPURI DE STRATURI METALICE	127
22	VASILE MANOLE și IOAN ALEXANDRU - ASPECTE TEORETICE ASUPRA PROCESELOR FIZICE DE LA CONTACTUL A DOUĂ METALE	135
23	FLORIN MUNTEANU, MIHAI GAFIȚANU și PAUL BOTEZ - UZURA PRIN DEFORMARE VÂSCO-ELASTO-PLASTICĂ A UNEI CUPE COTILOIDE DIN UHMWPE DE LA NIVELUL UNEI ENDOPROTEZE TOTALE DE ȘOLD	143
24	POPO RODION – RESPINGEREA CIRCUITELOR KMOS CJ CARE POT AVEA DEFECTE	151
25	NASTACA TIMOFTE și BOGDAN NICOLAU - STUDIUL NISIPURILOR DE CAPUS (JUDETUL CLUJ) IN VEDEREA UTILIZARII IN TURNATORIE	157
26	URSE MARIA, CHIRIAC HORIA, GRIGORAS MARIAN și MOGA ANCA-EUGENIA - STUDIU COMPARATIV PRIVIND PROPRIETĂȚILE MICROSTRUCTURALE și MAGNETICE ALE STRATURILOR SUBȚIRI FePt și Fe/FePt	163
27	CRISTINA PRISACARIU, PAUL C. BUCKLEY și VICTOR ADRIAN PRISACARIU - ASPECTE PARTICULARE PRIVIND DEFORMAȚIA și RUPEREA UNOR NOI ELASTOMERI POLIRETANICI CU STRUCTURI DIBENZILICE, DE CRISTALINITATE VARIABILĂ	169
28	STEFAN GRIGORAS și CRISTEL STIRBU - IMBINARE PENTRU MATERIAL TUBULAR. CERCETARI TEORETICE SI EXPERIMENTALE	177
29	CRISTEL STIRBU și STEFAN GRIGORAS - SOLUTII TEHNICE PENTRU IMBINARI FILETATE ALE TEVILOR DE EXTRACTIE SI BURLANELE DE TUBAJ	183
30	LEANDRU-GHEORGHE BUJOREANU, VASILE DIA, VIORICA DAVID, CORNELIU MUNTEANU și FLORIN MAXIM - EFECTELE REVENIRII ASUPRA MICROSTRUCTURII și COMPORTĂRII LA TRACȚIUNE A UNUI ALIAJ Cu-Zn-Al CU MEMORIA FORMEI	191
31	FLORIN DIACONESCU, IOAN ALEXANDRU și IOAN CARCEADES - CERCETĂRI PRIVIND INFLUENȚA TEMPERATURII DE PREÎNCĂLZIRE A COCHILEI ASUPRA PROPRIETĂȚILOR MECANICE ALE UNUI BRONZ ANTIFRICȚIUNE TURNAT CENTRIFUGAL	195
32	FLORIN DIACONESCU și ROMEU CHELARIU - CERCETĂRI PRIVIND INFLUENȚA TEMPERATURII DE PREÎNCĂLZIRE A COCHILEI ASUPRA DISTRIBUȚIEI Pb ÎN PIESELE TURNATE CENTRIFUGAL DIN BRONZ Cu-Pb10-Sn10	201
33	FLORIN DIACONESCU și ROMEU CHELARIU - CERCETĂRI PRIVIND INFLUENȚA TURAȚIEI COCHILEI ASUPRA DISTRIBUȚIEI Pb ÎN PIESELE TURNATE CENTRIFUGAL DIN BRONZ CuPb10Sn10	207
34	DIACONESCU FLORIN, ALEXANDRU IOAN și CARCEA IOAN - CERCETARI PRIVIND INFLUENTA TURATIEI COCHILEI ASUPRA PROPRIETATILOR MECANICE ALE UNUI BRONZ ANTIFRICTIUNE TURNAT CENTRIFUGAL	211

35	FLORIN BRÎNZĂ, CRISTIAN PÎRGHIE, NICOLAE SULIȚANU – O POSIBILĂ METODĂ DE OBȚINERE A MATERIALELOR COMPOZITE POLIMER-METAL PRIN DEPUERE ELECTROLITICĂ	217
36	MIHAI GRAMATICU, SILVIU GABRIEL STROE – OPTIMIZAREA DURIFICĂRII PISELOR DE REVOLUȚIE PRIN INDUCȚIE	221
37	MIHAI MIHALCUT, PAUL-DORU BARSANESCU, CONSTANTIN BITCA – OBOSEALA LA SOLICITARI COMPUSE A UNOR OTELURI	229
38	PETRU MOLDOVAN, GABRIELA POPESCU, IOANA APOSTOLESCU, MARIANA ZSIGMOND – MODIFICAREA SI FINISAREA GRANULATIEI MATERIALELOR MULTIFUNCTIONALE IN SISTEMUL Al-Si-Mg PRIN ADITIA DE Sr, Ti si B	235
39	ROMANIȚA TEODORESCU, MARIA GHEORGHE – TEHNOLOGIE DE VALORIFICARE A UNOR METALE GRELE DIN NAMOLURI GALVANICE ÎN VEDEREA DEPOLUĂRII MEDIULUI	241
40	MIRELA SOHACIU, AVRAM NICOLAE – EXEMPLU DE OPERAȚIONALIZARE A CONCEPTULUI DE DEZVOLTARE DURABILĂ LA NIVELUL UNUI SEGMENT METALURGIC	249
41	DOINA RĂDUCANU, TOM SAVU, MIHAI TĂRCOLEA, IONEL NEGULESCU, ION CINCA, VASILE DĂNUȚ COJOCARU – SISTEM INTEGRAT DE ACHIZIȚII DE DATE ÎN ȘTIINȚA MATERIALELOR	255



## THE INFLUENCE OF SOME THERMAL TREATMENT PARAMETERS ON STRUCTURE AND MICROHARDNESS OF SOME TITANIUM ALLOYS

BY

ROMEO CHELARIU\*, D.M. GORDIN\*\*, T. GLORIAN\*\*,  
IOAN CARCEA\*, COSTEL ROMAN\*

**Abstract.** Among ( $\alpha + \beta$ ) titanium alloys, the Ti-Al-  $\beta$ -stabilizer alloys are largely used. The ( $\alpha + \beta$ ) titanium alloys are used in either annealed state or solution-treated and aged state. The most important technological parameters of solution-treating and aging are: heating rates, temperature and time of solution treating and aging, and quenching rates. This paper presents the experimental results concerning on the influence of solution-treating temperature and cooling rate after solution-treating on the morphology, size and shape of  $\alpha$  phase and  $\alpha/\beta$  ratio.

**Keywords:** titanium alloys, heat treatment, structure, microhardness

### 1. INTRODUCTION

In case of ( $\alpha+\beta$ ) titanium alloys, the control of structure is possibly by means of secondary metallurgical processes /1, 2/. Thus, the structure of these alloys depends on the chemical composition, heating temperature (above  $\beta$ -transus temperature or within ( $\alpha+\beta$ ) temperature range), and subsequent metallurgical processing (plastic deformation, thermal treatment, thermo-mechanical treatment, complex treatment etc) /1,2, 3, 4, 5/. The  $\beta$  phase decomposes by either nucleation followed by growth, which is a diffusion process, or martensitic transformation, diffusionless process /6/.

The first situation is observed for both the low cooling rates or isothermal maintenance /6/. The structure consists in coarse lamellae of  $\alpha$ -phase whose dimensions are depended by cooling rate, and which are found inside a retained  $\beta$  phase matrix /2,6/. The certain decomposition conditions of  $\beta$ -phase can results in a *Widmanstätten* type of microstructures /6, 7, 8/. The nucleation and growth of  $\alpha$ -phase separations take place on the  $\beta$ -phase grain boundaries. Thus, an unbroken network of allotriomorphic precipitates on the grain boundaries is developed. The morphology of precipitates is depended by their development conditions /6, 7, 8/. Also, the ultimate proportions of the two phases do not correspond necessary with those corresponding with the phase equilibrium. The  $\alpha/\beta$  ratio is depended on the decomposition conditions of  $\beta$ -phase /6/.

The second situation is observed when the quenching take places with high cooling rates from a temperature above  $\beta$ -transus temperature, because the  $M_s$

temperature of alpha-beta titanium alloys is great than the room temperature. In this case within the structure there is  $\alpha'$  or  $\alpha''$  martensitic phase [2, 6]. The two phases have the same chemical composition as well as prior  $\beta$ -phase, but they being supersaturated in alloying elements [6].

It is worthy of note that the mechanical properties of alpha-beta titanium alloys are depended by the proportion, size, shape and morphology of phases  $\alpha$  and  $\beta$  as well as the  $\alpha/\beta$  density interfaces [7, 9, 10].

Titanium alloys are heat treated for the following purposes [5]:

- ✓ To reduce residual stresses developed during fabrication (stress relieving);
- ✓ To produce an optimum combination of ductility, machinability, and dimensional and structural stability (annealing);
- ✓ To increase strength (solution treating and aging);
- ✓ To optimize special properties such as fracture toughness, fatigue strength and high-temperature creep strength.

The ( $\alpha+\beta$ ) titanium alloys can be heat treated by all types of heat treatment. To produce required values of titanium alloys properties, which depend on structure of alloys, involves the control of technological parameters of heat treatments.

When alpha-beta titanium alloys are solution treating and aging, the critic technological parameters are [1,11]:

- ✓ solution-treating temperature and time;
- ✓ aging temperature and time;
- ✓ heating rate for both solution-treating and aging;
- ✓ cooling rate for both solution-treating and aging.

## 2. MATERIALS AND EXPERIMENTAL METHODS

The Ti6Al4V, Ti6Al7Nb, Ti5Al2.5Fe, and Ti6Al2Nb1Ta1Mo alloys was supplied by IMNR Bucharest (Institute for Non-ferrous and Rare Metals) as cast condition. The as cast products from titanium alloys were processing by plastic deformation, turning and annealing (720...750 °C, 4 h, furnace cooling). The samples subjected the heat treatments were obtained by metal cutting of prior semi-finished products. To analyse the influence of both temperature and cooling rate of the solution-treating, the titanium alloy samples were subjected to the heat treatments shown in Table 1.

Table 1 Heat treatments and their technological parameters

Heat treatment	Technological parameters		Symbol
	Naming	Value	
0	1	2	3
Solution-treating	Heating rate, [°C/min]	12	TC1
	Temperature, [°C]	950...970	
	Time, [h]	1	
	Quenching medium	water	
	Cooling rate [°C/s]	180	

Table 1 (continued)

0	1	2	3
Solution-treating	Heating rate, [ $^{\circ}\text{C}/\text{min}$ ]	12	TC2
	Temperature, [ $^{\circ}\text{C}$ ]	950...970	
	Time, [h]	1	
	Quenching medium	furnace	
	Cooling rate, [ $^{\circ}\text{C}/\text{s}$ ]	0.05	
Solution-treating	Heating rate, [ $^{\circ}\text{C}/\text{min}$ ]	12	TC3
	Temperature, [ $^{\circ}\text{C}$ ]	850...870	
	Time, [h]	1	
	Quenching	water	
	Cooling rate, [ $^{\circ}\text{C}/\text{s}$ ]	180	
Solution-treating	Heating rate, [ $^{\circ}\text{C}/\text{min}$ ]	12	TC4
	Temperature, [ $^{\circ}\text{C}$ ]	850...870	
	Time, [h]	1	
	Quenching	furnace	
	Cooling rate, [ $^{\circ}\text{C}/\text{s}$ ]	0.05	
For all samples solution-treating			
Aging	Heating rate, [ $^{\circ}\text{C}/\text{min}$ ]	12	
	Temperature, [ $^{\circ}\text{C}$ ]	700...710	
	Time, [h]	2	
	Quenching	air	
	Cooling rate, [ $^{\circ}\text{C}/\text{min}$ ]	17	

The all treatments of solution-treating and aging took place inside of argon atmosphere furnace. The scheme of furnace is shown in Figure 1.

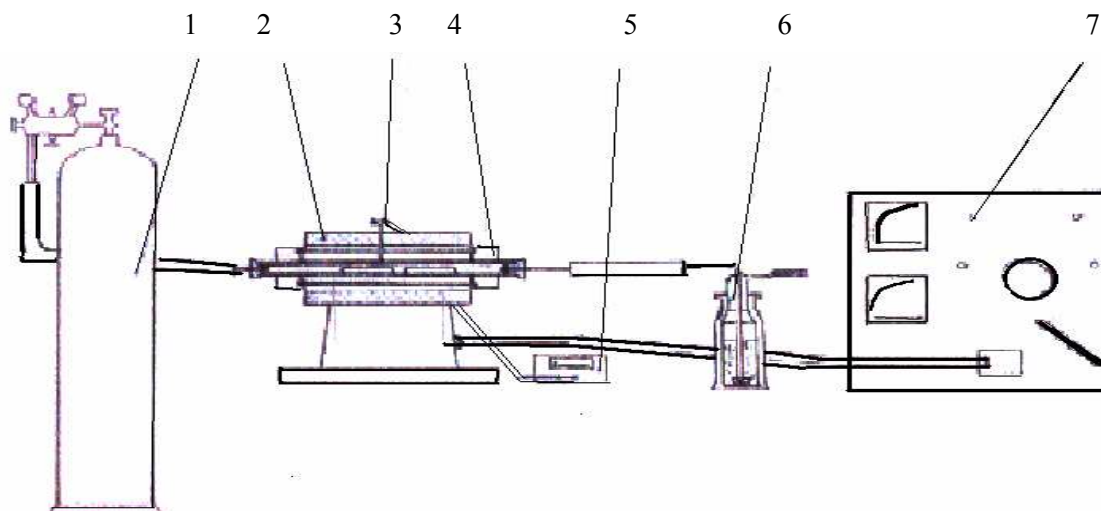


Figure 1. The scheme of inert atmosphere furnace: (1)-argon cylinder; (2) – heating electric furnace; (3) Pt/RhPt thermocouple; (4)-ceramic tube; (5) temperature recorder; (6)- glass vessel; (7) – adjustable electric energy source.

The chemical compositions of titanium alloys were determined by means of both rapid analysis and humid analysis to speciality laboratory of IMNR Bucharest. The actual chemical compositions were corresponded with the standard nominal chemical composition of titanium alloys.

Both optical microscopy and X-ray diffraction were used for the analysis of existence, size, shape and morphology of phases  $\alpha$  and  $\beta$ , and new phases, respectively. To prepare the microspecimens the mechanical grinding, intermediate etching, mechanical polish, and final etching were used. The optical micrographies were obtained by means of METAVAL optical microscope equipped with a camera. Qualitative X-ray diffraction analysis was performed to Institut National des Sciences Appliquées de Rennes (INSA Rennes).

The same samples were used to measure the microhardness of titanium alloys. To measure the microhardness a PMT 3 the microdurometer was used. The tests were performed using the following test conditions: 50 g load weight and 15 s loading time. To calculate the values of microhardness the following equation was used:

$$H_V = 19421.38 \cdot \frac{P}{N^2}, [\text{daN/mm}^2] \quad (1)$$

where  $P$  is the loading weight, in grams, and  $N$  represents the number of divisions measured on the diamond-pyramid impression.

To characterize the effects of temperature and cooling rate of solution-treating on the microhardness of titanium alloys, the two-factor factorial design of experiment was used. The experimental data were statistical analyzed using a model with fixed effects.

### 3. EXPERIMENTAL RESULTS

The representative micrographies and diffractograms are shown in Figures 2÷4.

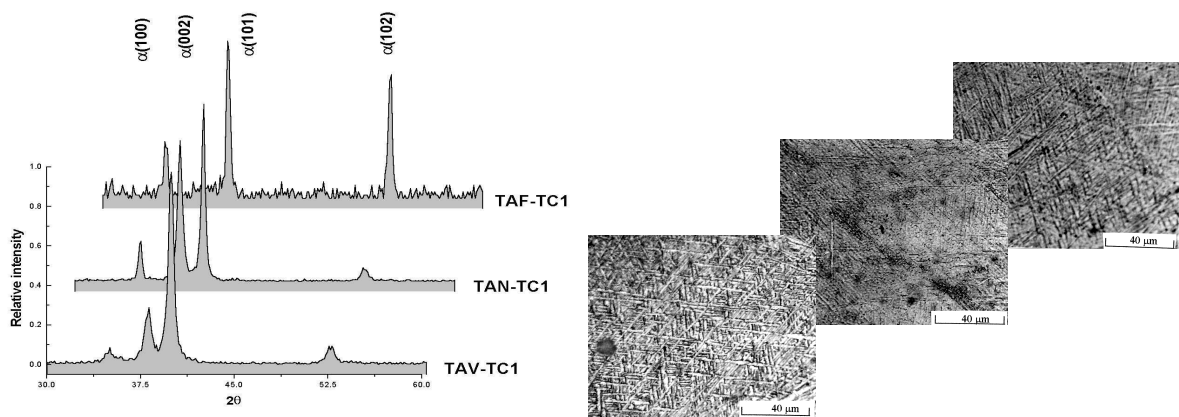


**Figure 2.** Diffractograms and microstructures of titanium alloys subjected TC1 heat treatment.

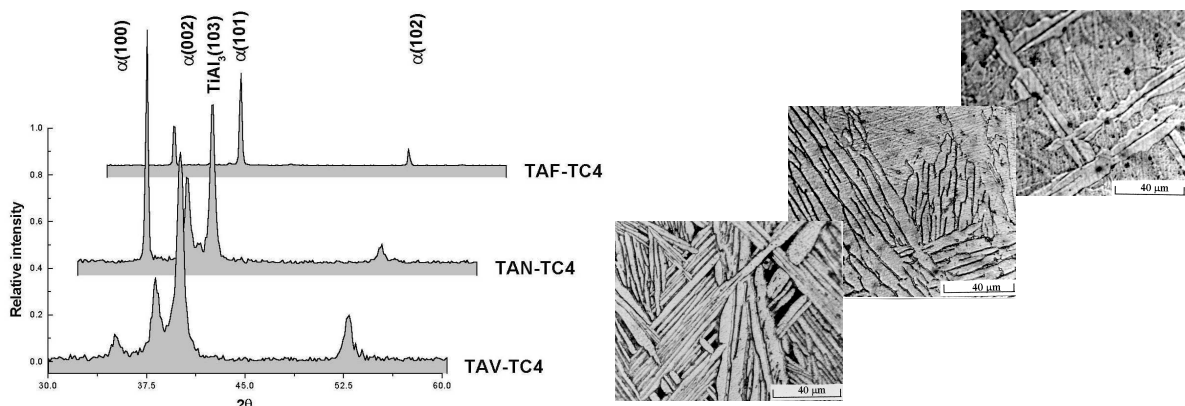


**Figure 3.** Microstructures and diffractograms of titanium alloys subjected TC4 heat treatment.

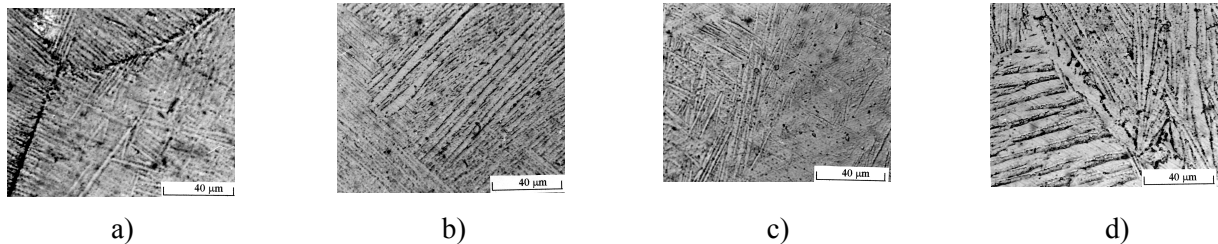


**Figure 4.** Microstructures of Ti6Al2Nb1Ta1Mo alloy heat treated: a) TC1; b) TC2; c) TC3; d) TC4.

The microstructures analysis shows that in the case of the water cooling, after TC1 solution-treating followed by aging, either a fine lamellar  $\alpha$ -phase or martensitic morphologies were developed. The furnace cooling after the same solution-treating temperature and time (TC2 heat treatment) determined lamellar morphologies of  $\alpha$ -phase with different sizes to develop.

In the case of decrease of solution-treating temperature in conditions of the same treating time, coarse lamellar morphologies of  $\alpha$ -phase were developed. A high cooling rates (TC3 solution-treating and aging) determined short lamellae by comparison with the lamellae developed by low cooling rates (TC4 solution-treating and aging).

In the case of TC2 and TC4 heat treatments, the qualitative X-ray diffraction analysis made evident that the  $TiAl_3$  intermetallic compound was developed. This fact was possibly because of low cooling rates, which allowed the intermetallic compound to be formed.

The experimental data of mean values of microhardness are shown in Table 2, and the results of statistical analysis of the fixed effects model in the Table 3.

Table 2 The mean values of microhardness

Alloy	Microhardness (mean value (st.dev.)), [daN/mm <sup>2</sup> ]			
	Heat treatment			
	TC1	TC2	TC3	TC4
Ti6Al4V	248.96 (28.87)	206.26(22.06)	230.40(21.03)	224.34(21.49)
Ti6Al7Nb	245.75(23.17)	192.89(16.14)	230.27(22.08)	195.17(17.17)
Ti5Al2.5Fe	265.67(21.15)	208.00(21.87)	238.71(15.01)	193.24(21.34)
Ti6Al2Nb1Ta1Mo	250.16(24.36)	189.37(13.48)	243.50(11.45)	202.59(25.89)

Table 3 The results of statistical analysis

Alloy	Processing parameters						Result
	Temperature		Cooling rate		Interaction		
	F <sub>c</sub>	F <sub>t</sub>	F <sub>c</sub>	F <sub>t</sub>	F <sub>c</sub>	F <sub>t</sub>	
Ti6Al4V	0.003	4.04	16.178	4.04	9.288	4.04	Cooling rate- significant Interaction-significant
Ti6Al7Nb	1.686	4.04	74.234	4.04	3.048	4.04	Cooling rate-significant
Ti5Al2.5Fe	16.639	4.04	101.727	4.04	1.425	4.04	Cooling rate-significant Temperature-significant
Ti6Al2Nb1Ta1Mo	0.420	4.04	100.721	4.04	3.849	4.04	Cooling rate-significant

The mean values of microhardness are represented graphically in Figure 5.

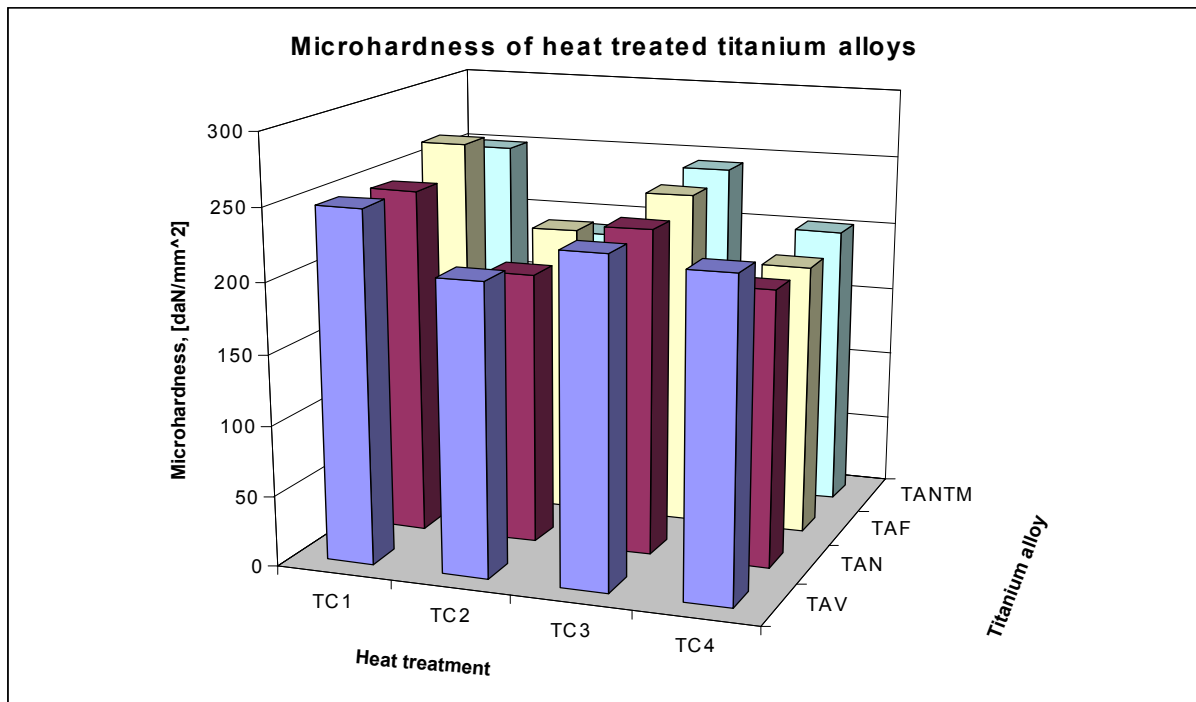


Figure 5. Mean values of microhardness of heat treated titanium alloys.

The statistical analysis of experimental data shows that the cooling rate after solution-treating, regardless of chemical composition of titanium alloy, has the great importance when the microhardness is considered. Depending on chemical composition, either temperature of solution-treating or interaction between two process parameters, influences the microhardness of titanium alloy. These observations are very good seen in the graph from Figure 5.

#### 4. CONCLUSIONS

The  $\alpha$ -phase morphologies of titanium alloys are influenced by heat treatments. Thus, the thickness of  $\alpha$ -phase lamellae is influence both of solution-treating temperature and cooling rate. Thus, the high cooling rates lead to a fine lamellar morphology of  $\alpha$ -phase, in contrast with low cooling rates that lead to a coarse lamellar morphology.

The influence of cooling rate is very important for the microhardness of titanium alloys, regardless of chemical composition of these.

Received April 15<sup>th</sup>, 2005

\* The "Gh.Asachi" Technical University of Iasi

\*\* Institut National des Sciences Appliquées de Rennes, France

#### REFERENCES

1. Chelariu, R. , *Cercetări privind sinteza și analiza structurală a materialelor metalice medicale*, Teză de doctorat, Universitatea Tehnică " Gh. Asachi", Iași, 2001.

2. Wagner, L., Gregory, J.K., *Improve the fatigue life of titanium alloys*, Part I, *Advanced Materials & Processes*, nr.3, 1994, pp. 36v, W,J,Z.
3. Donachie, M.J.Jr., *Introduction to Titanium and Titanium Alloys*, Titanium and Titanium Alloys, Source Book, Matthew J, Donachie, Jr (Ed), American Society for Metals, 1982, pp.3-9.
4. \*\*\* *Relation of Properties to Processing for Wrought Titanium Alloys*, Titanium and Titanium Alloys, Source Book, Matthew J, Donachie, Jr (Ed), American Society for Metals, 1982, pp.211-221.
5. \*\*\* *Heat Treating of Titanium and Titanium Alloys*, Titanium and Titanium Alloys, Source Book, Matthew J, Donachie, Jr (Ed), American Society for Metals, 1982, pp. 330-341.
6. Angelier, C., *Métallurgie du titan et de ses alliages*, *Traitement Thermique*, nr.286/287, 1995, pp.59-67.
7. Kohn, D.H., *Materials for Bone and Joint Replacement*, *Materials Science and Tehnology*, vol.14, Medical and Dental Materials, VCH Verlagsgessellschaft mbH, Weinheim (FRG), 1992, pp. 29-110.
8. Ohmori, Y., Nakai, K., Ohtsuba, H., Tsunofuri, M., *Formation of Widmanstätten Alpha Structure in a Ti-6Al-4V Alloy*, *Materials Transactions, JIM*, vol.35, nr.4, 1994, pp. 238-246.
9. Kawabe, Y., Muneki, S., *Strengthening and Toughning of Titanium Alloys*, *ISIJ International*, vol.31, nr.8, 1991, pp.785-791.
10. Niinomi, M., Kobayashi, T., *Toughness and Strenght of Microstructurally Controlled Titanium Alloys*, *ISIJ International*, vol.31, nr.8, 1991, pp. 848-855.
11. Polkin, I.S., Kolachev, B.A., *Transformation de phases, traitements thermiques et thermomécanique pour les alliages de titane*, *Traitement thermique*, nr,241, 1990, pp.35-39.

#### INFLUENTA TRATAMENTULUI TERMIC ASUPRA STRUCTURII ALIAJULUI Ti6Al4V

(Rezumat)

Aliajele de titan bifazice cu cea mai largă utilizare în diverse domenii sunt cele pe baza sistemelor ternare Ti-Al-element  $\beta$  stabilizator. Aliajele de titan bifazice se utilizează fie în stare recoaptă, fie în stare călită prin punere în soluție urmată de îmbătrânire. În cazul tratamentelor termice de călire de punere în soluție și îmbătrânire, pe lângă viteza de încălzire atât la călire cât și la îmbătrânire, temperatura și timpul de menținere și viteza de răcire la îmbătrânire, un rol important îl au și temperatura și timpul de menținere la călire, precum și viteza de răcire la călire. Prezenta lucrare prezintă rezultatele cercetărilor privind influența temperaturii de menținere și a vitezei de răcire la călire asupra structurii și microdurității unor aliaje de titan.





## THEORETICAL AND EXPERIMENTAL CONSIDERATIONS CONCERNING THE DETERMINATION OF THE OPTIMUM OF THE COLD ROLLING FORCE

BY

MIHAI ALEXANDRU\*, ADRIAN DIMA\*\*, GHEORGHE BADARAU\*\*  
PETRICA VIZUREANU\*\*, NECULAI SCANTEIANU\*\* and DOINA HINCU\*

**Abstract:** Because the cold rolling mills use a considerable quantity of energy and materials it appears the necessity to optimise the technological parameters that are being involved in the process. The paper shows the way of optimisation of the cold deformation force using a technical optimization criterion of the deformation limit and the practical solving of the problem with the program ALGOR 9.0 FEA Processing system.

**Key words:** cold forming, optimization, limit deforming, ALGOR 9.0 program package

The main stages in solving the optimization problems are:

- the obtaining the mathematical model of the process;
- the choice and the determination of the technical and economical criteria;
- the building of the objective function of the process;
- finding the optimum.

The mathematical model of the process represents a system of relations that link the variable of the processes that take place inside the semi-product during rolling.

The cold deformation force is one of the main parameters of the process and for its determination one can use the relation:

$$F = \frac{\pi E_c (\sqrt{\delta + \delta_1 + \delta_2} + \sqrt{\delta_2})^2 (\delta - R \arccos^2(1 - \frac{\delta}{2R}))}{16R(1 - \nu) \arccos(1 - \frac{\delta}{2R})}, \text{ (daN/mm}^2\text{)} \quad (1)$$

Analysing the relation we can see that the value of the force depends on the constructive characteristics and those of material of the equipment as well as of the semiproduct itself and also by the tension state created.

Optimization is done using the technical criteria of optimization for the limit forming  $\varepsilon^*$ . This is obtained by using the plastical instability theory and by the influence of the non uniformity factors.

Solving with the finite element method enables the determination of the forming limit  $\varepsilon^*$  in each finite element of the part. The strip between the tensions represents the general law of Hook's for homogenous and isotropic materials.

Using the relation of the cold forming force and the optimum value of the forming limit determined by the theory of plastic instability one obtains the optimum values of the tension

The optimum value of the forming force must satisfy the following conditions:

$$\text{Opt}_x(x); x \in E^n$$

$$h_j(x) = 0; j = 1, 1$$

$$g_j(x) \leq 0; j = j+1, m$$

$x$  is the vector of variables

Optimization is being achieved in the following stages :

- a point  $P_1(x_{i1})$   $i=1, n$  is chosen in the space having  $n$  dimensions in which we define this function;
- the value of a size is being taken, knowing that the accuracy of estimations is proportional with  $1/a$ ;
- $P_j(x_{ij})$   $j=2, n+1$  is determined in the condition that the distance between two established points is constant and equal with  $a$ ;
- we calculate  $f(P_1) \dots f(P_{n+1})$  and then we determine the most unfavourable value:

$$X_i^{(N)} = \left( \frac{2}{n} \left( \sum_{j=1}^{n+1} x_i^{(j)} - x_i^{(R)} \right) \right) - x_i^{(R)} \quad (2)$$

where:  $x_i^{(N)}$  is the coordinate of the new point;

$x_i^{(R)}$  is the coordinate of the rejection point that gives the worst value for  $f$ .

The practical solution was obtained by using a modified program of the Algor 9.0 processing system for a part «guard rail profile type A» after the german standard – RAL – RG 620 U ST 37 – 2 DIN 17100 – 80.

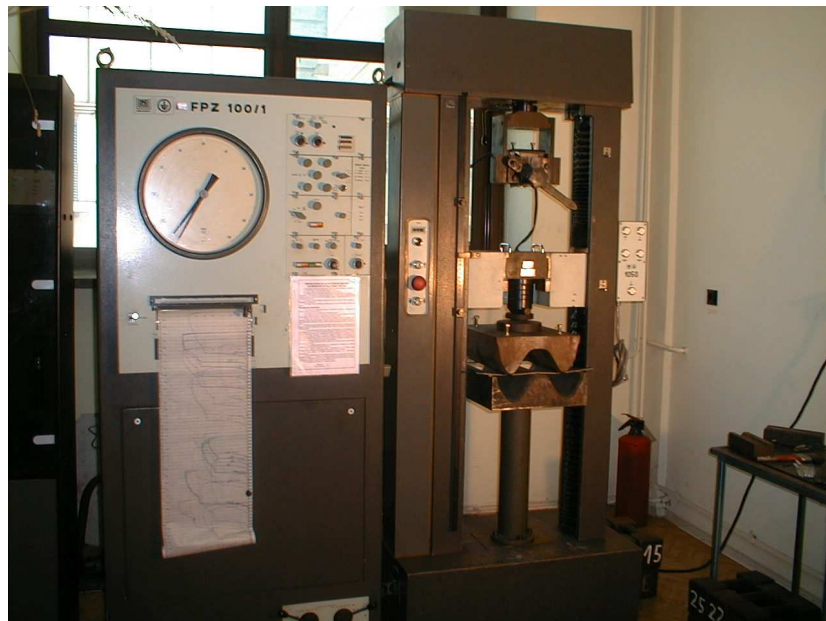


Fig. 1. The universal mechanical testing machine Heckert –FPZ 100/10

For the study of the deformability and determination of the parameters it was used the univesal mechanical type Heckert FPZ 100/1, made in Germany for which a special palte was designed fig.1.

The main characteristics of the machine are :

Maximum range of force	100 000 N
Measurement range for the traction force	0- 100 000 N
Transducers for the traction force for smaller domains	0 – 40 N 0 – 400 N 0 – 10 000N
Force measuring error	≤ 1% (precision class 1) according to EN 10002-2 -95
Donenii de masurare pentru forta la compresiune	0- 100 000 N
Mobile cross rail range	10 – 935 mm
Speed range of the cross rail	20 μm – 600 mm/min
Connection frequency	0,1 Hz
Operation power	4 KVA
Supplying tension	380 V
Speed of the diagram drawing device	2/4/10/20/60/120/300/600 mm/min
Testing programs	F-Δl (force – displacement) F/t (constant growing of force) Δl/t (constant growing of the elongation)
Tests that can be performed	- traction test - compresion test - cyclic fatigue test

There were used samples form Ol 37 k sizes 470x20x3 mm, material used at the fabrication of the type A profile and imposed by the present rules.

We proposed to obtain a profile of this kind but shorter (20mm) and for which to practicaly determine the necessary force for deformation and study the phenomena that occur during deformation.

The developed length calculated and practicaly correlated is  $470^{\pm 1}$  mm, lungimea profilului de 20 mm si grosimea bandei de 3 mm.

The die was designed and executed for obtaining the finite shape of the rail gurd type A profile, having the possibility to obtain any intermediary shape identical with those obtained during rolling. The die was formed from two parts as it can be seen in the photograph.

So, in a number of tests it was dertermined  $F_{max}$  having a value of approximative 30 KN.

Knowing  $F_{max}$ , it was equally devided in the 13 deformation steps of the rolling mill, resulting a force of 2,3 KN/step.

step	0 1	0 2	0 3	0 4	0 5	0 6	0 7	0 8	0 9	10	11	12	13	14
Fstep [kN]	2.3	4.6	6.9	9.2	11.5	13.8	16.1	18.4	20.7	23	25.3	27.6	29.9	30
h profile [mm]	38	41	43	49	55	61	63	69	71	73	76	78	79	79

From the graph shown in Fig.2 one can see the linear zone when at the value 2,3 KN, h profile has the magnitude 38 mm.

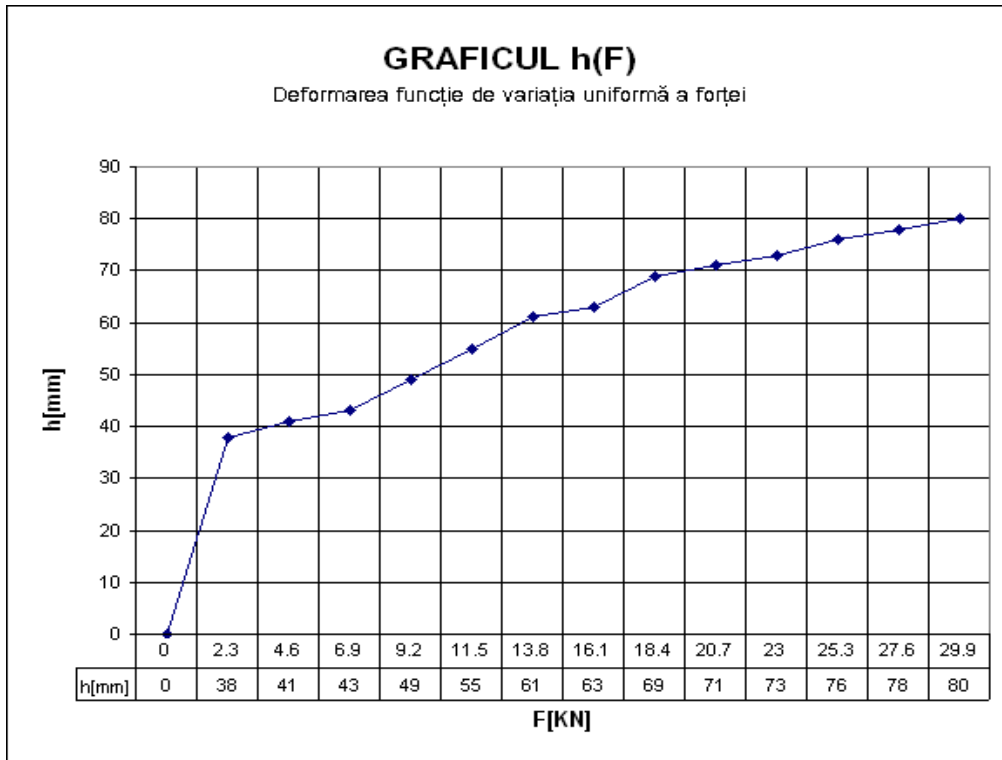


Fig. 2 Variation of the de formation as a function of the uniform increment of force

Using this deformation method one can see that at small values of the force significant values of  $h$  can be obtained leading at the idea of reducing the number of deformation steps.

This was the basis of the calculus and new designing of the new rolling mill, obtaining a perfect optimization, reducing the numebr of deformation steps from 13 to 9 and a reduction of the efforts on each step.

The only restriction at the limiting of the steps number was the value imposed by the distance between cajes (imposed) and the rapport between the diameters of inferior and superior cilindrs.

Starting from these imposed characteristics of the rolling mill, from the constructive point of view, the maximum value of profile tightening (profile width as a function of jump) from step to step it can not overcome the value of 15 mm (7,5 mm left - right) until it reaches the focus of the step (centre of roles).

For sizes bigger than 15 mm the profile margins are strongly affected even cut out when the sheet touches the superior cilinder and until it reaches the focus.

So, for avoiding these phenomena as well as for the sheet centering, instead of horizontal cages there were mounted vertical cages, easy to regulate and more simple as a construction.

Starting from the experimental dates obtained using MAT CAD 2002 we determined the mathematical equations on the basis of which one can build the graphs  $F(h)$ , Fig.3 and  $h(F)$ , Fig.4 and making them able to use for every cold formed semi-product on a rolling mill constructed in this way.

Coefficients 1 - 8

-5.7509e-027 4.9602e-024 -1.9936e-021 4.9585e-019 -8.5485e-017 1.0842e-014 -  
1.0479e-012 7.8886e-011

Coefficients 9 - 16

-4.6869e-009 2.2138e-007 -8.3330e-006 2.4947e-004 -5.9021e-003 1.0910e-001 -  
1.5481e+000 1.6415e+001

Coefficients 17 - 21

-1.2484e+002 6.3696e+002 -1.9287e+003 2.5758e+003 -1.5044e-001

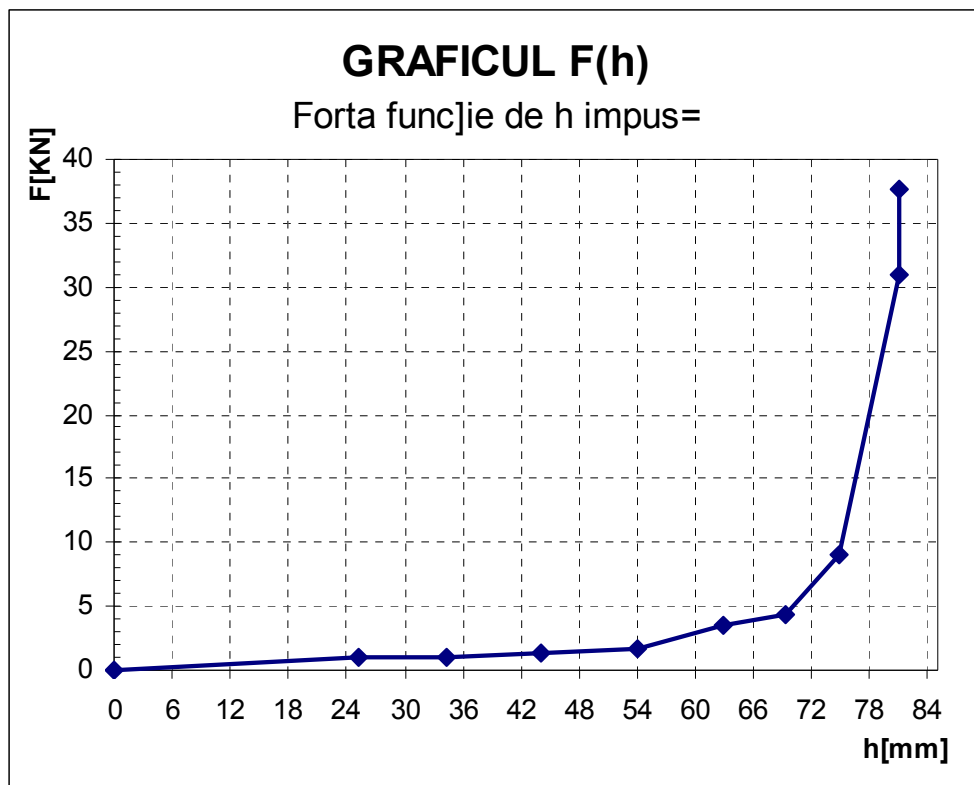


Fig. 3 Variation of force as a function of imposed deformation

Coefficients 1 - 8

-9.3162e-010 1.6572e-007 -1.2402e-005 5.0842e-004 -1.2481e-002 1.8893e-001 -  
1.7584e+000 9.7558e+000

Coefficients 9 - 13

-3.0146e+001 4.5683e+001 -3.1284e+001 4.2506e+001 4.7939e+000

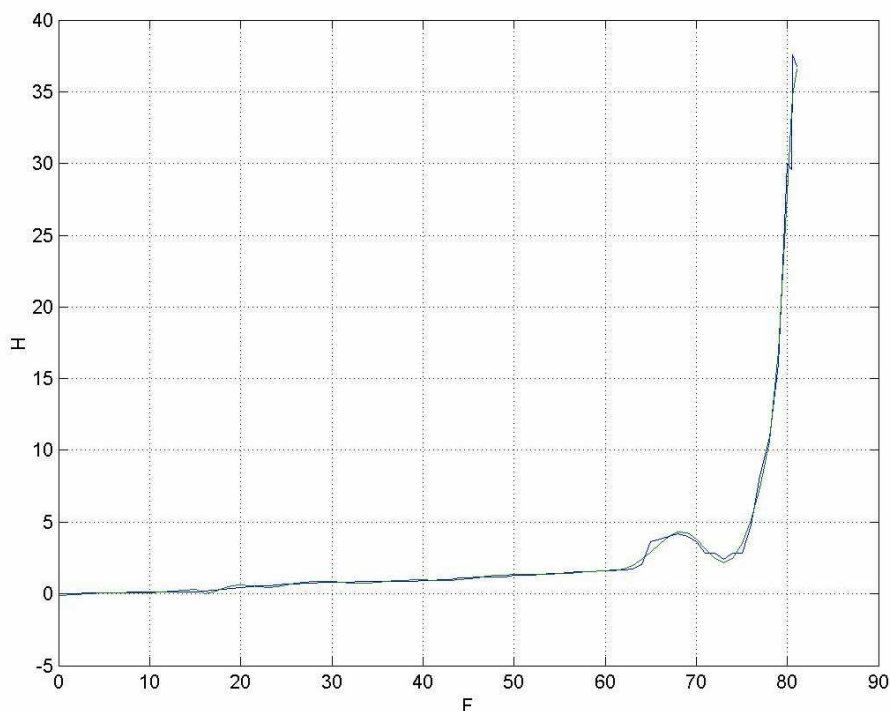


Fig. 4 Variation of deformation as a function of imposed force

Received: May 17 2005

\* The "Stefan Procopiu" School Group, Iasi

\*\* The "Gh.Asachi" Technical University from Iasi

#### REFERENCES

1. Cazimirovici E. –Calibrarea cilindrilor de laminare–Ed. Did. si Ped.,Bucuresti 1995
2. \*\*\* - Cold Strip Mill Profile, Flatness and Surface Seminar Proceedings, february 25-26 1992
3. Belzo O., Fokt V.- Fabricarea profilelor laminate la rece din banda de otel - Iasi
4. William L. Roberts – Cold Rolling of Steel – New York
5. Weber E. – Stadiul actual si tendinte noi in tehnica laminarii, Stahl Eisun, nr.8 1987, pg. 359 - 366
6. Banabic D., Ioachim R.D. – Deformabilitatea tablelor metalice subtiri. Metoda curbelor limita de deformare., Bucuresti 1992
7. \*\*\* - Teoria e practica della laminazione – Italian Partnership of Metallurgy, Milano 1982
8. Alexandru M. – Contributii teoretice privind imbunatatirea parametrilor constructivi si functionali ai unei linii de laminare la rece – Teza de doctorat, Iasi 2004

#### CONSIDERATII TEORETICE SI EXPERIMENTALE PRIVIND DETERMINAREA OPTIMA A FORTEI DE LAMINARE LA RECE

##### (Rezumat)

Rezumat: Deoarece liniile de laminare la rece utilizeaza o cantitate cosiderabila de energie electrica si materiale, apare ca necesara optimizarea parametrilor tehnologici ce intervin in cadrul procesului. Lucrarea arata caile de optimizare a fortei de deformare la rece utilizand un criteriu tehnic de optimizare a limitei de deformare si rezolvarea practica a problemei, cu programul modificat ALGOR 9.0 FEA Processing system.

## THEORETICAL AND EXPERIMENTAL CONTRIBUTIONS CONCERNING THE OPTIMATION OF THE ROLLING PARAMETERS

BY

MIHAI ALEXANDRU

**Abstract:** The paper shows an approach of the optimization of the parameters of the rolling process. There have been calculated in an analytical manner the deformation forces. Using the calculus relations of the Bland and Ford model adapted for the cold rolling and using an original program there resulted values of the rolling force on the width unit in good agreement with the experimental values obtained

**Keywords:** optimization, cold rolling, mathematical model

For the optimization of the parameters of the rolling process we have calculated in an analytical way the deformation forces, in which all the expressions that are constant were introduced as they are and the other were calculated using the dependency relations.

After a complex research we came along with a relation having the shape below. The relation is being derived from the Bland and Ford model adapted for the cold rolling and using an original program.

$$P = \frac{\pi E_c \left( \sqrt{\delta + \delta_1 + \delta_2} + \sqrt{\delta_2} \right)^2 \cdot \left( \delta - R \arccos^2 \left( 1 - \frac{\delta}{2R} \right) \right)^2}{16 R \left( 1 - \nu^2 \right) \arccos^2 \left( 1 - \frac{\delta}{2R} \right)} \quad (1)$$

We could do in this particular manner a comparison between the experimental values and the ones obtained in the analytical way for the rolling force on width unit (fig. 1 and fig. 2) remarking a good correlation of the mathematical model Bland and Ford with the programmed experiment.

Valorising the experimental results we determined the functions of variation and the regression equations that correlate the cold plastic deformation process of the profile with the compression test.

In table 1 there are shown the values of the growing coefficient of the force in the deformation steps for each of the seven samples studied as a function of the length growing.

For the string of dates shown in the table the regression equation was driven, a polynomial having the following shape:

$$L = -0,0012F^3 + 0,044F^2 + 0,3672F + 0,9643 \quad (2)$$

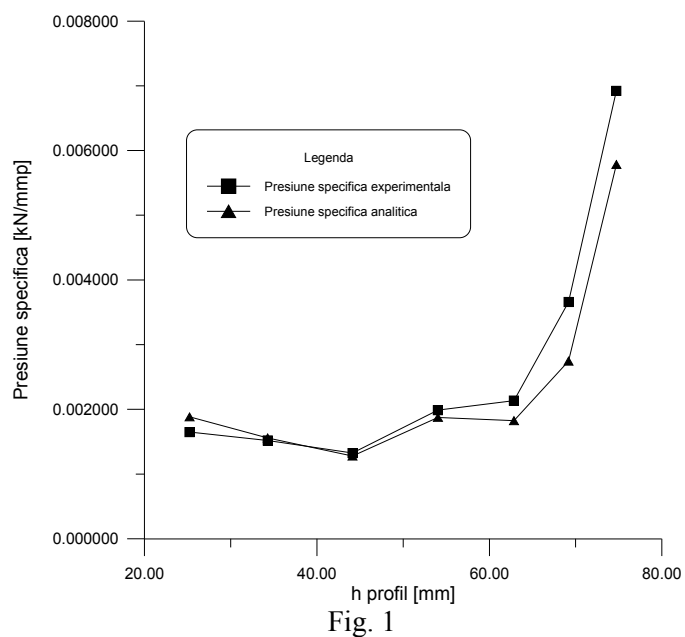


Fig. 1

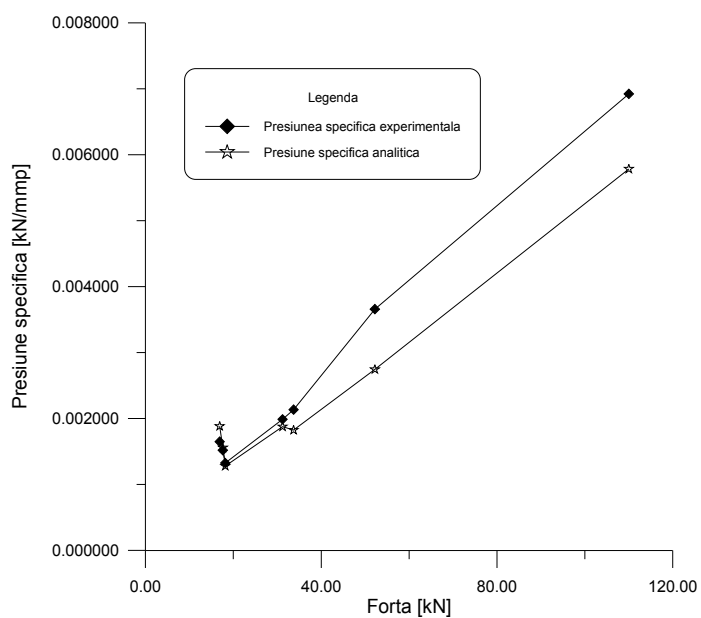


Fig. 2

Table 1

The coefficient of growing of the deformation force	The growing of the length of the samples
1.13	1.09
1.16	1.3
1.35	1.53
1.37	1.12
1.43	1.23
1.53	1.76



Table 1 (continued)

1.56	2
1.63	1.55
1.91	2.7
2.09	1.99
2.19	1.52
2.42	2.18
2.51	1.67
2.81	3.05
3.31	3.34
10.12	6
12.87	12
13.38	9.2
16.64	16.25
25.38	18.35
31.51	20.07

The graphic shows the 21 experimental points as well as the representation of the regression associated with these 21 points (table 1 and figure 3):

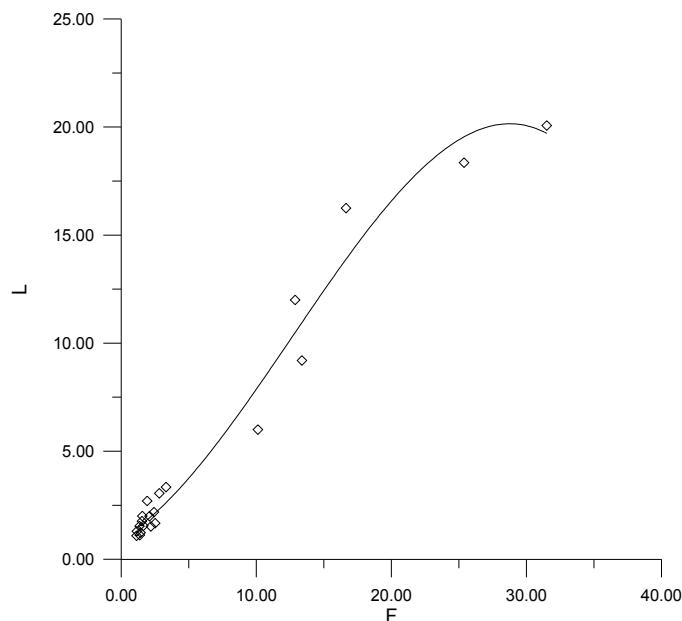


Fig. 3

The maximum value for the regression function is  $L = 19,39$  si  $F = 27,81$ .

There were considered a string of 9 experimental points, considered as representatives, for which the following dependency relation was determined:

$$L = -0,0013F^3 + 0,051F^2 + 0,28F + 1,25 \quad (3)$$

In table 2 there are shown the 9 points considered as representatives.

Table 2

The coefficient of growing of the deformation force	The growing of the length of the samples
1.16	1.3
1.56	2
3.31	3.34
10.12	6
13.38	9.2
12.87	12
16.64	16.25
25.38	18.35
31.51	20.07

The figure 4 presents the experimental points as well as the regression variation polynomial curve associated.

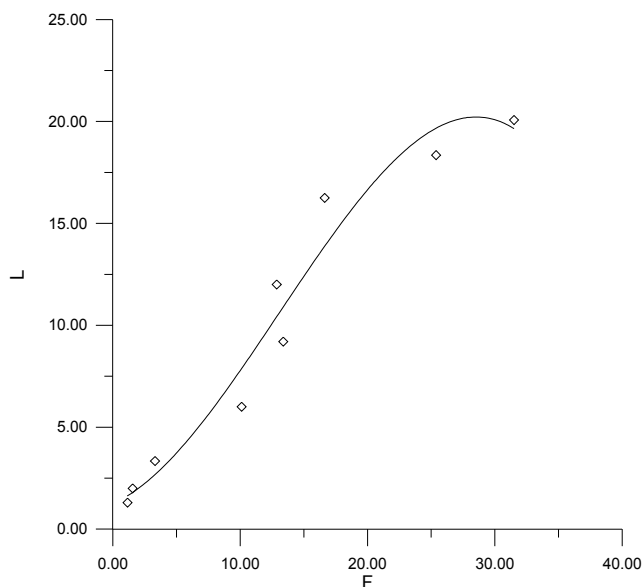


Fig. 4

The maximum value of the regression function is  $L = 20,56$  si  $F = 28,46$ .

Both the regression equation and the maximum of the function ensures that the 9 points are representatives for the chosen domain.

The theoretical curve based on the experimental dates comprises the phenomenon, demonstrating the correspondence in the studied field, expressing the close interdependency between the linear sizes variation and the deformation forces.

---

---

**CONTRIBUȚII TEORETICE ȘI EXPERIMENTALE PRIVIND OPTIMIZAREA PARAMETRILOR  
PROCESULUI DE LAMINARE**

**(Rezumat)**

Rezumat: Lucrarea prezintă o abordare a optimizării parametrilor procesului de laminare. S-au calculat analitic forțele de deformare, în care toate expresiile care sunt constante au fost introduse ca atare, iar celelalte sunt calculate utilizând relațiile de dependență. Utilizând relațiile de calcul al modelului Bland și Ford adaptat pentru laminarea la rece și folosind un program original, au rezultat valori ale forței de laminare pe unitatea de lățime în concordanță cu valorile experimentale obținute.



## **MODERNIZATION TRENDS IN THE COLD ROLLING OF THE RAIL GUARD PROFILE TYPE A**

**BY**

**MIHAI ALEXANDRU\*, GHEORGHE BADARAU\*\*, PETRICA VIZUREANU\*\*,  
ALINA-ADRIANA MINEA\*\*, ROMICA MANEA\* and CONSTANTIN ALEXANDRU\*\***

**Abstract:** The paper refers to the study of the rail guard profile type A, cold formed and pinched in flow. It aims to underline the main preoccupations of the producers of this kind of profiles in view of meeting the higher quality of products the market requests.

**Keywords:** cold rolling, modernization, optimization

### **1. Introduction**

In the cold rolling profile manufacturing, in the last decay, it was seen an interesting behavior of the market. So, small enterprises appeared having one or two products in the production of which they are completely specialised. From the point of view of the quality and price of the products these enterprises are competitive becoming a real threat for the big rolling mills.

In these circumstances appeared some technical reactions that we will present in this paper.

The lines of pinched profiles are based on the same technological principle as the classic rolling mills for profiles. Actually these lines have the same fundament with the ones for light profiles.

A presentation of a typical technological scheme and of the components of a rolling line is achieved in the figure. The calibration of the rolling mills can be different as well as the way of obtaining of the holes necessary for mounting.

The elements of originality brought by the authors of the paper in some previous studies consists mainly in the optimization of the number of cages of deformation and geometry of the rolling bodies in view of perfecting the working performances, rolling parameters.

### **2. Modern preoccupations concerning the directions of modernisation and the trends of development in the field of cold rolling.**

In the present paper, after analysing a great number of specialty publications, we draw the conclusions that the main directions in which the specialists and researches work do not imply the construction of new rolling units but the modernisation of the existing ones.

The modernisation of the Sakai rolling mill can be included in this current. This modernization started in 1989 by the introduction of the fourth cage beside the three existing ones (3TM) and it continued with the introduction of the continuous decapation line (2CP). Once these modifications made there were achieved important technological modifications too. The aim of these important modifications is the enhancing of the productivity, quality improvement and diversifying of the products.

The scheme of positioning of the modernised line is shown in the next figure.

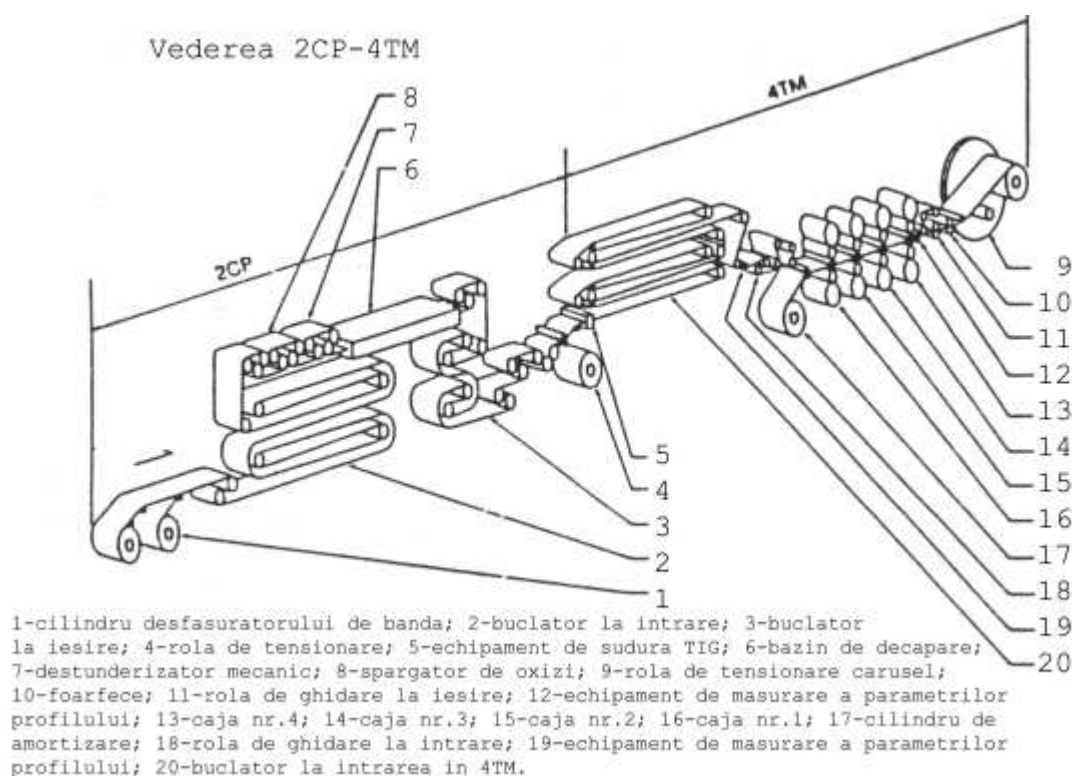


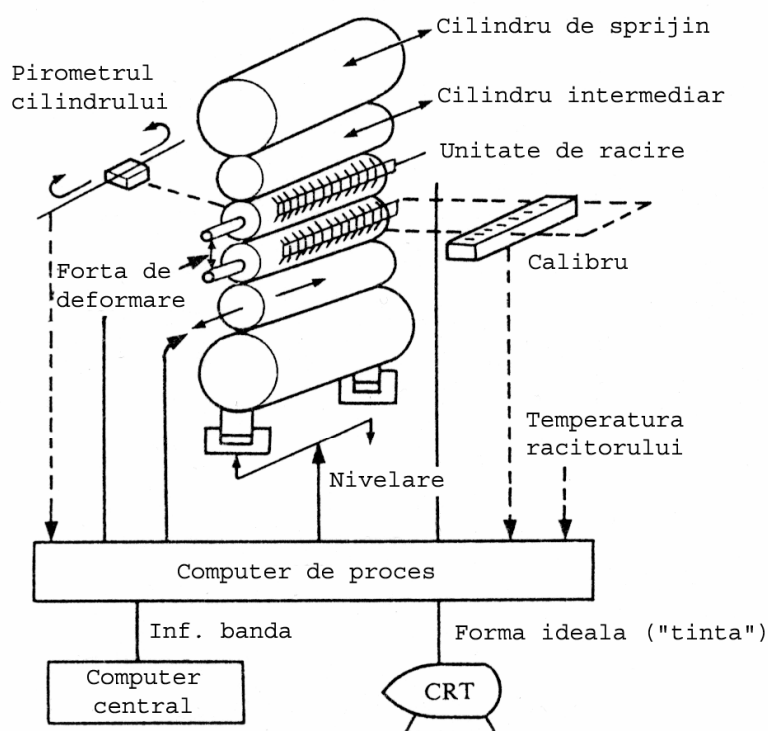
Fig. 1 The scheme of principle of the assembly 2CP – 4TM 1 - cylinder of the strip developer; 2 - entrance loop maker; 3 - exit loop maker; 4 – tensioning roll; 5 – TIG welding equipment; 6 – decapation tank; 7 – mechanical cleaner; 8 – oxides breaker; 9 – tensioning carousel roll; 10 – scissors; 11 – guiding roll; 12 – profilometer; 13 – cage no.4; 14 – cage no. 3; 15 – cage no. 2; 16 – cage no. 1; 17 – shock absorber cylinder ; 18 – guiding roll; 19 – profilometer; 20 – loop maker at the 4TM entrance.

After the modernisation and coupling of the lines 2 CP and 3 TM into a continue unit 2 CP – 4 TM, the quality and the productivity were significantly improved. An indicator that ascertain the quality improvement is the rate of the finite products achieved before the deformation line that enhanced with 0,6 %. In what concerns the productivity the enhancement was spectacular overcoming the value of 50 % if one includes the production obtained in independent operations.

The update of the rolling mill of 2030 mm at British Steel from Port Talbot was an another important project in the field.

The aim of the modernisation of the rolling mill, fig. 2 was to adjust the quality of the products at the higher requests of the steel sheet users by improving the tolerances and the surface quality.

The steel producers have introduced cages having six cylinders in height and cooling units, both having a good capacity of shape control. Sometimes these systems can be combined. The same type of methods gave satisfaction at the Nagoya Works at the number 3 rolling mill. Actually there were used the control of bending of working cylinders, intermediary cylinders, conventional elements of control that are symmetrical on the horizontal in what concerns the control capacity and which compensate in sectors. The other measures, using level regulation with screws being non symmetrical in the horizontal plan and without linear compensation fig. 2. These methods did not bring the desired performances in what concerns the high order deviations of shape as the thermal influenced zones.



Cofiguratia sistemului de control al formei

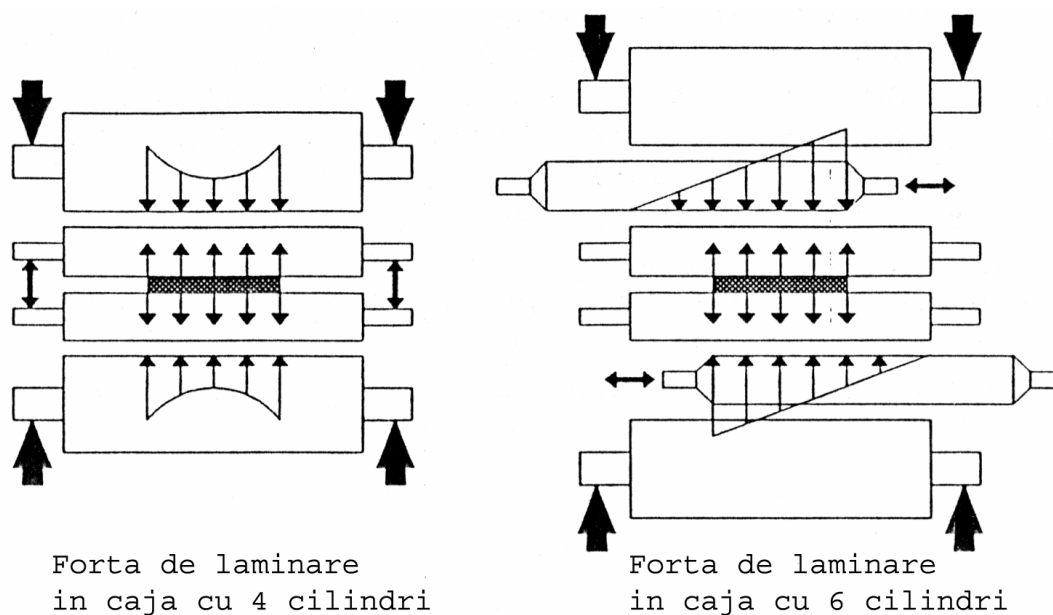
Fig. 2. Configuration of the shape control system

More than this, some authors said that the classical methods of control were even obstacles in the enhancing of the control.

For solving this type of problem the tendency is to introduce cooling systems controlled by a computer system and an appropriate software.

The principle of separation of the regulation actions remains in force so on the final elements one can get the most from the classical systems and what remains will be solved by the cooling system.

The new rolling mill from USS POSCO combines the most recent methods of control, figure 3.



Comparatia intre distributia fortei de laminare.

Fig. 3 Comparison between the distribution of the rolling force

The researches from Japan conducted researches and created even a computer data base. The software is conceived to solve the problem of the optimum cage number and roll profile designing.

### 3. Conclusions

The performances of the product quality in the cold rolling of steel sheets in profiles like rail guard type A will be achieved the most probable not by enhancing the control apparatus precision but changing the algorithms of control. In the last period this is the way of ensuring progress: combining classical methods with computers and adequate software, even creating experts systems.

It is not yet the moment to say that the specialist is no longer needed, the human experience and inspiration being more than hard to program.

*Received: May 17 2005*

*\* The "Stefan Procopiu" School Group, Iasi*

*\*\* The "Gh.Asachi" Technical University from Iasi*

### REFERENCES

1. **Huisman, R.L., Galma, M.E., Bruinsma, H.**- The application of a Mathematical Model Based on Physical Relations for an On Line Preset Model for Cold Rolling, The Science and Technology of Flat Rolling, vol. 2, Deauville, France, 1987, pp.35-42;
2. **Zhou Guo Yng**- Calculul fortelor de laminare in cazul laminarii la rece, Neue Hutte, Germania, vol 35, nr.9, 1990, pp.331-335;
3. **Trillo, C.T.** - Controlul procesului la laminorul la rece de la Novi Ligure, Associazione Italiana di Metallurgia, Centro Lavorazioni Plastiche, 1981, pp.206-224;



4. **Alexandru, M.** – Cercetari experimentale, interpretarea rezultatelor si contributii fundamentale –aplicative privind imbunatatirea parametrilor constructivi si functionali ai unei linii de laminare la rece-referatul 3, Universitatea Tehnica „Gh. Asachi”, Facultatea SIM, Iasi 1997;
5. **Alexandru, M.** – The Mathematical Model Based on Plastic Instability Theory of Roll Forming Force – Buletinul Institutul Politehnic Iasi, sectiunea Stiinta si Ingineria Materialelor, Tomul XLII (XLVI), Lucrarile celui de-al Doilea Congres International, 27-31 mai Iasi 1997
6. **Alexandru M.** – Contributii teoretice privind imbunatatirea parametrilor constructivi si functionali ai unei linii de laminare la rece – Teza de doctorat, Iasi 2004

#### **TENDINTE DE MODERNIZARE IN LAMINAREA LA RECE A PROFILELOR PARAPET TIP A**

##### **(Rezumat)**

In ultimii cincisprezece ani, pe piata profilelor laminate au aparut si se dezvoltă mici intreprinderi specializate in fabricarea unei game foarte restranse de produse in conditii de calitate si pret deosebite, concurenti din ce in ce mai seriosi pentru marile intreprinderi. Lucrarea prezinta masurile tehnice luate in lupta pentru pastrarea pietei de catre marii producatori de profile laminate la rece.



## RESEARCHES CONCERNING PROCESSING BIOACTIVE MATERIALS

BY

GH. T. POP and LILIANA VERESTIUC

**Abstract** Bioactive materials are called those materials which spontaneously bond to living bone. Among such materials one could mention Bioglass, Sintered Hydroxyapatite and Glass Ceramic. The Bioactive materials form a bone-like apatite layer on their surfaces in the living body and bond to bone through this apatite layer. Such properties are induced by functional groups: Si-OH, Ti-OH, Zr-OH, H<sub>2</sub>PO<sub>4</sub> and ~COOH. These fundamental findings provide methods for preparing new bioactive materials with improved mechanical properties such as titanium alloy, silica-ceramic and inorganic-organic composites through biomimetic process. Titanium metal (Ti) and its alloys are very tough, and have been widely used as orthopedic and dental implants. They are, however, non-bioactive, and therefore, are usually coated with HA by using a high-temperature process, such as the plasma spraying method, which partially decomposes and melts the HA. It has been suggested that such HA coatings are liable to delaminate from the substrate, and to dissolve in a short period after implantation. In view of the composition of the above functional groups effective for apatite nucleation, titanium metal and its alloys have the potential to exhibit intrinsic bioactivity by a surface modification, by biomimetic processes, which has been used to deposit micronic bone like apatite, such we did in this work.

**Keywords:** bioactivity; apatite; biomimetic process; simulated body fluid (SBF); bone like apatite.

### 1. Introduction

Materials used for implants have to present some specific properties, such as: biocompatibility, good mechanical properties for application field (especially regarding wearing resistance and Young's modulus) and bio-reactivity, for producing of strong bonds at implant – bone interface. Such properties are assured by a limited group of materials, which have to combine high mechanical characteristics with a controlled biocompatibility. These materials were intensively researched in last decade and they are usual metallic -ceramic composites and ceramic-polymeric systems obtained through biomimetic processes at relative low temperatures.

In paper are presented researches about processing and characterization of a metallic-ceramic nanocomposite biomaterial with applications in orthopedic and dental surgery. The reasons, which justify biomimetic techniques using, are based on superior properties of the biological materials by comparison to equivalent synthetics, as can be observed in Table 1.

Some essential aspects result from previous table data:

-natural biological materials like as ceramic-polymeric composites have lower modules of elasticity but they are a little rigid;

-the tensile strength of the natural materials is relatively reduced but the tenacity is increased by comparison to synthetic materials, which have a tensile strength, instead reduced tenacity;

-high tenacity and reduced modules of elasticity, specific to natural materials are also present at synthetic composites, aspect which confers to them properties of flexibility and fatigue resistance;

Table1. Physical-mechanical characteristics of the natural and synthetic biomaterials

Material	Volume of inorganic fraction, %	Modulus of elasticity, GPa	Tensile strength, MPa	Tenacity, J/mp
Dental enamel	92	45	75	100-200
Dentine	48	12	250	500
Femora	65	20	250	1500
Alumina	100	350	500-1000	7-10
Pearl	95	70	160	600-100
Natural hydroxyapatite	100	30-50	400-500	-
Ceramic-polymeric composite	35	20	160	3000

By studying the structure for some natural composites, like as bone, dentine, mollusk shells, etc, was found a fibrous or lamellar shape of the reinforcing phase from these materials which explain the increased tenacity. Originating to these findings were studied and realized various techniques for synthetic composite materials processing. For example, by sol-gel method from metallic alcoxides high performance composite materials have been obtained, like polymeric composites filled with  $\text{TiO}_2$  fibers (Figure 1) or superficial covering with dense bioactive on metallic and ceramic surfaces by biomimetic methods, at low temperatures.

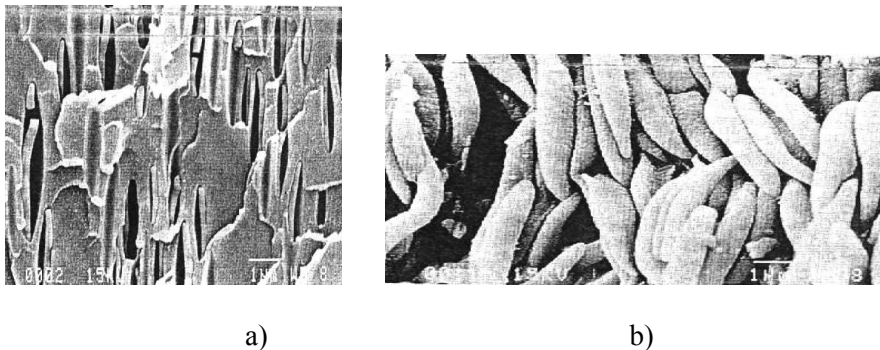


Fig.1. Microscopic structures of ceramic-polymeric composites  
a) in situ grown  $\text{TiO}_2$  fibres in a polymeric matrix ;  
b) in situ formed  $\text{TiO}_2$  lamellas in a polyvynil chloride matrix.

The biomimetic treatments do not modify mechanical properties of the metallic materials instead the deposited superficial layer ( having few microns) is gradually fitted in basic metal and form a microstructure at metal – ceramic interface (Figure 2).

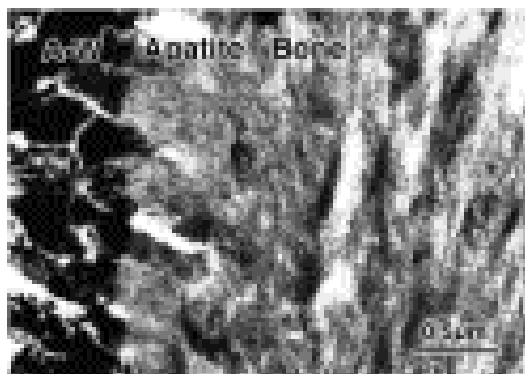


Fig. 2. The interface in apatite – metal composite

## 2 Materials and Method

### 2.1 SBF preparation

SBF solution was prepared by dissolving the reagent grade chemicals in the following order: NaCl, NaHCO<sub>3</sub>, KCl, Na<sub>2</sub>HPO<sub>4</sub>·2H<sub>2</sub>O, MgCl<sub>2</sub>·6H<sub>2</sub>O, CaCl<sub>2</sub>·2H<sub>2</sub>O and Na<sub>2</sub>SO<sub>4</sub> into deionized water. The fluid was buffered at pH=7.4 and 37°C with tris-hydroxymethyl-aminomethane ((HOCH<sub>2</sub>)<sub>3</sub>CNH<sub>2</sub>) and 1M hydrochloric acid (HCl) solution (Table 2).

Table 2. The SBF chemical composition

No.	Reactif	Concentration(g/l)
1.	NaCl	6.547
2.	NaHCO <sub>3</sub>	2.268
3.	KCl	0.373
4.	Na <sub>2</sub> HPO <sub>4</sub> ·2H <sub>2</sub> O	0.178
5.	MgCl <sub>2</sub> ·6H <sub>2</sub> O	0.305
6.	CaCl <sub>2</sub> ·2H <sub>2</sub> O	0.368
7.	Na <sub>2</sub> SO <sub>4</sub>	0.071
8.	(CH <sub>2</sub> OH) <sub>3</sub> CNH <sub>2</sub>	6.057

Comparisons between ion concentrations in SBF and human blood plasma are given in Table 3.

The Na<sup>+</sup>, K<sup>+</sup>, Mg<sup>2+</sup>, Ca<sup>2+</sup> ions from prepared SBF was determined by micro-analytical methods and atomic absorption spectroscopy. For Cl<sup>-</sup> anion dosing also micro-analytical method was used. The HPO<sub>4</sub><sup>2-</sup> anions (using also Blue Molybdenum method), HCO<sub>3</sub><sup>-</sup> and SO<sub>4</sub><sup>2-</sup> were dosed by UV spectroscopy.

Table 3. The ionic concentrations in SBF and human plasma

Type of ion	Prepared SBF (mM)	Kubota et colab.SBF (mM)	Human plasma (mM)
Na <sup>+</sup>	142.0	142.0	142.0
Cl <sup>-</sup>	121.4	147.8	103.0
HCO <sub>3</sub> <sup>-</sup>	27.0	4.2	27.0
K <sup>+</sup>	5.0	5.0	5.0
Mg <sup>2+</sup>	1.5	1.5	1.5
Ca <sup>2+</sup>	2.5	2.5	2.5
HPO <sub>4</sub> <sup>2-</sup>	1.0	1.0	1.0
SO <sub>4</sub> <sup>2-</sup>	0.5	0.5	0.5

## 2.2 Hydroxyapatite deposition on Ti and Ti alloy (Ti6Al4V)

The method of superficial covering with bioactive apatite on Ti and Ti alloys consisted of following thermo-chemical processes:

a) The metallic samples with plate shape and adequate prepared ( polished and cleaned - all samples were rinsed with water, cleaned in an ultrasonic bath of acetone for 10 min. and then of ethanol, rinsed once again with deionized water and then dried at 40°C) were immersed and maintained in a 0.5M NaOH solution, thermostated at 50 C, for 24 hours;

b) The samples were then thermal treated at 500°C for 1hour;

c) The samples were immersed in 25 ml SBF, at 37°C, in a thermostatically controlled environment for 3 days.

## 3. Results and conclusions

The mechanism of bioactive apatite micronic superficial layers forming on metallic and ceramic surfaces were intensely studied in the view to obtain layers which are able to assure an advanced biointegration of the metallic or ceramic implants. The bioactive apatite superficial layer deposited by biomimetic methods has special properties, similar with natural hydroxyapatite which form bones, dentine, dental enamel, etc. Among these exceptional properties are mentioned the strong adhesion to support, regeneration and bioactivity – manifested through capacity to form and activate biologic bonds with adjacent live tissue – for surgical implants.

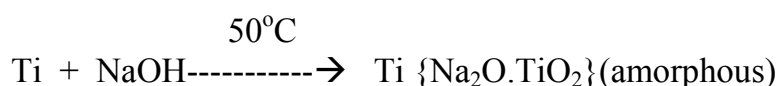
The bioactive apatite layer can be induced only on functional materials, which have the capacity to form hydroxyl chemical combinations: Si-OH, Ti-OH, Zr-OH, -COOH. These materials have property to charge with negative electrical components in biological fluids and induce apatite forming, as calcium compounds like as: calcium silicate and amorphous calcium phosphate.

In the present paper were made researches about Ti and Ti6Al4V alloy, biocompatible materials wide used in medical fields like orthopedic, stomatology and neurosurgery. These materials have not bioactive properties instead are well tolerated by organism and have ideal mechanical properties for applications in recuperation medicine. To obtain HA coatings on metallic implants, various methods have been

applied, including plasma spraying, electrophoretic or PLD. Commercially HA coatings obtained by plasma spraying are already available on market. Nevertheless, it is nowadays generally accepted that this method is not reliable enough and produces coatings with poor crystallinity and lower adherence to the substrate.

Because of Ti and its alloys, like other few mentioned materials possess an intrinsic potential for activation, it is possible to induce on their surface forming of bioactive apatite layer, through chemical and thermal processes, at relative low temperatures.

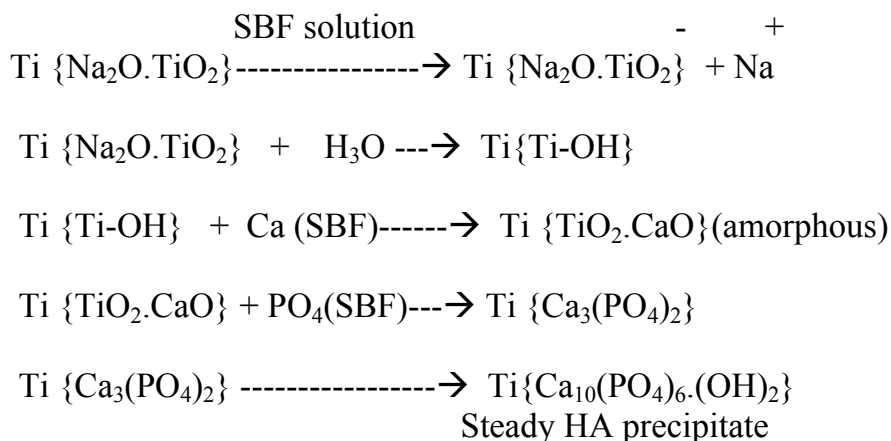
When Ti and Ti6Al4V is treated with NaOH solution at 50°C the metallic surface is covered by a micronic layer of amorphous sodium titanate:



By treating the micronic layer with thermal process, at 500°C, amorphous sodium titanate layer is transformed in crystalline one, strong bonded at metallic surface:



In simulated biological fluid, with a chemical composition similar with human plasma, by ionic interchanging reaction, a micronic bioactive apatite layer (similar to bone-like apatite) is generated, with high adhesion to the metallic surface.



Experimental studies have verified concrete conditions for bioactive apatite forming on Ti and Ti6Al4V support, the most used materials in orthopaedic and dental surgery. Different metallic samples (plate shape) have been chemical and thermal treated and analysed.

It is noticed that technical procedure for superficial bioactive apatite forming on surface of implants is relative simple, doesn't need complex devices and operations; these practical aspects make as the procedure to present a special value for implantological practice.

In our experiments were verified technical procedures on metallic materials, chemical solution preparing, the thermal treatment parameters and physical parameters of the deposited ceramic layer.

The preliminary experimental results confirmed the value of technical principles and further researches will be made.

The superficial layer of bioactive apatite deposited on metallic materials was analysed by scanning electronic microscopy (SEM) and the microstructure of the interfacial metal – apatite zone is presented in figure 3.

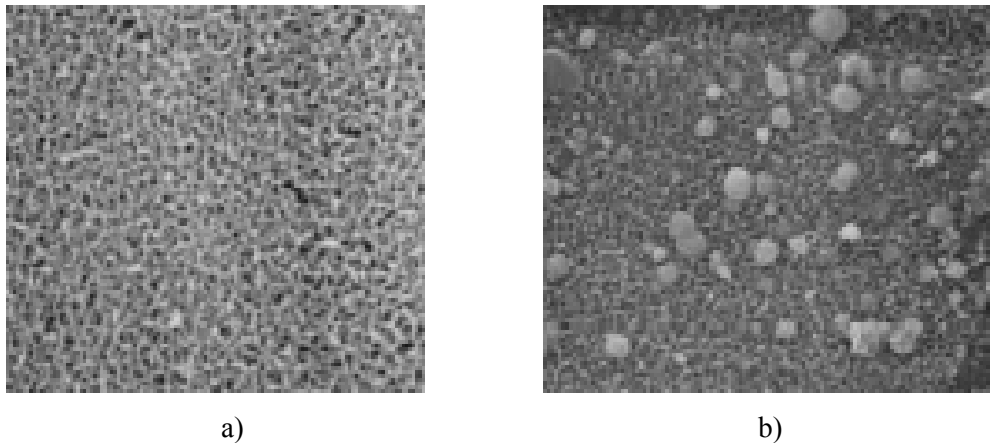


Fig.3. Scanning electronic microscopy(SEM) data for bioactive apatite deposited on Ti by biomimetic method; a) after NaOH and thermal treatment, b) after NaOH, thermal and SBF treatment.

#### 4. Conclusions

The conclusions developed by our study are:

Ti and Ti alloys permits superficial covering with an apatite layer by using biomimetic processes;

The formed apatite layer on metallic surface is homogenous, adherent and bioactive, according to preliminaries experiments has essential aspect for being used in implantological surgery;

Experimental parameters of the used procedure have shown the possibility to cover Ti and Ti alloys with apatite, by using biomimetic principles at relative low temperatures;

Further experiments will be made for optimal parameters for thermal treatment and chemical growing process establishing, deposited layers analysis from composition point of view and tests on metallic implants.

These new materials, with bioactive properties, are expected to replace in a near future the classical materials used in osseous surgery.

Received May 13 2005-05-18

The "Gr.T.Popa" University of  
Medicine and Pharmacy, Iasi

#### REFERENCES

1. Kokubo T. *Novel bioactive materials*, Ed. Elsevier Science-2003
2. Kokubo T. *Spontaneous formation of bonelike apatite layer on chemical treated titanium metal*. Journal American Ceramic Societet-1996



3. Kim H.M. *Apatite-forming ability of alkali-treated Ti metal in body environment*. Journal Japan Ceramic Societete-1997
4. Kokubo T. *Formation of biologically active bone like apatite on metals and polymers by a biomimetic process*. Termodinamica Acta-2003
5. Frauchiger L., Taborelli M., Aronsson B.O., Descouts P., *Ion adsorption on titanium surfaces exposed to a physiological solution*, Applied Surfaces and Science, 143, pp.67-77, 1999
6. Ishikawa K., Yakani S., Chow L.C., Ishikawa Y., Eanes E.D., Asaoka K., *Behavior of a calcium phosphate cement in simulated blood plasma in vitro*, Dent. Mater, 10, pp.26-32, 1994
7. Wolke J.G.C., van der Waerden J.P.C.M., de Groot K., Jansen J.A., *Stability of radiofrequency magnetron sputtered calcium phosphate coatings under cyclically loaded conditions*, Biomaterials, 18, pp.483-488, 1997
8. Shi J., Ding C., Wu Y., *Biomimetic apatite layers on plasma-spray titanium coatings after surface modification*, Surface and Coatings Technology, 137, pp.97-103, 2001
9. Ferraz M.P., Monteiro F.J., Serro A.P., Saramago B., Gibson I.R., Santos J.D., *Effect of chemical composition on hydrophobicity and zeta potential of plasma sprayed HA/CaO-P<sub>2</sub>O<sub>5</sub> glass coatings*, Biomaterials, Vol.22, Nr.23, pp. 3105-3112, 2001
10. Clèries L., Fernández-Pradas J.M., Sardin G., Morenza J.L., *Application of dissolution experiments to characterise the structure of pulsed laser-deposited calcium phosphate coatings*, Biomaterials, Vol.20, Nr.15, pp.1401-1405, 1999
11. Fernández-Pradas J.M., Clèries L., Martínez E., Sardin G., Esteve J., Morenza J.L., *Influence of thickness on the properties of hydroxyapatite coatings deposited by KrF laser ablation*, Biomaterials, Vol.22, Nr.15, pp. 2171-2175, 2001
12. Darimont G.L., Cloots R., Heinen E., Seidel L., Legrand R., *In vivo behaviour of hydroxyapatite coatings on titanium implants: a quantitative study in the rabbit*, Biomaterials, Vol.23, Nr.12, pp. 2569-2575, 2002
13. Radin S.R., Ducheyen P., J.Mater.Sci.: Mater. Med., 3, pp.33, 1992

## CERCETARI PRIVIND PROCESAREA DE NOI MATERIALE BIOACTIVE

### (Rezumat)

*Materiale bioactive sunt denumite acele materiale care au proprietatea de a se lega in mod spontan cu tesutul viu; printre acestea se mentioneaza Bioglasul, Hidroxiapatita si Sticlele ceramice.*

*Materialele bioactive au capacitatea de a forma pe suprafata lor un film micronic de apatita, cu structura si compozitie chimica asemanatoare osului, daca sunt introduse in medii fiziologice. Asemenea proprietati sunt conditionate de capacitatea materialelor de a forma asa numite grupe functionale ca : Si-OH, Ti-OH, Zr-OH, -COOH, etc*

*Titanul si aliajele sale sunt materiale tenace, cu exceptionale proprietati fizico-mecanice, motiv pentru care sunt larg utilizate in medicina implantologica; insa acestea nu poseda proprietati bioactive. Totusi asemenea metale dispun de un potential intrisec de a se acoperi cu un strat micronic de apatita bioactiva, prin tratamente chimice si termice speciale, bazate pe procese biomimetice. O asemenea procedura tehnica, aflata in faza de cercetare experimentală, este tratata in lucrarea de fata.*



## COMPUTERIZATED QUANTITATIVE MICROGRAPHICAL ANALYZIS OF DEPOSED LAYERS BY ELECTRICAL DISCHARGE IN IMPULSE ON AN HIGH ALLOYED TOOLS STEEL

BY

ADRIAN ALEXANDRU, SORIN IACOB STRUGARU, IOAN ALEXANDRU,  
LAURENTIU CIOBANU and SORIN TANASUCA

**Abstract:** This paper work presents the experimental results of optical quantitative computerisated analyze concerning the characterisation of the deposited layers by electrical discharge in impulse on a 155MoVCr115 steel.

**Keywords:** electric impulse, electric discharge, quantitative analyze

### 1. Introduction

The superficial thermic treatments technologies or deposition of thin layers, have each some disadvantages, so, today we trying to combine two or more technologies in order to increase the performances of the machine parts or tools.

The obtaining of thin layers by electrical discharge in impulse has some advantages as: very good adherence of the coverings the possibility of deposition of all kind of materials with electric conductivity, the simplicity of the devices and technologies, but also presents some disadvantages: large roughness and residual stress in the deposited layer.

We can say that joining alloying and deposition by electric impulse with a superficial thermic treatment, many of those disadvantages will disappear.

Deposition and alloying by discharge in electric impulse uses inverse electroerosion, which means that the parts is the cathode and the tool electrode is the anode.

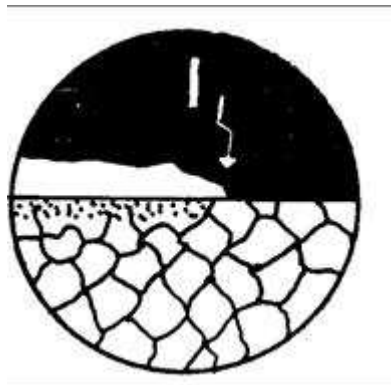


Fig.1 The process of superficial hardening by discharge in electric impulse

The experimental computerized quantitative optical research has as scope a complete characterisation of the deposited layers on studied samples and carbide characterisation.

Also was chasing the influence of deposition of these layers above the initial structure of superficial layer of the material and the influence of some treatments after deposition above the deposited layers.

## 2. Experimental procedure

The sample by which were made the deposition is from high alloyed tool steel 155MoVCr115 with electrode from Ti15Co6, WCo8, and W. The chemical composition of the 155MoVCr115 steel is presented in table 2.

Table 1

Sample	Steel	Chemical composition											Obs.	
		C	Mn	Si	P	S	Cr	Mo	Ni	V	Al	Cu		
1	155MoV Cr115	1.5	0.18	0.1										STAS 3611-88  determinate
		÷	÷	÷	≤0.03	≤0.03	11÷ 12	≤0.6 ÷ 0.8	≤0.35	0.9 ÷ 1.1	-	≤0.30		
		1.6	0.45	0.4			11.7	0.72	0.16	1.05	0.03	0.23		

The mechanical properties and thermic treatments parameters for this type of steel are presented in table 2.

Table 2

Steel	Mechanical properties			Thermic treatment parameters							
				Annealing		Annealing		Quenching		Tempering	
	R <sub>p0.2</sub> , N/mm <sup>2</sup>	KCU <sub>2</sub> , J/cm <sup>2</sup>	HB daN/mm <sup>2</sup>	T, °C	Mediu	T, °C	Mediu	T, °C	Mediu	T, °C	Mediu
155MoV Cr115	-	-	255	880	c	-	-	1020- 1030	U, a	160-200	a

The processing by electrical discharge in impulse were made by hand on plane surface without oxides and impurityties, using electrodes from Ti15Co6, with cilindrical sections ( $\phi$  2 mm) and length 25 mm.

The samples from 155MoVCr115 steel, before deposition of layers by electrical discharge in impulse were superficial thermic treated. The superficial thermic treatments parameters applied before deposition by electrical discharge in impulse are presented in table 3, and in table 4 and Fig. 2 are presented the experimental duplex variats of thermic treatments.

Table 3

Thermic treatment variant	Steel	Thermic treatment parameters
High frequency current hardening	155MoVCr115	1 000 <sup>0</sup> C/sintetic medium
Volume hardening + tempering	155MoVCr115	1 030 <sup>0</sup> C/oil + 180 <sup>0</sup> C/air

Table 4

Variant	Stages
A	Volume hardening + tempering + deposition by electrical discharge in impulse
B	high frequency currents hardening + deposition by electrical discharge in impulse

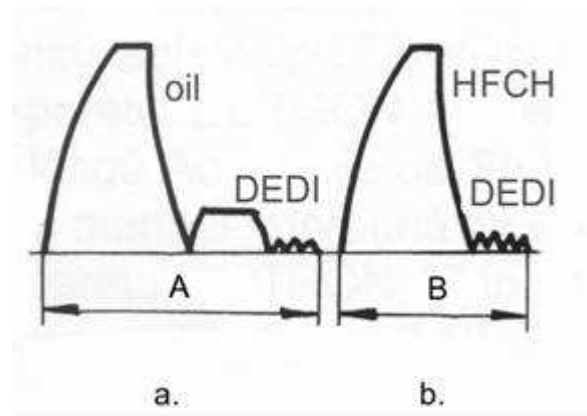


Fig. 2. The duplex variants of thermic treatments

The experimental researches of computerised quantitative analysis were made for a complete characterization of the deposited layers on studied samples and carbides characterization.

The computerised line of image analysis is composed from: optical microscope (REICHERT UNIVAR, video camera with adapter, computer, printer).

The main software component of image analysis line is a complex program – IMAGE PROPLUS, produced by MEDIA CYBERNETICS Company USA. This program is composed from a main general image analysis component and a component for quantitative metallographic determination – MATERIALS PROANALYZER.

The image processing takes place in this step:

- quantitative analyze of different images which have interest field as: grain limits, phases, particles etc;
- image processing, by hand or automatically when exists a controller for auto movement of the microscope table;
- quantitative measurement of interesting characteristics by using the A.S.T.M. agreed methods;
- determination of grain dimension;
- determination of dimension scale distribution of grains;
- determination of number and quantity of phases in poliphasic materials;
- quantitative determination of some particles by area, diameter, shape coefficients, perimeter etc;
- dimensional determination of the interdendritic spaces;
- thickness determination of singular or multiple layers.

On this computerized line for analyze were characterisated the carbides and the thickness the deposited layers with diverse electrodes on 155MoVCr115.

In Fig. 3 are presented the white layer parameters of the 155MoVCr115 steel quenched in volume and processed by electrical discharge in impulse with Ti15Co6 electrode, and in Fig.4 are presented the parameters of white layer from 155MoVCr115 quenched in high frequency current and after processed by electrical discharge in impulse with WCo8 electrode.

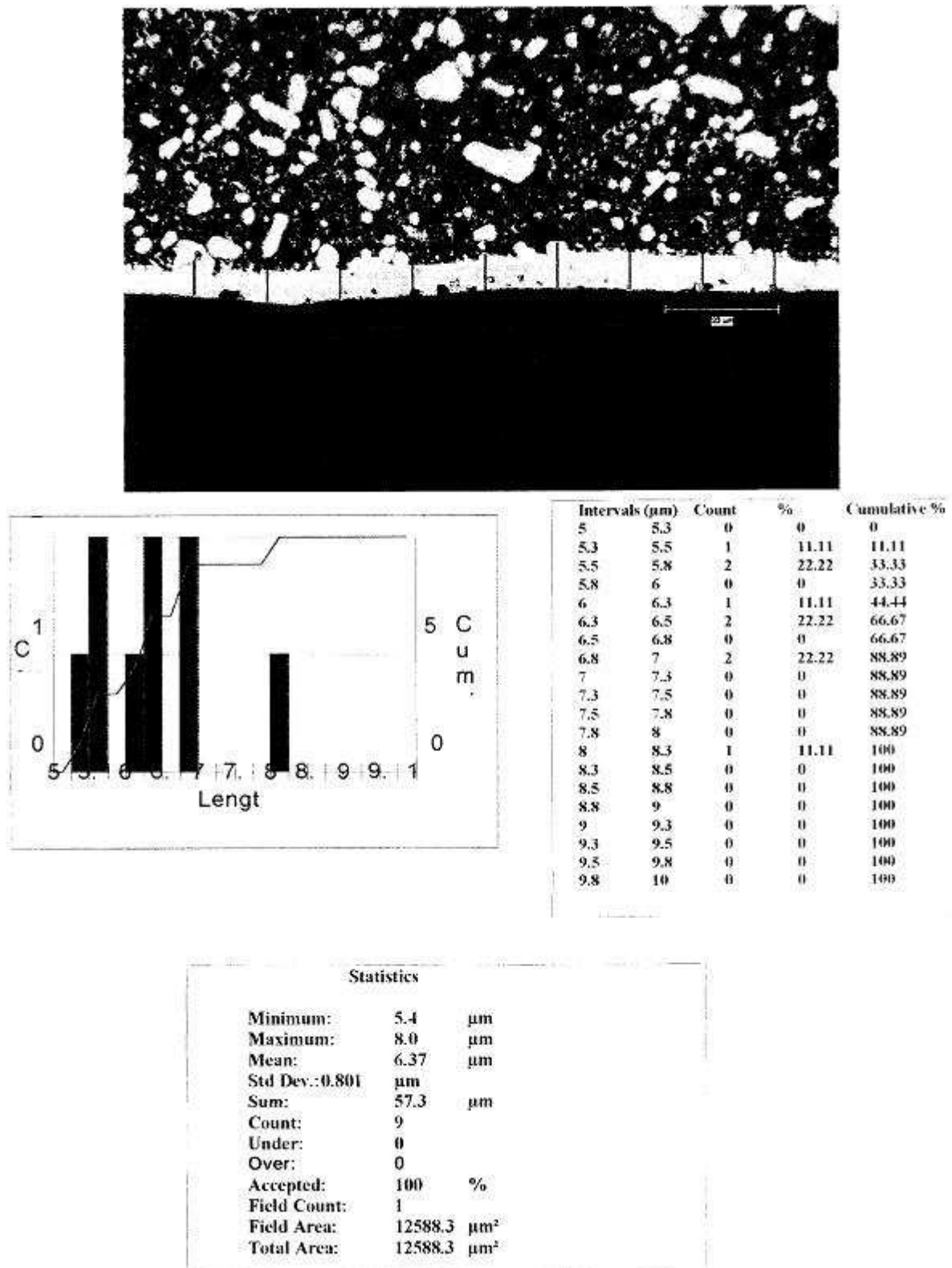


Fig. 3. White layer parameters of 155MoVCr115 steel quenched in volume and processed by electrical discharge in impulse with Ti15Co6 electrode

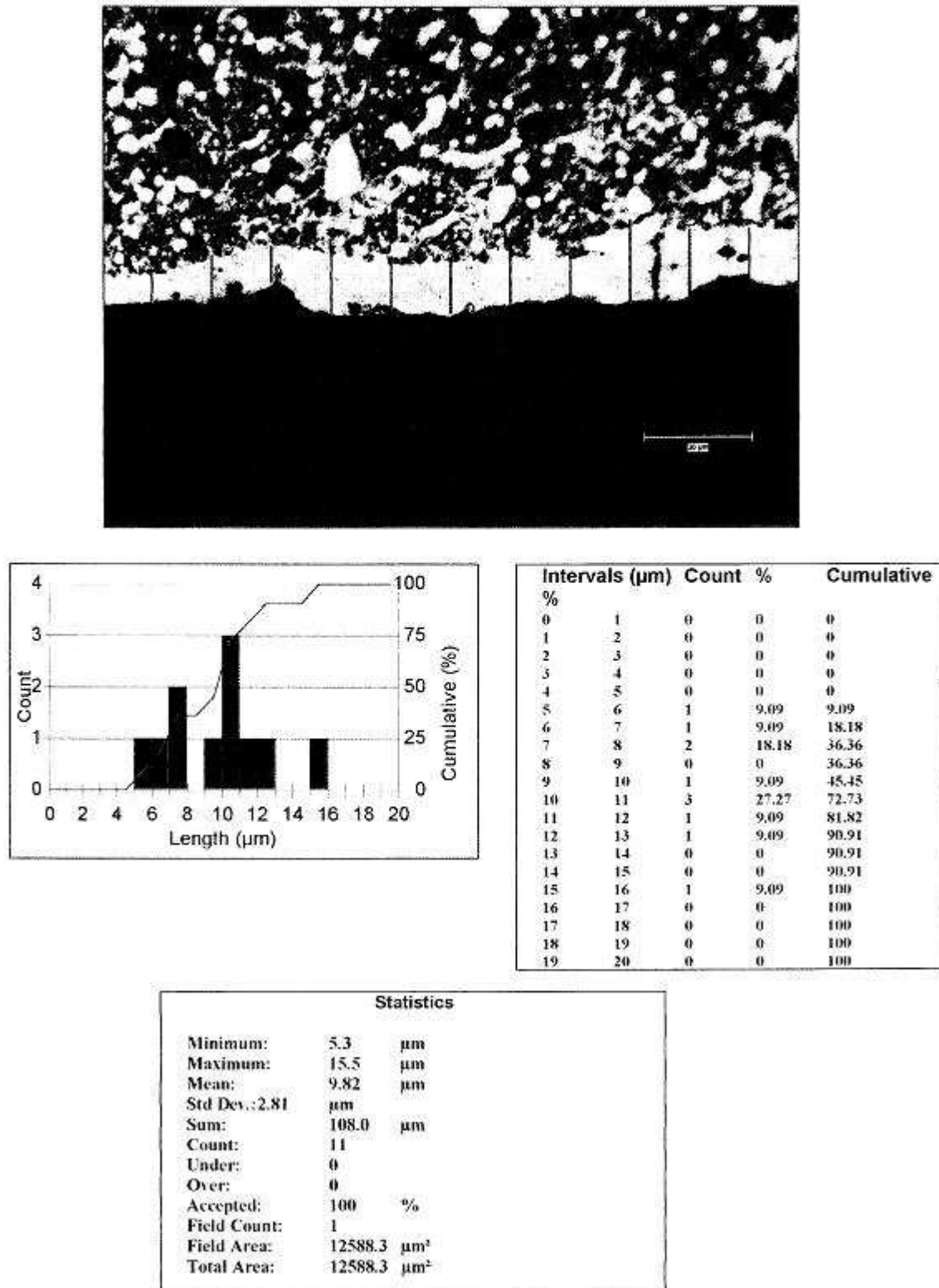


Fig.4. White layer parameters of 155MoVCr115 steel quenched in high frequency current and processed by electrical discharge in impulse with WCo8 electrode

### 3. Conclusions

- i. The obtained layers by thermic treatments variants at which the last process is the electrical discharge in impulse are more large;

- ii. The adherence and the compactity of the white layers with the transition sublayers is good;
- iii. The results obtained by quantitative computerized analyze are the same with those obtained by direct measurements with the PMT 3 device.

*Received 17 may 2005*

*The "Gh.Asachi" Technical University Iași*

#### REFERENCES

1. Alexandru, A. **Doctorate Thesis**, January 2002.
2. Alexandru, A., Pop, F. **Metallic materials with hardened deposit created by electric arc with vibrating electrode**. Proceedings EUROMAT-JUNIOR, Lausanne, 1994.
3. Pop, D., Pop, F., Alexandru, A. **Hardened deposition with tungsten carbides on steel specimens**. Proceeding, vol. II, EUROMAT, Lisabona, 1998.

#### ANALIZA MICROGRAFICĂ CANTITATIVĂ COMPUTERIZATĂ A STRATURILOR DEPUSE PRIN DESCĂRCĂRI ELECTRICE ÎN IMPULS PE UN OȚEL BOGAT ALIAT DE SCULE

##### (Rezumat)

Lucrarea prezintă rezultate experimentale de microscopie optică cantitativă computerizată privind caracterizarea straturilor depuse prin descărcări electrice în impuls pe un oțel bogat aliat de scule 155MoVCr115.



## CONSIDERATIONS REGARDING THE MODEL REFERENCE CONTROL SYSTEM FOR SPEED CONTROL OF DC MOTOR

BY

BAHRIN V. and HABA C. G.

**Abstract:** The structure of the adaptive system with reference model is presented. Particularities of the control system with passive adaptive controller are specified and its block diagram is presented. The control system with reference model achieved with apparently adaptive controller is implemented for the speed control of a d.c. separately excited motor.

**Keywords:** adaptive system, control system,

### 1. Introduction

Model reference adaptive system (MRAS) consists of an internal feedback control loop and an external loop that adjusts the parameters of the internal loop. The model reference specifies the desired performances of the system in the main loop (controlled process and classic regulator). The error, the difference between system output and reference model output, is applied to adaptive element. The performances of the adaptive system are specified with the reference model and the regulator parameters are adjusted based on the system error.

In this paper, we discuss some aspects regarding the realization of a model reference control system implemented with an apparently adaptive controller used in speed control of a DC motor.

### 2. The implementation of the model reference control system with apparently adaptive controller

One of the important problems related to MRAS is the model following problem. This can be stated in the case of automatic systems with adjustable parameters MRAS as the way of adjusting the parameters in such a way that the transfer function of the closed loop is as closer as possible to the prescribed model. The problem can be solved using a pole-allocation method. The model following problem is stated correctly if the poles-zeros excess of the model reference is bigger than the poles-zeros excess of the controlled process.

In practice, for MRAS implementation we need to make some approximations. A rapid response can be obtained using the feed-forward connection. When both model reference and process model are non-linear there are no special problems regarding system stability because these are restricted to the feed-forward compensator path. The operation of MRAS in the range of low frequencies is imposed through feedback.

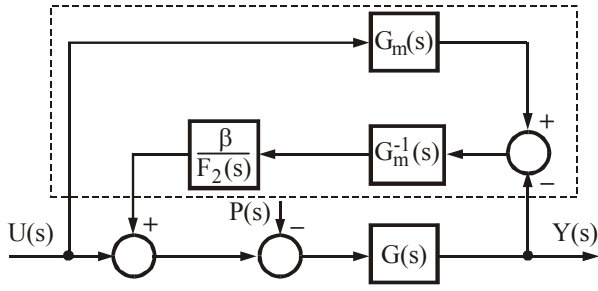


Fig. 1

In the case of smooth systems, the block diagram of the ensemble motor-passive adaptive controller is depicted in Fig.1.  $G(s)$  is the transfer function of the ensemble rectifier-motor, and  $G_m(s)$  and  $G^{-1}(s)$  are the transfer function and the inverse of the dynamics corresponding to the model of the ensemble rectifier-motor respectively.

The gain factor,  $\beta$ , is used to modify system sensitivity when parametric variations occur. The low-pass filter,  $1/F_2(s)$ , satisfies condition  $\lim_{s \rightarrow 0} F_2(s) = 1$  and it is necessary because  $G_m^{-1}(s)$  is usually a transfer function whose numerator has a greater degree than those of the denominator.

The transfer functions of the output with respect to the reference signal and with respect to perturbation have the following expressions:

$$\frac{Y(s)}{U(s)} = \frac{1}{\frac{F_2(s)}{F_2(s) + \beta} \delta(s) + 1} G_m(s). \quad (1)$$

$$\frac{Y(s)}{U(s)} = \frac{1}{\frac{F_2(s)}{F_2(s) + \beta} \delta(s) + 1} \cdot \frac{F_2(s)}{F_2(s) + \beta} G_m(s). \quad (2)$$

The term  $\delta(s) = \frac{G_m(s) - G(s)}{G(s)}$  represents the difference between the dynamics of motor for rating values,  $G_m(s)$  and the dynamics of motor parameters at present moment,  $G(s)$ . For the ideal case when  $G(s) = G_m(s)$ , the MRAS does not influence the obtained answer because the control signal is null.

In the case when the poles-zeros excess of transfer function  $G_m(s)$  equals 1, the low-pass filter  $F_2(s)$  can take the following form:

$$F_2(s) = \frac{1}{\tau_2 s + 1}. \quad (3)$$

DC electric drives can be identified with high accuracy therefore, transfer functions  $G(s)$  and  $G_m(s)$  can have same gain factor and  $\delta(s)$  zeros in stationary regime. Under these considerations, the stationary regime value does not modify when parametric variations of the fixed part occur.

In the dynamical regime, considering time constant  $\tau$  smaller then time constants of the fixed part, the term  $\frac{F_2(s)}{F_2(s) + \beta}$  determines a reduction of  $\frac{1}{1 + \beta}$  times of the influence of term  $\delta(s)$ . The growth of the gain factor results in a reduction of system sensitivity at parametric variations.

In the stationary regime, if  $G(s)$  and  $G_m(s)$  have the same gain factor, the output error related to perturbation will be reduced.

Consider the DC motor with separate excitation controlled using armature voltage using a command rectifier and modeled as a proportional block with gain  $K_{ee}$ . The transfer function of fixed part is:

$$G(s) = \frac{\omega(s)}{U(s)} = \frac{K_t K_{ee}}{(Ls + R)Js + K_t K_e}, \quad (4)$$

where  $L$  and  $R$  are the armature inductance and resistance respectively,  $U$ -armature voltage,  $\omega$ -motor speed,  $J$ -motor torque inertia and  $K_t$  and  $K_e$  are motor torque and voltage constants.

The motor model, a transfer function of first order, can be simplified neglecting the electromagnetic time constant  $T_e = L/R$ , resulting in a simplification of the control algorithm.

The transfer function of the ensemble controlled rectifier- motor has the following expression:

$$G_m(s) = \frac{K_{ee}/K_e}{\frac{JR}{K_t K_e} s + 1} = \frac{K_m}{T_m s + 1}. \quad (5)$$

Figure 2 illustrates the block diagram of the control system using a passive adaptive controller. The control algorithm can be obtained by the discrimination of the transfer functions  $\frac{\beta K_e}{K_{ee}} \cdot \frac{T_m s + 1}{\tau_2 s + 1}$  and  $\frac{K_{ee}/K_e}{T_m s + 1}$  found in controller structure.

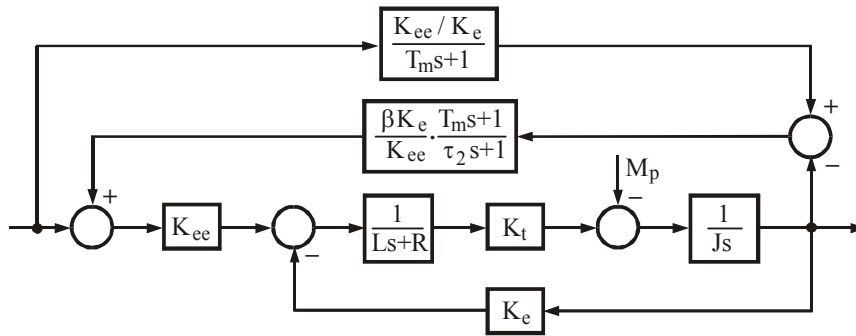
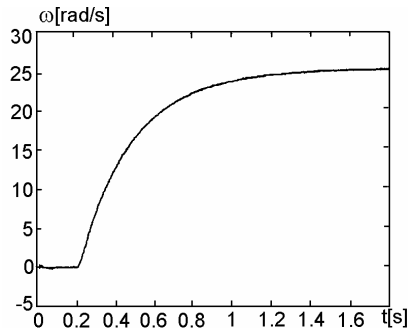


Fig. 2

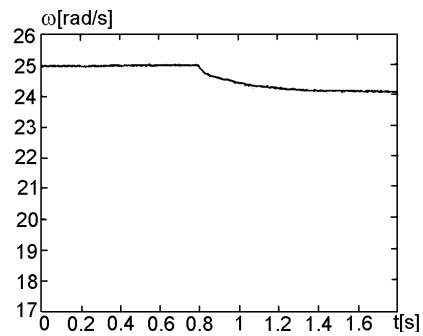
### 3. Experimental results

The control algorithm presented in previous chapter was applied on a DC motor controlled using a controlled 4-quadrant rectifier. DC motor parameters are:  $U_N = 110$  V,  $P_N = 0.25$  kW,  $I_N = 3.3$  A,  $\omega_N = 1750$  rpm, armature resistance  $3.1 \Omega$  and armature inductance  $0.16$  H. The gain is  $\beta = 10$ , and the time constant of filter  $F_2$  is  $\tau_2 = 0.002$  s. Rectifier gain factor is  $K_{ee} = 13.98$ .

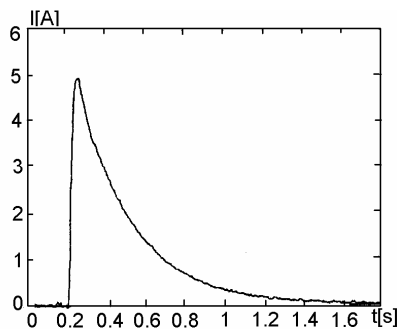
In Fig. 3 is depicted motor speed and armature current for rating values of motor parameters when the resistive torque is zero. The indicial answer of the control system with passive adaptive controller is identical to the motor answer for a step variation of the control voltage on the controlled rectifier.



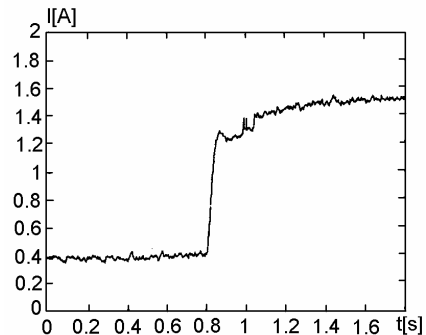
a



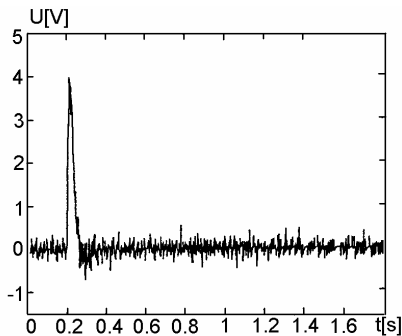
a



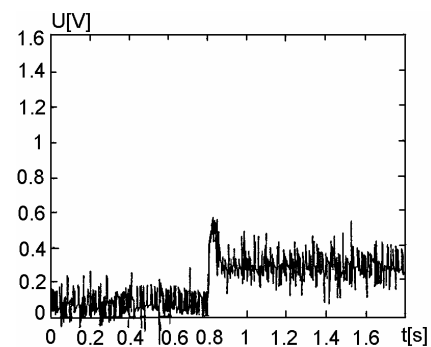
b



b



c



c

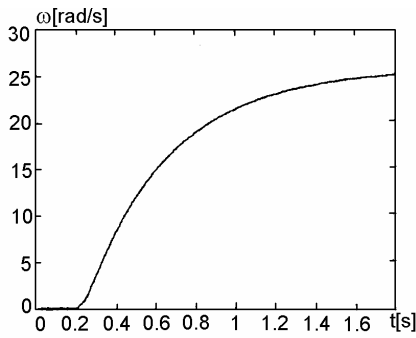
Fig. 3

Fig. 4

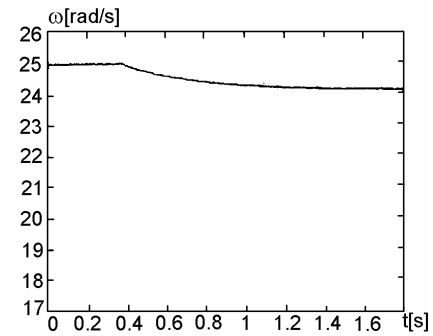
In Fig. 4 is represented system answer when a step perturbation  $\Delta M_r = 0.75$  N.m. Observe the reduction of system sensitivity to perturbations.

Fig. 5 illustrates the control system indicial answer in the situation when a parametric variation  $\Delta J = 4J_N$  occurs. The dominant time constant of the fixed part increases 5 times and the modification of transitory regime duration is insignificant.

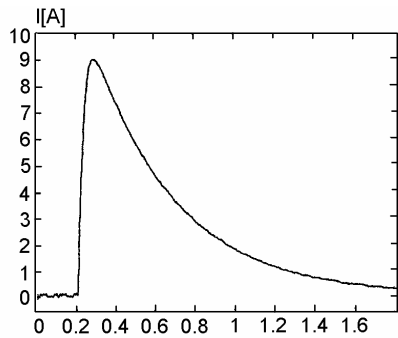
We can see in Fig. 6 the answer of the control system when a parametric perturbation occurs:  $\Delta J = 4J_N$ . The system is disturbed by a step perturbation torque  $\Delta M_r = 0.75$  N.m.



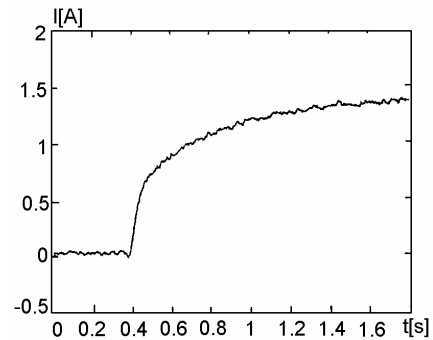
a



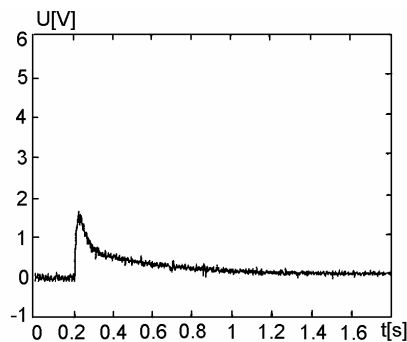
a



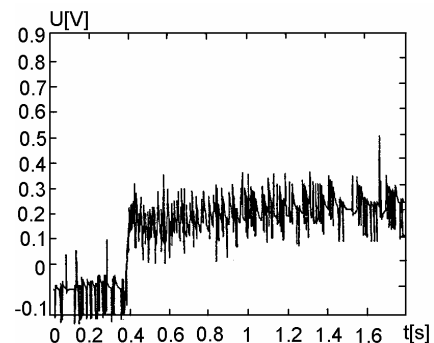
b



b



c



c

Fig. 5

Fig. 6

Received 13 may 2005

The "Gh.Asachi" Technical University Iași

## REFERENCES

1. Călin S., Belea C. *Sisteme automate adaptive și optimale*. Ed. Tehnică, București, 1971.
2. Ionescu V., Popea C. *Optimizarea sistemelor*. Ed. Didactică și Pedagogică, București, 1981.
3. Voicu M. *Sisteme automate multivariabile*. Ed. "Gh. Asachi", Iași, 1993.
4. Bahrin V., Cojocaru-Filipiuc C. *Reglarea turației motorului de curent continuu prin sisteme adaptive cu model de referință*. A treia Conferință Internațională de Sisteme Electromecanice și Energetice SIELMEN 2001, Chișinău, 4-5 Octombrie, 2001, vol. III, pp. 93-96.
5. Bahrin V., Haba C. G., Cojocaru-Filipiuc C. *Considerations Regarding Optimal Control of DC Motor Drive Systems*. 5<sup>th</sup> International Conference on IEEE Power Electronics and Drive Systems PEDS 2003, Singapore, 17-20 November, DS4-07, pp.1619-1623.

**CONSIDERAȚII PRIVIND SISTEMUL DE CONTROL AL MODELULUI DE REFERINȚĂ PENTRU CONTROLUL VITEZEI UNUI MOTOR CC****(Rezumat)**

The structure of the adaptive system with reference model is presented. Particularities of the control system with passive adaptive controller are specified and its block diagram is presented. The control system with reference model achieved with apparently adaptive controller is implemented for the speed control of a d.c. separately excited motor.

## STUDY CONCERNING THE INFLUENCE OF VIBRATIONS ON THE COMPOSITION AND HARDNESS OF AN INGOT

BY

GELU BARBU

**Abstract:** In this paper we propose the research of chemical segregation and of hardness for the private case of the vibration of the steel, while casting into the casting equipment, with the frequency of 100 Hz. Hardness increases its uniformity grade by attaching the vibrations at solidification with 38.9% and the segregation, decreases without reserve with 27.8%. A more marked effect of vibrations, regarding the shrinking of segregations appears at chemical elements which constitutes steel carbide and less intense when elements form solid solutions.

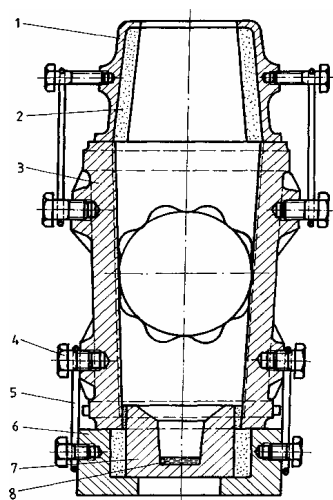
**Keywords:** vibrations, casting, hardness, steel

### 1. General conditions

We propose to investigate the influence of vibrations on a weak steel confederate with molybdenum, chromium and nickel.

Thus we propose the research of chemical segregation and of hardness for the private case of the vibration of the steel, while casting into the casting equipment, with the frequency of 100 Hz.

For the previous mentioned analysis it shapes through geometrical similitude and, referring to the theory of physical and analogic simulation of the solidification



process, the casting equipment necessary for the casting of the steel in the metallic mould SFAC 1300. The casting equipment has been geometrically shaped at the range of 1:10.

In Fig. 1 are presented the assembly sketch of the model for the casting equipment, which comprises: 1 – hot top; 2 – reluctant corning mixture; 3 – cast-iron mould; 4 – bolt for stiffness; 5 – stiffness system ; 6 – base stand; 7 – bottom; 8 – steel.

The knock-out bushing has the purpose to knock-out the ingot model from the casting equipment when the knock-out is tough.

Fig.1. The assembly sketch of the model for the casting equipment: 1 – hot top; 2 – reluctant corning mixture; 3 – cast-iron mould; 4 – bolt for stiffness; 5 – stiffness system ; 6 – base stand; 7 – bottom; 8 – steel.

The preheating temperature of the casting equipment was 300°. The temperature of the steel at exhaust was 1580° C. The exhausted steel into the electric

furnace with heating through electric arc with the capacity of 20 t, faced with alkaline chemical nature fireproof material.

The chemical composition of the steel was the next one: C = 0.57%; Mn = 0.77%; Si = 0.25%; P = 0.024%; S = 0.17%; Cr = 0.70%; Ni = 1.45%; Mo = 0.19%; V = 0.17%; (the chemical composition of the steel was after the exhaust). The steel had been casted in a small capacity bull ladle, (approaching 40kg), by hand.

## 2. Experiments

The casting-model equipment vibrated during the casting and after the end of it, without reserve in 30 seconds. The time in which it maintained in the metallic cast was approaching 30 minutes. The two ingot models, after their feeding heads have been removed by cutting with abrasive blade, they have been longitudinally coped through the symmetrical axe, in the same way.

Then, the four ingot halves have been transverse coped and the requisite distribution to find the hardness and the other analysis, according figure 2.

1.1	1.2	1.3	1.4	1.5
2.1	2.2			
3.1				
4.1				
5.1				
6.1				
7.1				
8.1				
9.1				
10.1				
11.1				
12.1				

Fig.2. Placing in the longitudinal section of the points where the hardness measuring were done

For the analysis of the influence of vibrations on the structure and, implicit on the properties, measures for the chemical segregation have been done, comparative, between the casted ingot and the vibrated one.

The spectral analysis has been accomplished at a PGS – 2 machine with diffraction network and recording on photo plates, measuring the difference of blackening – straight proportional with the strength. The blackening valours for six elements, metals, have been determined, through the counterpart pairs of analytical lines, given below in table 1.

Table 1

Nr.	Element	The analytical lines A	Comparative line for Fe
1	Cr	3147,20	3154,20
2	Ni	3414,80	3465,90



The results of the measurements have been systematized in table 2.

In table 2 the variation of toughness is presented, regarding that the distribution presented in figure 2 with the chemical segregation represented by the difference of blackening between the analysing line of the alloying element and the comparison line of the iron, for the static and vibrating cast ingots.

Table 2

Points	Duritatea, [HB]		Nichel		Crom	
	unvibrated	vibrated	unvibrated	vibrated	unvibrated	vibrated
1	2	3	4	5	6	7
1.1	95	96	14	19	57	65
1.2	93	93	14	12	61	58
1.3	81	86	13,5	8,5	66	48
1.4	87	94	12,5	10	58	34,5
1.5	93	95	10	11,5	30,5	49
2.1	89	92	14	11	63	56,5
2.2	84	87	13,5	12	66,5	55
2.3	80	85	13,5	10	62	38
2.4	85	88	12,5	10,5	60	35,5
2.5	88	91	12,5	11,5	54	36,5
3.1	91	91	11	9	32	44,5
3.2	86	88	16,5	10,5	80	56
3.3	82	86	15	7,5	82	44
3.4	86	89	11,5	8,5	65,5	32
3.5	94	92	10	8,5	65,5	35
4.1	92	90	16,5	7,5	72	55
4.2	91	89	19	10	81	59,5
4.3	83	86	14	5	68,5	20
4.4	87	87	11,5	6,5	57,5	14,5
4.5	93	91	10	8	60	24
5.1	94	91	20	10	85	44
5.2	90	90	20	8,5	81	59
5.3	81	87	14	10	62	52
5.4	86	89	12	9	59,5	37
5.5	88	92	10	7,5	39	32,5
6.1	93	92	23	6	78	31,5
6.2	89	89	25	6,5	92	31,5

Table 2 (continued)

6.3	82	85	20,5	8	79	18
6.4	87	87	10	9,5	45	40
6.5	89	89	8	11	30	58,5
7.1	94	93	16,5	13,5	67	66
7.2	90	90	16	9	59	48
7.3	82	88	18	12	75	63
7.4	92	89	12,5	12	65,5	57,5
7.5	93	90	10,5	13	70	59
8.1	90	92	18	15	58,5	68
8.2	84	89	14	11	55,5	57
8.3	78	87	13,5	14	57,5	67
8.4	82	88	16,5	12	59,5	54
8.5	88	90	19,5	14	77,5	54,5
9.1	91	91	13	14	67,5	68,5
9.2	84	88	18	16	73,5	70
9.3	77	88	13	15	50	70,5
9.4	83	87	16,5	16,5	70,5	74
9.5	89	91	13,5	12	43	60
10.1	90	90	12,5	13,5	67	59
10.2	85	89	14,5	17	54	70
10.3	78	88	19,5	15,5	73,5	62
10.4	82	90	13	14	37	58
10.5	91	91	12	14	49,5	63
11.1	92	91	12,5	11	62,5	46,5
11.2	84	88	14,5	11	62	46
11.3	77	88	14	15	54	64
11.4	80	87	12,5	13	46,5	55
11.5	91	90	11,5	13	30	67
12.1	90	90	13	14	14,5	50
12.2	86	88	22,5	15	75	44
12.3	79	87	21	16	76	62
12.4	85	88	12	13	35,5	58
12.5	92	91	8	15	50,5	68

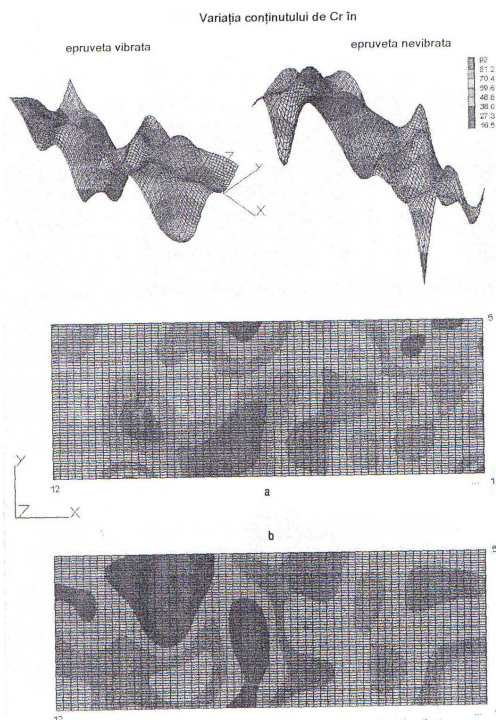
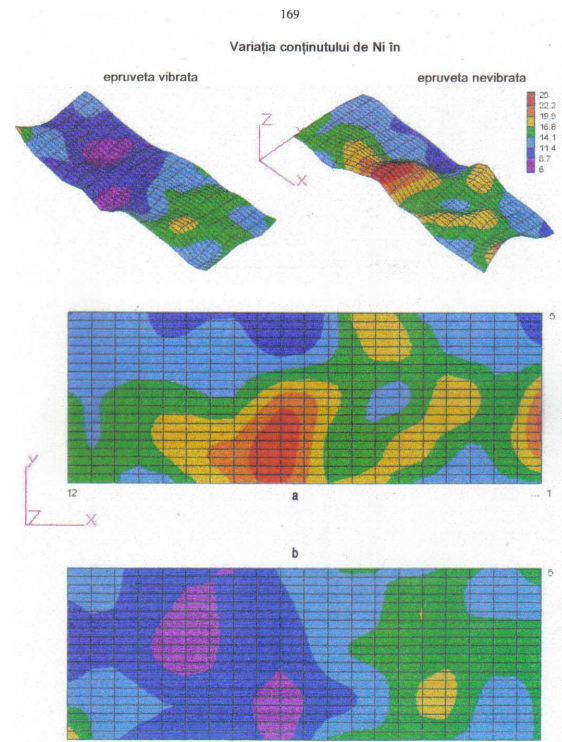
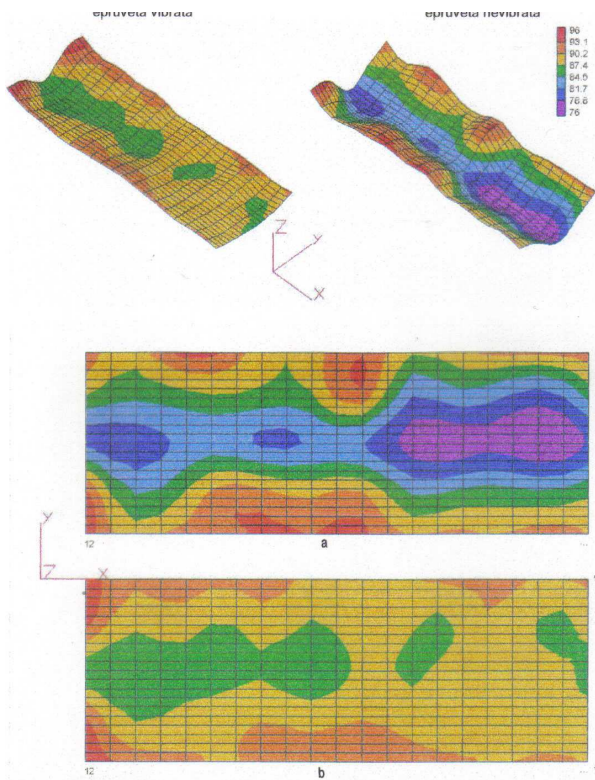


Fig. 6.69. Variația conținutului de crom pe secțiunea lingoului: a - nevibrat; b - vibrat.

### 3. Conclusions

Hardness increases its uniformity grade by attaching the vibrations at solidification with 38.9% and the segregation, decreases without reserve with 27.8%.

A more marked effect of vibrations, regarding the shrinking of segregations appears at chemical elements which constitutes steel carbide and less intense when elements form solid solutions.

Received:  
May 13 2005

The "Gh.Asachi Technical  
University from Iasi

**REFERENCES**

1. Efimov V. – “Casting and crystallization of steels” ,”Editura tehnica”, Bucuresti, 1980
2. Gâdea S., Petrescu M. – “Physic metallurgy and the study of metals”, “Editura didactica si pedagogica”, Bucuresti, 1979

**STUDII PRIVIND INFLUENTA VIBRATIILOR ASUPRA COMPOZITIEI SI DURITATII UNUI LINGOU****(Rezumat)**

In lucrare sunt prezentate cercetari asupra segregarii chimice si a duritatii pentru cazul vibrarii unui otel, când se utilizeaza o instalatie de vibrare cu o frecventa de 100 Hz. La lingourile vibrante creste uniformitatea si valoarea duritatii cu 38,9 iar segregarea scade pe ansamblu cu 27,8 %. Un efect al vibrarii la solidificare este si faptul ca micșorarea segregatiilor este mai accentuata la elementele care formeaza carburi si mai puțin la cele care formeaza solutii solide.

## THE CONNOTATIONS ON HARDNESS AT DYNAMIC CAST PIECES

BY

GELU BARBU

**Abstract:** The alloy which contains 99.4% Al, 0.18% Si, 0.13 Fe, is being vibrated circular-horizontally through an original vibrating system, studying the variation of hardness on longitudinal and transversal direction at some samples casted in shape of moulding sand and in metallic mould. The fact that bigger differences between the valours of hardness at the samples casted under the influence of vibrations and the one statically casted appear at the extremities of the pieces, when casted in moulding sand, and in the case when the pieces were casted in metallic moulds, the bigger hardness differences are at the middle of the pieces, on horizontally direction. In all the cases the samples casted under the influence of vibrations have higher hardnesses than the ones statically casted.

**Key words:** vibrating system, in metallic mould

### 1. General considerations

When the vibrations are being applied, a series of physical processes appear, like the action of count forces, the mass macroscopic transfer, cavitation phenomenon, the amplification of the overcooling degree and the changing of the conditions of solid-fluid equilibrium. Thus, shearing forces appear, which act on the growing dendrites, at the solid-fluid severance limit. The macroscopical mass transfer depends on the correlation between the amplitude and the frequency of the movement, the crystals which belong to the moving fluid will come into collision with the branch of the dendrites in the bracket, resulting a breaking effort  $\tau_r$ , given by the relation:

$$\tau_r = \frac{1}{2} \rho_c W^2$$

In which  $\rho_c$  is the density of the crystals and  $W$  – the speed of the fluid.

The displacement of the alloy accomplishes in flowing regime given by the Reynolds criterion, in the expression intervening the amplitude and the casting frequency. When the relative speed between the fluid and the crystals is bigger than a critical speed, the cavitation phenomenon appears.

After the destruction of the cavitation bubble, the gases from the interior of it compresses itself almost adiabatic. The performing implosion is attended by an important rising of the local pressure, which may have as an impact the crashing of the crystals current growing.

But the possibility that at high amplitudes of the vibrating movements also exists, and also, to appear voids in the casted material and splashes at the exterior surface.

The mechanic-physical treatments, applied to the alloys in liquid state intensifies the vibration in the limitation layers, which conduces towards collateral

currents, changes the hydrodynamical situation at the limit between the solidified layer and the walls of the shape, so it changes the conditions of the heat convector transfer and the macroscopical mass transfer; thus, the speed grows and the solidification time reduces.

The vibrations influence the superficial tension between the phases (solid-liquid) in the purpose to reduce it, to conduce to the shrinking of the minimum radius of the nucleuses on which these do not remelt but they follow a development process.

The propitious effect on the appearance on the solid phase owes to the conglomerate processes of the subcritical germs and the activation of the heterogeneous surfaces.

Among the technological effects of the application of the vibrations at solidification: the homogenization and the finishing of the solidification structure, the amplification of the compactation of the casted material, the degasing of the alloy, the shrinking of the segregations, the expulsion of unmetallic inclusions and the increase of the capacity of yielding alloy.

It is known that through vibration, while solidification of the metallic material structure it finishes, by finishing obtaining and emending some mechanic-physic properties.

## 2. Experiments

There have been done attempts to study the influence of the cooling speed and the vibrations applied at the aluminum solidification. Thereby shapes have been casted in moulding sand and in metallic moulds, static and under the influence of the vibrations.

*Table 1 The chemical composition of the cast shapes*

No. ingot	Mould	Pouring conditions	Al	Si	Fe
1	moulding sand	static	99,4	0,17	0,13
2	moulding sand	vibrated	99,3	0,21	0,16
3	metallic mould	static	99,4	0,17	0,12
4	metallic mould	vibrated	99,4	0,17	0,13

For melting there has been used an electric furnace, with resistances, using pure metals, prealloys and alloy anterior melted, the liquid bath being protected with a layer of agent of fusion.

The casting temperature was 730°C, and the shapes have been preheated at a temperature of cca.100° C.

There have been casted control cylinders, in section, which were coped, and in the section were determined the valours of hardness in 28 points, according to Fig.1 , the results of the determinations being comprised in tables 2, 3, 4 and 5.

	a	b	c	d
1				
2				
3				
4				
5				
6				
7				

Fig.1. Placing in the longitudinal section of the points where the hardness measuring done

Table 2. Hardness values, [HB], for the ingot 1.

	A	b	c	D	media
1	63	64,5	63,8	64	63,83
2	63,3	63,3	64,9	62,9	63,6
3	63,5	63,5	65,4	64,7	64,28
4	61,1	64,4	64,9	64,3	63,68
5	62,2	62,5	64,3	65,3	63,58
6	60,8	62,2	63,6	65	62,9
7	62,1	61,2	63	58,6	61,23
media	62,28	63,09	64,27	63,54	

Table 3. Hardness values, [HB], for the ingot 2

	A	b	c	d	Media
1	66,6	65,1	65,1	65,5	65,58
2	65,4	65,1	64,5	65,0	65,0
3	65,4	64,1	65,7	64,5	64,98
4	65,1	62,9	65,3	63,4	64,18
5	63,0	64,4	63,4	64,3	63,78
6	65,8	63,8	63,5	64,8	64,48
7	61,2	65,3	62,6	65,6	63,68
media	64,67	64,39	64,3	64,73	

Table 4. Hardness values, [HB], for the ingot 3.

	A	b	c	d	media
1	67,8	66,3	66,1	66,3	66,63
2	67,1	65,7	67,2	65,6	66,4
3	67,8	63,3	67,2	66,5	66,2
4	66,9	62,4	67,3	66,5	65,78
5	66,9	64,5	67,8	66,1	66,33
6	67,0	64,8	66,8	67,1	66,43
7	67,7	65,1	67,4	67,4	66,9
media	67,3	64,5	67,11	66,5	

Table 5. Hardness values, [HB], for the ingot 4

	A	B	c	d	media
1	66,7	68,2	67,7	67,9	67,63
2	67,1	67,5	65,1	67,3	66,75
3	67,7	78,8	67,8	67,8	67,78
4	68,3	67,9	68,9	67,1	68,05
5	67,2	68,2	68,2	66,3	67,48
6	67,6	68,6	67,1	66,9	67,55
7	67,8	68,7	66,9	67,0	67,6
media	67,49	68,17	67,39	67,19	

In Fig. 2, 3, 4 and 5 are shown the variations of hardness in longitudinal plan for the experiment ingots.

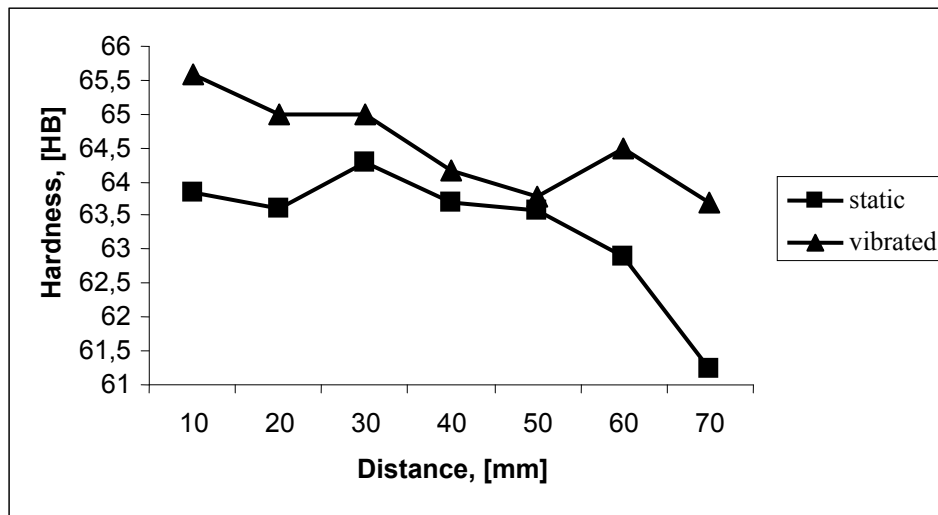


Fig. 2 Variation of the hardness in longitudinal plan for ingot casted in moulding sand

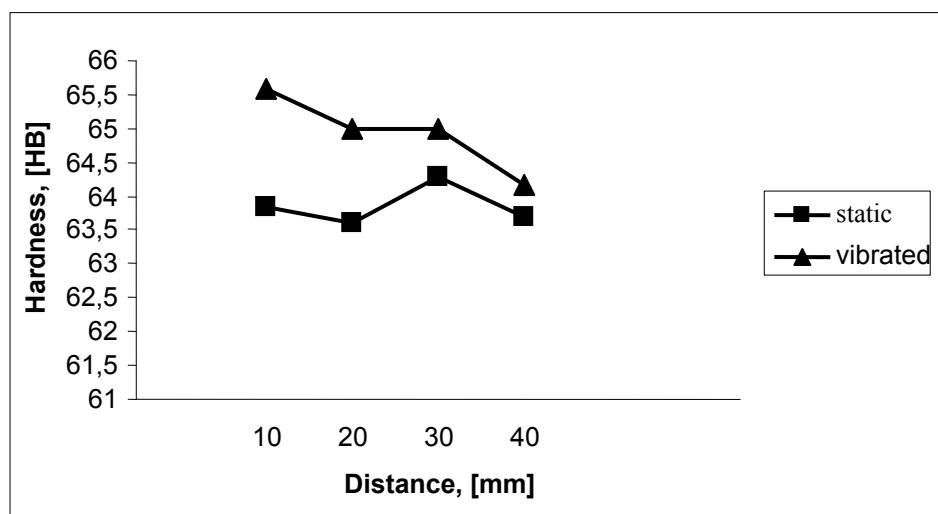


Fig. 3 Variation of the hardness in transversal plan for ingot casted in moulding sand



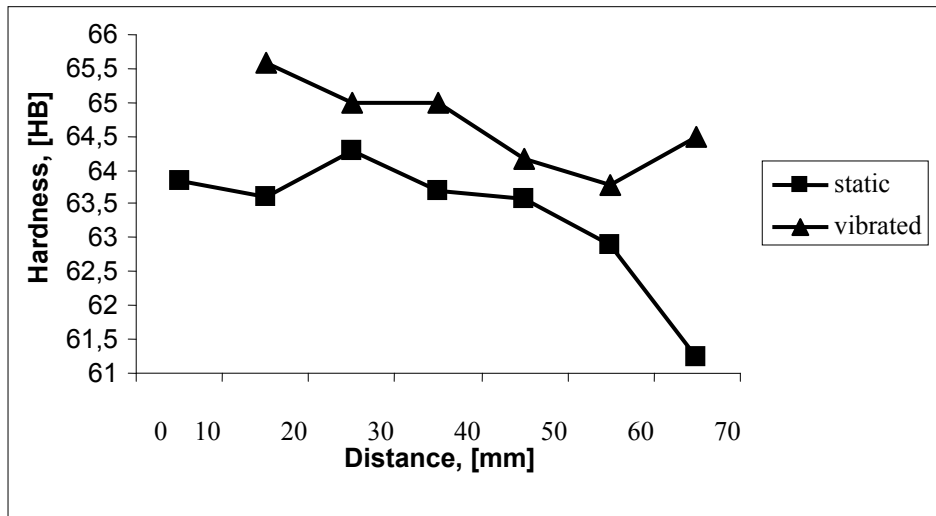


Fig.4 Variation of the hardness in longitudinal plan for ingot casted in metallic mould

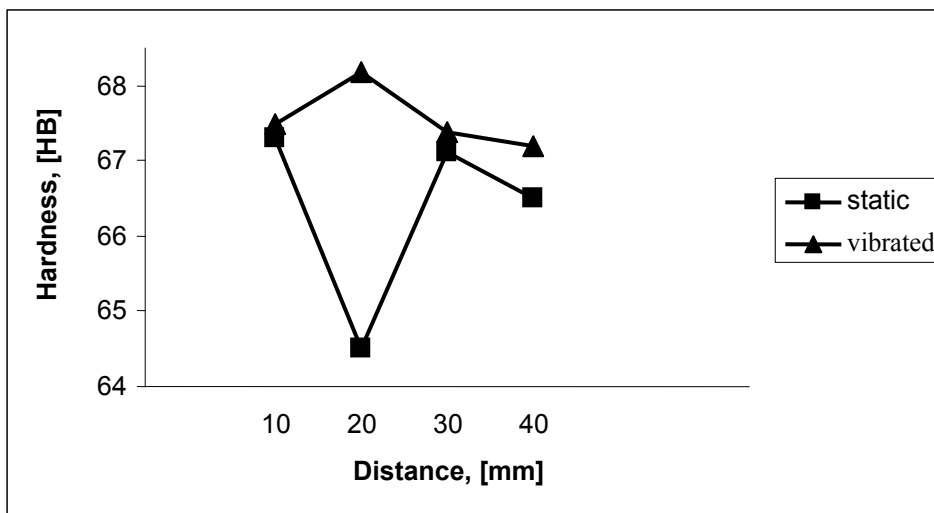


Fig.nr.5. Variation of the hardness in transversal plan for ingot casted in metallic mould

### 3. Conclusions

Bigger differences between the values of hardness at the shapes casted under the influence of the vibrations and the one statically casted appear at the extremities of the pieces, when casting in shapes of moulding sand.

In the case when the pieces, casted in metallic moulds the bigger differences of hardness are at the middle of the pieces, on horizontally course.

In all the cases the pieces casted in metallic shapes have bigger hardnesses than the one statically casted.

**REFERENCES**

- 1.Dittmann, O. ș.a. Verfahren zur Herstellung von Bassen aus Ferrolegerung, Kupfer-Legierungen, Aluminium – Legierungen unde de glehen – Anmelder; Umeura, Ikno,Tokio,Bundesrepublik Deutschland Deutsches Pateentamt, nr. 2.334.544.06.06.1973.
- 2.Barbu Gelu - Solidificarea aliajelor sub influența vibrațiilor, Iași, 2003.
- 3.Barbu Gelu, Cojocaru, V.Carcea – Instalație de turnare cu vibrație, brevet de invenție, România, nr.108.934 B1 – 1994.

**CONOTATII ASUPRA DURITATII LA PIESELE TURNATE DINAMIC****(Rezumat)**

Se vibrează aliajul ce conține 99,4% Al, 0,18% Si, 0,13% Fe, circular-orizantal, prin intermediul unui sistem de vibrație original, studiindu-se variația durității pe direcție longitudinală și transversală în cazul unor probe turnate în forme din amestec de formare și metalice. Se observă că diferențe mai mari între valorile durității la probele turnate sub influența vibrațiilor și cele turnate static apar la extremitățile pieselor, în cazul turnării în forme din amestec de formare, iar în cazul pieselor turnate în forme metalice diferențele mai mari de duritate sunt la mijlocul pieselor, pe direcție orizantală. În toate cazurile probele turnate sub influența vibrațiilor au durități mai ridicate decât cele turnate static.

## NANOSTRUCTURED COMPOSITE COATING Ni-SiC OBTAINED BY ELECTRODEPOSITION

by

LIDIA BENE<sup>\*</sup>, PIER LUIGI BONORA<sup>\*\*</sup> and FRANÇOIS WENGER<sup>\*\*\*</sup>

**Abstract:** Due to their high wear resistance and the low cost of ceramic powder, nickel – silicon carbide composites have been investigated to the greatest extent and successfully commercialized for the protection of friction parts. The present work has the purpose of realisation and investigation of the nanostructured composite coatings by using nano sized silicon carbide particles (mean diameter 20nm) in electrodeposition process with nickel. The possibility of codeposition and some effects of nanosized SiC particles on the mechanism of metal deposition were investigated. A sulphate - chloride nickel plating bath was used. The embedded nano sized particles affect the metal matrix surface morphology and structure. Cathodic polarization and impedance diagrams were performed in the electrolyte without and in the presence of nano - dispersed phase to observe the influence of dispersed nanocrystals of SiC on the nickel reduction. The uniformity of the dispersed phase distribution and the surface quantitative analysis of the composite coatings were examined by SEM with an EDX system. SEM also revealed the comparative surface morphology of pure nickel and composite coatings. The presence of particles inside of the composite coatings was detected by X-ray diffraction and directly observed by TEM.

**Keywords:** nanostructured layers, nanoparticles, composite, silicon carbide, nickel matrix, electrodeposition.

### 1. INTRODUCTION

Due to their high wear resistance and the low cost of ceramic powder, Ni-SiC composites have been investigated to the greatest extent and successfully commercialised for the protection of friction parts. To achieve a combination of wear and heat resistance, the electrodeposited composite coatings contained mixtures of dispersed particles, or were composed of sublayers differing in the nature of inclusions and of metal matrix. In order to provide better adhesion to the substrate, a ceramic-free ductile underlayer was plated in a separate nickel bath before plating the Ni-SiC layer. In most cases the particle size was ranged from 1 to 40  $\mu\text{m}$ . The most recent works on the Ni-SiC system used modulated current in order to obtain SiC gradient distribution or layer by-layers with different SiC content. The dimensions of dispersed SiC powder are in the range of micrometers and the shapes from round to acicular or a mixture of them are reported [1-11]. Some additives influence on SiC incorporation rate are presented in the paper [6]. Paper [5] present the influence of micrometric sized SiC particles (1.1-17 $\mu\text{m}$ ) on the cathodic polarization curves and cathodic impedance diagrams correlated with the structure changes of nickel matrix.

The present work has the purpose of realization and investigation of the nanostructured composite layers by using (for the first time) nanocrystals of silicon

carbide (mean diameter 20 nm). There is a lack of information regarding the mechanism of codeposition process, therefore our work aims to examine the possibility of codeposition, some effects of nanosized SiC particles on the mechanism of nickel deposition from a sulfate - chloride nickel plating bath and how this inclusion affect the nickel matrix surface morphology and structure.

Cathodic polarization and impedance diagrams were performed in the electrolyte without and in the presence of particles in order to observe the influence of dispersed nanocrystals of SiC on the nickel reduction. The uniformity of the dispersed phase distribution and the surface quantitative analysis of the composite coatings were examined by SEM with an EDX system. SEM also revealed the comparative surface morphology of pure nickel and composite coatings in relation with their grain size. The presence of particles inside of the composite coatings was detected by X-ray diffraction and directly observed by TEM. It is shown that the incorporation the nano SiC modify the impedance and cathodic polarization diagrams in correlation with the changes observed surface morphology of nickel matrix. The corrosion properties of composite coating are improved comparative with pure nickel coating (electrochemical, salt spray and wear corrosion). These properties will be discussed in a further paper.

## 2. EXPERIMENTAL SET-UP

### 2.1 Influence of nano SiC particles on nickel electrocrystallisation

The SiC - nickel nanocomposite films were electrodeposited from a suspension of SiC nanoparticles (20 nm) in aqueous nickel sulphate - chloride electrolyte. The particles size dimension was observed by transmission electronic microscope (TEM), as we can see on Figure 1. The mean diameter was calculated at 20 nm.

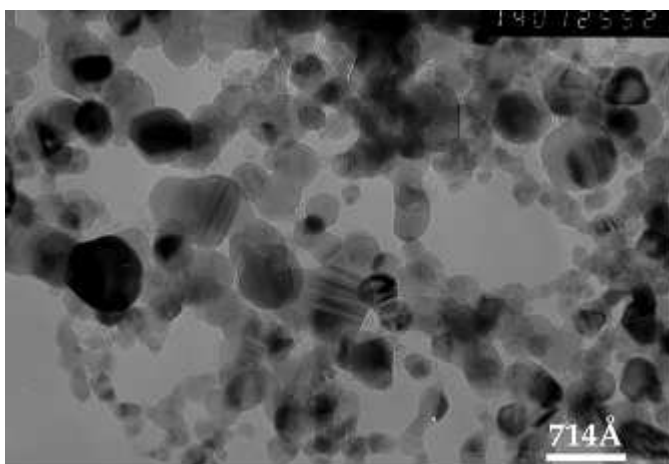


Fig.1 TEM image of nano SiC particles:  
surface area=109m<sup>2</sup>/g  
Density=3.4  
g/dm<sup>3</sup>diameter=11-67 nm

Suspensions were prepared by adding SiC nanoparticles to the solution to give a concentration of 10-50 wt. %. The suspension were stirred for 24 hours before deposition. Electrodeposition of pure Ni and nanocomposite films was carried out on interchangeable rotating nickel disk electrodes. The same experiments were performed on cylindrical and planar cathodes in order to compare if codeposition could be obtained on different cell arrangements. The electrochemical investigations presented were performed only on rotating disk electrode. The plating cell was a glass container

with an outer jacket for water circulation. The solution temperature was maintained by water circulation at thermostated temperature of 45°C. Potential was controlled by a potentiostat/galvanostat (EG&G M273). Nickel cylindrical plate was used as anode and a Ag/AgCl (207 vs. NHE) was used as reference electrode. Magnetic stirring was employed at the cell bottom to maintain an uniform particle concentration in the bulk solution. Sodium dodecyl sulfate was used as additive to improve the particles wettability. The slow potentiodynamic polarization at a sweep rate of 0.5 mV/s were acquired with a programmed potentiostat interfaced to a computer. Electrochemical impedance spectra were acquired in the frequency range of 30 kHz to 3 mHz with a 10 mV amplitude sine wave generated by a frequency response analyzer.

## **2.2 Comparative structure of nanocomposite and pure nickel coatings.**

The morphology of deposits was examined by scanning electron microscopy (SEM) with energy disperse analyzer system (EDX) in order to perform the composition of nanocomposite coating on the same surfaces. The performed analyze is only for informative comparison and not done as absolute values. Using transmission electron microscopy (TEM) the shape and size dimensions of nanoparticles was evidenced. The presence of nanoparticles inside of nanocomposite coating was established using TEM and X-ray diffraction methods.

## **3. RESULTS AND DISCUSSION**

### **3.1 Influence of nano SiC particles on nickel electrodeposition**

Figures 2-4 show the potentiodynamic and impedance diagrams plotted at different cathodic potential with and without dispersed nanoparticles in the nickel plating bath at two electrode rotation speeds (200 rpm and 100 rpm).

The addition of silicon carbide nanoparticles displaces the nickel reduction curve (Fig. 1) to more positive potentials. The shift in reduction potential were attributed to an increase in the active surface area due to the adsorbed particles on the cathode and to a possible increase in ionic transport by nanoparticles with their ionic layers adsorbed. It is supposed that the nanoparticles are surrounded by a thin layer of ( $\text{Ni}^{2+}$ ) and ( $\text{H}_3\text{O}^+$ ) ions adsorbed after the particles were introduced in the electrolyte. These positively charged particles could reach the cathode surface. The negatively charged particles will be rejected to the bulk of the solution. The same displacement of the curve to more positive potential was observed by Watson [5] using micrometric SiC sized particles (1.1 to 17 $\mu\text{m}$ ) codeposited with nickel in a sulfate nickel bath. The fixation of the particles has been often ascribed to the reduction of metallic ions adsorbed at the particle surface [1, 6].

Electrochemical impedance spectroscopy (EIS) were performed in the nickel plating bath with and without silicon carbide particles to further distinguish the effects of a semiconductive nanoparticles on the mechanism of nickel deposition (Figs. 3-4).

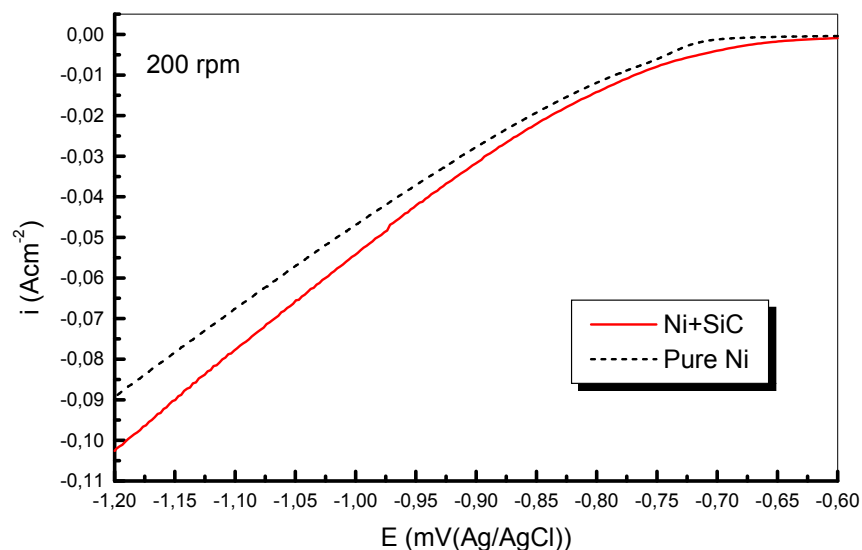


Fig. 2. Cathodic potentiodynamic diagrams for: (solid line)-codeposition of nano-SiC particles with nickel (50 g/l SiC in the electrolyte), (dash line)- pure nickel electrodeposition. Sweep rate 0.5 mV/s

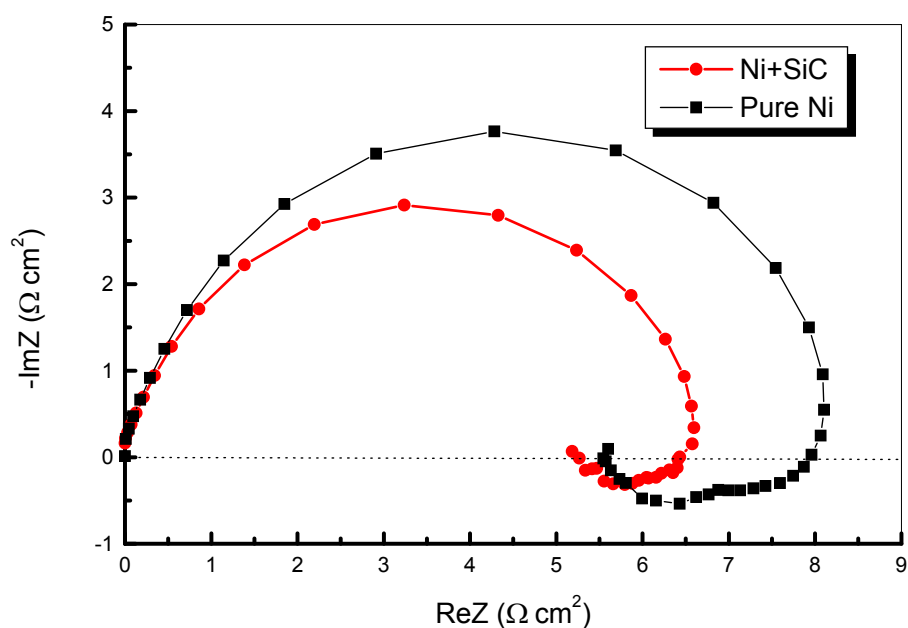


Fig. 3. Impedance diagrams performed at cathodic potential of  $-750$  mV (Ag/AgCl): (solid circle)-codeposition of nano-SiC with nickel (50 g/l SiC in the electrolyte), (solid square)-pure nickel electrodeposition. Disks rotation 200 rpm.

The characteristic inductive loops at low frequency observed from the Nyquist plots are larger for pure nickel reduction than that for codeposition of nanoparticles with nickel. The adsorption / desorption process of intermediates at/from cathode surface seems to have different times constant in the case of nanoparticles codeposition. The charge transfer resistances were lower in the presence of nano SiC particles and very well defined at  $-750$  mV (Ag/AgCl) reduction potential. Thus in

Fig. 3 the charge transfer resistance is about  $6.5 \Omega\text{cm}^2$  for nanocomposite deposition and  $8.2 \Omega\text{cm}^2$  for pure nickel plating at same reduction potential ( $-750\text{mV}$ ).

The influence of nanoparticles on the impedance diagrams during electroplating is higher at smaller rotation of cathode disks. We can see that, at 100 rpm the shift of charge transfer resistance in presence of nano SiC is bigger at the same cathodic reduction potential of  $-750 \text{ mV}$  (Ag/AgCl), Fig. 4. This could confirm the supposition that the nanoparticles enhance the ionic transport to the cathode surface by their adsorbed ionic layer. At smaller rotation rate of the disks, where the nickel plating could be dependent on mass transport (not only charge transfer controlled) the influence of nanoparticles are significant on impedance diagrams.

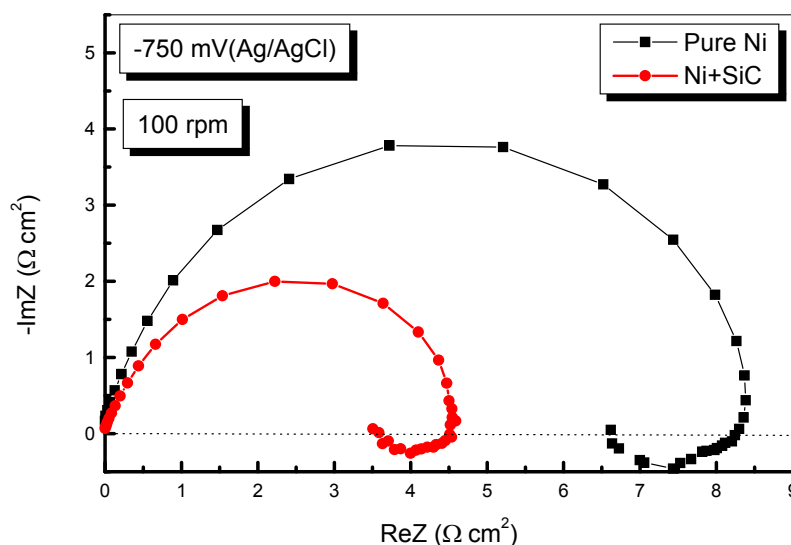


Fig. 4. Impedance diagrams performed at cathodic potential of  $-750\text{mV}$  (Ag/AgCl): (solid circle)-codeposition of nano-SiC with nickel (50 g/l SiC in the electrolyte), (solid square)-pure nickel electrodeposition. Disks rotation 100 rpm

The effect of micrometric sized SiC particles codeposited with nickel on impedance diagrams is observed also in the paper [5], but the diagrams are very poorly defined in the low frequency part. Using the Epelboin et al. mechanism [12,13] the author consider that the addition of micrometric SiC particles are preferentially catalyzing a  $H_{(ads)}$  intermediate and no a  $Ni_{(ads)}^+$ . We consider that by decreasing the charge transfer resistance the nanosized SiC particles activate the nickel reduction. In the same Ebelboin et al. mechanism we consider that the preferentially catalyzing intermediate is  $Ni_{(ads)}^+$ . It is well known that electrodeposition process is a competition between nucleation and crystal growth. The nano SiC particles acts as more nucleation sites in detriment of crystal growth. The corresponding nickel matrix will have smaller crystal size according with this mechanism.

### 3.2 Structural aspects of nanocomposite coating

X-ray diffraction showed that the silicon carbide powder was a  $\beta$  SiC cubic face centered cubic. TEM (Fig. 1) showed particles to be spherical with diameters between 11 and 67nm. The diameter of 20 nm given by the producer can be considered as a

mean diameter. The specific surface area of nanoparticles, as reported by the producer, is  $109 \text{ m}^2\text{g}^{-1}$ . The density value for silicon carbide is  $3.2 \text{ g/dm}^3$ . Due to the small dimensions, low density, and low adsorption of electrons it is difficult to distinguish the particles from the nickel matrix using SEM.

Figs. 5 - 7 compare a pure nickel coating and nanocomposite coating, carried out with  $50 \text{ g l}^{-1}$  of SiC in the plating bath at  $4 \text{ Adm}^{-2}$ , on the rotating disk electrodes. The pure nickel deposit has a rather regular surface, whereas the composite coating develops in a nodular disturbed surface structure. The silicon carbide particles are not clearly visible on the surface because of their small dimensions (white particles in Fig. 6). At a higher magnification and by plating the surface with gold we could observe better the nanosized SiC particles using the electronic microscope (SEM), Fig.7. Figs. 6 and 7 show good uniformity of the dispersed nano-SiC phase in the composite coating. Smaller nickel grain size could be observed in the composite coating (Fig. 6) than in pure nickel coating (Fig. 5). The surface structure of the two types of coatings is different and we expect to have different behavior to corrosion and especially in wear corrosion systems [14,15].

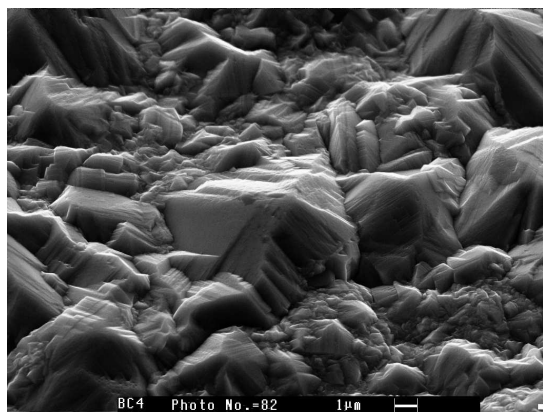


Fig. 5. SEM surface morphology of pure Ni electroplating.  
(Current density  $4 \text{ Adm}^{-2}$ )

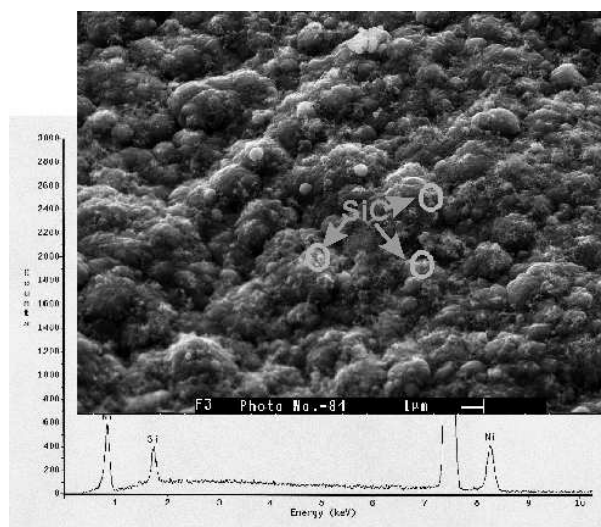


Fig. 6. SEM surface morphology of Ni+SiC nano-structured composite coating  
(Current density  $4 \text{ Adm}^{-2}$ ,  $50 \text{ gl}^{-1}$  SiC in the plating bath, disk cathode)

TEM investigations (Fig. 8) shows the presence of nanosized SiC particles inside of the composite coatings. X-ray diffraction of the same composite layer showed a low texture of nickel matrix with orientation (110), in agreement with electrochemical measures which show a disturbance of free growth of nickel crystals in presence of nanoparticles. In the presence of silicon carbide particle the nickel matrix result in a random than preferred orientation.

In the paper [5] the author consider that hydrogen included in the composite coating (Ni with microsized SiC) explain the smaller crystallite size obtained. We suppose that the higher nucleation sites with nanosized silicon carbide particles perturb the growth of nickel matrix resulting in smaller grain size and random orientation of nano composite coating.



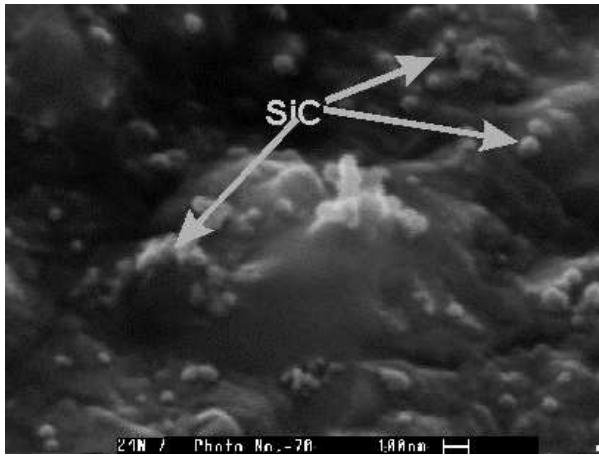


Fig. 7. SEM surface morphology of Ni+SiC nano-structured composite coating at higher magnification

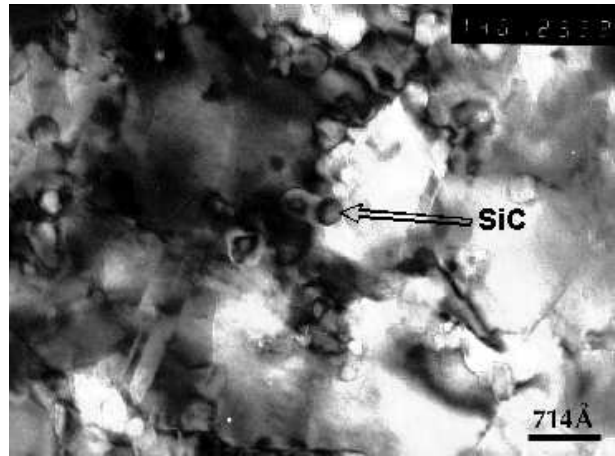


Fig. 8. TEM image inside of a nickel nano-structured composite coating obtained on a disk electrode

### 3.3 Quantitative analysis of SiC amount in the nanocomposite coating

Si content of the composite coatings was measured using a SEM with EDX. Figs. 9 (A) and (B) present the general surface analysis and the point analysis on a presumed silicon carbide phase.

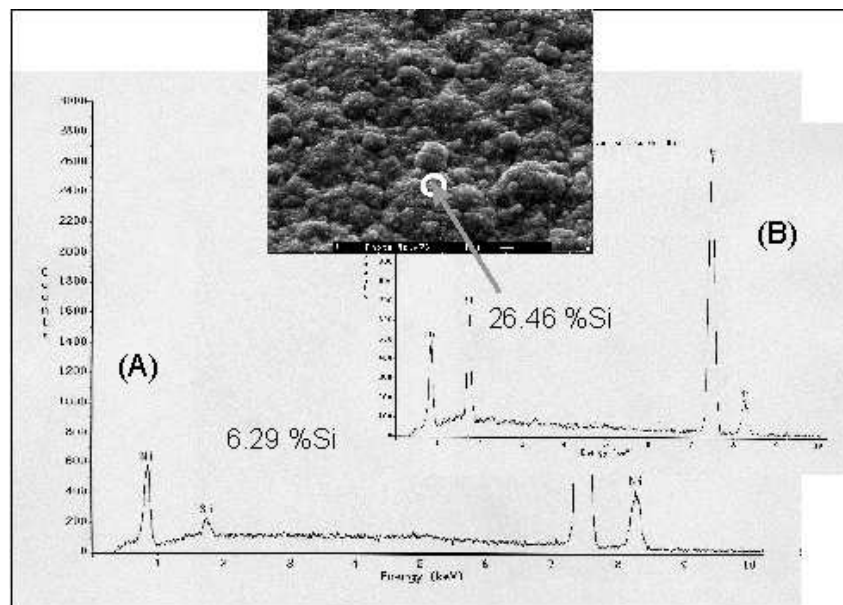


Fig. 9. EDX analysis of composite surface: (A) general surface analysis, (B) point analysis on SiC particles (white particles in Figs. 6, 7)

The results were transformed to SiC in weight and volume percent using a value of  $3,2 \text{ g/cm}^3$  for the density of silicon carbide. For Ni-SiC structures presented in Figs. 6-8, the total amount of nano SiC particles inside the deposit was calculated at 9% weight percent (25 vol.%).

By increasing their content in the electrolyte we could increase the amount of SiC nanoparticles in the composite layer. It must be mentioned that before adding sodium dodecylsulfate in the nickel electrolyte the amount of nano SiC particles in the

coating was very small, 1 wt % in an agglomerated distribution dispersion. The addition of sodium dodecylsulfate was benefit to improve the amount and uniformity of dispersed particles in the nanostructured layer.

The anti corrosion properties of nanostructured Ni-SiC composite coatings are improved comparative with pure nickel coatings [14,15].

#### 4. CONCLUSIONS

Our work proved that nanosized silicon particles (20 nm mean diameter) could be codeposited with nickel to obtain nanostructured composite coating.

The effect of nano SiC particles on the nickel electrodeposition by cathodic polarization and impedance spectroscopy measurements has been studied experimentally.

According to the experimental findings the nano silicon carbide particles affected the shape of the nickel reduction by displacing the curve to lower reduction potential and lower charge transfer resistance.

The influence of nanoparticles in the composite electrodeposition suggest an activation of entire deposition by increasing the ionic transport on the cathode surface due to the ionic layer adsorbed on nanoparticles surfaces. The results suggest the effect of nanosized SiC particles was to increase the nucleation site in detriment of crystal growth resulting in smaller grain size of nickel matrix.

The surface morphology of nano structured composite layers are different compared with pure nickel coating. The surface structure is disturbed by SiC nanoparticles. The smaller grain size of nickel could be observed on surface SEM images The crystal growth of nickel matrix result in a preferentially random than in a oriented one.

The addition of sodium dodecylsulfate improved the uniformity and amount of dispersed particles in the composite coating but their mechanism must be studied.

Received: 17 May 2005

\* The "Dunarea de Jos" University Galati

\*\* Trento University, Italy

\*\*\* Ecole Centrale Paris, France

#### REFERENCES

1. N. Guglielmi, *J. Electrochem. Soc.* **8**, 119 1009-1012 (1972).
2. L. Benea, *Composite Electrodeposition -Theory and Practice*, Ed: PORTO FRANCO, Romania, ISBN 973 557 490 X, (1998).
3. J. Fransaer, J. P. Celis and J.R.Roos; *J. Electrochem. Soc.*, **139**, 413-425 (1992).
4. J. Fransaer, J. P. Celis and J. R. Roos; *Metal Finishing*, **91**, 97-100 (1993).
5. S. W. Watson; *J. Electrochem Soc.*, **140**, 2235 (1993).
6. G. Maurin and A. Lavanant; *J. Appl. Electrochem.*, **25**, 1113-1121 (1995)
7. L. Benea and G. Carac, *Metallurgy and New Materials Researches V No 2*, 1-19(1997).
8. L. Benea, Proceeding volume "*Passivity and Its Breakdown*" P.M. Natishan, H.S. Isaacs, M. Janik-Czachor, V.A. Macagno, P. Marcus, and M. Seo, Sept. 1997, ISBN 1-56677-179-X.
9. L. Benea, *Materials and Manufacturing Processes*, Vol 14, N° **2**, 231-242, 1999.
10. L. Orłowska, N. Pereine, M. Kurtinaitiene, S. Survilione; *Surface and Coating Technology* **111**, 234-239. (1999).
11. Sun Kyu Kim, Hong Jae Yoo; *Surface and Coating Technology* **108-109**, 564-569, (1998).
12. I. Epelboin, M. Jousselein, and R. Wiart, *J. Electroanal. Chem.*, **119**, 61 (1981).

- 
13. E. Chassaing, M. Jousselein, and R. Wiart, *J. Electroanal. Chem.*, **157**, 75 (1983).  
14. BENE A L., BONORA P.L., BORELLO A., MARTELLI S.; *Materials and Corrosion*, 53, 23-29 (2002)  
15. Lidia Benea, Pier Luigi Bonora, Alberto Borello, Stefano Martelli, *Wear* **249**, Issue: 10-11, Nov, pp 995-1003 (2001).

**INVELISURI DIN Ni-SiC COMPOZITE NANOSTRUCTURATE OBTINUTE PRIN  
ELECTRODEPUNERE**

**(Rezumat)**

Prezenta lucrare are scopul de a realiza o investigatie a acoperirilor din compozite nanostructurate prin utilizarea carburilor cu dimensiuni nanometrice (diametrul mediu 20 nm) in procesul de electrodepunere cu nichel.



## THE USES AND CLASSIFICATION OF BIOMATERIALS

BY

VASILE BULANCEA\*, ȘTEFAN LĂCĂTUȘU\*\* and IOAN ALEXANDRU\*

**Abstract:** The present thesis gives a concise account of the definition of biomaterials, biomaterials' fields of usage, organs that may accept different devices in their normal functioning, but also several criteria of biomaterials' classification.

**Keywords:** biomaterials, definitions, uses, classifications, selections.

### 1. INTRODUCTION

The achievements in the field of biomaterials are based on three scientific areas: chemistry, biology and physics, the technical applications or "the making of" reaching their climax with the clinical achievements.

Man has always been interested in the restoration of some parts of the human body, which had been deteriorated or lost because of some accidents or illnesses. Among man's first concerns there was the restoration of the denture which usually became spoilt because of the way of living and eating.

The quality of a material for making an implant, has to respect the following two criteria: the biochemical criterion and biomechanical criterion.

According to biochemical criterion, a material applicability is related to its biocompatibility, and from the biomechanical viewpoint is the fatigue strength, the most important parameter, but not the only one. Therefore, the material used for making an implant, concerning to recollect criteria, is called biomaterial. A biomaterial is a *synthetic material used to replace part of a living system or to function in intimate contact with living tissue*.

The Clemson University Advisory Board for Biomaterials has formally defined a biomaterial to be «*a systemically and pharmacologically inert substance designed for implantation within or incorporation with living systems*» /Hench/.

The role of biomaterials has been influenced considerably by advances in many areas of medicine (for example: the advent of antibiotics or advances in surgical technique).

## 2. USES OF BIOMATERIALS

The use of biomaterials depends by the performance of materials in the body. First, it may consider biomaterials from the point of view of the problem area that is to solved, as in Table 1.

Table 1 Uses of Biomaterials

Problem area	Examples
Replacement of diseased or damaged part	Artificial hip joint, kidney dialysis machine
Assist in healing	Sutures, bone plates and screws
Improve function	Cardiac pacemaker, contact lens
Correct functional abnormality	Harrington spinal rod
Correct cosmetic problem	Augmentation mammoplasty, chin augmentation
Aid to diagnosis	Probes and catheters
Aid to treatment	Catheters, drains

Second, it may consider the body on a tissue level, an organ level (Table 2), or a system level (Table 3). Third, it may consider the classification of materials as metals, polymers, ceramics, and composites as is done in Table 4.

In that vein, the role of such materials as biomaterials is governed by the interaction between the material and the body, specifically the effect of the body environment on the material, and the effect of the material in the body.

Table 2 Biomaterials in Organs

Organ	Examples
Heart	Cardiac pacemaker, artificial heart valve
Lung	Oxygenator machine
Eye	Contact lens, eye lens replacement
Ear	Artificial stapes, cosmetic reconstruction of outer ear
Bone	Bone plate
Kidney	Kidney dialysis machine
Bladder	Catheter

It should be evident in any of these perspectives that most current applications of biomaterials involve structural functions even in those organs and systems that are not primarily structural in their nature, or very simple chemical or electrical functions. Complex chemical functions such as those of the liver, and complex electrical or electrochemical functions such as those of the brain and sense organs, cannot be carried out by biomaterials.

Table 3 Biomaterials in Body Systems

System	Examples
Skeletal system	Bone plate, total joint replacements
Muscular system	Sutures
Digestive system	Sutures
Circulatory system	Artificial heart valve, blood vessels
Respiratory system	Oxygenator machine
Integumentary system	Sutures, burn dressings, artificial skin
Urinary system	Catheters, kidney dialysis machine
Nervous system	Hydrocephalus drain, cardiac pacemaker
Endocrine system	Microencapsulated pancreatic islet cells
Reproductive system	Augmentation mammoplasty, other cosmetic replacements

### 3. CLASSIFICATION OF BIOMATERIALS

An usual classification of the biomaterials is the structural one, in large classes of materials : metallic, ceramic, polymeric and composites, Table 4.

The metallic biomaterials like Fe, Cr, Co, Ni, Ti, Ta, Mo and W, used for implants , are tolerated by the living tissues in small quantities, although some of the materials in their natural state are essential for the cellular functions. Another special category of alloys is one with « form-memory alloys », that after plastic deformation they return to their initial form by simply hitting them.. [Medical applications: for intercranial aneurysms, filters for cava vein, for orthopedic implants i.e.]

Ceramic biomaterials usually are polycrystalline inorganic composites: metallic oxides (alumina), carbides, refractory hybrids, sulphids, selenids. [The most important ceramic materials are usually used in dentistry: dentures, for a special aesthetic look, for a greater resistance to compression and for it not to react with the human body's liquids.]

Composite biomaterials are formed by two or more distinct phases with distinct proprieties from the ones of the homogenous material. The added material in a composite may take the form of particles, fibers or stripes. Fibrous or laminated striped composite materials are anisotropic composites, and those who take the form particles, uniformly arranged all along the matrix are isotropic composites. The anisotropic composites have a greater resistance than the isotropic ones. The anisotropic composites can be used only if we know the direction of the application of the tension. It is necessary too that every constituent not to be degraded from the body environment. [Medical applications: dental composites for fillings, methilmetacrillate reinforced with carbon fibers and bone particles, zirconia, bone cement.]

Polymeric biomaterials are materials obtained by binding smaller molecules (mers) by primary covalent bindings in a main chain. [Medical applications: implants for the replacement or the remaking of soft human tissues – sutures, blood veins, artificial skin]

Table 4 Materials for Use in the Human Body

Materials	Advantajes	Disadvantajes	Examples
<b>METALS</b> Titanium Stainless Steels Co-Cr alloys Gold	Strong, tough Ductile	May corrode Dense	Joint replacement, bone plates and screws, dental root implants
<b>POLYMERS</b> Nylon Silicones Teflon Dacron	Resilient Easy to fabricate - -	Not strong Diform with time May degrade -	Sutures, blood vessels, Hip socket,, ear, nose, other soft tissues
<b>CERAMICS</b> Aluminum oxide Carbon Hydroxyapatite Zirconia Sticlele ceramic	Very biocompatible, Inert Strong in compresion - -	Brittle Difficult to make Not resilient - -	Dental; hip socket
<b>COMPOSITES</b> Carbon-Carbon	Strong, tailor-made	Difficult to make	Joint implants; heart valves

Other classification, introduces a new criterion regarding the origin of biomaterials (Muster).

According to this criterion, we may classify biomaterials in:

### 1. Biomaterials which are not of living origin:

#### 1.1. Metallic biomaterials:

- Pure metals: - precious (Au, Ag, Pt)  
- non precious (Ti, Ta, Nb, W)
- Metallic alloys : - austenitic stainless steels  
- titanium (TiAl)  
- cobalt-chrom type (with or without W, Mo, Ni)
- Intermetallic composites : - dental amalgams  
- composites or alloys with form memory

#### 1.2 Ceramic biomaterials

- Bioinert – based on oxides ( $Al_2O_3$ ,  $ZrO_2$ )  
- based on carbures and nitrides (Si, Ti)
- Bioactive – calcium phosphate based (hydroxiapatite – HA, tricalcic phosphate – TCP)  
- other calcium salts based (carbonates, sulphates, aluminates)

#### 1.3 Synthetic polymer – base biomaterials

- Ellastomers : silicones, polyurethanes
- Plastic materials: - thermohardenable (epoxy resins, triazines)



-thermoplastics (PMMA, PHEMA, PVA, polyethylene, PTFE, polysulphon, PEEK)  
- bioresorbable: polyglycolic acid – PGA, polylactic acid – PLA)

#### **1.4. Synthesis composite – basis biomaterials:**

- organo-organic type
- mineralo –mineral type
- organo-mineral type

### **2. Biomaterials of biological origin**

### **3. Mixed composite biomaterials**

But from all these types of biomaterials that are described, there are few that are used and this because of the small biocompatibility of some of them. As for a higher technique, research is made on some spongy materials, but at the same time with small mechanic resistance. In this category we can include polyurethanic foam or the foamish metallic alloys where live cells can be cultivated in order to form live tissues, that is with very high biocompatibility.

In order to select biomaterials and to make an implant, it is necessary to take into account many factors: economic, mechanic, electric, the chemical environment, the biological insurance, thermal, surface, performance and research (Bunea).

## **4. CONCLUSIONS**

The evaluation of biomaterials interacting with human tissues acquires a special importance for several International Medical Associations which recommend to the International Standard Organization to accept standardization practice in the field of biomaterials in order to augment their quality.

Nowadays, there is a certain “boom” of new biomaterials. But, in order for these materials to get to be successfully used, we must take into account the new medical requirements. We may improve the materials used only if there is a continuous collaboration with the medical staff. We must not forget that each material should adapt to the needs of each beneficiary, that is the patient, who may not accept standardized form or dimension. The price, that is the economic factor of today’s market economy could be considered another important factor in the acquisition of a material. This is why, in the present conditions, we use mostly cheap materials obtained by medium techniques, but which mustn’t lower the biocompatibility and biofunctionality characteristics.

*Received May 12, 2005*

*\*The Technical University “Gh. Asachi” of Iasi,*

*\*\* The “Gr.T.Popa” University  
of Medicine and Pharmacy*

**REFERENCES**

- Agarwal, B.D., Broutman, L.J., *Analysis and Performanc of Fiber Composites*, J. Wiley & Sons, N.Y., 1980
- Bunea, D., Antoniac, V., Bunea, Zoe, Miculescu, Marian, - *A Classification of Biomaterials and Selection Criteria*, Volum CNMSM, Ed. PRINTECH, Buc., 2001, ISBN 973-652-389-6;
- Craig, Robert G., *Restorative Dental Materials*, 1997, Ed. Mosby-Year Book, Inc.
- Gibson, L.,G., Ashby, M.,F., *Cellular Solids*, Pergamon Press, Elmsford, N.Y.
- Hench, L.L. and Ethridge, E.C., *Biomaterials: An Interfacial Approach*, Academic Press, New York, 1982;
- Muster, D., *Biocompatibilit  et  volution de l'utisation des biomat riaux metaliques in Actualit s en Biomat riaux*, vol. V, Ed. Romillat, 2000;
- Park, J.B., *Biomaterials Science and Engineering*, Plenum Press, New York, 1984;
- Webster, J.G. (ed), *Encyclopedia of Medical Devices and Instrumentation*, J.Wiley and Sons, New York, 1988.

**UTILIZAREA  I CLASIFICAREA BIOMATERIALELOR****(Rezumat)**

Lucrarea prezint  într-un mod concis, definirea biomaterialelor, domeniile de utilizare ale biomaterialelor, organele care pot accepta diverse dispozitive  n scopul func ion rii lor normale, sistemele corpului uman care accept  dispozitive pentru restabilirea bunei func ion ri a lor precum  i diverse criterii de clasificare a biomaterialelor.

## **CRYOGENIC TREATMENTS APPLIED TO STEELS**

BY

**VASILE BULANCEA, IOAN ALEXANDRU, ADRIAN ALEXANDRU,  
DORIN CONDURACHE**

**Abstract:** In the well-known American Journal “GEAR TECHNOLOGY” published in Illinois USA, issue no from March-April 1993, the professor Pete Paulin from 300° Below, Inc. Decatur presented the paper “Frozen Gears” in which he undertakes a comprehensive and comparative study of the researches in the field of cryogenic treatments carried out by a group of Jassy researchers directed by Ph.D Eng. Ioan Alexandru, pointing out the growing importance of the cryogenic thermal treatment in the USA and in the world. This acknowledgement of our activity determined us to publish a general presentation about cryogenic treatment.

**Keywords:** HSS, Heat Treatment, Cryogenic Treatment, Cryogenic Temperatures, Microstructures.

### **1. GENERAL ASPECTS**

The techno-intrinsic value of the products is owed to the following attributes: functionality, economy, durability and reliability.

The durability, an important feature of the concept of reliability, is conditioned by the intrinsic resistance properties and by the actual conditions of exploitation of the product and represents the basic criterion for defining the quality of a tool.

The cryogenation of metals is a process known for 50 years as an efficient method for enhancing the durability or the “wear life” and for decreasing the residual tensions of the steels from the tools. The thermal treatment under 273 K (0°C) called also cryogenic treatment constitutes a modern thermal processing which is efficient and opportune and which, when applied correctly in the chain of the technological operations, determines important increases of the exploitation characteristics of the pieces and tools made of alloy steel and richly alloyed steel. The method of cryogenic treatment for tools is not expensive, and affects the entire mass, not only the surface of the tool. The tools may be new or used, sharp or blunt, and the sharpening cannot affect the treatment.

### **2. THEORETICAL ASPECTS**

The cryogenic treatment may be efficient provided that at the environmental temperature, after the ordinary toughening, the austenite quantity is very large (exceeds 10%). Also, with a view to reduce the residual austenite quantity, there may be made a combination of the cryogenic treatment by resuming it once or twice.

The literature confirms the fact that when the separation of carbon takes place, the intern tensions from the martensite are reduced reducing thus the microfissure susceptibility. The wide distribution of the hard and fine carbids precipitated during the cryogenic treatment enhances the wear resistance, through a denser molecular structure and a wider contact surface, which reduces friction and wear.

Some metallurgists are skeptical regarding cryogenic processing because this does not causes evident visible changes of the metal. Their view is based on the idea that thermal treatment changes 85% of the residual austenite into martensite, while the cryogenic treatment transforms additionally only 8-15%, concluding thus that the cryogenic treatment is an inefficient processing method. The basic idea is correct, but the conclusion is false. The deep cooled metals develop a more even and fine microstructure with a higher density. The cryogenic treatment determines the appearance of the microfine carbids which fill the spaces remained from the microhollows leading thus to a much denser and more consolidated structure of the steel. The particles (microcarbids) were identified and numbered by means of an electronic microscope with quantification and they are responsible to a great extent for the increase of the wear resistance. Unlike the surface treatments, the caused change is uniform, in mass and will be preserved until the total wear of the tool, regardless of ulterior finishing, sharpening operations etc. It is an irreversible and permanent molecular change /2/.

The two microphotographs of 100 x (500 x or 1000 x), from Fig. 1, represent samples from the same steel (M1) treated classically (a) and cryogenically (b).

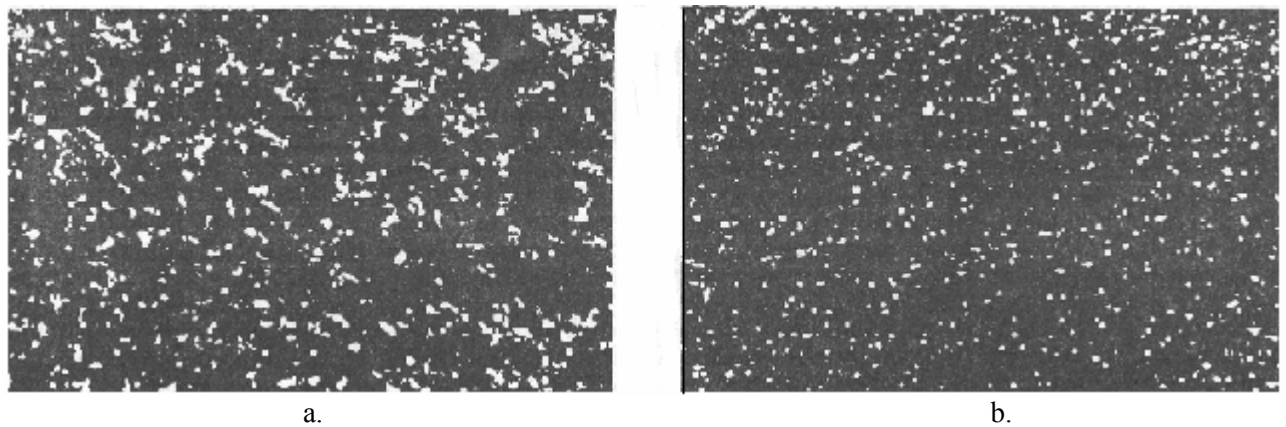


Fig. 1: Fast treated steel M 1's micro photos (a) classically; (b) cryogenically.

### 3. THE EFFICIENCY OF THE CRYOGENIC TREATMENT

Cryogenic processing is an extension of the classical treatment and causes an important enhancement of the durability.

Ph.D. R. F. Barron from the Technological Institute of Louisiana, USA, presents in the "Cryogenics" magazine Issue No. 8/82 a series of results regarding the enhancement of the wear resistance through cryogenic treatments (2). Barron's researches are mentioned also by Ph.D. Dreger in "Machine Design" /4/. He subjected to cryotreatments 12 steels for tools, 3 stainless steels and other 4 steels and cast iron in order to determine the difference between toughening at  $-84^{\circ}\text{C}$  and toughening at

-196°C. The tool steels presented a clear raise of the abrasive wear resistance after toughening at -196°C and a very small raise after the toughening at -84°C (fig2).

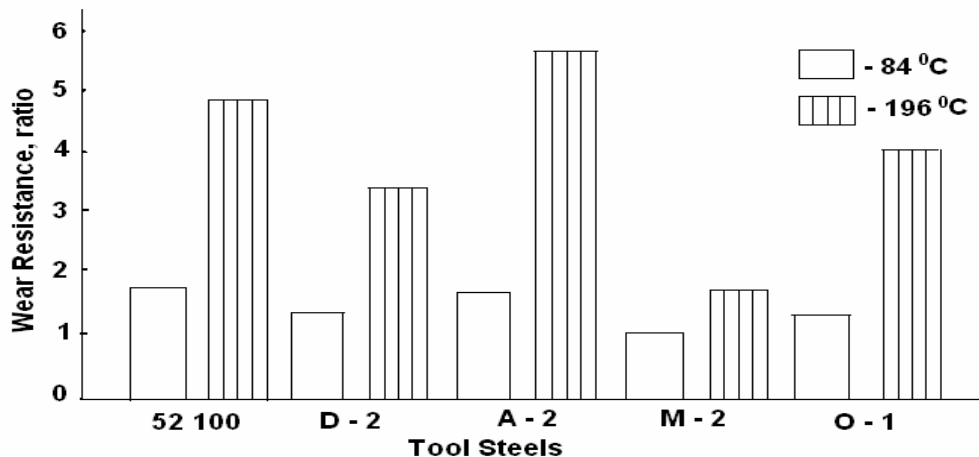


Fig. 2: Resistance at wear, ratio.

Increases of the wear resistance were synthesized by Barron in table 1.

Table 1

Increase the resistant percents at wear after cryogenic treatment			
AISI Standard	Materials	- 84 °C	-196° C
D – 2	Carbons steel / steel with Cr.	316%	817%
S – 7	Tools steel with Si.	241%	503%
S 2 100	Carbons steel of tools	195%	420%
A – 10	Tools steel graffitists	230%	264%
M – 1	HSS with Mo	145%	225%
M – 2	HSS with W-Mo	117%	103%
T – 1	HSS with W	141%	176%
440	Martensite inox steel	128%	121%
430	Ferrite inox steel	116%	119%
303	Austenitic inox steel	105%	110%

In 1982 the company “Mangrove Enterprise Inc.” from Houston, USA, patented a method of cryogenic processing which has as result an important increase of the wear and corrosion resistance of the tools and different machine components /11/. The cryogenic treatment has lead to a residual austenite content of only 0,5% and to the even distribution of the carbids permitting thus the increase of the wear resistance with a factor of 3 at valves, valve seats and insertions for the pumps used at the petrol drill plants, with a factor of 31 at the centrifugal pumps from the paper industry and 5,1 at the components of the mechanical saws, from 5,5 to 8 for the tools used at the pneumatic hammers.

The company “Materials Improvements Inc.” USA, treated cryogenically different materials through a method called by them CryoTech, /12/. This method was employed by the company “Packaging Inc” in the case of rapid steels for processing wood. Through this method, the chopping knives are changed only once a day, whereas before they were changed at each turn.

The company “Amcry Corporation” from USA has created a similar method, the company “Hewland Engineering” from USA treated under 0°C the steel gearings with Ni from the race car engines /5/, the company “BOC International Ltd.” proposed and applied the method of toughening with laser and cooling under 0°C of the camshafts, mechanisms with levers, knives etc /10/.

The first researches on the cryogenic treatment were carried out by Russian researchers, Gulaev A.P. in 1937 and Petrosian P.P. in 1957. The cryogenic treatment became an object of study in USA, France (Institute International de Froid), Scotland, England, Germany, Russia (with many patents in the domain), some attempts being registered also in Bulgaria. In our country, the treatment was a research object in the University Centers of Jassy (where the first school in this domain was founded) and of Cluj-Napoca, as well as ICSITPCSM Bucharest.

The companies specialized in such treatments, the numerous inventions in the domain, the researches from our country speak about the good results of the cryogenic technologies. Thus, it was referred to a minimum raise by 2-3 times of the optimal functioning time of the knives from the paper cutting machine /4/, raises of the wear resistance by 7-8 times /6/, /9/, decrease of the damaging percentage of the layers of the working surfaces by pitting /9/, increase of the dimensional stability by 70-80%, /7/, /9/, decrease of the metal consume, /7/, reduction of the thermal treatment time by 1,5 – 2 times, /6/, reduction of the energetic consume.

#### 4. INDUSTRIAL TESTING IS CONFIRMED BY THE LABORATORY TEST

The most recent studies regarding cryogenic treatment confirms the theory according to which this method enhances to a great extent the wear resistance.

By using modern equipments, the group of researchers from the Technical University “Gh. Asachi”, Iasi, provided relevant results which are part of a comprehensive study (1). The study employed 13 variants of thermal treatment (A-N Fig. 3).

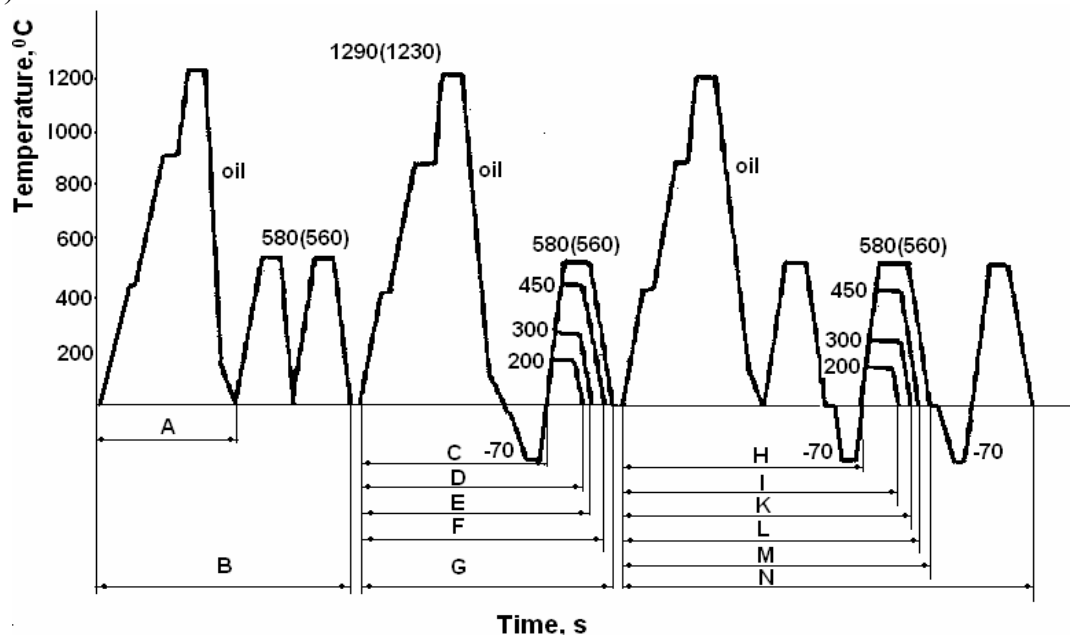


Fig.3: Heat treatment variants tested.

The used samples were taken out of rapid steels T1(W) and M2 (W-Mo), AISI Standard, each sample having the carbids particles numbered physically, both before and after the cryogenic treatment. The results confirmed evidently the precipitation of the carbids during the cryogenic treatment.

The samples were heated simultaneously at 1290°C and 1230°C, respectively, and then toughened in oil, 11 of them were subject to cryogenic treatment at -70 °C.

The results of the research end with the following conclusions and analyses which compare the classical thermal treatment with cryogenic treatments:

- The austenite decreases from 27,1% to 0,9%;
- The HRC hardness increased from 60,10 to 66,10;
- The durability from 20 min to 45 min

The results of Barron study are in accordance with the conclusions of the Jassy researchers group.

## **5. OPPORTUNITY OF THE THERMAL CRYOGENIC TREATMENTS**

In the literature concerning the applicability of the cryogenic thermal treatments there are still serious debates. In the past, the improvements brought to the tools ranged from a small improvement to an over 100% durability increase. Today it has become harder and harder to reach consistent improvements.

In the case of the cryogenic treatment the secret for increasing the durability and reliability consists in processing. The heat exchange must be controlled in a rigorous manner in order to achieve relevant results. If a product is introduced in liquid N<sub>2</sub> it may get chapped. The computer-based processing solves this problem. The computer can optimize the cooling curve exactly according to time. The carrying out of cryogenation only by immersing the product into a cryogenic liquid does not present an adequate control. The new cryogenation systems reach considerable results. Moreover, its price gives the tools manufacturers the possibility to improve their product, profit and to enhance their contribution to the market with a product of superior quality.

The new equipments for thermal treatment operate by controlling the thermal treatment. "Controlled" means in fact: that the process is carried out according to a preset timetable. A PC may be used as a controller of the process which consists in heating, rapid cooling in oil, slow cooling up to -196°C, preserved for 20...60 h, heated at slackening temperature and then cooled slowly at room temperature. This process is "dry" meaning that, in comparison to other deep cryogenic tempering processes, it does not imply the immersion of the material in liquid N<sub>2</sub> which may cause damages through thermal shock.

## **6. THE EFFICENCY OF THE CRYOGENIC TREATMENT**

The costs of the cryogenic processing of tools and of machine components are not high in comparison to the resulted benefits of improving the durability and the performances of the treated tools. For example, tool steel of superior quality may be obtained (T15 with 11, 5%-12,5% W and 0,7% Mo) at a half price, by cryogenic treatment of steel M7 with 1,5%-2% W and 8%-9,2% Mo. Some authors state that the cryogenic treatment increases by 15% the costs of a tool or machine component. Liquid N<sub>2</sub> constitutes the most expensive element in the cryogenation of tools. The newest systems of thermal treatment are designed for a more efficient cold transfer from liquid

N<sub>2</sub> to the metal parts which are treated without losing the cold in the exterior. These systems have reduced the processing costs to 50%, determining thus an economical processing of all parts and tools made of steel.

## 7. CONCLUSIONS

Most of the tools react to this method. By this method one may make tools of superior quality and may reduce a lot of expenses. The cryogenic thermal treatment constitutes today a key factor in the machine building industry reflected by the following:

- Improvement of durability and hardness of the cutting and plastic deformation tools;
- I) Improvement of the resistance properties of the stainless steel parts;
- II) Increase of the resistance properties of the cemented parts or of the parts covered with TiN;
- III) Reconditioning of the used measuring tools;
- IV) Correction of some thermal treatments carried out inadequately;
- V) Increase of the magnetic properties of the steels with special magnetic properties;
- VI) The increase of the cutting-ability of some alloy steels, aluminium, titanium, phenol resins etc;
- VII) Improvement of the physico-mechanic qualities of the high pressure ships and containers made up of stainless steel at the plants for great depths.

Received May 12, 2005

The Technical University "Gh. Asachi" of Iasi,

## REFERENCES

- /1/ Alexandru, I., Contribuții privind influența tratamentului termic sub 0°C ale oțelurilor bogat aliate asupra proprietăților de așchiere, Teza de doctorat, Iași, 1980,
- /2/ Barron, R.F., Cryogenic Treatment of Metals to Improve Wear Resistance, Rev.Cryogenics, Vol.22,nr.8, 1982,
- /3/ Bulancea, V., Influența tratamentului criogenic asupra aspectelor legate de substructura oțelurilor bogat aliate și caracteristicile funcționale ale sculelor așchietoare, Teza de doctorat, Iași, 1992,
- /4/ Dreger, D., The Promise of Cryogenic Processing, Machine Design, USA, vol.53, nr.2, ian., 1981,
- /5/ Hartley John, Gear Failures in Ni Steels Reduced by Subzero Treatment, Engineer, USA, 17, May, 1973,
- /6/ Kalesnikov, V.P., Metodă de tratament termic, Brevet de invenție, Rusia, C12 D6-04, nr.815051-1981,
- /7/ Paletaev, A.V., Metodă de călire colorată a pieselor, Brevet de invenție, Rusia, C 12 D1/56, nr. 740840/1980,
- /8/ Pete Paulin, Frozen Gears, Rev.Gear Technology, USA, March – April, 1993,
- /9/ Silov, V.I., Metodă de tratament termic a fabricatelor din oțeluri de scule, Brevet de invenție, Rusia, C12 D9/24, C12 D6/04, nr. 779421/1980,
- /10/ Tayloe, J., Heat Treatment Hots up with Laser, Metal Production, USA, nr,9, 1979,
- /11/ \*\*\*, Cryogenic Processing ups Wear Properties, Metal Progress, USA,, vol. 122, 6, 1982,
- /12/ \*\*\*, Utilizarea criogeniei în industria prelucrării lemnului (scule), Wood and Wood Products, USA, 87, nr. 3/1982

## TRATAMENTUL CRIOGENIC APLICAT OȚELURILOR

### (Rezumat)

Prezentare generală a aplicării criogeniei în tratarea sculelor având ca referințe lucrări din străinătate și cercetări din țara noastră, mai ales ale autorilor. Rezistența la uzare crește prin aplicarea acestui tratament cu un factor de la 3 până la 8 în cazul sculelor pentru lemn. În cazul oțelurilor rapide rezistența la uzare crește de 3x, iar austenita scade de la 13...17% la 1 ...2%.



## EXPERIMENTAL DETERMINATION OF PERFORATED PLATES HOLES DISTORTION DUE TO MULTIPASS WELDING

BY

DORU CANTEMIR<sup>a</sup>, LEONARDO BERTINI<sup>b</sup>, MARCO BEGHINI<sup>b</sup>, and PAUL DORU BÂRSĂNESCU<sup>a</sup>

**Abstract:** An experiment aimed to study the effects of multipass welding on perforated plates is presented, with a focus on modification of tube holes diameters. The experimental set up and some results are presented and discussed. A welding process involving two heat sources acting concomitantly was employed. The obtained results are useful for validation of this joining process in tubesheet fabrication as well as for finite element welding models verification.

**Keywords:** multipass welding, manual arc-welding, welding distortion, perforated plate, P355NL1 steel

### 1. Introduction

Large heat exchangers are used in ethylene oxide, methanol and methyl tertiary-butyl ether production plants. They can contain several thousand tubes, and their tubesheets could have diameters of 8 meters or even more. Such tubesheets have to be fabricated by welding together two or more pieces, preferably drilled before the joining process, in order to get a reasonable productivity.

Welding is a reliable and efficient joining process, widely employed in the fabrication of large structures. Due to extremely localized heating and cooling processes associated, residual stress and distortion are produced in the weldments, affecting significantly strength, integrity and in service behavior. A practical method to reduce welding distortion is to employ two heat sources that act concomitantly, from opposites directions, on the two plate sides is used in order to reduce the distortion.

There are numerous factors that influence welding distortion: fabrication and material parameters, plate thickness, joint type and structure's geometry [1]. In addition, a series of complex phenomena take place during welding, like transiently modification of structural stiffness as the filler metal is deposited, complex dimensional changes, modifications of the three-dimensional coupling between local weld zone and global structure, etc. As a result, it's very difficult to simulate numerically all these effects of welding, strong simplifications being needed in order to achieve reasonable computational costs. Therefore, it is essential to have experimental data regarding the process under study in order to examine the possible simplifications and to check to what extent the mathematical solution reflects reality. Experiments are very important in welding simulation, for validation and in order to obtain modeling data.

An experimental test has been carried out in order to study the arc-welding thermo-mechanical effects on perforated plates [2]. The thermal history experimental

determination is discussed elsewhere [3] while this paper is focusing on the modification of tube holes diameters due to joining process. These are important parameters, considering the tubesheet role, their dimension tolerances being about 1 mm, a very small value for a big structure like an 8 meters diameter plate.

## 2. Experimental set up

Two perforated plates, with a double-groove joint between them, were fabricated from hot rolled P355NL1 (according to EN-10028-3: 92) carbon steel for pressure vessels. The geometry, size and holes disposition are presented in Fig. 1, Fig. 2 and Fig. 3. The dimensions have been chosen in order to get welding effects on the plate, practically independent from edge effects.

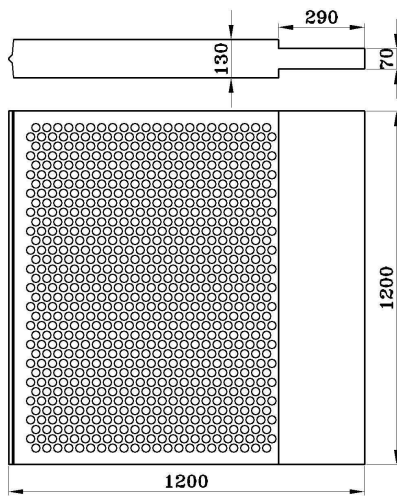


Fig. 2. One of the two perforated plates

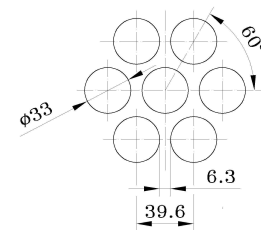


Fig. 1. Penetration pattern

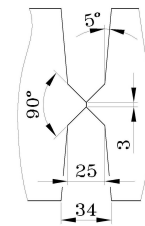


Fig. 3. Chamfer geometry

The plates have been manually arc butt-welded with two sources acting concomitantly, from opposite directions. The welding conditions are presented in Table 1. To complete the job, a total of 210 weld passes were laid.

Table 1. Welding conditions

Weld pass number	Electrode diameter	Amper range	Voltage range	Welding speed	Heat input	Pre-heating temperature	Inter-pass temperature
	mm	A	V	mm/s	J/mm	°C	°C
1	3.2	120 -140	10 -12	3	309.8	230 °C	220-250 °C
2 -105	4	160 -170	19 - 20	3	697.1		

The plates have been fixed in vertical position using a support (Fig. 4) designed in order to assure the stability but also to permit free distortion. A rigid frame, 2, was fabricated from steel section HE180A (European wide flange beam) with dimensions according to Euronorm 53-62. The plates to be weld, 1 and 3, have been inserted in this frame, being free to move on vertical and lateral directions. Some elastic pieces, 4, have been inserted between these ones and the frame, in order to secure the plates but,

in the same time, to permit displacement on thickness direction. For major safety, some bolts, 5, have been also utilized. It is believed that the effect of these security measures on the global distortion of weldment is small, given the much greater dimensions of plates.

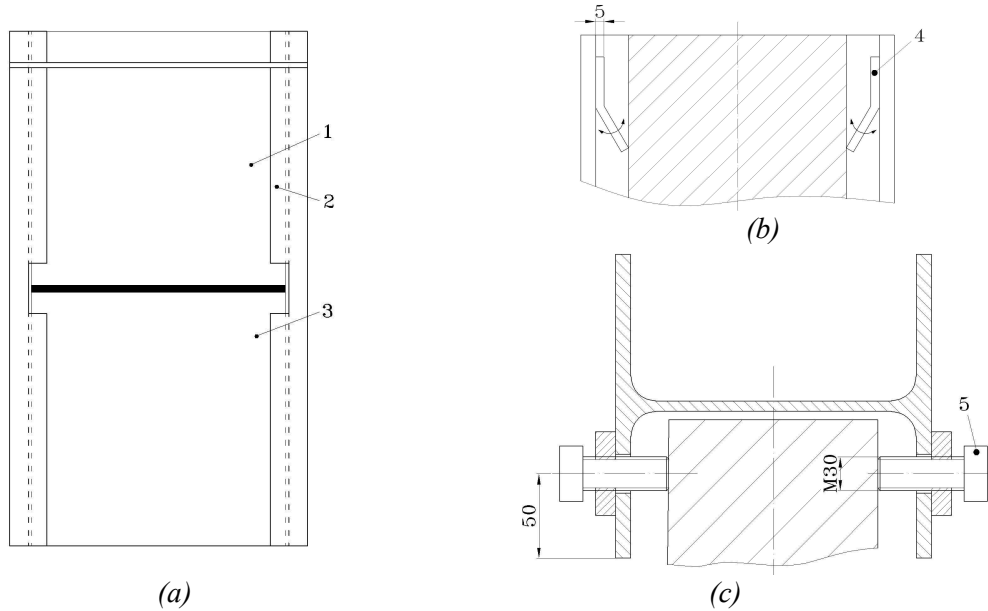


Fig. 4. Plates fixture; a-general view; b-springs detail; c-bolts detail

### 3. Results and discussion

To assess the distortion due to welding, 104 holes from a region considered critical – the one evidenced in Fig. 5 – were evaluated, before and after welding. Their diameters have been measured on two directions, the welding direction and the perpendicular one, on plate's surface and at half of its thickness (Fig. 6).

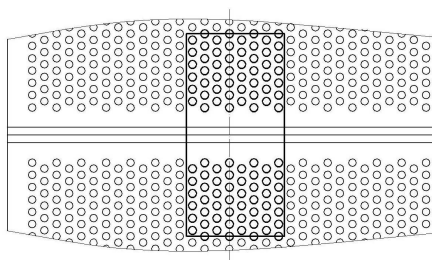


Fig. 5. Region for holes measurement

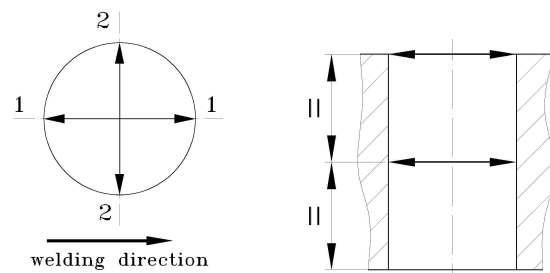


Fig. 6. Measuring directions

In order to reduce the errors due to the existing variation of nominal initial diameters value, a parameter more appropriate than the simple diameters difference was employed for distortion assessing - the hole diameter modification, E, calculated with the following formula:

$$E = \frac{D_f - D_i}{D_i} \tag{1}$$

where  $D_i$  and  $D_f$  are the diameters measured before and after welding, respectively.

The dependence of diameter modification with distance from weld line to hole center is shown in the following graphs. There are reported the experimentally determined points and, also, the polynomial trend lines together with them equations.

As could be observed in Fig. 7 and Fig. 8, for the holes near to weld line, the diameters decrease on welding direction, increasing in the perpendicular one, this trend being then inverted and, next, reversed again as the distance augment. The maximum variations are approximately 0.2 mm on direction 1-1 and 0.1 mm on direction 2-2 (see Fig. 6).

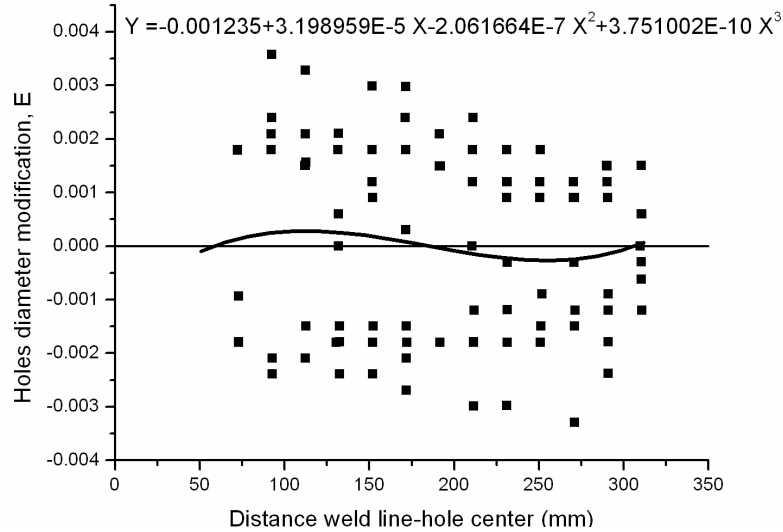


Fig. 7. Holes distortion in the longitudinal direction, at plate's surface

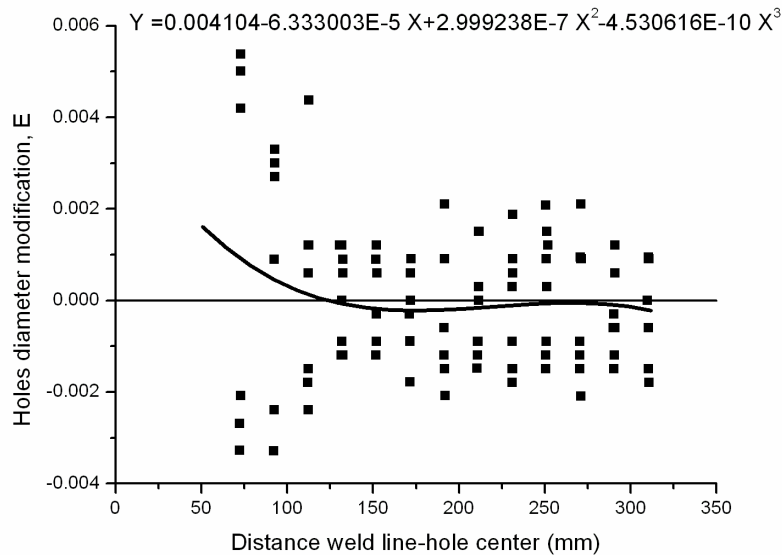


Fig. 8. Holes distortion in the transversal direction, at plate's surface

In the section situated at half of plate's thickness, the diameter modifications have a similar trend for both measurement directions, but bigger values are observed on longitudinal direction. However, the maximum diameter variations are fairly equal: approximately 0.09 mm on direction 2-2 and 0.12 mm on direction 1-1.

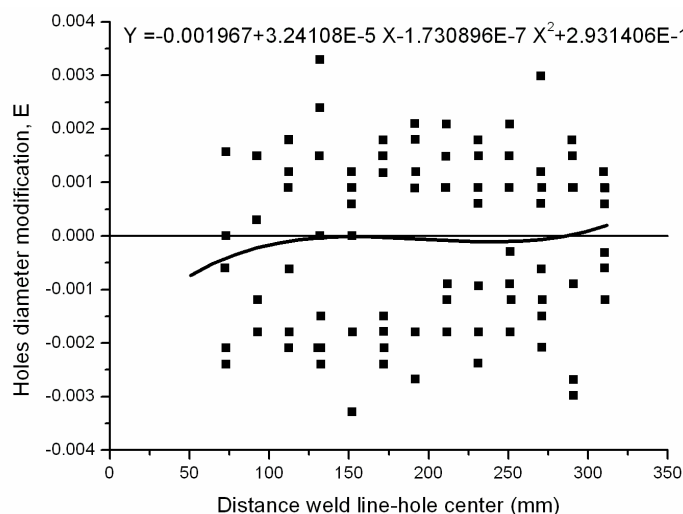


Fig. 9. Holes distortion in the longitudinal direction, at plate's half thickness

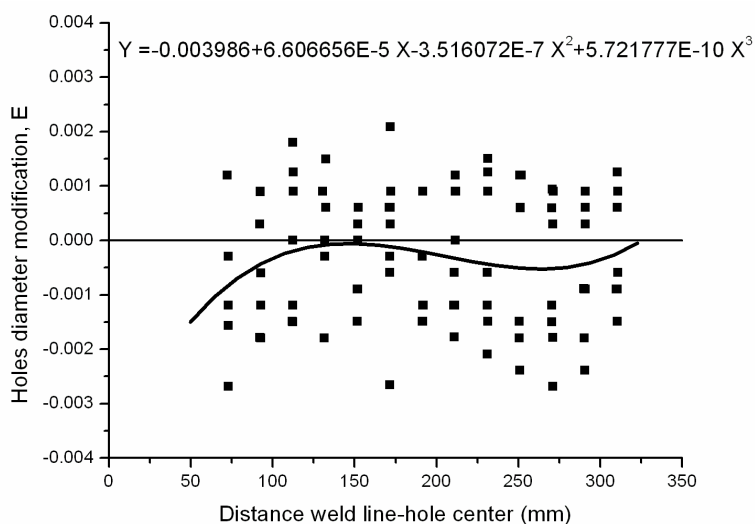


Fig. 10. Holes distortion in the transversal direction at plate's half thickness

The experimental results are useful for validation of the employed joining process in tubesheet fabrication. Also, it was used in order to validate a finite element procedure developed by authors in order to estimate distortion in large tubesheets fabricated by welding [4].

From the results obtained, some observations could be made:

1. The welding with two heat sources that act concomitantly, from opposite directions, permits the achievement of little tube holes distortion, much smaller than dimension tolerances.
2. The tube holes diameters modifications at the plate's surface are bigger than the corresponding ones at plate's half thickness.
3. The thickness effect also influences the holes distortion evolution with respect to distance from weld line.

4. The enormous dispersion of data underlines the complexity of the studied joining process and structure and, also, the difficulty of its numerical simulation.
5. The results obtained are also useful for verification of resulted predicted by finite element models.

#### 4. Conclusions

A experiment was carried out in order to study welding effects on perforated plates. The diameter modifications due to the joining process had been evaluated for 104 tube holes. The experimental set up and the results are presented and discussed. The two-heat source welding process employed in this experiment is proved to be appropriate for tubesheet welding, as the resulted distortion doesn't exceed the imposed tolerances.

#### Acknowledgements

One of the authors (D. Cantemir) gratefully acknowledges his Ph.D. grant from the University of Pisa.

Received May 8, 2005

<sup>a</sup> Technical University of Iassy, Romania

<sup>b</sup> University of Pisa, Italy

#### REFERENCES

1. Masubuchi K., *Analysis of Welded Structures*, Pergamon Press, Oxford, 1980
2. Beghini M., Bertini, L., Cantemir, D., Barbieri, L., Nicodemi, L., Spadaccini, F., *Simulation of temperature evolution during multipass butt-welding of a large tubesheet*. 12th Int. Conf. on Exp. Mech., Bari, 2004
3. Cantemir D., Bertini, L., Beghini, M., *Experimental determination of temperature distribution during multipass welding of P355NL1 steel*, to be published, 2004
4. Beghini M., Bertini, L., Cantemir, D., *A finite element procedure for assessment of a large tubesheet holes distortion due to welding*. 15th Italian ABAQUS User's Meeting, Bari, 2004

#### DETERMINAREA EXPERIMENTALA A OVALIZARII GAURILOR UNOR PLACI PERFORATE SUDATE MULTISTRAT

In lucrare este prezentat un experiment efectuat pentru studierea modului in care procesul de sudare multistrat afecteaza plăcile perforate, discuția fiind concentrata asupra modificării diametrelor găurilor acestora. Sunt incluse, alături de prezentare instalației experimentale, o serie de rezultate și concluzii. Experimentul a demonstrat ca sudarea cu doua surse acționând concomitent, din direcții opuse, poate fi folosita cu succes in sudarea plăcilor perforate, ovalizarea găurilor acestora nedepășind tolerantele admisibile. De asemenea, rezultatele au fost folosite pentru calibrarea unei proceduri propuse de autori in vederea estimării deformațiilor plăcilor perforate cu ajutorul metodei elementelor finite.

## **SYNTHESIS AND MAGNETIC PROPERTIES OF Ni AND Ni-Fe NANOPARTICLES FOR BIOMEDICAL APPLICATIONS**

**BY**

**HORIA CHIRIAC\*, ANCA-EUGENIA MOGA\*, CARMEN GHERASIM\*\* and DUMITRU-  
DANIEL HEREA\*\***

**Abstract:** In this work we present our experimental results on the preparation and magnetic properties of Ni and Ni-Fe nanoparticles. Nickel and nickel-iron alloy nanoparticles have been synthesised by polyol reduction method. The morphology and size of the nanoparticles were studied by scanning electron microscopy (SEM). Magnetic characteristics of the nanoparticles were determined at room temperature by using a vibrating sample magnetometer (VSM), in an external magnetic field of 15 kOe. To ensure the stability and biocompatibility, the as-prepared nanoparticles were coated with a thin layer of polyvinylpyrrolidone (PVP) or styrene – maleic anhydride copolymer.

**Keywords:** nickel, iron, nanoparticles, polyol process

### **1. Introduction**

Magnetic nanoparticles have potential applications in many biological and medical applications such as drug delivery, hyperthermia, magnetic resonance imaging and cell separation. In these application the nanoparticles must be water dispersible and biocompatible.

Nanomaterials properties are strongly dependent on the size particle. Consequently, properties of the nanoparticles such as magnetic, optical, thermal or catalytic are different from bulk materials.

Nanoparticles that possess magnetic properties offer exciting new opportunities for delivering drugs to targeted areas in the body, replacing radioactive tracer materials, improving the quality of magnetic resonance imaging and producing smaller data storage devices. By modifying the surfaces of the particles with monoclonal antibodies, peptides or proteins, the nanoparticles can avoid the rapid uptake by reticuloendothelial system and prolong their blood circulation time [1, 2].

In this work we present our experimental results on the preparation and magnetic properties of Ni and Ni-Fe nanoparticles obtained by a chemical method called the polyol process [3]. This method is a simple and a single-step process for preparing nanoparticles, involving the suspending the corresponding metals salts in a polyol such as ethylene glycol and subsequently bringing the resulting mixture to refluxing temperature. Ethylene glycol acts as a solvent for the starting metallic compounds and subsequently is also used to reduce them into metals.

## 2. Experimental

Nanoparticles of Ni and Ni-Fe were prepared by refluxing an ethylene glycol solution containing their suspended sulphates. To obtain Ni nanoparticles we used a nickel sulphate bath with a molar concentration of 0.035 M in ethylene glycol. To obtain alloy nanoparticles, nickel sulphate and iron sulphate were suspended in ethylene glycol so that the final molarity of the nickel sulphate and iron sulphate were 0.032 M and 0.007 M, respectively. Upon heating, as both Ni<sup>II</sup> and Fe<sup>II</sup> are quantitative reduced by ethylene glycol itself, the Ni/Fe ratio in the metallic Ni<sub>x</sub>Fe<sub>(100-x)</sub> nanoparticles depends only on their initial ratio. From the above mentioned molarity ratio were obtained Ni<sub>80</sub>Fe<sub>20</sub> alloy nanoparticles.

For the preparation of Ni and Ni-Fe nanoparticles, the pH of solutions were adjusted to 11–12 by addition of NaOH prior to reduction process.

The refluxing temperature and the reaction time are specific for obtaining either nanoparticles type: 190°C–193°C and 10 hours for Ni nanoparticles and 175°C–180°C and 7 hours for Ni<sub>80</sub>Fe<sub>20</sub> nanoparticles, respectively. In all cases, the solutions turned black within a few minutes of reaching refluxing temperature.

The metal-ethylene glycol mixtures were cooled to room temperature, filtered, and then the collected precipitates were dried in vacuum.

The morphology and size of the nanoparticles were characterized by scanning electron microscopy (SEM) and atomic force microscopy (AFM).

Room temperature magnetic characteristics of the nanoparticles were determined by using a vibrating sample magnetometer (VSM), in an external magnetic field of 15 kOe.

To improve the stability and biocompatibility, the as-prepared nanoparticles were isolated with oleic acid, and after this process were coated with a thin layer of polyvinylpyrrolidone (PVP). This coating process was performed in the following steps:

1. Preparation of oil phase. For a good dispersion, the nanoparticles were mixed with oleic acid.
2. Preparation of organic phase. PVP was dissolved in an organic solvent - ethylic alcohol.
3. Preparation of aqueous phase. The polyvinyl alcohol (PVA) was used as a stabilizer and was dissolved in water. Then nanoparticles coated with oleic acid will be added to this aqueous phase, thus forming micelles with magnetic nanoparticles core.
4. Emulsification. The above two phases were mixed together and homogenized at high speed. Speed mixing was varied for a good homogeneity.
5. Biocompatible magnetic nanoparticles formation. Water was subsequently added to the emulsion, leading to the diffusion of PVP to the micelles in aqueous phase. This process yields to the formation of core-shell structured nanoparticles.
6. Removal of non-magnetic nanoparticles. The biocompatible magnetic nanoparticles were collected with a permanent magnet and non-magnetic particles remain in solution.



### 3. Experimental results and discussion

Fig. 1 shows the SEM micrograph of the as-prepared Ni nanoparticles obtained by polyol process. In Fig. 2 is presented the SEM micrograph of the coated Ni nanoparticles.

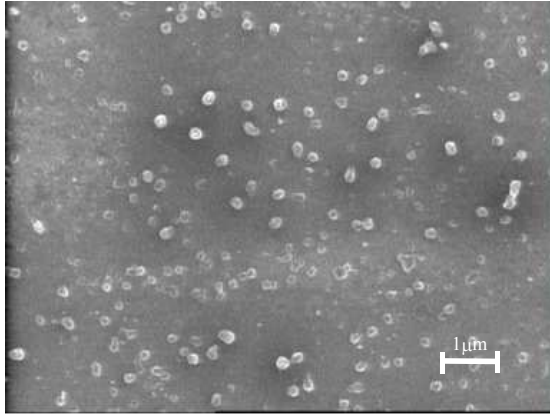


Fig.1 SEM micrograph of as-prepared Ni nanoparticles

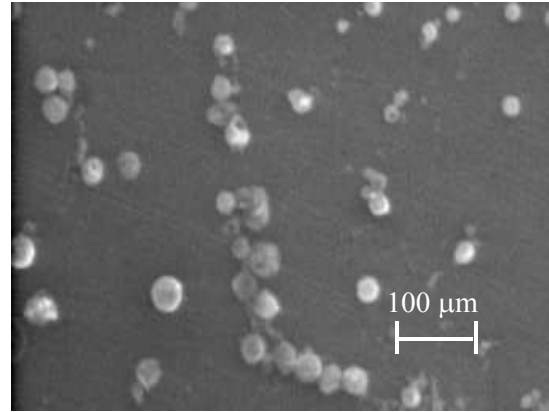


Fig.2 SEM micrograph of coated Ni nanoparticles

As shown in Fig. 1, the size of the as-prepared and coated Ni nanoparticles ranges between 80-400 nm and 5-25  $\mu\text{m}$ , respectively. Due to the large surface to volume ratio and strong magnetic attraction forces, the nanoparticles tend to agglomerate in order to minimize the total surface energy of the system.

The hysteresis curves of as-prepared and coated Ni nanoparticles are presented in Fig. 3 and Fig. 4.

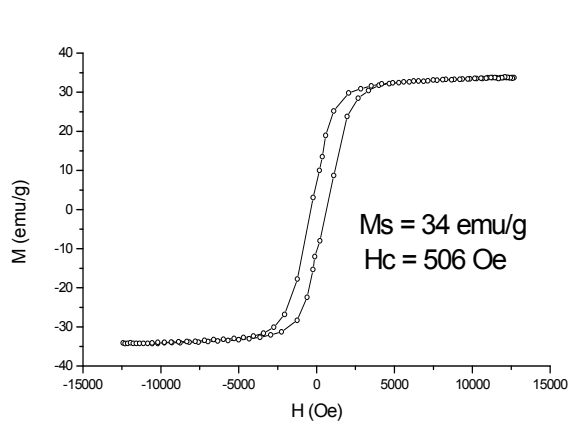


Fig. 3 Hysteresis curve of as-prepared Ni nanoparticles

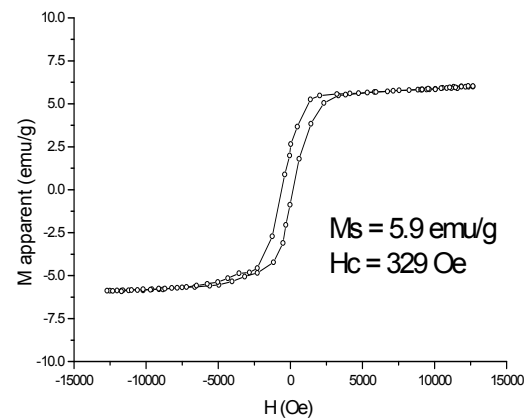
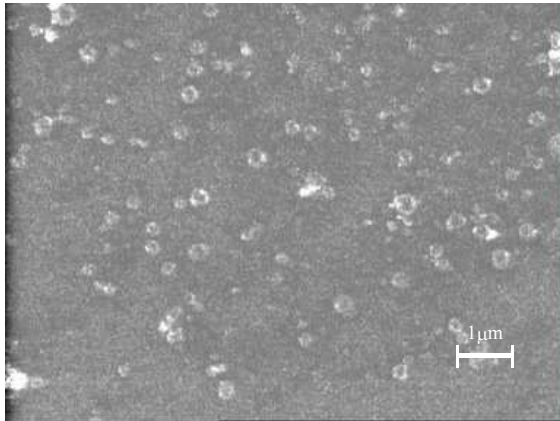


Fig. 4 Hysteresis curve of coated Ni nanoparticles

The saturation magnetization value for as-prepared Ni nanoparticles was 34 emu/g and the coercive field value was 506 Oe. Apparent saturation magnetization value for coated Ni nanoparticles was 5.9 emu/g and coercive field value was 329 Oe.

In Fig. 5 and 6 are presented the SEM micrographs of the as-prepared and coated  $\text{Ni}_{80}\text{Fe}_{20}$  nanoparticles.



*Fig.5 SEM micrograph of as-prepared  $\text{Ni}_{80}\text{Fe}_{20}$  nanoparticles*

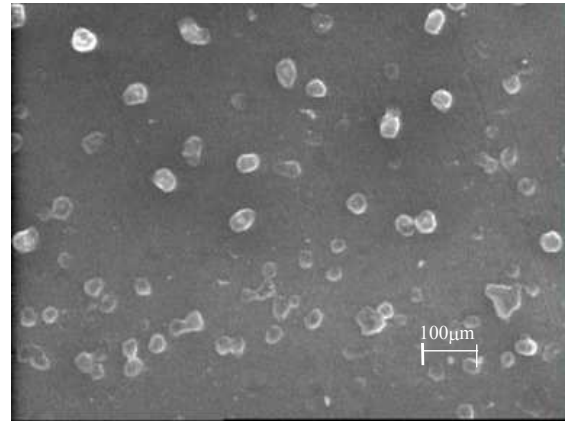


*Fig.6 SEM micrograph of coated  $\text{Ni}_{80}\text{Fe}_{20}$  nanoparticles*

The SEM micrograph presented in Fig. 5 reveal that the Ni-Fe nanoparticles are mostly spherical. The size of the as-prepared Ni-Fe nanoparticles ranges between 50-200 nm and the size of coated Ni-Fe ranges between 3-30  $\mu\text{m}$ .

Also, the size and the shape of Ni-Fe nanoparticles were determined using AFM images. In Fig. 7, Fig. 8 and Fig. 9 are shown AFM images of as-prepared Ni-Fe nanoparticles.

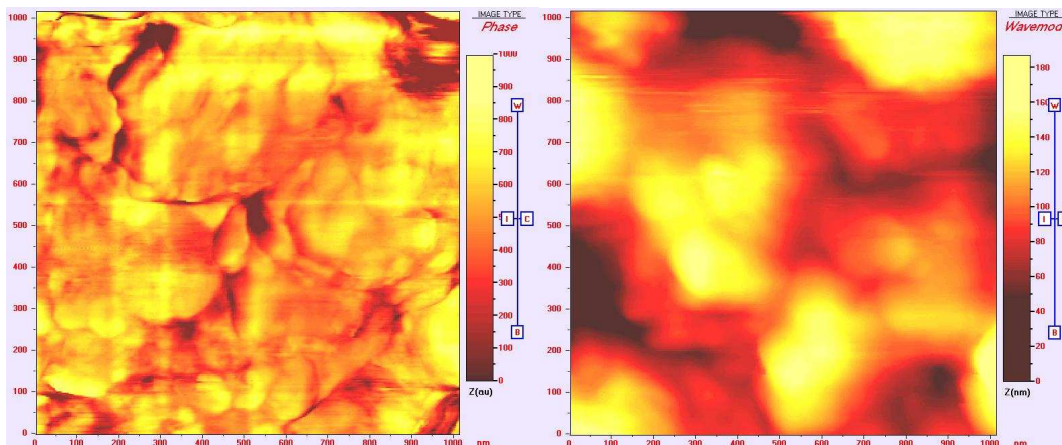


*Fig.7 AFM image: phase image of Ni-Fe nanoparticles*

*Fig.8 AFM image: topography of Ni-Fe nanoparticles*

From the AFM phase and topography images it can be observed that the size of the Ni-Fe nanoparticles ranges between 30 nm and 150 nm and their size is very uniform. Also, it can be observed that the shape of the nanoparticles is spherical.

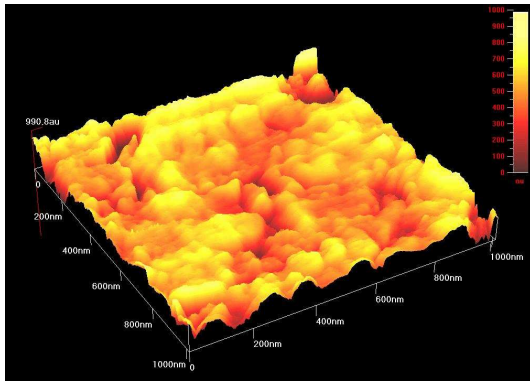


Fig. 9 AFM images of Ni-Fe nanoparticles: 3d image

The hysteresis curves of as-prepared and coated  $\text{Ni}_{80}\text{Fe}_{20}$  nanoparticles are shown in Fig. 10 and Fig. 11.

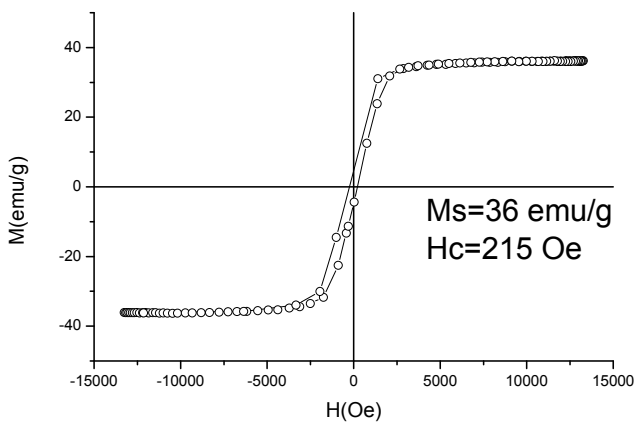


Fig. 10 Hysteresis curve of as-prepared  $\text{Ni}_{80}\text{Fe}_{20}$  nanoparticles

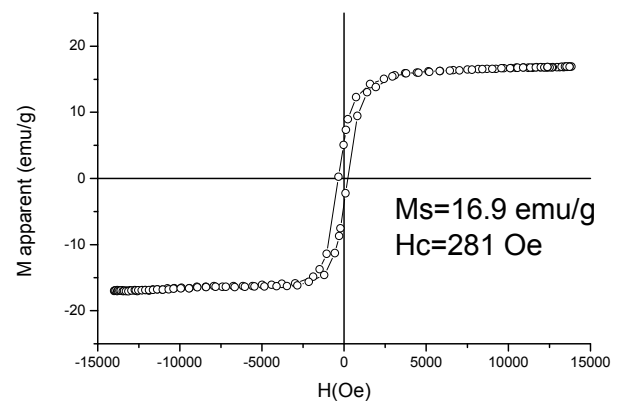


Fig. 11 Hysteresis curve of coated  $\text{Ni}_{80}\text{Fe}_{20}$  nanoparticles

Saturation magnetization value for as-prepared  $\text{Ni}_{80}\text{Fe}_{20}$  nanoparticles was 36 emu/g and coercive field value was 215 Oe. Apparent saturation magnetization value for coated  $\text{Ni}_{80}\text{Fe}_{20}$  nanoparticles was 16.9 emu/g and coercive field value was 281 Oe.

From the hysteresis curves it is observed that the values of saturation magnetization of coated nanoparticles are smaller than the values of saturation magnetization of non-coated nanoparticles.

#### 4. Conclusions

By control of the parameters of polyol process (molarity, pH and refluxing temperature of solutions), Ni and Ni-Fe nanoparticles with good magnetic properties were obtained. Ni and Ni-Fe alloy nanoparticles prepared by polyol process and coated with a layer of polyvinylpyrrolidone, were found to be stable under ambient conditions, without undergoing oxidation. Saturation magnetization values were changed significantly due to coating with PVP. Control of particle size and the

dispersion process requires careful control of the nucleation and growth steps in the polyol process and elimination of aggregation during growth. The amount of PVP determines the final size stability of coated biocompatible nanoparticles.

#### REFERENCES

- [1] P. Tartaj, M.P. Morales, S. Veintemillas-Verdaguer, T. Gonzales-Carreno and C.J. Serna, *Journal of Physics D: Applied Physics, The preparation of magnetic nanoparticles for applications in biomedicine*, **36**, 2003, R 182-R 197
- [2] D. K. Kim, Y. Zhang, W. Voit, K.V. Rao, M. Muhammed, *Journal of Magnetism and Magnetic Materials, Synthesis and characterization of surfactant-coated superparamagnetic monodispersed iron oxide nanoparticles*, **225**, 2001, 30-36
- [3] L. K. Kurihara, G. M. Chow, S. H. Lawrence and P. E. Schoen, *Polyol- Derived Synthesis of Nanocrystalline Metals, Processing and Properties of Nanocrystalline Materials*, 1996, 49-58

\* National Institute of Research Development for technical Physics Iasi

\*\* Faculty of Physics, University "Al.I.Cuza" Iasi

#### SINTEZA ȘI PROPRIETĂȚILE MAGNETICE ALE NANOPARTICULELOR DE Ni ȘI Ni-Fe PENTRU APLICAȚII BIOMEDICALE

**Rezumat:** În această lucrare sunt prezentate rezultatele experimentale privind prepararea și proprietățile magnetice ale nanoparticulelor de Ni și Ni-Fe. Nanoparticulele de Ni și Ni<sub>80</sub>Fe<sub>20</sub> au fost obținute prin metoda reducerii chimice (metoda "polyol"). Morfologia și dimensiunile nanoparticulelor au fost studiate cu ajutorul microscopiei electronice (SEM) și a microscopiei de forță atomică (AFM). Din micrografiile prezentate se constată că majoritatea nanoparticulelor sunt sferice. Mărimea nanoparticulelor obținute variază între 50-900 nm. Caracteristicile magnetice ale nanoparticulelor au fost determinate la temperatura camerei utilizând un magnetometru cu probă vibrantă (VSM), într-un câmp extern de 15 kOe.

Pentru a asigura stabilitatea și biocompatibilitatea, nanoparticulele obținute au fost acoperite cu un strat subțire de polivinilpirolidonă (PVP). Mărimea microparticulelor de Ni și Ni-Fe acoperite variază între 3-30 μm.

## **POLYMER-COATED MAGNETIC MICROPARTICLES AS MARKERS FOR MAGNETIC BIOSENSORS**

**BY**

**HORIA CHIRIAC AND DUMITRU-DANIEL HEREA**

**Abstract:** Some results related to polymer-coated magnetic microparticles and polymer-functionalized surface of a magnetic sensor's sensing element based on giant-magnetoimpedance (GMI) effect are presented. Using an emulsion polymerization technique, polymer-coated magnetic microparticles in range of 5 to 30  $\mu\text{m}$  have been obtained. Styrene and maleic anhydride monomers were used for copolymerization process to cover the magnetic sensing element. Finally, the polymeric surface of the sensing element has been functionalized with carboxylic groups.

**Keywords:** polymer-coated magnetic microparticles, emulsion polymerization, magnetic sensing element, biomolecules

### **1. Introduction**

Polymer-coated magnetic nano/microparticles present an increasing interest in medicine, biology or biotechnology. They find multiple applications in biomedical domain. Thus, they can be used in "vivo" applications either in therapeutic procedures: hyperthermia, drug targeting, and obstructions of blood vessels, or in medical diagnosis: magnetic resonance imaging (MRI). Also, functionalized magnetic particles can be used for different applications "in vitro" for laboratory diagnosis: biomolecules separation/selection or as markers in some magnetic biosensors such as GMR/GMI-based biosensors.

There are different isolation methods of magnetic particles, but the most spread methods are based on polymers. The polymer plays multiple roles such as: to protect the particles in aggressive chemical media, to offer steric stability, to avoid their agglomeration, and to offer an adsorption surface, usually through physical bonds, for target biomolecules.

Among the most used methods developed for this goal, emulsion polymerisation is a method very used that is based on styrene as base-monomer.

Polymerization reactions cover a large domain of mechanisms, reactants, polymerisation media, and structures of reaction products. Among all possible combinations, emulsion polymerisation represents a reaction that uses a monomer or a mixture of monomers that are water emulsified and that are polymerised using a water soluble initiator. The reaction products consist of colloidal dispersions of micro/submicrometric particles inside an aqueous media, making so-called latex.

There are many advantages of emulsion polymerisation processes that are due mainly to the absence of organic solvents and to the apparition of reaction compartments. In such a system, water has many roles as it represents continuous inert

phase, maintains a low viscosity for final reaction products, and presents a very high caloric capacity. The polymerisation can be usually made at a very high output, and there is small residual polymer amount. However, the presence of additive mixtures, as surfactants and fragments of initiators, represents a disadvantage of the emulsion polymerisation for these substances could affect the quality of the final products.

The monomers used in emulsion polymerisation processes are generally low or moderate soluble in water (eg., styrene presents a solubility of 0.05 g/100 ml water) and can be selected depending on application requirements. The most used monomers as main participants in the emulsion polymerisation prescriptions are styrene, butadiene, vinyl acetate, acrylates, metacrylates and vinyl chloride [1]. Functional monomers are usually used together with those that work as base-monomers to adjust the polymer properties or the latex colloidal properties or to permit postpolymerisation reactions. The functional monomers are added in minute quantities and they are characterised by numerous types of reactive groups.

The emulsion polymerisation can be used to obtain polymer-coated magnetic microparticles that are useful as magnetic markers in some magnetic biosensors represented, in our case, by giant-magnetoimpedance (GMI) biosensor. Furthermore, the sensing element of the GMI-based magnetic biosensor can be covered with copolymer by emulsion copolymerisation to offer a functionalised layer for further coupling with biomolecules and magnetic markers.

In this paper we present some results concerning cobalt-based functionalized magnetic microparticles obtained in an emulsion polymerisation process and, also, the covering process of the GMI-biosensor sensing element by styrene-anhydride copolymer.

## 2. Experimental procedure

The first set of experiments was carried out using the emulsion polymerisation method to obtain polymer-coated cobalt magnetic microparticles functionalized with reactive carboxylic groups. Styrene was used as base-polymer and maleic acid was used as functional partner.

For this reason, we used Co bare magnetic microparticles with range between 0.6-0.9 micrometers having spherical shape (Fig.1). First, Co microparticles have been covered with oleic acid and agitated 1 h at 85°C using mechanical agitation. Oleic acid is a surfactant that avoids the microparticles agglomeration.

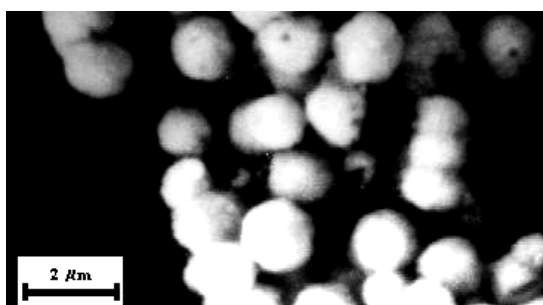


*Fig.1 SEM image of cobalt bare magnetic microparticles of 0.6 – 0.9 μm in diameter*

After this operation, magnetic microparticles have been immersed in styrene (2 g) (solution I) obtaining homogenous spatial distribution of the microparticles. Simultaneously, a solution of maleic anhydride (solution II) was prepared. Thus, 0.1 g maleic anhydride have been dissolved in 30 ml sodium dodecyl sulphate aqueous solution 0.2 %. In aqueous solutions, maleic anhydride transforms in maleic acid.

Separately, potassium persulphate aqueous solution 0.1 % (solution III) was prepared and used to initiate radical polymerisation process.

To obtain the emulsion, solution II was gradually added in solution I under vigorous agitation, obtaining after short time an opalescent solution that is specific for emulsions (Fig.2). Hexadecane was added in solution as osmotic agent to prevent so-called Ostwald ripening. Practically, hexadecane maintains constant the micelle sizes formed by emulsifying the emulsion component.

The emulsion has been maintained under mechanical agitation 1 h at room temperature. Then, the emulsion temperature was progressively raised at 60°C and the new work conditions, including agitation, have been maintained another 2 h. Thereafter, solution III was added in system and the emulsion temperature was raised at 72°C and maintained, in the same mechanical agitation condition, 4 h.

Finally, the emulsion has been cooled and centrifuged 15 min. at 3000 rpm, and washed three times with sodium dodecyl sulphate aqueous solution. The magnetic particles separation was carried out using a rare earth magnet (4000 Oe) for 10 min.

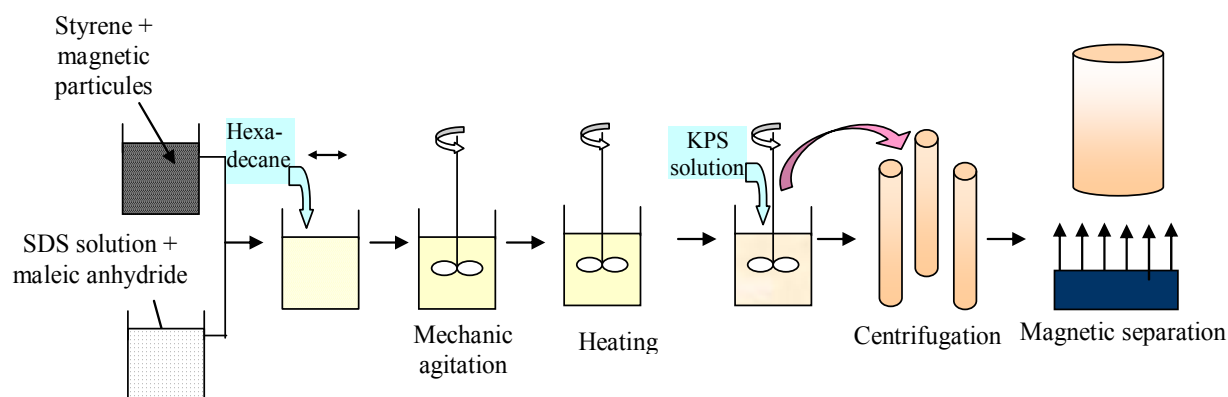


*Fig.2 The main steps in the procedural chain for obtaining polymer-based cobalt magnetic microparticles*

The second set of experiments has been carried out to obtain a functionalized sensing element for the GMI-biosensor using styrene-maleic anhydride copolymer. The sensing element of the magnetic biosensor is represented by a glass-covered magnetic microwire of 40  $\mu\text{m}$  in diameter that can detect very low magnetic fields, including induced magnetic field of the magnetic markers (Fig.3). This magnetic microwire should be functionalized in order to make it able to receive on its surface different target biomolecules and, respectively magnetic markers.

To obtain styrene-maleic anhydride copolymer we used the respective monomers in molar ratio of 1:1 and benzoyl peroxide as polymerization initiator, using a polymerization technique in organic media (benzene). The copolymer, insoluble in benzene, has been obtained at 85°C after 40 min. The copolymer has been dissolved in acetone to reach a concentration of 7 g %.

Thereafter, the microwires have been cleaned with pure ethylic alcohol and washed with distilled water. Immediately, they have been immersed in copolymer solution and retired progressively after 60 s. For the acetone presents a high evaporation speed, the copolymer was quickly formed on microwire glass surface.

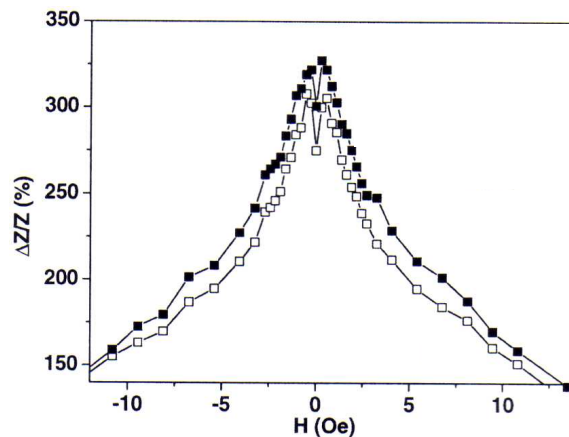


Fig.3 The dependence of the sensing element magneto-impedance on magnetic field with and without Dynal polymer-based magnetic microparticles [2].

Finally, the microwires have been treated with chloride acid 1 M in order to open the anhydride groups to form carboxylic groups [3].

The functionality of the microwire surface has been verified using Estapor magnetic microparticles that are covered with streptavidin – a protein with affinity for carboxylic groups.

### 3. Experimental results and discussion

Using scanning electron microscopy (SEM) we obtained different images of polymer-coated magnetic microparticles with dimensions between 5-30  $\mu\text{m}$  (Fig. 4).

The SEM images show magnetic microparticles with integral polymer coverage, having spherical shapes.

The initial magnetic microparticles (0.6-0.9  $\mu\text{m}$ ) have been embedded in a polymer matrix to reach final dimensions of 5-30  $\mu\text{m}$ . The polymer-coated magnetic microparticles should present on their surface reactive carboxylic groups, but this aspect will be investigated in our further work.

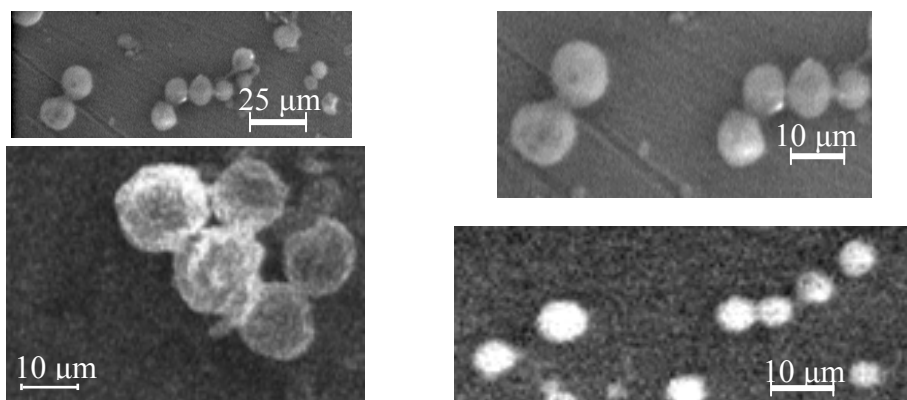


Fig.4. SEM images for different samples of polymer-coated Co magnetic microparticles



To investigate magnetic properties of the polymer-coated magnetic microparticles we used vibrating sample magnetometry (VSM) to evaluate saturation magnetization and coercive field. Fig. 5 shows that saturation magnetization (13.8 emu/g) is making the polymer-coated magnetic microparticles able to be used as markers in GMI-based biosensor.

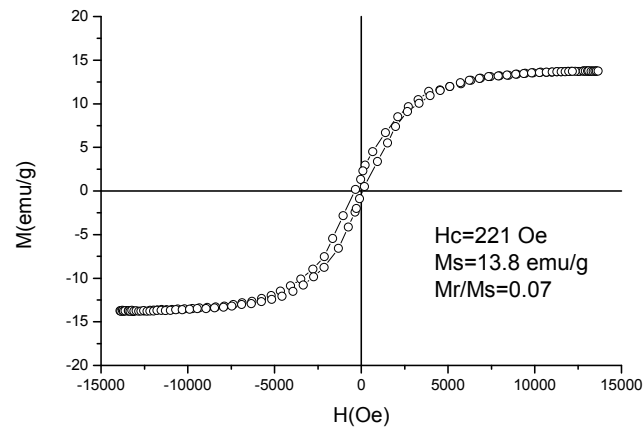


Fig.5 Magnetization dependence on applied magnetic field for polymer-based cobalt magnetic microparticles

The atomic force microscopy (AFM), used to investigate polymer-coated microwire surface, revealed maximum level differences of only 16 nm (Fig.6) that recommend the polymer-coated microwire to be used for biodetection events.

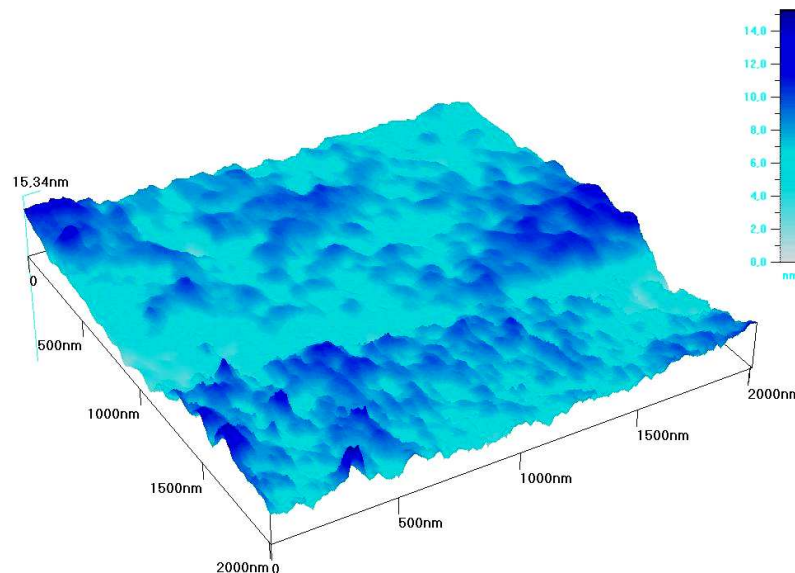


Fig.5 AFM 3D image of the styrene-maleic anhydride copolymer layer on the microwire surface. The 3D image shows a maximum level variation of the polymeric layer of about 16 nm.

SEM images showed that microwire surface has bound Estapor microparticles (1.9  $\mu\text{m}$  in diameter), revealing that copolymer-coated microwire presents functional carboxylic groups (Fig.7).

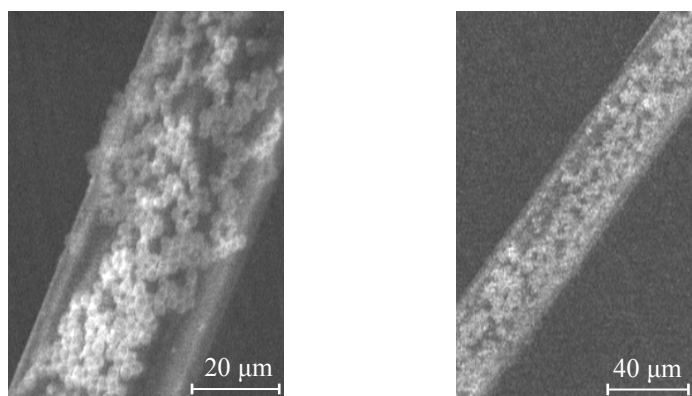


Fig.5 Microwires functionalized with carboxylic groups that have been covered with streptavidin- functionalized Estapor magnetic microparticles.

By SEM images we could receive information concerning the degree of microwire coverage with Estapor microparticles. Thus, the images revealed some zones with lower density of Estapor microparticles meaning some regions of polymer are not fully functionally. It is possible that plasma treatments should open more anhydride groups.

#### 4. Conclusions

Using polymerization methods, polymer-covered magnetic microparticles have been obtained. Their magnetic characteristics, sizes and shape recommend them as markers in some magnetic biosensors such as GMI-based biosensors. Also, by polymerisation method, magnetic sensing element with functionalized surface has been carried out.

The evaluation of the carboxylic groups on the polymer-covered magnetic microparticles and tests with such microparticles in the GMI-based magnetic biosensors in real work conditions will form the subject of our further research.

#### REFERENCES

1. Xu, P., Zhong, W., Wang H., Tong R., and Du, Q., *On the copolymerization of acrylates in the modified microemulsion process*, **Colloid Polymer Science** (2004) 282: 1409–1414.
2. Kurlyandskaya, G., Levit, V., *Magnetic Dynabeads detection by sensitive element based on giant magnetoimpedance*, **Biosensors & Bioelectronics** 20 (2005) 1611-1616.
3. Ivanova, E.P., Papiernik, M., Oliveira, A., Sbarski, I., Smekal, T., Grodzinski, P., and Nicolau, D.V., *Feasibility of using carboxylic-rich polymeric surfaces for covalent binding of oligonucleotides for microPCR applications*, *Smart Material and Structure*, 11 (2002) 783-791.

#### MICROPARTICULE MAGNETICE ACOPERITE CU POLIMER CA MARCHERI ÎN BIOSENZORI

**Rezumat:** Sunt prezentate unele rezultate privind microparticule magnetice acoperite cu polimer și câteva rezultate privind suprafața funcționalizată cu polimer a elementului de detecție al unui biosensor magnetic bazat pe efectul magnetoimpedanței gigant. Utilizând o tehnică de polimerizare în emulsie, s-au obținut microparticule magnetice acoperite cu polimer cu dimensiuni cuprinse între 5 și 30 μm. Au fost utilizați monomeri de stiren și anhidridă maleică pentru copolimerizare în scopul acoperirii elementului de detecție magnetic. În final, suprafața polimerică a elementului de detecție a fost funcționalizată cu grupe carboxil.

## POINT OF VIEW GIVEN SPHEROIDIZING OF GRAPHITE

BY

VASILE COJOCARU-FILIPCIUC

**Abstract:** The paper takes the moistening phenomenon of graphite by the metallic matrix into consideration, finding the limits of free enthalpy of the graphite-metallic matrix interface.

Having as base the definition of isobar thermodynamic potential, this one is expressed depending on entropy, volume, pressure, chemical potential, interphase tension and graphite surface, all these from the graphite-metallic interface.

Then, the graphite surface is expressed during eutectic transformation and transformation what takes, place at temperatures bigger than eutectic temperature. So, it is established a mathematical model of that surface. For being nodular, graphite must have minimum surface, well, spheroidizing factors have to determine a minimum surface of graphite.

The spheroidizing factors what operate directly are chemical composition and temperature.

The spheroidizing factors what operate undirectly are enthalpy, graphite-metallic matrix interphase tension, thermodynamic activity of the chemical elements, specific heat, eutectic temperature and overheating temperature in liquid state.

Cooling rate operates on graphite spheroidizing undirectly.

Graphite increases nodularly into spheroidal place among particles from liquid iron or into bubbles of gaseous inoculant.

**Key words:** graphite-metallic matrix interface, moistening, free enthalpy, enthalpy, graphite surface, nodular graphite.

### 1. Aspects regarding geometry of the cooling curves

Nodular graphite is obtained by iron inoculating and malleable annealing, in specific conditions.

Nodular graphite is obtained in the case of Ni-C, Co-C, Pt-C, Rh-C, U-C etc. alloys, too, s1t.

According to s2t, in the case of grey cast iron, usually, the cooling curves, by inoculating for obtaining of nodular graphite iron, tolerate some changing, as in Fig. 1 – in zone of eutectic transformation. Fig. 1 shows that iron what is inoculated crystallizes with a small undercooling ratio.

Perhaps, the cooling rate, because changes the geometry of the cooling curves like the inoculants what are antigraphitizer, by increasing, has effect on graphite nodulizing.

The cooling curves are a manifestation of some properties of the alloys in liquid and solid state, the properties being dictated by chemical composition, temperature, cooling rate, metallographic microstructure and acceleration due to gravity. That's why the geometry of the cooling curves are a consequence of the modification

phenomenon what, in his turn, depends by a lot of factors – chemical composition of iron what is inoculated and of the inoculants, inoculating temperature, quantity of iron what is inoculated and of inoculant, state of aggregation of the inoculant, size of granulation inoculant, time between inoculating and beginning of crystallizing etc. At the same time, it must takes effects of the inoculating into consideration, for example, the size of graphite nodules, sphericity ratio of the graphite nodules, uniformity ratio of the inoculating etc. So, by some programmes, one order differential of the cooling rates are analyzed and the profile diagrams are elaborated. Finally, by expert systems, the results obtained are interpreted, so obtaining some information about the inoculation consequences and some factors what act on iron modification.

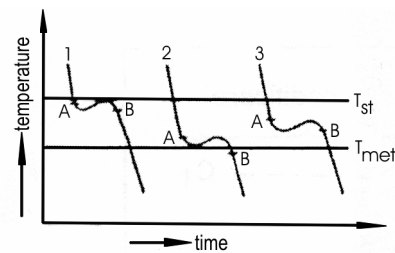


Fig.1. Cooling curves at eutectic transformation what represent initial iron (curve 1), iron inoculated by inoculants what are antigraphitizer (curve 2) and iron inoculated by inoculants what are graphitizer (curve 3), that's final iron: A – beginning of eutectic crystallization; B – final of eutectic crystallization;  $T_{st}$  – eutectic temperature of stable equilibrium;  $T_{met}$  – eutectic temperature of metastable equilibrium

## 2. Aspects regarding moistening phenomenon of graphite by metallic matrix

It is taken moistening phenomenon of the graphite by metallic matrix in consideration – Fig.2.

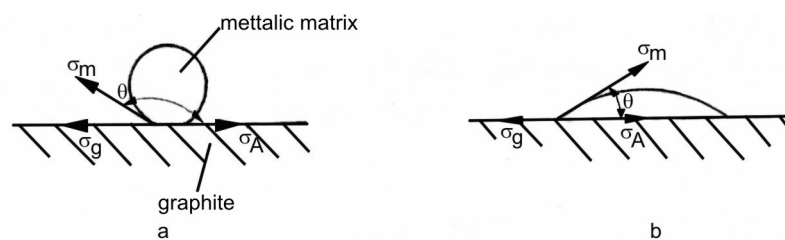


Fig.2. Representation of the moistening angle of graphite by liquid metallic matrix:  $\sigma_m$  – surface tension of the metallic matrix;  $\sigma_A$  – graphite-metallic matrix interphase tension;  $\theta$  – moistening angle.

Taking the vectorial model from Fig.2, at equilibrium, into consideration, it must realize the (1) relation.

$$\sigma_g - \sigma_m \cdot \cos \theta - \sigma_A = 0, \quad (1)$$

where  $\sigma_g$  is graphite surface tension;  $\sigma_m$  – metallic matrix surface tension;  $\sigma_A$  – graphite-metallic matrix interphase tension;  $\theta$  – moistening angle.

According to s4t source, the variation of free enthalpy of the graphite-metallic matrix interface –  $\Delta G_A$  –, taken the (1) relation, too, into consideration, is the next one:

$$\Delta G_A = \sigma_g - \sigma_m - \sigma_A = \sigma_m (\cos \theta - 1), \quad (2)$$

Moistening angle varies between 0 and 180 degrees.

In the case when  $\theta=0$  degrees, it results that  $\Delta G_A = 0$  and moistening of the graphite is maximum.

Fig. 2 shows that in the case when moistening angle has small values, moistening is big, graphite having a big surface – graphite is flaky.

Because maximum moistening is in the case when  $\theta=0^0$  and in the case when  $\theta=0^0$  free enthalpy variation is zero, this situation involves the maximum moistening is realised when there are equilibrium conditions. The equilibrium conditions are obtained when the cooling rate is very small. Well, depending up on thermodynamic considerations, the very small cooling rates involve separating of flake graphite.

In the case when  $\theta=180^0$ , it results that  $\Delta G_A = 2\sigma_m$ .

Because  $\sigma_m > 0$ , it results that  $\Delta G_A < 0$  when  $\theta=180^0$ .

Because the moistening angle has the maximum value of  $180^0$ , it results that, for this value, one obtains contact minimum surface between graphite and metallic matrix – one obtains the minimum moistening of graphite by metallic matrix. The minimum moistening is according to the spheroidal geometry of graphite, that's to value of  $-2\sigma_m$ .

Because, in the case when the moistening angle has value of  $180^0$ , graphite is not moistened by metallic matrix – spheroidal graphite floats – it results that  $\Delta G_A$  must not has the value of  $-2\sigma_m$ . Because, at equilibrium,  $\Delta G_A$  has the value zero and the equilibrium conditions are not in practice, it results that

$$-2\sigma_m < \Delta G_A < 0 \quad (3)$$

Inequality (3) gives information about the value of free enthalpy variation of graphite-metallic matrix interface, but gives not information about the surface tension of the metallic matrix. For example, if  $\sigma_m$  has very small values, it results the  $\sigma_m$  tends to have zero value, that's  $\Delta G_A$  tends to have zero value in the case when  $\theta=180^0$ , that's in the case of maximum moistening equilibrium conditions one realized. Well, inequality (3) has just a qualitative rôle.

The anterior conclusions shows that do not emphasize a conclusion about implicating of the cooling rate on modification process.

Practice shows that, in the case of castings having thick walls, nodular graphite is floated – is separated at the surface of the metal bath.

Taking (1) relation into consideration it results moistening angle  $\theta$  – the

$$\theta = \arccos \frac{\sigma_g - \sigma_A}{\sigma_m} \quad (4)$$

same think from (2) relation.

$$\theta = \arccos \frac{\Delta G_A + \sigma_m}{\sigma_m} \quad (5)$$

Well, according to (5) relation moistening angle  $\theta$  depends of free enthalpy variation of graphite-metallic matrix interface and surface tension of liquid iron.

### 3. Aspects of the implicating of graphite-metallic matrix interface thermodynamic potential

Taking the definition of free enthalpy into consideration, in the case when

metallic bath has minimum two chemical elements infinitesimal variation of free enthalpy of the graphite-metallic matrix –  $dG_A$  – is given by (6) relation, s5t.

$$dG_A = -S_A dT_A + V_A dp_A + \sum_{z=1}^m \mu_z^A dn_z + \sigma_A dA, \quad (6)$$

where  $S_A$  – entropy of isobar cooling of the interface;  $T_A$  – interface temperature;  $V_A$  – interface volume;  $p_A$  – interface pressure;  $\mu_z^A$  – chemical potential of chemical elements from the interface;  $\sigma_A$  – graphite-metallic matrix interphase tension;  $A$  – surface of the graphite-metallic matrix interface;  $m$  – number of chemical elements from metallic bath.

Taking modification process is at constant pressure into account, it results that  $dp_A = 0$  and (6) relation becomes (7) one.

$$dG_A = -S_A dT_A + \sum_{z=1}^m \mu_z^A dn_z^A + \sigma_A dA \quad (7)$$

One considers a eutectic transformation, that is than when eutectic cells are crystallized and increase.

Because during eutectic transformation the temperature is constant, it results that  $dT_A = 0$  and (7) relation becomes the (8) one.

$$dG_A = \sigma_A dA + \sum_{z=1}^m \mu_z^A dn_z^A \quad (8)$$

If (8) relation is integrated by isothermal conditions, it results the value of  $G_A$ , that is

$$G_A = A\sigma_A + \sum_{z=1}^m \mu_z^A dn_z^A \quad (9)$$

The (9) relation involves the surface of the graphite-metallic matrix interface, that is

$$A = \frac{G_A - \sum_{z=1}^m \mu_z^A \cdot n_z^A}{\sigma_A} \quad (10)$$

One knows that

$$\mu_z^A = RT_A \ln a_z^A, \quad (11)$$

where  $R$  represents gas constant;  $a_z^A$  – thermodynamic activity of the chemical elements from interface.

So, it results a new expression for surface  $A$ , that is

$$A = \frac{G_A - \sum_{z=1}^m RT_A n_z^A \ln a_z^A}{\sigma_A} = \frac{G_A - \sum_{z=1}^m n_z^A \mu_z^A}{\sigma_A} \quad (12)$$

Nodular graphite corresponds to minimum surface of graphite.

To obtain a minimum value for  $A$ , according to (12) relation,  $G_A$ ,  $T_A$ ,  $n_z^A$ ,  $a_z^A$  and  $\sigma_A$  must have optimum values. In addition, the next inequality have to be:

$$G_A > \sum_{z=1}^m RT_A n_z^A \ln a_z^A \quad \text{or} \quad G_A > \sum_{z=1}^m n_z^A \mu_z^A \quad (13)$$

Consequence, the condition that  $\sigma_A$  to be very big it's not enough.

So, it seems that one is the cause that aluminum do not be inoculant (aluminum

increases surface tension of the metallic matrix).

In the case of separating of nodular graphite before liquidus line and between liquidus and eutectic temperature, integrating the (7) relation on a little temperature interval one obtains the next expression for  $G_A$ :

$$G_A = -S_A T'_A + A\sigma_A + \sum_{z=1}^m \mu_z^A n_z^A, \quad (14)$$

where  $T'_A$  is the interface temperature but different of eutectic temperature.

Taking (11) relation and defining A it results the next result:

$$A = \frac{G_A + S_A T'_A - \sum_{z=1}^m n_z^A R T'_A \ln a_z^A}{\sigma_A} = \frac{G_A + S_A T'_A - \sum_{z=1}^m n_z^A \mu_z^A}{\sigma_A} \quad (15)$$

To obtain a minimum value for A – to obtain nodular graphite – it must that  $G_A$ ,  $S_A$ ,  $T'_A$ ,  $a_z^A$ ,  $n_z^A$ ,  $\mu_z^A$  and  $\sigma_A$  to have optimum values. In addition, it must that to be the next inequalities:

$$G_A > -S_A T'_A + \sum_{z=1}^m n_z^A \mu_z^A \text{ or} \\ G_A > -S_A T'_A + \sum_{z=1}^m R T'_A \ln a_z^A \quad (16)$$

(12) and (14) relations exclude the direct implicating of the cooling rate in nodulizing process.

#### 4. Implication of chemical composition and temperature of liquid iron on modification

Having as base (11) relation, definition of  $G_A - G_A = H_A - T_A S_A$ , where  $H_A$  is interface enthalpy, definition of  $a_z^A - a_z^A = f_z^A \cdot C_z^A$ , where  $f_z^A$  is thermodynamic activity coefficient of z element from interface and  $C_z^A$  is concentration on z element from interface and definition of  $\sigma_A$ , during the eutectic transformation, graphite surface A depends of temperature and chemical composition.

In addition, when temperature is bigger than eutectic one, it must take as base the definition of  $S_A - S_A = C_p^A \ln \frac{T_s}{T'_A}$ , where  $C_p^A$  is specific heat of interface and  $T_s$  is

overheating temperature. So, it results that chemical potential of the chemical elements from interface must be correlated with specific heat of interface and ratio between overheating temperature and current temperature (another than eutectic one).

When the chemical composition of interface is constant, it results from inequalities (16) than if the overheating is increased, thermodynamic potential is increased too, and so, it is possible that graphite surface to have minimum values.

#### 5. Implication of interface enthalpy on graphite nodulizing

If it considers the definition of isobar thermodynamic potential –  $G_A = H_A - T'_A S_A$  – where  $H_A$  is interface enthalpy it results a new expression for surface A – (17) relations in the case of temperatures bigger than eutectic temperature.

$$A = \frac{H_A - \sum_{z=1}^m n_z^A \mu_z^A}{\sigma_A} = \frac{H_A - \sum_{z=1}^m RT_A \ln a_z^A}{\sigma_A} \quad (17)$$

In cases when temperature is eutectic, surface A has value as in (18) expressions.

$$A = \frac{H_A - T_A S_A - \sum_{z=1}^m n_z^A \mu_z^A}{\sigma_A} \quad \text{or}$$

$$A = \frac{H_A - T_A C_p \ln \frac{T_s}{T_A} - \sum_{z=1}^m n_z^A \mu_z^A}{\sigma_A} \quad \text{or} \quad (18)$$

$$A = \frac{H_A - T_A C_p \ln \frac{T_s}{T_A} - \sum_{z=1}^m RT_A n_z^A \cdot \ln a_z^A}{\sigma_A}$$

The factors what influence graphite nodulizing must be considered cumulatively at both temperatures – eutectic and bigger then eutectic. Well, the factors what have to be correlated for obtaining a minimum graphite surface – nodular graphite – are the next:  $H_A$ ,  $T_s$ ,  $T_A$ ,  $n_z^A$ ,  $a_z^A$ ,  $C_p$ ,  $a_z^A$  and  $\sigma_A$ . The means to activate on those ones are chemical composition, temperature and cooling rate. Those factors have to be optimum to obtain a minimum graphite surface. A relation more exact between those factors is (19) one.

$$H_A > T_A C_p \ln \frac{T_s}{T_A} - \sum_{z=1}^m RT_A n_z^A \cdot \ln a_z^A \quad (19)$$

When one tends to  $H_A = T_A C_p \ln \frac{T_s}{T_A} - \sum_{z=1}^m RT_A n_z^A \ln a_z^A$ , graphite tends to be point - like and iron tends to be motley.

When  $T_A C_p \ln \frac{T_s}{T_A} = \sum_{z=1}^m RT_A n_z^A \ln a_z^A$ , iron is solidified in Fe-C metastable system – interface becomes cementite – metallic matrix.

## 6. Implication of cooling rate on graphite nodulizing

Cooling rate influences undercooling ratio. So, cooling rate influences the temperature of the graphite-metallic interface. As a results, cooling rate influences the values of chemical potentials, entropy, specific heat, interphase tension and enthalpy. Well, all relations where those ones intervene, are conditioned by the cooling rate, too.

## 7. Implication of thermodynamic activity on graphite nodulizing

(18) relation, where thermodynamic activity intervenes is the base for analysis.

Considering the definition of thermodynamic activity, (19) relation becomes (20) one.



$$A = \frac{H_A - T_A C_p \ln \frac{T_s}{T_A} - \sum_{z=1}^m [RT_A (\ln f_z^A + \ln C_z^A)]}{\sigma_A}$$

(20)

In (20) relation there is a very important factor –  $f_z^A$  – what depends, for a chemical element, by another chemical elements from the interface.

Well, one knows the general relation (21) for chemical element  $E_1$ .

$$\lg f_{E_1}^A = \%E_1 \cdot e_{E_1}^{E_1} + \%E_2 \cdot e_{E_1}^{E_2} + \%E_3 \cdot e_{E_1}^{E_3} + \dots + \%E_m \cdot e_{E_1}^{E_m} \quad (21)$$

where  $E_1, E_2, \dots, E_m$  represent the chemical elements from interface and  $e_{E_1}^{E_m}$  represent the interaction coefficient of  $E_m$  chemical element on  $E_1$  chemical element.

In (18) and (20) relations, among other things, for graphite surface to be minimum, it must  $\sum_{z=1}^m n_z^A \ln a_z^A$  to be maximum. Well, for unalloyed irons, for example, the main chemical elements are Fe, C, Si, Mn, S and P.

If carbon has not a big thermodynamic activity, there is the risk that iron to solidify by Fe-C metastable system. Consequence, it must have a minimum thermodynamic activity of carbon for iron to solidify greyly and it must have a maximum thermodynamic activity of carbon for graphite to have a minimum surface. This one, one obtains in the case of big concentrations of carbon and silicium – s8t. Manganese decreases carbon thermodynamic activity – well, it must have small concentration.

In the case of an unalloyed iron, a carbon concentration less than 3,4% put under the question mark the graphite nodulizing by treatment of iron with magnesium.

It seems that it is very important that inoculant to be in interface and, in the same time, to have a big thermodynamic activity.

Well, inoculants as Mg, Ce, Y, Ca, Li, Na etc. must be adsorbed at interface and, in addition, confer it a maximum  $\sum_{z=1}^m n_z^A \ln a_z^A$ .

Adsorption capacity of inoculants at graphite surface results from adsorption isotherm of Gibbs –  $\Gamma_z = -\frac{a_z}{RT_A} \cdot \frac{d\sigma_A}{da_z}$  – where  $\Gamma_z$  is adsorption coefficient of the  $z$  chemical element. Well, for adsorption, it must that

$$\frac{d\sigma_A}{da_z} < 0 \quad (22)$$

The source s4t indicates, in the case of iron inoculating with magnesium, by experiment, magnesium distribution in the graphite-metallic matrix interface and silicium distribution in the metallic matrix but next to graphite-metallic matrix interface. Silicium increases strongly carbon thermodynamic activity. This experiment conform the theoretical analysis.

In the case of unalloyed irons, the most important chemical element from interface is carbon what must have a big thermodynamic activity – big quantity and big thermodynamic activity coefficient. The s9t source indicates (23) relation for

carbon thermodynamic activity coefficient  $f_c$ .

$$\lg f_c = -0,23 + 0,049 [\%_A C], \quad (23)$$

where  $\%_A$  represents atomic percentages. Well, beginning from about 5 atomic percentages up,  $f_c$  becomes positive and, so, influences significantly carbon thermodynamic activity.

### 8. Increasing place of nodular graphite – hypothesis

One estimates that nodular graphite germinates and increases in the blanks of spheroidal geometry from the particles from liquid iron.

In metals in liquid state there are microcavities among particles (molecules, atom, ions), microcavities what are in metals in solid state too, and what have big size in metals in gaseous state, s5t.

According source s4t, the microcavities geometry dictates the graphite geometry what is obtained in solid iron by transformation of cementite by thermal treatment (it is about of the obtaining of nest graphite and nodular graphite by special conditions – big sulphur concentration or spheroidal microcavities caused by special thermal treatment) and liquid iron by magnesium bubbles whose geometry is almost spheroidal. These aspects are verified experimentally.

Nodular graphite germination process excludes the presence of the graphite inclusions (specially the flaky ones) in liquid iron – excludes the heterogeneous structure of liquid iron what there is between liquidus line temperature and 1,400...1,410<sup>0</sup>C temperature. Well, that one excludes the temperatures of liquid iron under 1,400...1,410<sup>0</sup>C temperature. If liquid iron is not overheated at the temperatures bigger than 1,400...1,410<sup>0</sup>C and if the charge contains metallic sorts with flake graphite, the flake graphite cannot be eliminated from liquid iron. Superheating iron excludes non-metallic inclusions in a large measure.

Nodular graphite germinates in a liquid iron whose structure is homogeneous.

Sulphur is adsorbed on residual graphite surface and keeps residual graphite until temperatures about 1.500<sup>0</sup>C. So, it results that the sulphur content have to be small or when it is accepted the big contents it must increase the superheating ratio. Big equivalent carbon increases the stability of residual graphite. That's why, chemical elements as Si, P, S, Al, Sn etc. involve big superheating ratio if iron what must be inoculated.

One estimates that the propriety what conditions the geometry of the microcavities is the cluster-metallic matrix interphase tension.

There is a favorable chemical composition, influenced by inoculants too, what involves that cluster-metallic matrix interphase tension to have big values and the microcavities to have a quasispheroidal geometry.

In the case when the inoculant there is in the gaseous state, it must that the bubble – metallic matrix interphase tension to be big, the result being a quasispheroidal geometry for bubbles. So, a small inoculant quantity in liquid iron, involves for inoculant bubbles a unspheroidal geometry – unspheroidal graphite.

Graphite germinates on microcavities surface, increasing along base hexagonal plans – very much – and perpendicular on base hexagonal plans – not so much.

Increasing of graphite along the base hexagonal plans is stopped of meeting with

another base hexagonal plans what come from another graphite nucleus.

## 9. Conclusions

9.1. For obtaining nodular graphite, it must that graphite surface to be minimum;

9.2. Variation of free enthalpy of graphite-metallic interface has values in  $-2\sigma_m \dots 0$  interval, where  $\sigma_m$  is surface tension of the metallic matrix;

9.3. The moistening angle of graphite by liquid metallic matrix,  $\theta$ , depends of metallic matrix surface tension,  $\sigma_m$ , and free enthalpy variation of the graphite-metallic matrix interface,  $\Delta G_A$ , by the next relation:  $\theta = \arccos \frac{\Delta G_A + \sigma_m}{\sigma_m}$ ;

9.4. Graphite surface,  $A$ , depends directly by the next factors: superheating temperature of liquid iron,  $T_s$ , specific heat,  $C_p^A$ , thermodynamic activity of chemical elements,  $a_z^A$ , chemical composition of iron, graphite-metallic matrix interphase tension,  $\sigma_A$ , enthalpy of that interface,  $H_A$ , and eutectic temperature,  $T_A$ , the interdependence being the next:

$$A = \frac{H_A - T_A C_p^A \ln \frac{T_s}{T_A} - \sum_{z=1}^m R T_A n_z^A \ln a_z^A}{\sigma_A};$$

9.5. In the case when one tends to equation

$$H_A = T_A C_p \ln \frac{T_s}{T_A} - \sum_{z=1}^m R T_A n_z^A \ln a_z^A, \text{ graphite tends to be point-like, and iron tends}$$

to be motley. In the case of that equation, iron is solidified by Fe-C metastable system – interface becomes cementite-metallic matrix.

9.6. Cooling rate is implicated indirectly on the graphite surface, activating on undercooling ratio – exchanging the eutectic temperature value;

9.7. To obtain nodular graphite, the liquid iron structure have to be homogeneous;

9.8. In the case of unalloyed irons – grey irons – a big carbon content is imposed;

9.9. Because an enough big number of factors activates on graphite nodulizing, graphite nodulizing is a complex problem;

9.10. Graphite nodulizing, imposes, for unalloyed irons, big contents for C and Si;

9.11. Graphite nodulizing is conditioned of the inoculant presence in graphite-metallic matrix interface, too;

9.12. One estimates that nodular graphite germinates and increases in the microcavities whose geometry is quasispheroidal or in the bubbles of inoculant of quasispheroidal geometry, too;

9.13. The most important factor what determines the quasispheroidal geometry of the microcavities among particles – among the clusters, for example – is the cluster metallic matrix interphase tension (big values);

9.14. The base factors what influences graphite nodulizing directly, are chemical composition of iron and iron temperature;

## REFERENCES

1. Sofroni, L., Ștefanescu, D.M. and Vincenz, C. *Fonta cu grafit nodular*. Editura Tehnica, Bucuresti, 1978;
2. Sofroni, L. and Ștefanescu, D.M. *Fonte modificate cu proprietati superioare*. Editura Tehnica., Bucuresti, 1971;
3. Cosneanu, C. and Ghiu, M. *Tehnologii moderne in productia de piese turnate*. Revista de Turnatorie, Bucuresti, No 2, 2000, p. 17...21;
4. Itofuji, H. *Proposal of site theory*. Translated by Sofroni, L. – Cu privire la teoria formarii grafitului nodular. Revista de Turnatorie, Bucuresti, No. 5, 6, 2004, p. 5...12;
5. Oprea, F., Taloi, D., Constantin, I. And Roman, R. *Teoria proceselor metalurgice*. Editura Didactica si Pedagogica, Bucuresti, 1978;
6. Sofroni, L. *Elaborarea si turnarea aliajelor*. Editura Didactica si Pedagogica. Bucuresti, 1975;
7. Vermesan, E., Ionescu, I. and Urseanu, A. *Chimie metalurgica*. Editura Didactica si Pedagogica, Bucuresti, 1981;
8. Vacu, S. et. al. *Elaborarea otelurilor aliate. Vol. I*. Editura Tehnica, Bucuresti, 1980;
9. Tripsa, I., Oprea, F. and Dragomir, I. *Bazele teoretice ale metalurgiei extractive*. Editura Tehnica, Bucuresti, 1967.

Thanks to Mr. Mihai Ștefan, assist. Prof. At the Technical University „Gh. Asachi” for some mathematics suggestions.

Vasile Cojocaru-Filipiuc, D.Sc.Prof., Technical University „Gh. Asachi”, Bv. Mangeron, nr. 61, Iași, Romania

## PUNCT DE VEDERE PRIVIND NODULIZAREA GRAFITULUI

**Rezumat:** Se ia in considerare fenomenul de umectare a grafitului de catre matricea metalica, aflându-se limitele intre care variaza potentialul termodinamic izobar al interfetei grafit-matrice metalica.

Plecând de la definitia potentialului termodinamic izobar, se expliciteaza acest parametru de stare in functie de factori ce actioneaza asupra interfetei grafit-matrice metalica – entropie, volum, presiune, potential chimic, tensiune interfazica, aria grafitului, temperatura eutectica, temperatura de supraincalzire in stare lichida si caldura specifica.

Ulterior, se expliciteaza aria grafitului la transformarea eutectica si la temperaturi mai mari decât temperatura eutectica, stabilindu-se un model matematic al acesteia in care figureaza factorii ce o influenteaza.

Conditia de nodulizare a grafitului este aceea de arie minima a grafitului, adica de valori ale factorilor implicati in nodulizarea grafitului care sa determine un minim al ariei grafitului.

Factorii principali implicati direct in nodulizarea grafitului sunt compozitia chimica a fontei si temperatura fontei.

Factorul indirect implicat in nodulizarea grafitului este viteza de racire.

Se estimeaza ca grafitul creste nodular in golurile sferice dintre particule, din fonta lichida, sau in bulele de modificador.

## EXPERIMENTAL DATA ACQUISITION FOR BALL BEARING FRICTION TORQUE MEASURING

BY

IOAN DAMIAN, VIOREL PALEU and SPIRIDON CREȚU

**ABSTRACT.** In ball bearings, the friction moment developed at both the inner and outer race level, can be experimentally estimated for complex load conditions (axial and radial load, and misalignment effect), similar to the running conditions found in practical applications. The paper presents the experimental rig, and the structure of the experimental data acquisition chain. The experimental measured values are in good agreement with those found in literature.

**Key words:** ball bearings, friction moment, data acquisition.

### 1. Introduction

For the estimation of the friction torque in the ball bearing there is a multitude of experimental devices which determines only the friction torque developed in the inner ring. The working conditions of the ball bearings make the modification of the rotation angle between the ball bearing rings which also produces a modification of the friction torque in the bearing.

Thus, it is necessary an experimental device which allows the friction moment measurement in the ball bearing, in the case of a complex loads conditions and also the simulation of the rotation angle between the bearing' rings because of the modification of the shaft rigidity under the running condition action.

### 2. Experimental device

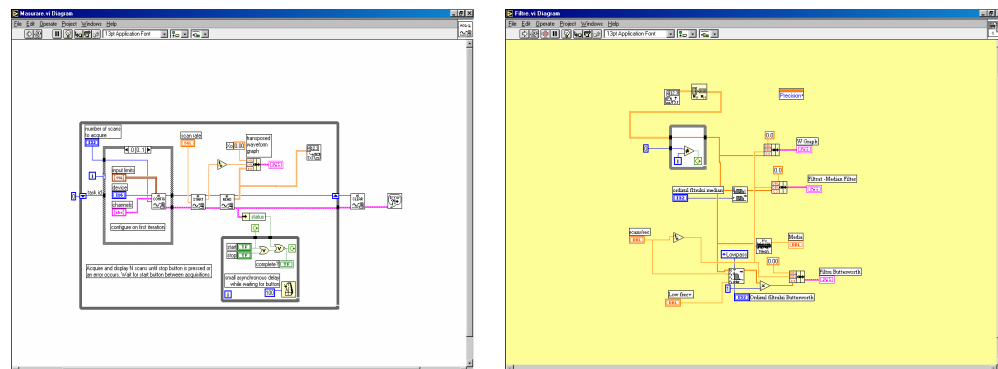
For the measurement of the friction torque in the angular ball bearing , an experimental device was designed and developed ,Damian (2002), presented in fig.2.1. The device allows the making of a complex load formed by a radial force  $F_r = 0 \div 2000$  N, an axial load  $F_a = 0 \div 700$  N and a misalignment between the tested bearing rings  $\gamma_z = 0 \div 15$  min , for a rotation range  $n = 0 \div 8000$  rot./min and the determination of the friction moment on both inner ring and outer ring in the bath oil lubrication condition.

For obtaining the experimental data it was used a measurement chain, which consists of the torque transducer, the measuring bridge, the device data acquisitions, and the soft LabView for working out this data.

The measurement chain diagram made with the aid of the LabVIEW program , fig. 2.2, offers the possibility to collect and to work out the experimental data obtained for the friction torque developed in the angular ball bearing.



Fig.2.1 The experimental setup



(a)

(b)

Fig.2.2 Block diagrams: (a) data acquisition: (b) data processing

### 3. Experimental results

The friction torque developed in the angular ball bearing 7012 CTA P4 was measured with the aid of the experimental device, for the following conditions:

- the axial load: 350 N ; 700 N.
- the radial load: 500 N, 1000 N, 1500 N, 2000 N.
- the rotational speed of the inner ring:  $N_i = (0 \dots 8000)$  rot/ min.
- the lubricant viscosity: 0.033 Pa·s; 0.095 Pa·s.
- the misalignment between bearing's rings:  $\gamma_y = 0^\circ ; 5^\circ ; 10^\circ ; 15^\circ$ .

The experimental results of the friction moments in the angular ball bearings present its evolution in the condition of following influences:

- the influence of speed running fig.3.1,
- the influence of axial force  $F_a = F_z$ , fig.3.2,
- the influence of radial force  $F_x = F_r$ , fig.3.3,
- the misalignment influence  $\gamma_y$ , fig.3.4,
- the viscosity influence  $\eta$ , fig. 3.5.

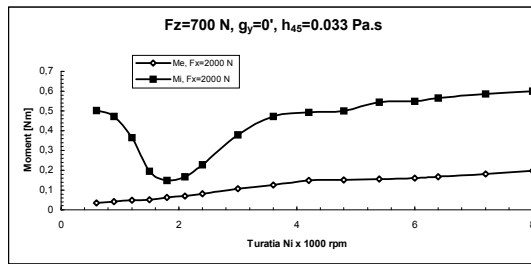


Fig. 3.1.

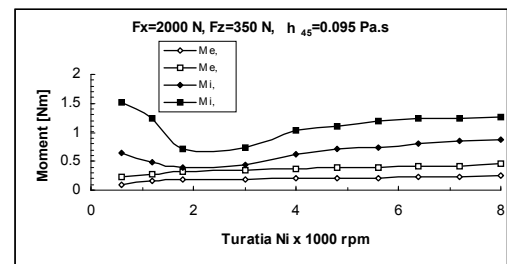


Fig.3.2.

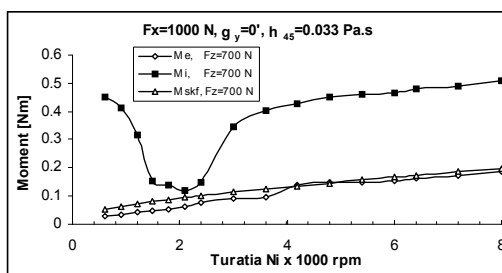


Fig.3.3.

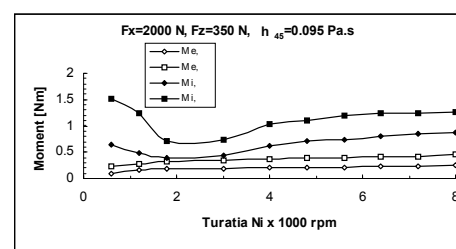


Fig.3.4.

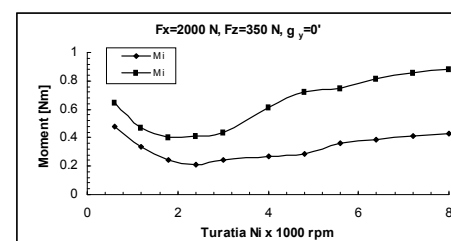
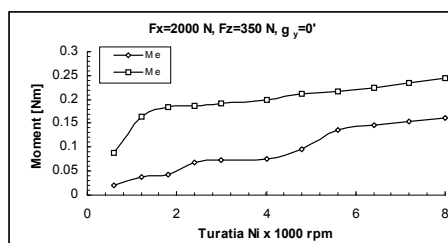


Fig.3.5.

### 1. Conclusions

By analysing the experimental results we reach the following conclusions:

-the measured torques in the outer ring “ $M_e$ ”, are in the same values range as those obtained by the SKF Catalogue (1989);

-the friction moment in the inner ring “ $M_i$ ” measured on the device has an evolution which is similarly with the variation of the lubricant parameter, in the case of superior coupling.(Stribeck)(Damian 2002);

-the continuous increasing of the friction torque “ $M_e$ ”, is explained by the fact that at the outer contact level the balls displacement gets close more by the rolling domain, the traction force from the outer contact having the values smaller than those from the inner contact;

-both a high speed increase of the friction moment “ $M_e$ ” and also of the friction torque “ $M_i$ ” takes place when a misalignment “ $\gamma_y$ ” is present between the two rings ;

-the increasing of the oil viscosity lead to the increasing of the friction torque values, both the outer ring “ $M_i$ ”, and the inner ring “ $M_e$ ”

Received April 20, 2005

Technical University “Gh.Asachi”, Jassy,  
 \*Department of Internal Combustion  
 Engine and Automotive Vehicles  
 and  
 \*\*Department of Machine Design  
 and Tribology

#### REFERENCES

1. Damian I. Teza de Doctorat: *Contributii privind influenta conditiilor de exploatare asupra pierderilor prin frecare din rulmenti*. IASI 2002.
2. Damian I. Brevet de Inventie nr. 118093 B, Int. Cl. G 01 M 13/04 , 28.11.2002.
3. *S.K.F. General Catalogue 4000* / I.E. Industries INC. 1989.

#### ACHIZIȚIE DE DATE EXPERIMENTALE PENTRU MĂSURAREA MOMENTULUI DE FRECARĂ DIN RULMENȚII CU BILE

#### (Rezumat)

În rulmenții cu bile este posibilă aprecierea pe cale experimentală a momentului de frecare dezvoltat la nivelul ambelor căi de rulare, în condiții de încărcare complexă (forță radială, forță axială și înclinare relativă a inelelor), similare condițiilor de funcționare din aplicațiile practice. Se prezintă standul experimental și structura lanțului de achiziție a datelor experimentale. Valorile măsurate pe cale experimentală sunt în concordanță cu cele oferite de literatură.



## HEAT PROCESS OPTIMIZATION IN INDUSTRIAL FURNACES

BY

**ADRIAN DIMA, ALINA ADRIANA MINEA and  
IULIA MARGARETA DIMA**

***ABSTRACT:** Materials Science represents, by its applications, the beginning of the industrial society transformations in well develop society from society in developing. The large spectrum of activities of the materials science principles and laws in industrial societies goes to identification of the basis development directions, which contributes to gain the new materials and production technologies that are indispensable in a future industry society. This has, also, a benefice on ecology and rational utilization of the natural mineral resources. Materials engineering represent the applicative side of materials science and puts the basis of materials obtaining technologies, which are very important in the actual stadium of the industrial society development. Using the computer assisted modelling leads to the development of the energetic bases, which involves a complete elimination of rejects, a decrease of costs and an increased productivity.*

***Keywords:** furnace, materials engineering, optimization, computer modelling*

### 1. Introduction

Materials Science represents, by its applications, the beginning of the industrial society transformations in well develop society from society in developing. The large spectrum of activities of the materials science principles and laws in industrial societies goes to identification of the basis development directions, which contributes to gain the new materials and production technologies that are indispensable in a future industry society.

This has, also, a benefice on ecology and rational utilization of the natural mineral resources.

Materials engineering represent the applicative side of materials science and puts the basis of materials obtaining technologies, which are very important in the actual stadium of the industrial society development and also, creates the premises of an ulterior develop.

Metals heating, in a furnace, are conditioned by heating time in a furnace with known characteristics. Temperature control and uniformity present essentially the same problems in heat treating as they do in hot forging.

Good temperature control and uniformity throughout the furnace and load are required for all heat operations. Recommended temperature is generally those that are least critical and that can be used with practical time cycles.

## 2. Contributions

The general methods for heat treating include the use of molten salt – baths, air – chamber furnaces and induction heaters. The choice of heating equipment depends largely on the alloy and the configuration of the parts to be processed.

The heat in a furnace can be obtained in two principal ways:

- by burning – chemical process that consist in a chemical reaction between the fuel and an optimum quantity of air;
- by electricity – physical process that consists in obtaining heat from electrical energy.

Air furnaces are used more widely because they permit greater flexibility in operating temperature. Air furnaces are also more economical when the product mix includes a few parts; holding temperature of a large volume of salt in readiness for an occasional part is far more expensive than heating an equal volume of air.

In air furnaces, careful attention should be given to arrangement of the load. Air flow and natural temperature distribution within the furnace should be arranged to:

- offer minimum resistance to air flow
- produce the least disturbance in the natural temperature distribution
- afford constant replenishment of the envelope of air around each part.

Fuel furnaces are used because they are low costs equipments and permit wide processes at high temperatures.

Using fuel furnaces appear some problems with the evacuated gases. These gases create pollution and it must be evacuated using special equipments.

Fuels that are used in furnaces are:

- natural fuel
- artificial fuel.

Also, in industry are used solid, liquid or gaseous fuels. In the most applications are used gaseous fuels because of their advantages:

- easy transport
- burning in a minimum quantity of air
- the possibility of directing the heat on many burners
- the absence of ash.

Industrial heating furnaces are complex thermal units with high energy consumptions that are producing heat at optimal using parameters. It is commonly known by specialists in hot working that substantial energy decreases may be achieved by:

- strictly maintaining the working parameters,
- loading all units at nominal capacity,
- daily surveillance according to norms of energy and fuel consumptions.

In our opinion, the main levels to reduce energy consumptions in industrial furnaces are divided in two important categories:

- analytical calculation of billets heating processes. The calculus is referred to the steel, the size and geometrical configuration of the billet; the furnace type and to the hot working process which the heated billet will be later subjected to.
- accurate knowledge of the optimal functioning of the furnaces and its auxiliary units, in order to obtain a certain heating cycle. This operation is known in the literature as “know how”.

Obtaining an optimum functioning cycle for the industrial furnace, with “know how” procedure, uses the following main directions:

- from what
- with what
- to what.

The procedure of the furnaces functioning surveillance is described in figure 1.

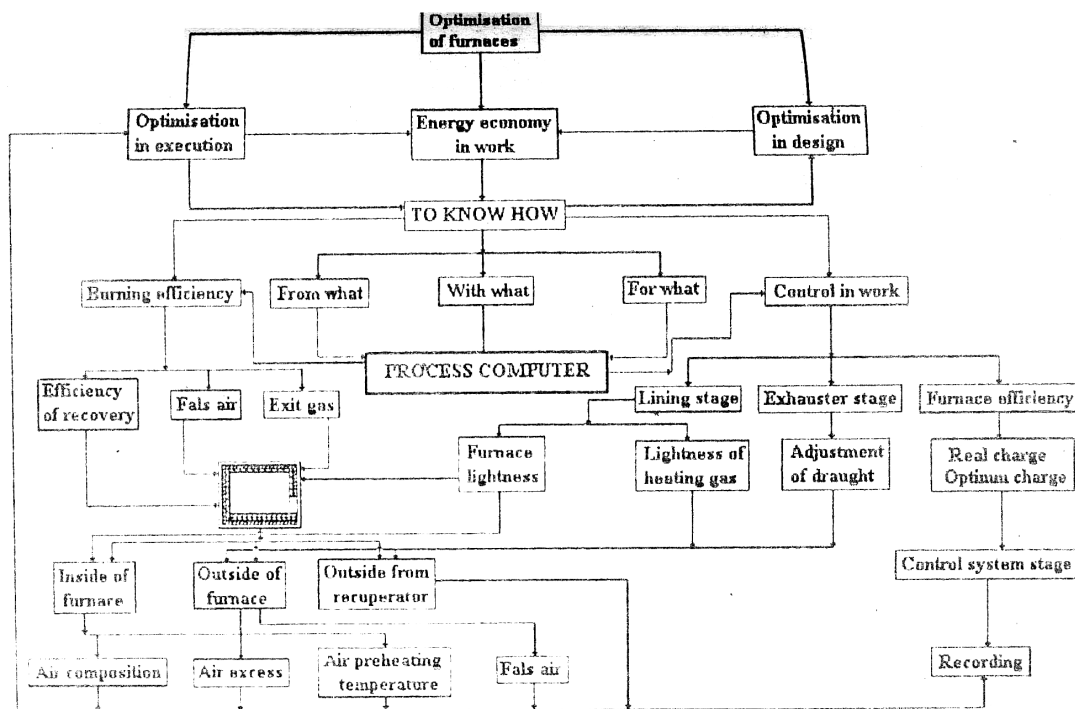


Figure 1.

The research direction using optimal heating technologies must be studied with “know how” technology that involves the following steps:

- critical analysis of heating technologies;
- redesigning industrial furnaces;
- introducing modern burners and heating process;
- analytical and theoretical design for thermal cycles;
- computer assisted optimization of the research theme.

Computer assisted optimization of the research theme is possible on the basis of establishing the needed input data:

- furnace chamber size;
- the ingots number of the charge;
- chemical composition of the material subjected to the heating processes;
- ingot geometry;
- the temperature gradient of the ingot core and surface;
- the final heating temperature for the ingot;
- physical characteristics variation with temperature;
- the criteria variation.

All of these data must be included in a computer program that is conceived from many modules that make possible the calculation of the heating time, ingot core and surface temperature variation in the process, as well as the stress variation.

### 3. Conclusions

Materials Science represents a science in full evolution in concordance with the necessities of a modern society. Without modern materials and without European integration we can not conceive a society development at the needed level.

As a conclusion, we must say that the use of the computer assisted mathematical models leads to the development of the energetical bases that involves a complete elimination of the rejects, a decrease of production costs and an increased productivity.

#### *References*

- 1 A. Dima, I. Alexandru, A. Simionescu, C. Ciochina, E. Andrei (1997) Stiinta si ingineria materialelor in societatile de tranzitie, cu particularizare in societatea romaneasca. Stiinta la sfarsit de mileniu. Academia Oamenilor de Stiinta din Romania. Bucuresti, pp. 140.
- 2 A. A. Minea (1996) Studies concerning the improvement of the construction and functioning parameters of aluminum alloys heat treatment furnaces. Bul. I.P.Ia[i]
- 3 A. A. Minea, A. Dima (2002) Influence of the heating process on aluminum alloys failure. Materials Engineering, vol. 13, n.3, pp. 265-267, ISSN 1120-7302.
- 4 A. Dima, A.A. Minea (2002). Theoretical contributions regarding atmosphere circulation in a radiative furnace. Materials Engineering, vol. 13, n.2, pp. 187-190, ISSN 1120-7302
- 5 A.A. Minea (2003) Heat transfer and thermic instalations. Ed. Cermi, Iasi.
- 6 A.A. Minea , A. Dima(2005) Energy and mass transfer. Ed. Cermi, Iasi
- 7 A. Dima, A.A. Minea (2005) Furnaces and heating installations. Ed. Cermi, Iasi

**A. DIMA, A.A.MINEA, I.M. DIMA, "GH. ASACHI" TECHNICAL UNIVERSITY OF IASI, ROMANIA**

#### **OPTIMIZAREA PROCESELOR DE INCALZIRE IN CUPTOARELE INDUSTRIALE**

**REZUMAT:** Stiinta materialelor reprezinta izvorul transformarilor societatilor industriale din societati in curs de dezvoltare in societati puternic dezvoltate. Ingineria materialelor reprezinta latura aplicativa a stiintei materialelor prin intermediul careia se pun bazele tehnologice de obtinere a materialelor necesare stadiului actual al dezvoltarii societatilor industriale.

Folosind optimizarea asistata de calculator a proceselor se ajunge la dezvoltarea bazei energetice, ceea ce implica o eliminare completa a rebuturilor, o descrestere a costurilor si o crestere semnificativa a productivitatii.

## STUDIES CONCERNING THE ENHANCING OF THE MECHANICAL CHARACTERISTICS OF THE ALUMINUM CAST ALLOYS BY HEAT TREATMENTS

BY

ADRIAN DIMA\*, IULIA MARGARETA DIMA\*\* and ALINA MINEA\*

*Abstract:* The experimental research concerning the determination of the variation of the dynamic and static mechanical properties, during the heat treatments put into evidence the structural changes of the aluminum alloys leading at the drawing of the diagrams for these mechanical characteristic features.

*Keywords:* aluminium alloys, mechanical properties, heat treatment

### 1. Introduction

Because of the structural changes that take place during the heat treatment process the static and dynamic mechanical characteristics of the material change too. So, hardness, and traction characteristics as well as the fatigue behavior of the cast aluminium alloys change significantly.

### 2. Material and experiment

The experiments were conducted for determining the breaking resistance to traction and for hardness determination. Two types of aluminium alloys were tested according STAS 201-2-1971.

The tested pieces were obtained in a technological flow of casting in metallic moulds, in the same technological conditions as in the industrial production.

For the determination of the ultimate tensile strength value, there a set of five samples was used, for each type of thermal cycle (heat treatment).

Also for the determination of the average value of the hardness, with the Brinell method, there were used five experimental values. Table 1 shows the average tensile strength and the hardness obtained in the tests without any heat treatment.

Alloy	Ultimate strength [dan/mm <sup>2</sup> ]	Hardness Brinell
ATC Si 10 Mg	20.1	65.4
ATC Si 5 Cu - 1	17.3	72.3

The figures 1 and 2 show the change in the ultimate strength values of the two studied alloys.

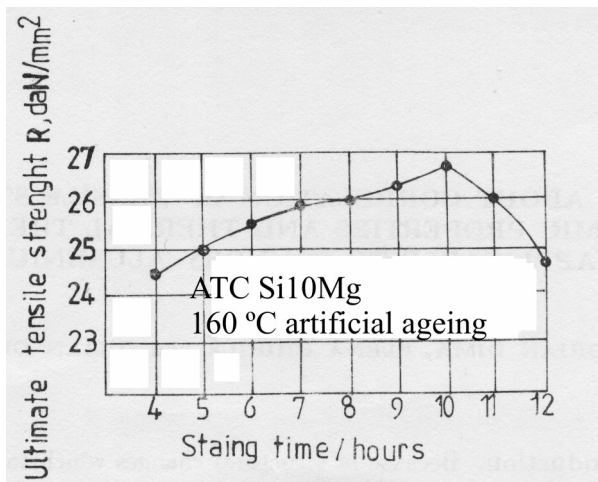


Fig. 1

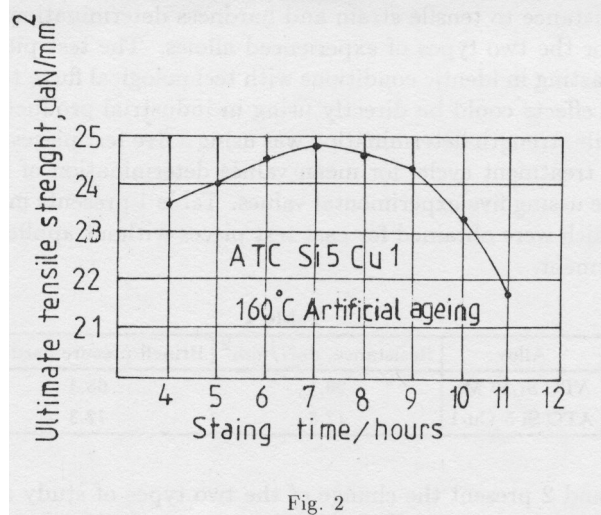


Fig. 2

Figures 3 and 4 show the change in the hardness Brinell for the two studied alloys.

A general study of the average value curves of static tensile properties variation shows that the performing experiences point out the structural changes.

The optimum values of static tensile properties studied for those two alloys (ATC Si 10 Mg and ATC Si 5 Cu -1) result from using complex heat treatment: hardening and artificial ageing at 160 °C, by maintaining the first alloy during 10 hours and for the second one for 7-8 hours.

The fatigue behavior is one of the propertie that must be studied too because many of aluminum casting are being used as parts in cycling motion.

For determining the fatigue resistance, there were used Amsler test pieces and constant bending cycles.

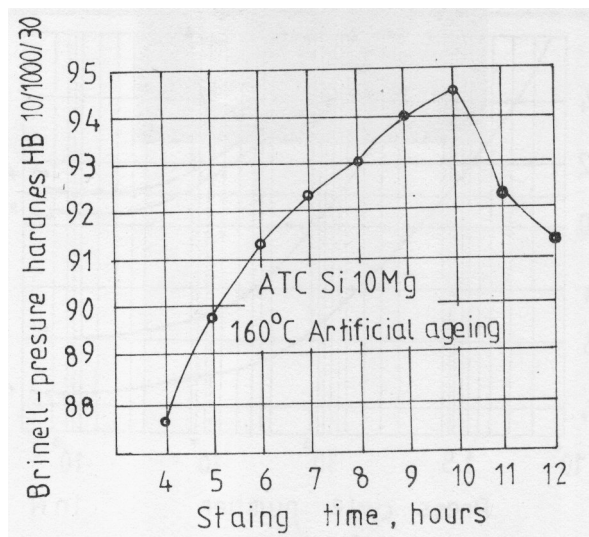


Fig. 3

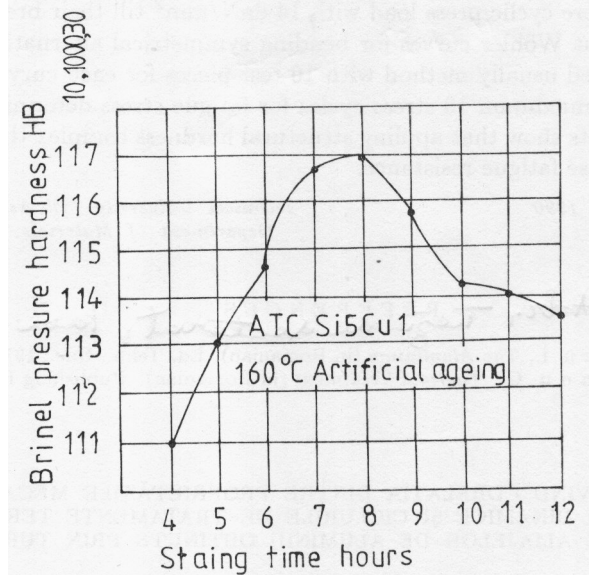


Fig. 4

The samples were cyclicly stress with  $14 \text{ daN/mm}^2$  until breaking.

For obtaining the fatigue curves simetrical bending cycles were applied to 16 samples for each curve.

The Wöhler curves obtained are shown in figure 5: 1- ATC Si 10 Mg; 2 – ATC Si 10 Mg after 6 hours of putting into solution at  $520^\circ\text{C}$ , quenching and artificial ageing for 10 hours at  $160^\circ\text{C}$ ; 3 – ATC si 5 Cu – 1; 4 – ATC si 5 Cu -1 after 6 hours of putting into solution at  $520^\circ\text{C}$ , quenching and artificial ageing for 8 hours at  $160^\circ\text{C}$ .

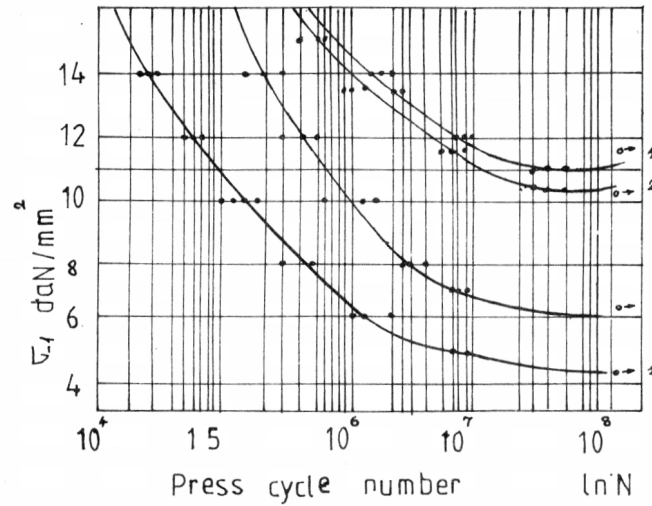


Fig. 5

### 3. Conclusions

For the studied alloys it can be seen that the fatigue resistance enhanced significantly after ageing, fact that is in accordance with the literature.

### References

1. Dima, A, Teza de doctorat, I.P. Iasi, 1980
2. Lazarescu, I., Alumiuniul, Ed Tehnica, Bucuresti, 1978
3. Vermesan, G., Tratamente termice, Ed. Dacia, Cluj-Napoca, 1978.

Adrian Dima  
Alina Minea  
Iulia Margareta Dima

\*Technical University Iasi  
\*\*District School Inspectorate Iasi

### STUDII PRIVIND CRESTEREA CARACTERISTICILOR MECANICE ALE ALIAJELOR TURNATE DIN ALUMINIUPRIN TRATAMENTE TERMICE

**Rezumat:** Cercetarile experimentale privind determinarea variatiilor proprietatilor mecanice, dinamice si statice in timpul tratamentelor termice pun in evidenta schimbarile structurale ale aliajelor de aluminiu conducand la trasarea diagramelor valorilor caracteristice mecanice si statice.



## CURRENT IN A 1D CIRCULAR WIRE

BY

MARIANA LATU

**Abstract** The paper reports a theoretical study of the electrical properties for a circular one-dimensional wire. We present a new derivation of the single-channel conductance formula. We consider the situation of a one-dimensional circular wire. From the Born-von Karman periodic boundary condition result the values for the electron wave function, energy and the density of states. Then we have calculated the total current flowing across the system and the conductance. The effects of the transmission coefficient on the conductance are studied.

**Key-words:** one-dimensional wire, electron wave function, energy, density of states, total current, transmission coefficient, conductance

### 1. Introduction

One important length scale characterizing quantum systems is the Fermi wavelength

$$\lambda_F = \frac{2\pi}{k_F} \quad (1)$$

where  $k_F$  is the Fermi wave number.

Consider a system confined into a box with sizes  $L_x$ ,  $L_y$  and  $L_z$  ( $L_x < L_y < L_z$ ). The system is a quantum wire (quasi 1D) if it is satisfied the relation [1]:

$$L_x < L_y \approx \lambda_F \ll L_z \quad (2)$$

The system is a one-dimensional wire (1D) if the relation is:

$$L_x < L_y < \lambda_F \ll L_z \quad (3)$$

Quantum structure have shown new phenomena associated with ballistic transport in which electrons can move without being scattering by impurities or random potential fluctuations, such as conductance quantization, the Coulomb blockade and Tomonaga-Luttinger liquid.

R.Landauer derived the relation between the conductance of a one-dimensional wire and the transmission and reflection probabilities at the Fermi level [2]. The sample is connected to two electron reservoirs by ideal 1D conductors. A stream of particles hits the barriers, a fraction  $R$  is reflected, and a fraction  $T$  is transmitted. The total current flowing across the system is given by

$$I = (-e)v \frac{\partial n}{\partial E} T(\mu_1 - \mu_2) \quad (4)$$

Here  $v$  is the Fermi velocity,  $\frac{\partial n}{\partial E}$  is the density of states for two spin directions and for carriers with positive velocity.  $\mu_1$  and  $\mu_2$  represent the quasi-Fermi energy. Taking into account that in one-dimension the density of states is:

$$\frac{\partial n}{\partial E} = \frac{1}{\pi \hbar v} \quad (5)$$

and the voltage difference between the reservoirs is given by:

$$(-e)V_{21} = (\mu_1 - \mu_2)R \quad (6)$$

for the conductance result:

$$G = \frac{e^2}{\pi \hbar} \frac{T}{R} \quad (7)$$

Landauer's formula has been extended to systems with higher dimensions having many-channels [3-6].

Transport quantities, other than the conductance, in one-dimension wire have also been studied [7-11].

## 2. The single-channel case

In this paper we present the derivation of the single-channel conductance of a one-dimensional circular quantum wire.

An approximation for the description of an electron gas is to neglect all interactions, the Coulomb interaction of the electrons with each other and the interaction of the electrons with the positive background (or the ion lattice). Every electron is then independent of every other and subject only to external force. This approximation is valid for the conduction electrons in monovalent metals and in many semiconductors.

If we neglect all interactions, the Schrödinger equation becomes:

$$-\frac{\hbar^2}{2m} \sum_j \nabla_j^2 \Phi = E\Phi \quad (8)$$

The wave functions  $\Phi$  are appropriate combinations of one-electron wave functions. If also write the energy  $E$  as a sum over one-electron energies  $E_j$ , the relation (8) splits into one-electron equations [12]:

$$-\frac{\hbar^2}{2m} \nabla_j^2 \Phi_{jj} = E_j \Phi_j \quad (9)$$

We can omit the index  $j$  and  $E$  will be the one-electron energy. In the spherical coordinates, the laplacean is:

$$\Delta = \nabla^2 = \frac{1}{r^2} \frac{\partial}{\partial r} \left( r^2 \frac{\partial}{\partial r} \right) + \frac{1}{r^2} \left[ \frac{1}{\sin\theta} \frac{\partial}{\partial \theta} \left( \sin\theta \frac{\partial}{\partial \theta} \right) + \frac{1}{\sin^2\theta} \frac{\partial^2}{\partial \varphi^2} \right] \quad (10)$$

For a circular wire, in  $xOy$  plane, we have:

$$r = \text{const.}, \quad \theta = \frac{\pi}{2} \quad (11)$$

and  $\Delta$  becomes:

$$\Delta = \frac{1}{r^2} \frac{d^2}{d\varphi^2} \quad (12)$$

With the notation:

$$k^2 = \frac{2mE}{\hbar^2} \quad (13)$$

the Schrödinger equation takes the form:

$$\frac{d^2\Phi}{d\varphi^2} + r^2 k^2 \Phi = 0 \quad (14)$$

The solution of the equation is:

$$\Phi(\varphi) = A_1 e^{irk\varphi} + A_2 e^{-irk\varphi} \quad (15)$$

The electron moves in the trigonometrical sense or in the other sense. Thus the solution (15) becomes:

$$\Phi(\varphi) = C e^{irk\varphi} \quad (16)$$

The Born-von Karman periodic boundary conditions is:

$$\Phi(\varphi) = \Phi(\varphi + 2\pi) \quad (17)$$

It follows from this condition that the wave vector of electron takes the following values:

$$k_n = \frac{n}{r}; \quad n = 0, \pm 1, \pm 2, \dots \quad (18)$$

The energy and the velocity of electron are:

$$E_n = \frac{n^2 \hbar^2}{2mr^2} \quad (19)$$

$$v_n = \frac{n\hbar}{mr} \quad (20)$$

From (19) we obtain the density of states for two spin directions:

$$\frac{\partial n}{\partial E} = \frac{mr}{\pi n \hbar^2} \Rightarrow \frac{\partial n}{\partial E} = \frac{1}{\pi \hbar v} \quad (21)$$

Using (6) and (21) in (4) result the conductance of a circular one-dimensional wire:

$$G = \frac{e^2}{\pi \hbar} \frac{T}{R} \quad (22)$$

### 3. The transmission coefficient

In this section, the effects of the transmission coefficient on the conductance are studies.

For example, we have considered a potential barrier described by a Dirac function

$$U(x) = K\delta(x - x_0) \quad (23)$$

In this case

$$T = \frac{1}{1 + \frac{mK^2}{2\hbar^2 E}} \quad (24)$$

If the difference between the quasi-Fermi energies  $\mu_1$  and  $\mu_2$  is chosen to be small enough so that the energy dependence of  $T$  within this range can be neglected, the conductance is

$$G = \frac{2e^2\hbar E}{\pi mK^2} \quad (25)$$

The conductance depends on the opacity of the wall.

If the energy dependence of  $T$  in the range  $(\mu_1 - \mu_2)$  can't be neglected, the current flow is given by

$$I = \frac{e}{\pi\hbar} \int_{\mu_1}^{\mu_2} T(E) dE \quad (26)$$

Result thus

$$I = \frac{e}{\pi\hbar} \left[ (\mu_1 - \mu_2) - \frac{mK^2}{2\hbar^2} \ln \frac{2\hbar^2\mu_1 + mK^2}{2\hbar^2\mu_2 + mK^2} \right] \quad (27)$$

If the wall is almost completely transparent ( $T=0$ ) we find the known relation

$$I = \frac{e}{\pi\hbar} V \quad (28)$$

#### 4. Conclusions

The conductance of a one-dimensional circular wire is the same of a linear one-dimensional wire. The current and the conductance depend on the expression of the transmission coefficient. The conductance depends on the opacity of the wall.

*Received: May 17 2005-05-18*

*The „Gh.Asachi” Technical University from Iasi*

#### REFERENCES

- [1] T.Ando, Y.Arakawa, F.Furuya, S. Komiyama, N. Nakashima, Mesoscopic Physics and Electronics, Springer Series in Materials Science, 1998
- [2] R. Landauer, Philos. Mag., 21, 863, (1970)
- [3] P.W. Anderson, D.J. Thouless, E.Abrahams, and D.S. Fisher, Phys.Rev. B 22, 3519, (1980)

- [4] ] P.W. Anderson, Phys. Rev. B 23, 4828, (1981)
- [5] M.Y. Azbel, J. Phys. C 14, L225, (1981)
- [6] M. Büttiker, Y. Imry, R. Landauer. and S.Pinhas, Phys. Rev. B 31, 6207 (1985)
- [7] U. Sivan and Y. Imry, Phys. Rev. B 33, 551 (1986)
- [8] P. Streda, J. Phys. Condens. Matter 1, 1025 (1989)
- [9] P.N. Butcher, , J. Phys. Condens. Matter 2, 4869, (1990)
- [10] C. Proetto, Phys. Rev. B 44, 9096 (1991)
- [11] Y. Okuyama, T. Sakuma, and N. Tokuda, Surf. Sci. 263, 258 (1992)
- [12] O. Madelung, Introduction to Solid State Theory, Springer, (1978)

### **CURRENTUL INTR-UN FIR CIRCULAR 1D**

#### **(Rezumat)**

Articolul studiaza teoretic o serie de proprietati electrice specifice unui fir circular unidimensional. Se prezinta o noua demonstratie a formulei conductantei pentru un fir unidimensional, in cazul unui singur canal. Din conditia de periodicitate Born-von Karman rezulta valorile pentru functia de unda a electronului, energie si densitate de stari. Apoi s-a calculat curentul total si conductanta. In penultimul paragraf se analizeaza efectul coeficientului de transmisie asupra conductantei.

## NUMERICAL AND EXPERIMENTAL CONTRIBUTION ABOUT THE ELECTRICAL RESISTANCE OF STEELS COVERED WITH DIFFERENT KIND OF METALIC LAYERS

BY

VASILE MANOLE and IOAN ALEXANDRU

**Abstract:** In order to establish the electrical resistivity of the materials a mechanism was built which allows the measurements on short cylindrical tests with the mechanism was conceived using the method of the 4 contacts obtained by studying the spreading of continuum electric field in big conductors. As usual temperature it results values of resistivity which are not influenced by the presence of the layer. This indicates that the spreading of electric field in the massive material remains unchanged. The presence of the coverings influence the variation coefficient of the resistivity with temperature. This result couldn't be linked nor by the values of electric resistivity of the materials, nor by the coefficient of variations of electric resistivity with temperature. This behaviour is given by the ohmic contact of the materials with massif methal.

### 1. Theoretical considerations

The electrical resistance of most of the metals is conditioned essentially by the spreading on the acoustic phonons. In the case of strong degeneration of electrons' gas and considering the detent time on the acoustic phonons, the electrical resistivity of the ideal metal, linked with the temperature can be written as [3]:

$$\rho = 4\rho_0 \left( \frac{T}{\theta_D} \right)^5 J_5 \left( \frac{T}{\theta_D} \right) \quad 1.$$

where  $\rho_0$  is a constant practically independent of temperature, Having the dimension of electrical resistivity,  $\theta_D$  the Debye temperature, and  $J_n(\theta_D)$  represents the Debye-Grüneisen function, which is a table function. At high temperatures ( $\theta_D \ll T$ ), developing the exponential from the function  $J_n$  and maintaining only the first level terms, we obtain, [3]

$$\rho = \rho_0 \frac{T}{\theta_D} \quad 2.$$

meaning the well-known linear dependence. For many metals  $\theta_D$  is of 300 - 400 K and the condition is not respected anymore Considering the superior level terms in developing of the exponential we'll obtain [3],

$$\rho = \rho_0 \frac{T}{\theta_D} \left( 1 - \frac{1}{18} \left( \frac{\theta_D}{T} \right)^2 \right) \quad 3.$$

valid for  $\theta_D \ll 4,23T$ .

When we form a dual alloy AB (solid solution), the electrical resistivity of metal increase, even when the A metal, with high electrical resistivity, is mixed with B

metal with low electrical resistivity [3]. This results appears because the introduction of the foreign atoms, the crystalline network is deformed and the spreading of the electrons increases. In the dual alloys the maximum of the electrical resistivity is obtained to a 50% atoms proportion and can be several times bigger than the compounds. The residual electrical resistivity (the equal value through the electrical resistivity tends during the decrease of temperature due of the spreading on the static imperfections) in the alloy case is described by a law:

$$\rho_R = \text{const} \cdot c(1 - c) \quad 4.$$

Called Nordheim rule, where  $c$  is the concentration. In this way the electrical resistivity of the basis solution of low impurities concentration is given by:

$$\rho = \rho_0 + \rho_R + \Delta\rho \quad 5.$$

where  $\rho_0$  is the electrical resistivity of the basis compound which depends of temperature and increase at the temperature increasing,  $\rho_R \sim c$ , and  $\Delta\rho$  express a subtraction due to the spreading on impurities, being proportional with their concentration.

## 2. Experimental considerations.

In order to establish the electrical resistivity of the materials a mechanism was built which allows the measurements on short cylindrical tests. The mechanism was conceived using the method of the 4 contacts [7], [4], [6], obtained by studying the spreading of continuum electric field in big conductors. When the four contacts are placed on the same line in space to equal distances (Fig.5.1.) on a surface which borders a half infinite volume, then the material's resistivity is given by:

$$\rho = 2\pi s \frac{\Delta U}{I} \quad 6.$$

where  $s$  is the distance between contacts, and 'I' the intensity of the current which past the test,  $\Delta U$  – the difference of voltage measured.

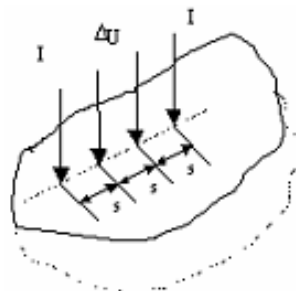


Fig. 1. The principle scheme of disposing the four points

For the surfaces which can't be considered half (6.) doesn't lead to exact results and it is necessary a correction using [1]:

$$\rho = \frac{2\pi s}{C} \frac{\Delta U}{I} \quad 7.$$

The  $c$  correction can be calculated for each situation, considering the placing ways of current and voltage contacts the dimensions of the test and the distances between contacts.



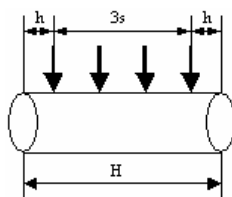


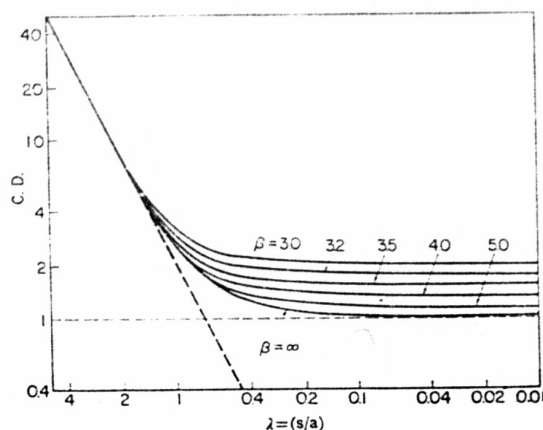
Fig.2. The disposing of the four contacts on the cylindr generatrix

If we consider a cylindr conductor of finite length (Fig.2.), of  $H$  length, having the distance between ends and current contacts  $h$  and  $a$  diametre, the  $C$  correction is given by [6]:

$$C = 2\lambda[\lambda + F(\lambda) - F(2\lambda)] + \sum_{n=1}^{\infty} 2\lambda[F(\lambda(n\beta - 2)) - F(\lambda(n\beta - 1)) - F(\lambda(n\beta + 1)) + F(\lambda(n\beta + 2))] \quad 8.$$

where  $\lambda = s/a$ ,  $\beta = H/s$ , and the marked with  $F$  function has the shape:

$$F(x) = \sum_{n=2}^{\infty} \frac{1}{x_{0n}} e^{-x_{0n}x} + \sum_{n=1}^{\infty} \sum_{k=1}^{\infty} \frac{2x_{kn}}{(x_{kn}^2 - n^2)} e^{-x_{kn}x}$$

Fig.3. The  $C$  correction value in function of  $\lambda$  and  $\beta$ .

where  $x_{kn}$  is the  $n$  order root of equation  $dJ_k(x)/dx = 0$ , and  $J_k(x)$  is the Bessel function of first degree and  $k$  order. In the Fig. 3. is represented the  $C$  correction dependent of  $\lambda$  and  $\beta$ . For high values of  $\lambda$ , the  $C$  can be approximated with enough precision  $2\lambda^2$ . For low values of  $\lambda$ ,  $C$  doesn't depend of  $\lambda$ . If current contacts are placed to the ends of the test ( $\beta = 3$ ), the current distribution at the test's surface is constant, irrespectively of the ray of the cylinder is bigger or smaller and  $C = 2\lambda^2$ .

The cylindrical used tests have the diameter of  $d = 2a = 10$  mm, the length  $H = 215$  mm, and the distance between electrodes  $s = 55$  mm. It results  $\lambda = 5$ ,  $\beta = 3,75$ , and  $C = 42$ . There were analysed tests of steel OLC60, covered with different types of materials: Ag, Cu,  $C_{\text{grafit}}$ , W, Al, Ni.

The imposed values of the intensity of the current were considered in (0-100) A, and the measured voltages between (0 - 0,5) mV.

### 3. Numerical consideration about the spreading of the electric field at settling of electric resistivity using the 4 contacts method.

The spreading of medium electric field of the type used in the previous method described is given by Poisson equation [3],

$$\Delta V = \frac{\rho}{\varepsilon} \quad 9.$$

where  $V$  is the electric voltage,  $\varepsilon$  the electric permittivity of the field, and  $\rho$  the volum density of electric charge-source of the field. Similar with the field of stationary curenrs and electrostatic field in the analysed situation the function  $\rho(\vec{r}, t)$ , in stationary conditions is given by [6]

$$\rho(x, y, z) = Q \cdot \delta(x - x_0) \delta(y - y_0) \delta(z - z_0) \quad 10.$$

where  $(x_0, y_0, z_0)$  are the coordinates of electric charge  $Q$ , given by [10]

$$Q = I \cdot \varepsilon \cdot \rho \quad 11.$$

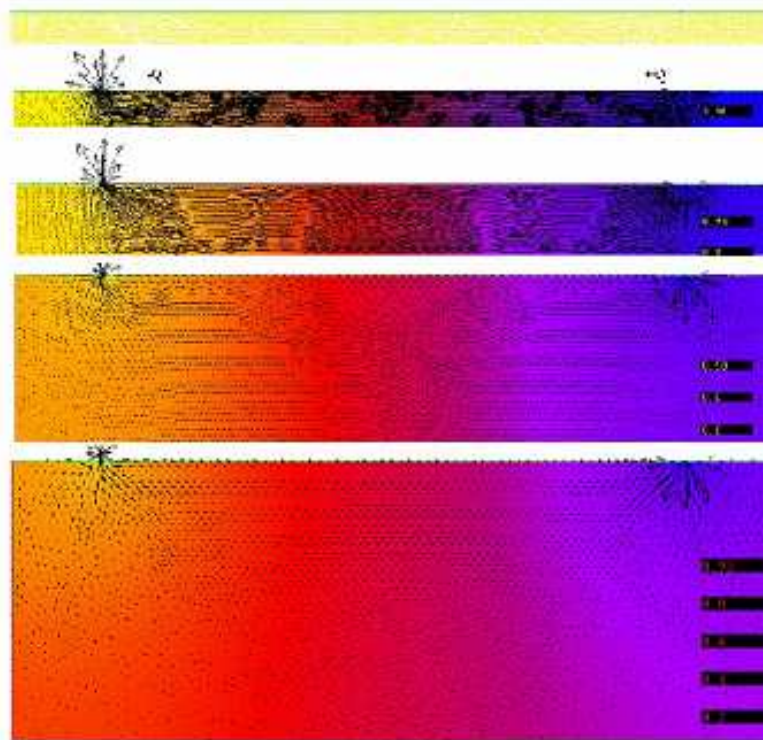


Fig.4.The spreading of electric potential and the intensity of electric field

Next there are presented the results obtained from the numeric key of the equation (9.) on a field of the type used in experimental works, using a method with finite differences. The transformed equation (9.) is discretised using the regressive algorithm Euler [5], [8]. The imposed conditions are linked by the orientation on the edgen of the intensity of electric field,  $\vec{E} = -\nabla V$ ,

$$\vec{n} \cdot \nabla V = 0 \quad 12.$$

where  $\vec{n}$  is the normal on surface. The electric charges  $\pm Q$  were considered on the superior frontier, indicated in (Fig.5.a). The integrate domain (Fig.4.a) is made by 4635 knots and 2236 triangular elements with six knots.

In Fig.4.b-e are depicted the spreading of the electrical potential and the intensity of the electric field for different thicknesses of integration domain (test's diametres),  $d = 10$  mm,  $d = 20$  mm,  $d = 50$  mm,  $d = 100$  mm. We mention by mean of  $\vec{j} = \sigma \vec{E}$ , where  $\sigma$  electric conductivity, the spreading of the intensity vectors of the electric field is equal with the spreading of the curent density vectors,  $\vec{j}$ . In fig.5. is depicted the variation of electric potential along the superior border (the generating line of the cylinder on wich are placed both curent electrodes and voltage electrodes) and for comparison was traced also the potential spreading in the case of half infinite medium. We observe that is real situation, when the contact of curent electrodes is made on a finite surface (the source of the field isn't pointshaped like in ideal case) the discontinuity of the pontential in these regions dissapear. The variation of the thickness of integration domain settle significant changes of the pontential's variation on the analysed border (fig.5.). So, for small diametres of tests ( $d = 10$  mm,  $d = 20$  mm) results a spreading almost linear of the electrical potential on the genereting line of the cylinder, while for big thicknesses ( $d = 50$  mm,  $d = 100$  mm) the function potential tend to the ideal case, for half infinite medium. These results were considered in the finding of electric resistivity using the four contacts method.

#### 4. Experimental results

In fig.6. we present the experimental results obtained from settling of the electric resistivity using the previous described method. It was shown the way by the coverage of the steel with different kind of materials influence the value of the electric resistivity and also the way of variation with the temperature.

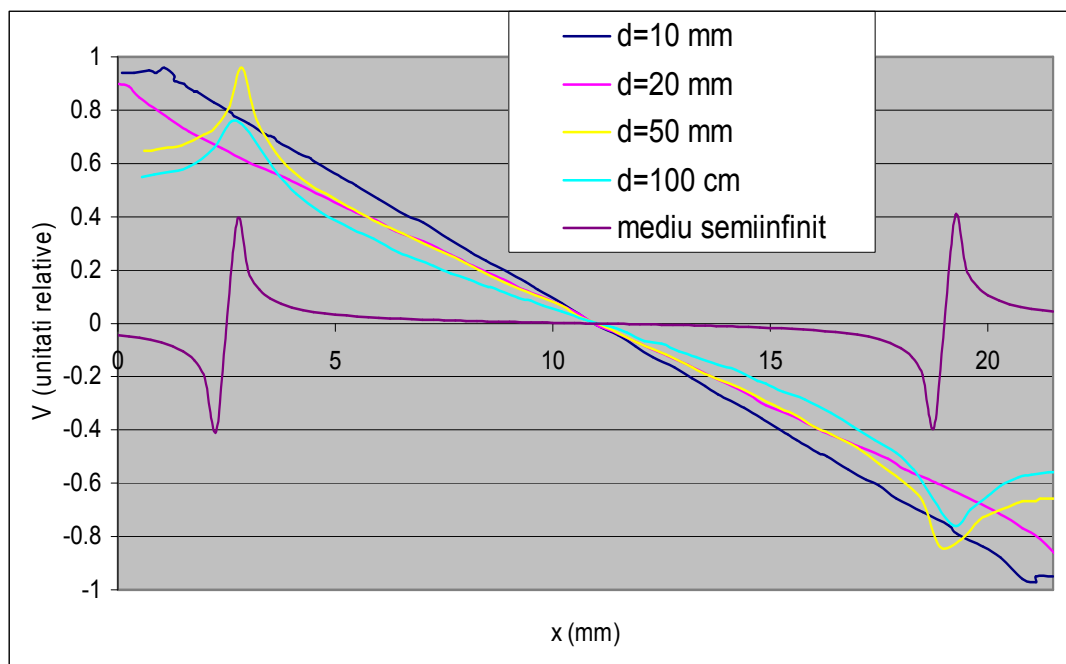


Fig.5. The variation potential on the analysed border depending of thickness variation of the integration domain

As usual temperature it results values of resistivity which are not influenced by the presence of the layer. This indicates that the spreading of electric field in the massive material remains unchanged. If we analyse the aspect of temperature's dependence, we can observe small deviations from the linear dependence (see 2.), in the limit of the measurement errors. Though the presence of the converings influence the variation coefficient of the resistivity with temperature (in fig.6 to see the equations of the lines marked using the methods of the smallest squares). This result couldn't be linked nor by the values of electric resistivity of the materials, nor by the coefficient of variations of electric resistivity with temperature [2]. This behaviour is given by the ohmic contact of the materials with massif methal. The variation of temperature leads to the chaging of the levels Fermi positions in the two materials and so the changing of the difference of contact potential [3], which affects the electric contact resistivity.

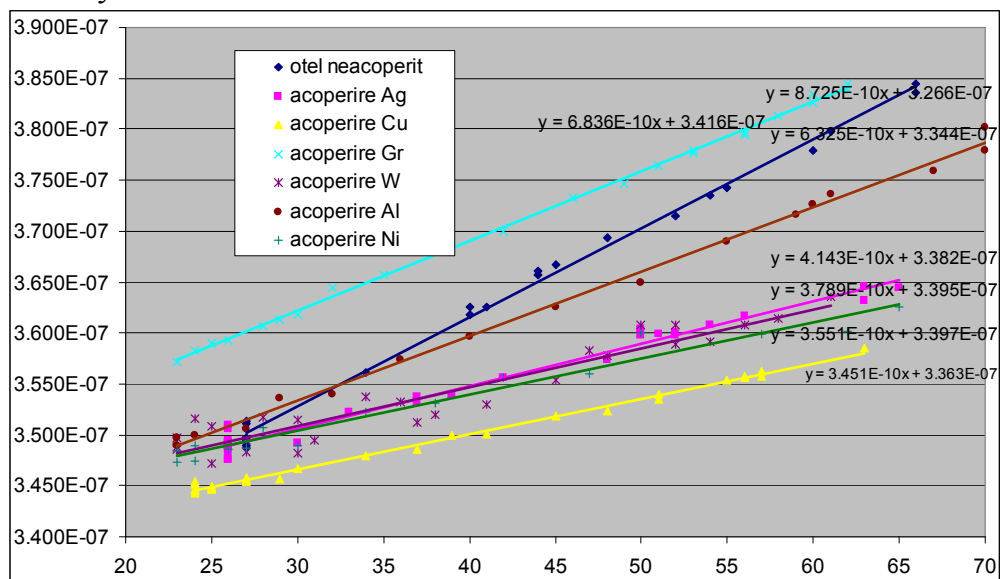


Fig.6. The experimental results obtained in the determination of the electric resistivity

## REFERENCES

1. Bowman F., *Introduction to Elliptic Functions with Applications*, English Univ. Press Ltd, London, 1955. p. 43
2. Brandes E. A., *Smithells Metals Reference Book*, Butterworth. London, 1983.
3. Lica, I. – *Fizică metalelor*, Ed. științifică și Enciclopedică, Bucuresti, 1986.
4. Murashima S., Kanamori H., *Jpn. J. Appl. Phys.*, 9 (1970), p. 58.
5. Shyy W., *Computational Modeling for Fluid Flow and Interfacial Transport*, Amsterdam: Elsevier, 1994.
6. Smits F.M., *Measurement of Sheet Resistivities with the Four Point Probe*, Bell Syst. Tech. J. 37 (1958), p. 711
7. Zet Gh., Ursu D., *Fizică Stării Solide. Aplicatii în inginerie*, Ed. Tehnica, Bucuresti, 1989
8. Zienkiewicz O.C., Taylor R.L., *The Finite Element Method*, McGraw-Hill, 1991.

---

**CONTRIBUȚII NUMERICE ȘI EXPERIMENTALE ASUPRA  
REZISTIVITĂȚII ELECTRICE A OȚELURILOR ACOPERITE  
CU DIVERSE TIPURI DE STRATURI METALICE**

**Rezumat:** Pentru determinarea rezistivității electrice a materialelor elaborate s-a folosit un dispozitiv care permite efectuarea măsurătorilor pe probe cilindrice scurte, ce are la bază metoda celor patru contacte elaborată prin studierea repartiției câmpurilor electrice continue în conductoare masive.

La temperatura camerei rezultă valori ale rezistivității care nu sunt influențate de prezența stratului depus. Aceasta indică faptul că distribuția câmpului electric în materialul masiv rămâne neschimbată.

Prezența acoperirilor influențează coeficientul de variație a rezistivității cu temperatura. Acest rezultat nu a putut fi corelat nici cu valorile rezistivității electrice ale materialelor depuse și nici cu coeficientul de variație a rezistivității electrice a acestora cu temperatura. Acest comportament este dat de contactul ohmic al materialelor de depunere cu metalul masiv.



## THEORETICAL ASPECTS ABOUT PHYSICAL PROCESSES OF TWO METALS CONTACT

BY

VASILE MANOLE and IOAN ALEXANDRU

**Abstract:** After theoretical and practical analysis it resulted then, when 2 metals are in contact there are developing structures of double electrical layers. In my opinion, the solution of the kind of pairs of concentration breathers correspond to the double electrical layer from the surface of contact metal- metal, and the solutions of the kind of concentration layers to the multiple electrical layers. The multiplication of the double electrical layers is made by self arrangement, meaning the generalised coherence.

When 2 metals are in contact there are developing structures of double electrical layers. Because of the great mobility of the electrons and the big difference of contact voltage, the electrons spread. It results a local field which hobbles the electrons' spread and goes off to the appearance of this structure of double layer. Their dynamics is described by this group of coupled equations,

$$\frac{\partial n_1}{\partial t} = D_{a_1} \Delta n_1 - \Gamma_2 n_2, \quad \frac{\partial n_{21}}{\partial t} = D_{a_{21}} \Delta n_2 + \Gamma_1 n_1$$

1.a,b

or using the adimensional parametres

$$\tau = \omega t, \quad \xi = kx, \quad \eta = ky, \quad \alpha_1 = (D_{a_1} k^2 / \omega), \quad \alpha_2 = (D_{a_2} k^2 / \omega), \quad 2.a-$$

i

$$\beta_1 = (\Gamma_1 / \omega), \quad \beta_2 = (\Gamma_2 / \omega), \quad \phi_1 = (n_1 / n_0), \quad \phi_2 = (n_2 / n_0),$$

$$\frac{\partial \phi_1}{\partial \tau} = \alpha_1 \left( \frac{\partial^2}{\partial \xi^2} + \frac{\partial^2}{\partial \eta^2} \right) \phi_1 - \beta_2 \phi_2, \quad \frac{\partial \phi_2}{\partial \tau} = \alpha_2 \left( \frac{\partial^2}{\partial \xi^2} + \frac{\partial^2}{\partial \eta^2} \right) \phi_2 + \beta_1 \phi_1$$

3.a,b

In the previous relations, the used dimensions have customary means from [1].

We'll solve the system 3.a,b using the method of finite differences. So, in the figure 1.a-i are shown numerical solutions for  $\alpha_1 = \alpha_2 = 1/3$ ,  $\beta_1 = 1,9$ ,  $\beta_2 = 1,8$ ,  $\tau = 0 - 2,25$  and the initial condition  $\phi_1(\xi, \eta, 0) \sim \exp[-(\xi^2 + \eta^2)]$ . It results the breather concentration for law sequences of time. We remind you that the breathers are bidimensional dark solitons [3]. In my opinion, the solution of the kind of pairs of concentration breathers correspond to the double electrical layer from the surface of contact metal- metal, and the solutions of the kind of concentration layers to the multiple electrical layers. The multiplication of the double electrical layers is made by self arrangement, meaning the generalised coherence (the relation in amplitude and phase of concentration breathers - for details see [4]).

The process is fractal because the equal spread by polar curves are curves of Koch Type - fig.2 (the fractal dimension of physical object from fig. 2. is  $D_F \approx 1,26$ - for details about fractal dimensions see [2].

Because of the fractal structure of selforganization, meaning the process of developing the double electrical layers, we can apply the theory of scale relativity [4]. So, for a contact surface metal – metal, the wave function of the entire system can be written like a superposition of two iron states, of  $\psi$  amplitude

$$|\psi\rangle = \psi_1|1\rangle + \psi_2|2\rangle \tag{4}$$

where (1) and (2) are the own states corresponding to the 2 metals which compound the contact surface.

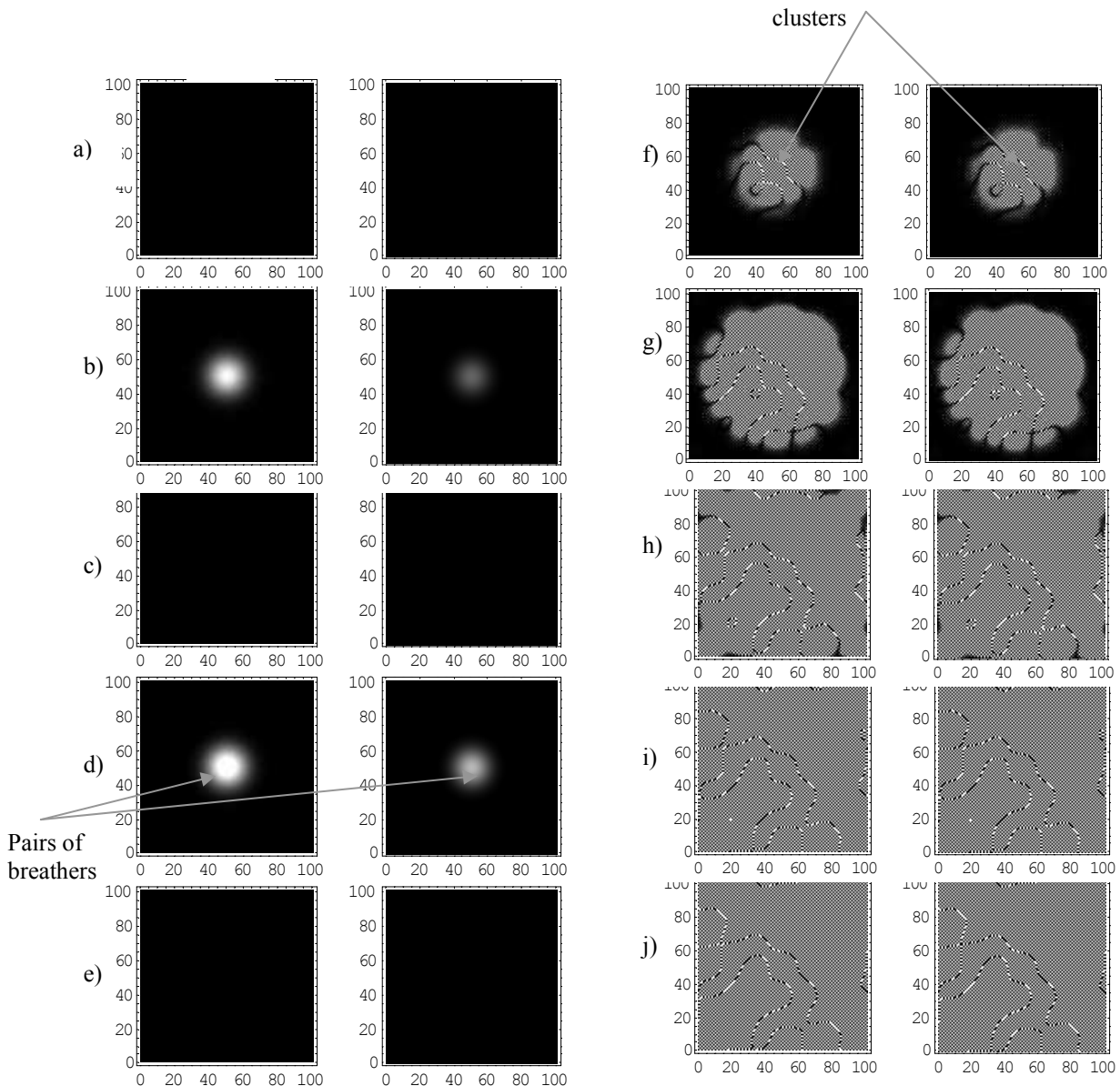


Fig. 1. The solution of the equations system for  $\alpha_S = \alpha_L = 1/3$ ,  $\beta_S = 1.9$ ,  $\beta_L = 1.8$ ,  $\tau(a) = 0 - \tau(j) = 2.25$ ,  $\Delta\tau = 0.25$  and the initial condition  $\phi_L(\xi, \eta, 0) \sim \exp[-(\xi^2 + \eta^2)]$

System's Hamiltonian has the shape

$$H = H_1 + H_2 + H_T \tag{5}$$

where



$$H_1 = E_1|1\rangle\langle 1|, H_2 = E_2|2\rangle\langle 2|, H_T = T(|1\rangle\langle 2| + |2\rangle\langle 1|)$$

6.a-c

and  $H_T$  the hamiltonian corresponding the transition by contact surface.



Fig. 2.: The Koch curves for 1, 2, 3, 4 iteratives

Because

$$2mDi \frac{\partial |\psi\rangle}{\partial t} = H\psi \tag{7}$$

introducing (4.), (5.), in (6.a) we'll have

$$2mDi \frac{\partial \psi_1}{\partial t} = E_1\psi_1 + T\psi_2, \quad 2mDi \frac{\partial \psi_2}{\partial t} = E_2\psi_2 + T\psi_1$$

8.a,b

If there is a voltage  $V$  in interface then

$$E_1 - E_2 = 2qV \tag{9}$$

Imposing the 0 value for the voltage, in the centre of the interface we have

$$E_1 = qV, \quad E_2 = -qV \tag{10}$$

and then (8.a,b) becomes

$$2mDi \frac{\partial \psi_1}{\partial t} = qV\psi_1 + T\psi_2, \quad 2mDi \frac{\partial \psi_2}{\partial t} = -qV\psi_2 + T\psi_1$$

11.a, b

We consider the solution  $\psi = \sqrt{n}e^{i\varphi}$ , meaning

$$\psi_1 = \sqrt{n_1}e^{i\varphi_1}, \quad \psi_2 = \sqrt{n_2}e^{i\varphi_2}$$

12.a,b

and returning at (11.a) we have

$$2mDi \left( \frac{1}{2} \frac{\dot{n}_1}{\sqrt{n_1}} e^{i\varphi_1} + i\sqrt{n_1} e^{i\varphi_1} \dot{\varphi}_1 \right) = qV\sqrt{n_1}e^{i\varphi_1} + T\sqrt{n_2}e^{i\varphi_2} \tag{13}$$

We separate the real by complex parts, meaning

$$-mD \frac{\dot{n}_1}{\sqrt{n_1}} \sin \varphi_1 - 2mD\sqrt{n_1} \cos \varphi_1 \dot{\varphi}_1 = qV\sqrt{n_1} \cos \varphi_1 + T\sqrt{n_2} \cos \varphi_2$$

$$mD \frac{\dot{n}_1}{\sqrt{n_1}} \cos \varphi_1 - 2mD\sqrt{n_1} \sin \varphi_1 \dot{\varphi}_1 = qV\sqrt{n_1} \sin \varphi_1 + T\sqrt{n_2} \sin \varphi_2$$

14.a,b

Solving the equation system, connecting with  $\dot{n}_1$  și  $\dot{\varphi}_1$  we'll obtain:

$$\begin{aligned}\dot{n}_1 &= \frac{T}{mD} \sqrt{n_1 n_2} \sin(\varphi_2 - \varphi_1) \\ \dot{\varphi}_1 &= -\frac{T}{2mD} \sqrt{\frac{n_2}{n_1}} \cos(\varphi_2 - \varphi_1) - \frac{qV}{2mD}\end{aligned}$$

15.a,b

In the same way, from (11.b) results:

$$\begin{aligned}\dot{n}_2 &= -\frac{T}{mD} \sqrt{n_1 n_2} \sin(\varphi_2 - \varphi_1) \\ \dot{\varphi}_2 &= -\frac{T}{2mD} \sqrt{\frac{n_1}{n_2}} \cos(\varphi_2 - \varphi_1) + \frac{qV}{2mD}\end{aligned}$$

16.a,b

So, with  $\varphi = \varphi_1 - \varphi_2$ ,

$$\begin{aligned}\dot{n}_1 = -\dot{n}_2 &= \frac{T}{mD} \sqrt{n_1 n_2} \sin(\varphi_2 - \varphi_1) \\ \dot{\varphi} = \dot{\varphi}_2 - \dot{\varphi}_1 &= \frac{qV}{mD}\end{aligned}$$

17.a,b

The current has the expression:

$$I = q(\dot{n}_1 - \dot{n}_2) = I_M \sin \varphi \quad 18.$$

with

$$I_M = \frac{2T}{mD} \sqrt{n_1 n_2}, \quad \varphi = \varphi_0 + \frac{q}{mD} \int V dt$$

19.a,b

and the potential, by 17.a, 18., 19.a,  $n_1 \approx n_2 = \sqrt{n_1 n_2}$  and the exchange energy:

$$\begin{aligned}W = \int P dt = \int IV dt &= \frac{2T}{q} \sqrt{n_1 n_2} \int \sin \varphi \partial_t \varphi dt = -\frac{2T}{q} \sqrt{n_1 n_2} \cos \varphi \approx \sqrt{n_1 n_2} qV \quad 20. \\ V &\approx V_M \cos \varphi, \quad V_M = -\frac{2T}{q^2}\end{aligned}$$

21.a,b

So, the variation in time of the phase difference and the concentration difference lead in the interface an electric voltage –see (17.b) and also an electric current – see (18.).

In the absence of a voltage in the contact surface, for  $I \leq I_M$ , in the surface contact is generated a continuous electrical current (stationary effect). In the presence of a voltage, the energy given by the electrical field to the pairs electron – ion positive generate in the contact surface electromagnetic waves of pulsation:

$$\omega_n = \frac{qV_n}{nmD}, \quad n=1, 2, 3 \dots$$

22.a,b

that's why the intensity of the current is modified with the same pulsation (unstationary effect). Let's explain this last effect for a voltage:

$$V(t) = V_0 + V_M \cos \omega t \quad 23.$$

It results firstly (19.b), the time dependency of phase difference,

$$\varphi(t) = \varphi_0 + \frac{qV_0}{mD}t + \frac{qV_M}{mD\omega} \sin \omega t \tag{24}$$

and with (18.) the curent:

$$\begin{aligned} I(t) &= I_M \sin\left(\varphi_0 + \frac{qV_0}{mD}t + \frac{qV_M}{mD\omega} \sin \omega t\right) = \\ &= I_M \sum_{n=-\infty}^{n=\infty} (-1)^n J_n\left(\frac{qV_M}{mD\omega}\right) \sin\left[\left(\frac{qV_0}{mD} - n\omega\right)t + \varphi'\right], \quad \varphi' = \text{const.} \end{aligned} \tag{25}$$

where  $J_n$  is the Bessel function of  $n$  order. When the pulsation  $\omega_0 = (qV_0 / mD)$  is equal with a whole multiple of the pulsation  $\omega$ , meaning  $\omega_0 = n\omega$ , the temporal average of  $I(t)$  hasn't the 0 value that's why there is a continous compound of the curent:

From (24.) we'll obtain resonances in continuum curent at the voltage  $V_n = (nmD\omega/q)$  and so negative resistance. Because in practical activities we use sources of continuum curent of high impedance, in stead of resonances, levels of curent will be induced without regions of negative resistance.

The Cantorian structure can be included by admitting some levels also to the harmonics  $V_\nu = \nu(mD\omega/q)$ , where  $\nu$  must be identified with Cantor set [4].

If we have curent densities:

$$\vec{j}_1 = qn_1 \vec{v}_1, \quad \vec{j}_2 = qn_2 \vec{v}_2, \quad \vec{v}_1 = 2D\nabla\varphi_1, \quad \vec{v}_2 = 2D\nabla\varphi_2 \tag{27.a-d}$$

and the continuity equations:

$$\frac{\partial(qn_1)}{\partial t} + \nabla \cdot \vec{j}_1 = 0, \quad \frac{\partial(qn_2)}{\partial t} + \nabla \cdot \vec{j}_2 = 0 \tag{28.a,b}$$

Making the substraction between (28.a,b), and considering (18.), (19.a),  $n_1 \approx n_2 = \sqrt{n_1 n_2}$ , we'll obtain the equation:

$$\Delta\varphi + k_0^2 \sin \varphi = 0, \quad k_0^2 = \frac{T}{mqD^2} \tag{29.a,b}$$

A first integral, using the energy preserving law in the single dimension means:

$$\frac{1}{2} \left(\frac{\partial\varphi}{\partial x}\right)^2 - k_0^2 \cos \varphi = \frac{\dot{\varphi}_0^2}{2} - k_0^2 \cos \varphi_0 \tag{30}$$

and lead to the expression:

$$\left(\frac{\partial\varphi}{\partial x}\right)^2 = 4k_0^2 \left\{ \left[ \left(\frac{\dot{\varphi}_0}{2k_0}\right)^2 + \sin^2\left(\frac{\varphi_0}{2}\right) \right] - \sin^2\left(\frac{\varphi}{2}\right) \right\} \tag{31}$$

We can distinguish two situations: i) For  $(\dot{\varphi}_0 / 2k_0)^2 + \sin^2(\varphi_0 / 2) > 1$ , the solution become:

$$\varphi = \pm \text{sn}[k^{-1}k_0(x - x_0)] \tag{32}$$

where sn is the elyptical function of ordinary sin of Jacobi [10] of  $k$  modul:

$$k^2 = \left[ \left( \frac{\dot{\phi}_0^2}{2k_0} \right)^2 + \sin^2 \left( \frac{\Phi_0}{2} \right) \right]^{-1} \tag{33}$$

In these conditions, the fractale structure of curent:

$$I = \pm I_M \sin[\text{sn}[k^{-1}k_0(x - x_0)]] \tag{34}$$

is given in the Fig. 3.a-k, and that of voltage falling

$$V = V_M \sin[\pm \text{sn}[k^{-1}k_0(x - x_0)]] \tag{35}$$

In Fig. 4.a-k. the results were obtained using the interative envelope of the appropriate functions.

In the particular case  $\left( \frac{\dot{\phi}_0^2}{2k_0} \right)^2 + \sin^2 \left( \frac{\Phi_0}{2} \right) = 1$ , the key has the shape:

$$\varphi = \pm \text{th}[k_0(x - x_0)] \tag{36}$$

So the coherence is obtained by kink (+), and antikink (-) [31].

If  $\left( \frac{\dot{\phi}_0^2}{2k_0} \right)^2 + \sin^2 \left( \frac{\Phi_0}{2} \right) < 1$ , the key, from  $k^2 = \left( \frac{\dot{\phi}_0^2}{2k_0} \right)^2 + \sin^2 \left( \frac{\Phi_0}{2} \right)$  has the expression:

$$\varphi = 2 \arcsin[k \cdot \text{sn}[k_0(x - x_0)]] \tag{37}$$

The fractale structure cab be found in the curent  $I = \pm I_M \sin[2 \arcsin[k \cdot \text{sn}[k_0(x - x_0)]]]$  (Fig. 5.a-k), and also in the voltage  $V = V_M \cos[2 \arcsin[k \cdot \text{sn}[k_0(x - x_0)]]]$  (Fig. 6.a-k), where in the graphic describe were values of the k module between 0 and 1, with periods of 0,1.

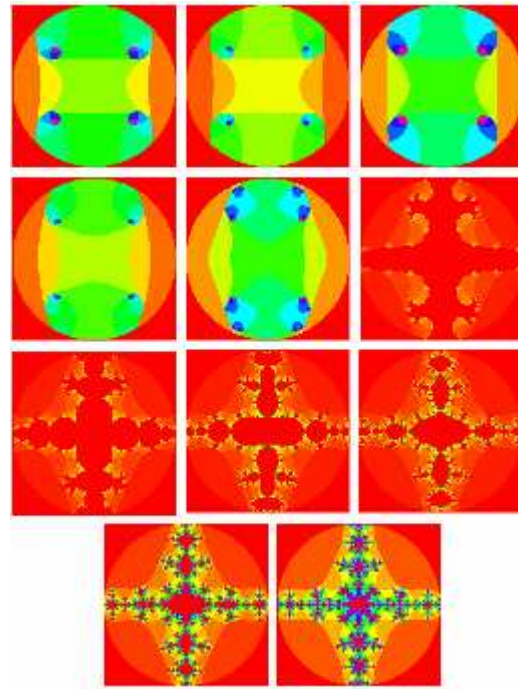
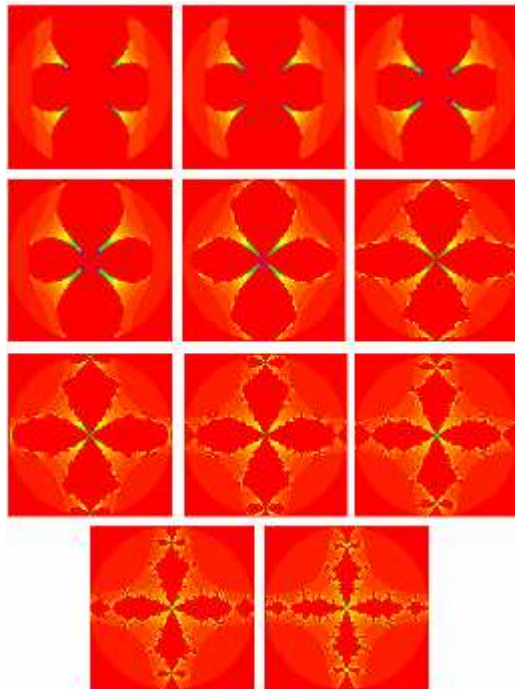


Fig. 3.a-k. The fractale structure of curent

Fig. 4.a-k. The fractale structure of voltage falling

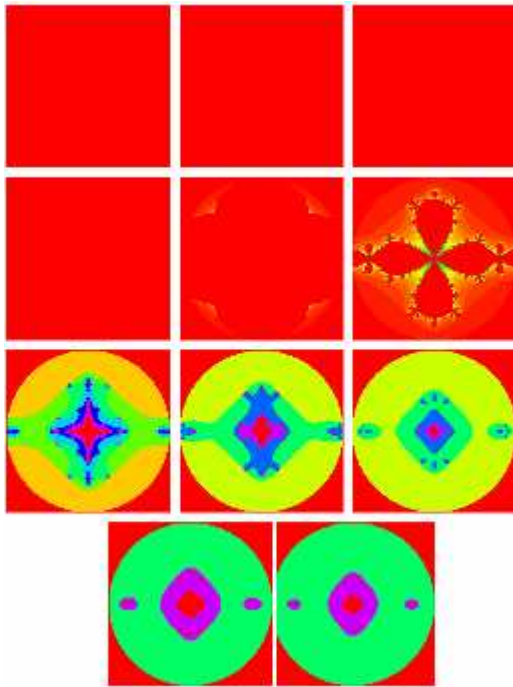


Fig. 5.a-k. The fractale structure of current  
(with  $K = 0-1$  and periods  $0,1$ )

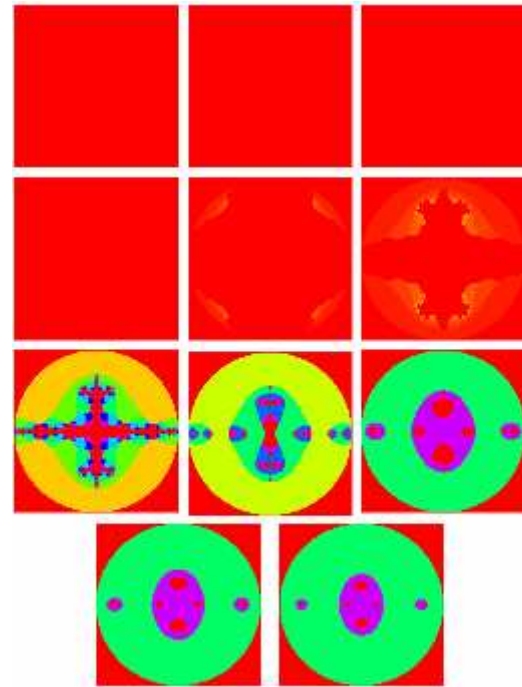


Fig. 6.a-k. The fractale structure of voltage falling  
(with  $K = 0-1$  and periods  $0,1$ )

## REFERENCES

1. Arzamasov B., *Materials Science*, Mir Publisher Moscow, 1989, p. 87.
2. Gouyet J.F., *Physique et Structures Fractales*, Masson, Paris, 1992.
3. Jackson E.A., *Perspectives of Nonlinear Dynamics*, Cambridge Univ Press, vol. I, 1991. p. 272
4. El Naschie M.S., Rössler O.E., Prigogine I., *Quantum Mechanics, Diffusion and Chaotic Fractals*, Oxford, Elsevier, 1995

## ASPECTE TEORETICE ASUPRA PROCESELOR FIZICE DE LA CONTACTUL A DOUĂ METALE

(Rezumat)

În urma analizei teoretice și practice a rezultat că la contactul a două metale se dezvoltă straturi duble electrice. Se pare că soluția de tip perechi de breather-i de concentrație corespunde stratului dublu electric de la interfața metal-metal, iar soluția de tip clusteri de concentrație straturilor multiple electrice. Generarea și multiplicarea straturilor duble electrice se realizează prin autoorganizare, adică prin coerența generalizată.



## UHMWPE ACETABULAR CUP WEAR BY VISCO-ELASTO-PLASTIC DEFORMATION

BY

**\*\*FLORIN MUNTEANU, \*MIHAI GAFIȚANU and \*\*PAUL BOTEZ**

**Abstract:** Atkinson (1995) observed experimentally that there isn't a straight relation between the mass and the volume of the material removed by the wear. Another way, in function of the removed material's mass results a smaller volume consequently a smaller depth of penetration that results from the measurements.

As we know from the recent studies, the UHMWPE has a visco-elasto-plastic behavior but it is specified only the polyethylene's creep behavior, unless the evaluation of the great importance of this behavior of late elasticity for the calculation of the depth of penetration. This work tries to demonstrate the fact that there is a component of the wear by deformation, which influence directly the visco-elasto-plastic behavior of the polyethylene with a big molecular mass.

**Keywords:** total hip implants, wear, penetration depth, visco-elasto-plastic behavior

### 1 - Introduction

This work tries to demonstrate the fact that there is a component of the wear by deformation, which influence directly the visco-elasto-plastic behavior of the polyethylene with a big molecular mass.

As it results from our own studies and the specialized literature [1, 2, 3, 5], the surface, which has a bigger degree of the wear, (in fact, a bigger penetration dept) is very smooth.

The phenomena is owed to plastically deformation of the polyethylene asperity's peaks, another way, maintaining constant the maximal level of the characteristic roughness for the UHMWPE's surface or a small variation of it, which medium is the value of the functional roughness.

Maintaining the value of the roughness between certain limits could be described this way: in the process of the wear it is noticed a growing of the maximum roughness value till the value for which the real pressure is bigger than the flow pressure. In this case, the asperity's peaks are plastically deformation till the value of the real pressure is equal to the elastic's limit of UHMWPE.

There is an elastic deformation but in the same time it appears a removal of the material by adhesive wear, (owed to the smaller value of the roughness), which will increase the maximal roughness.

The phenomena's is quite periodical repetition, leading finally to a supplementary dept of penetration considering the one, which was produced by the material's removal and of course, to maintaining a smaller roughness in the region of maximum penetration (contact area).

## 2 - Calculation of the dept of penetration owed to roughness deformation

For determination of the surface of UHMWPE maxim roughness variation, it is determinates the real pressure -  $p_r$  and after that, the limits for the pressure progress:

$$p_r = \frac{\bar{R}}{\eta \cdot A_n} \quad (1)$$

where:  $\bar{R} = 1015$  N average load by a gait cycles;

$A_n = \pi \cdot a^2 = \pi \cdot 13,690965^2 = 588,868$  mm<sup>2</sup> – nominal contact area;

$\eta = \frac{A_r}{A_n}$  - dimensionless real area:

$$\eta = \frac{b \cdot \nu}{d \cdot \nu - d - 1} \cdot \frac{L^2}{R \cdot (R_{\max O} + R_{\max P})} \cdot \left[ \left( \frac{D}{R_{\max O} + R_{\max P}} \right)^{\frac{1}{d}} \cdot p_0 \right]^{\nu-1}$$

where:  $D = (R_{\max O} + R_{\max P}) \cdot \left( k_\nu \cdot \frac{1}{b} \right)^{\frac{1}{\nu}} \cdot \left( \frac{1}{\Delta_r} \right)^{\frac{d}{2}} \cdot \left( \frac{1 - \nu_c^2}{E_c} \right)^d$

$$k_\nu = \frac{\nu_1 \cdot \nu_2 \cdot \Gamma(\nu_1) \cdot \Gamma(\nu_2)}{(\nu_1 + \nu_2) \cdot \Gamma(\nu_1 + \nu_2)} \quad d = \frac{2}{2 \cdot \nu + 1} \quad \Delta_r = \frac{R_{\max O} + R_{\max P}}{R \cdot b^\nu}$$

$E_c = 1400$  MPa – elasticity modulus și  $\nu_c = 0,3$  – UHMWPE Poisson coefficient

In this preview relation's  $b$  and  $\nu$  are the curve lift parameters:

$$b = b_1 + b_2 \quad \text{and} \quad \nu = \nu_1 + \nu_2.$$

In case of steel where  $R_a = 0,02$ ,  $\nu_1 = 0,9$ ,  $b_1 = 1$ , and for UHMWPE  $\nu_2 = 3$ ,  $b_2 = 3,5$  [6, 14]. The values of curve lift parameters are:  $b = 4,5$  and  $\nu = 3,9$ .

$$R - \text{roughness average curvature radius: } R = \frac{R_1 \cdot R_2}{R_1 + R_2}$$

where by consider [7]  $R_1 = 45$  μm (steel) and  $R_2 = 35$  μm (polyethylene), consequently  $R = 19,687$  μm.

$R_{\max}$  - maximum roughness defined:  $R_{\max} = R_{\max O} + R_{\max P}$

By consider [8],  $R_{\max O} = 0,08$  μm (steel) and  $R_{\max P} = 0,52$  μm, so  $R_{\max} = 0,6$  μm.

$L$  – specific length,  $p_0$  – maximum hertzian pressure.

It is considered that real pressure evolutes between the elasticity limit  $\sigma_e = 16,5$  MPa and the flow limit  $\sigma_c = 22$  MPa [8]. Also it is considered that the only parameter which varies in the real pressure expression is the  $R_{\max P}$ , such is mentioned in [5, 9, 10, 11, 12], the roughness of the femoral head remain approximate constant all the function period, growing 10% in 15-20 years.

On determine  $R_{\max P}$  for two limits of real pressure,  $p_{r1} = c \cdot \sigma_e = 49,5$  MPa

respective  $p_{r2} = c \cdot \sigma_c = 66$  MPa, ( $c = 3$  [7]):  $c = \frac{A_u \cdot b \cdot \nu}{\pi \cdot R \cdot R_{\max} \cdot n_a}$   $n_a$  – number of

contact asperities,  $A_u$  – contact area = wear area.



$$R_{\max P1}|_{pr1} = 5,12778 \cdot 10^{-4} \text{ mm} \quad R_{\max P2}|_{pr2} = 5,631532 \cdot 10^{-5} \text{ mm}$$

The evolution of the maximal roughness: when their value is maximal,  $p_{r2} = c \cdot \sigma_c = 66 \text{ MPa}$ , is deformed till the real pressure is the same with the elastic limit and after that the value of the maximal roughness is growing because of the remained material till the critical value of the real pressure.

In this condition, the maximum roughness expression for UHMWPE surface is:

$$R_{\max P}(t) = \begin{cases} R_{\max P1} + H(t) & p_{r1} \leq p_r < p_{r2} \\ R_{\max P2} + H(t) - \delta & p_r = p_{r2} \end{cases} \quad (2)$$

where:  $H(t)$  – removed material depth:  $H(t) = \frac{V(t)}{A_u}$ ,  $V(t)$  – removed material volume;  $A_u$  – calotte wear area:  $A_u = 2 \cdot \pi \cdot r_u \cdot h \cdot \frac{h + 2 \cdot r_c}{2 \cdot (h + r_c - r_u)}$ ,  $h = 0,090184$ ;  $r_c = 16.1 \text{ mm}$ ;  $r_u = 16 \text{ mm}$ ,  $\delta = \varepsilon \cdot R_{\max P2}$  – plastic roughness deformation, and  $\varepsilon$  specific deformation  $\varepsilon$ .

**Remarks.** The variation of the maximal roughness of the polyethylene surface represented in figure 1 is practically theoretic because in reality, periodicity is due to the dimensions of the polyethylene particles and could vary between with  $10^{-5} \text{ mm}$  (in slow wear regime) till  $0.5 \text{ mm}$  (in fast wear at the end of time of functioning the prosthesis) [13].

Considering the polyethylene's maximal limits and the period of time when we have the deformation (24000s), it is calculated total deformation  $h_d$  for the maximal roughness of the UHMWPE surface for a period of time of  $1,7 \cdot 10^6 \text{ s}$ :

$$h_d = (R_{\max P2} - R_{\max P1}) \cdot \frac{1,7 \cdot 10^6}{2,4 \cdot 10^4} = 0,003566 \text{ mm} \quad (3)$$

This value is summed with penetration depth due to the removed material for the same time interval.

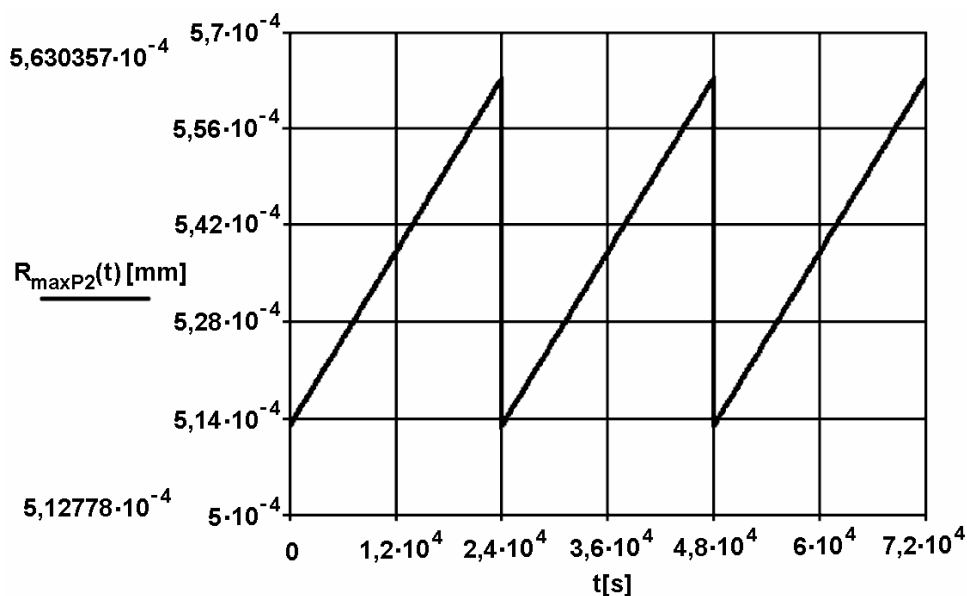


Fig. 1. Maximum roughness variation of UHMWPE

### 3 - Calculation of dept of penetration owed to the viscoelastic behavior of UHMWPE

Applying a force, it appears a late deformation with a exponential evolution (creep) and removing the force, it is also a exponential curve of the coming back (relaxing). Behind this process, de deformed dimension of the polyethylene doesn't come back the initial form, remaining a remnant deformation. The creep time hasn't the same value with the relaxing time [4], as also Abrahams, in 2000, confirmed experimentally:  $\theta_f = 9400$  (creep time),  $\theta_r = 13700$ (relaxation time). The evolution of the deformation, for the two cases, considering that the fluency take place between  $[0, t_1]$  and relaxation between  $[t_1, t_2]$  :

$$\delta_f(t) = \delta_m \cdot \left( 1 - e^{-\frac{t}{\theta_f}} \right) \quad \delta_r(t) = \delta_f(t_1) \cdot e^{-\frac{-t+t_1}{\theta_r}} \quad (4)$$

where  $\delta_m$  - deformation average for a gait cycle:

$$\delta_m = \left( \frac{3 \cdot \bar{R}(t) \cdot \zeta}{E'} \right)^{\frac{2}{3}} \cdot \frac{1}{2 \cdot \zeta} = 0,03638 \text{ mm} \quad \text{cu} \quad \bar{R}(t) = 1015 \text{ N} \quad (\text{average load}),$$

$E' = 3056,546 \text{ MPa}$  (equivalent elasticity module),  $\zeta = 2576 \text{ mm}$  (equivalent contact radius ball on flat).

Calculation of remnant deformation is for a 24 hours period (86400s) because it is considered that a patient's activity is the same for each day, excepting the weekends, so that it is considered a medium activity of 4500 steps/day. For 355 days it was tested the method, for 1,5 hours/day (5400s), for obtaining the 1700000s for a year.

In 24 h, the deformation for the same conditions, is:

$$h_{ve}(t) = \delta_m \cdot \left( 1 - e^{-\frac{t}{9400}} \right) + \delta_f(5400) \cdot e^{-\frac{-t+5400}{13700}} \quad (5)$$

where creep deformation act in a time interval  $[0, 5400\text{s}]$  and relaxation deformation act in a time interval  $[5401, 86400\text{s}]$ , so:  $h_{ve}(86400) = 8,91 \cdot 10^{-6} \text{ mm}$ . For the entire period the remnant deformation is:  $h_{veT} = h_{ve}(86400) \cdot 315 = 0,003566 \text{ mm}$ . The viscoelastic deformation for 24h is illustrated in fig. 2.

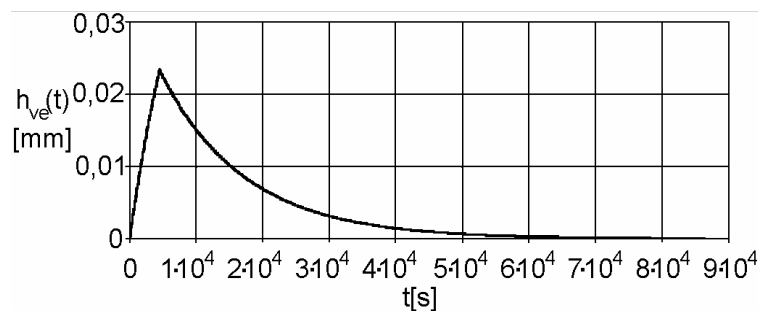


Fig. 2. The viscoelastic deformation for 24h in laboratory condition

It is interesting to know what happen if the charging interval is divided in two or three periods.

- The interval of loaning is divided in two parts, the relation of viscoelastic deformation is:

$$h_{ve}(t) = \delta_m \cdot \left(1 - e^{\frac{-t}{9400}}\right) + \delta_f(t_1) \cdot e^{\frac{-t+t_1}{13700}} + \delta_r(t_2) \cdot \left(2 - e^{\frac{-t+t_2}{9400}}\right) + \delta_f(t_3) \cdot e^{\frac{-t+t_3}{13700}} \quad (6)$$

Considering this time, that for an interval of 24h, the patient makes 4500 steps, the total value of the remnant deformation is for 365 days. This situation,  $t_1 = 3000s$ , the first interval is  $[0, 3000s]$ ,  $t_2 = 20000s$ , the unloading interval is  $[3001, 20000s]$ ,  $t_3 = 21500s$  the second loading interval is  $[21501, 86400s]$ , followed by the last unloading interval of  $[21501, 86400s]$ .

For one day, the remnant deformation is (fig. 3):  $h_{ve}(86400) = 5,49 \cdot 10^{-6} \text{ mm}$ , for the whole year, the remnant deformation is:  $h_{veT} = h_{ve}(86400) \cdot 365 = 0,002808 \text{ mm}$

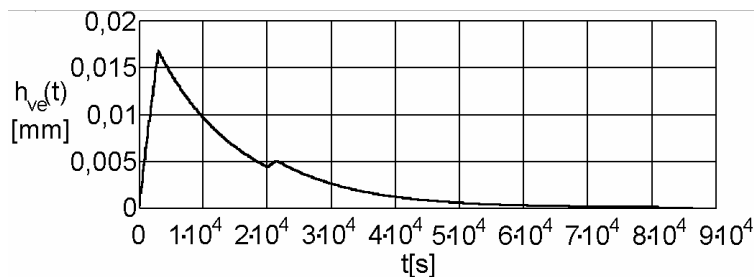


Fig. 3. Variation of the viscoelastic deformation in case of divided interval of loaning in two parts: a bigger one and a smaller one

- For the second situation,  $t_1 = 1000s$ , the first interval of loading is  $[0, 1000s]$ ,  $t_2 = 20000s$  the unloading interval is  $[1001, 20000s]$ ,  $t_3 = 23500s$  the second loading interval is  $[23501, 86400s]$ , followed by the unloading interval of  $[23501, 86400s]$ .

This case, the remnant deformation for one day is (fig. 4):  $h_{ve}(86400) = 2,41 \cdot 10^{-6} \text{ mm}$  and for the whole year the remnant deformation is:  $h_{veT} = h_{ve}(86400) \cdot 365 = 8,82 \cdot 10^{-4} \text{ mm}$ .

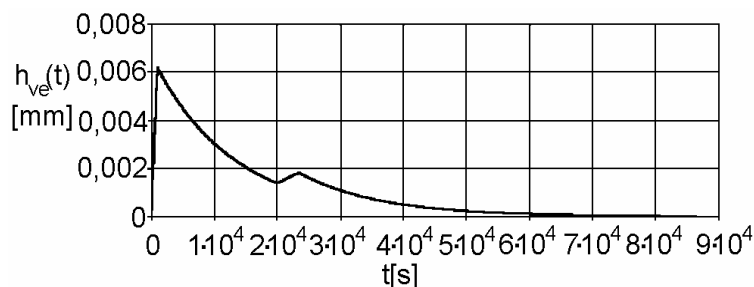


Fig. 4. Variation of the viscoelastic deformation in case of divided interval of loaning in two parts: a smaller one and a bigger one

- The interval of loading is divided in three parts. This case, the loaning interval is divided in three equal parts of 1500s, and for  $t_1 = 1500s$ , the first loading interval is  $[0, 1500s]$ , for  $t_2 = 10000s$ , the unloading interval is  $[1501, 10000s]$ , for  $t_3 = 11500s$  the second loading interval is  $[10001, 11500s]$ ,  $t_4 = 20000s$ , the second loading interval is

[11501, 20000s],  $t_5 = 21500$ s the third loading interval is [20001, 21500], and the last unloading interval is [21501, 86400s].

The viscoelastic deformation in this case is:

$$h_{ve}(t) = \delta_m \cdot \left( 1 - e^{\frac{-t}{9400}} \right) + \delta_f(t_1) \cdot e^{\frac{-t+t_1}{13700}} + \delta_r(t_2) \cdot \left( 2 - e^{\frac{-t+t_2}{9400}} \right) + \delta_f(t_3) \cdot e^{\frac{-t+t_3}{13700}} + \delta_r(t_4) \cdot \left( 2 - e^{\frac{-t+t_4}{9400}} \right) + \delta_f(t_5) \cdot e^{\frac{-t+t_5}{13700}} \quad (7)$$

The remnant deformation for one day, in case when the interval of loading is divided in three parts is (fig. 5):  $h_{ve}(86400) = 0$  mm, and for one year total remnant deformation is:  $h_{veT} = h_{ve}(86400) \cdot 365 = 0$  mm

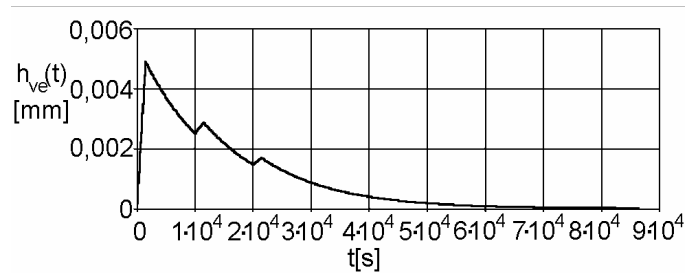


Fig. 5. The representation of viscoelastic deformation for the situation when the interval of loading is divided in three equal parts.

#### 4 - Discussion

As it was demonstrated, we can conclude that the regime of function for the prosthesis, imposed by the patient, has a real importance.

Form calculations, results that he value of the remnant deformation depends of the first loading interval. For a difference of the first loading interval of 2000s, (0,55h), for the situation when this interval was divided in two parts, it appears a remnant deformation, corresponding for an year of functioning, of 0,0061mm, so, it is a smaller remnant deformation for a smaller loading interval. Also, it is observed that for more than two small intervals of pause between the loading intervals, the remnant deformation is null. This fact is very important for the professional reintegration of the patient after the surgery intervention.

#### 5 - Conclusions

As it was calculated and measured before, we can conclude that the massic wear is smaller than the volume wear, fact owed to the plastically deformations of the roughness' picks and to the remnant deformations by late elasticity.

As result of laboratory testing, we conclude that the dept of penetration has three components; the first which corresponds to the volume of the removed material and which has the biggest percent from the total dept of penetration – 93,3%, the second which is owed to the plastically deformations from the level of roughness' picks, 3,69% and the third, as a result of viscoelastic remnant deformations, 3,01%.

As we mentioned before, the remnant deformations depend on the functionary regime of the prosthesis: even if is no a relative movement between the surfaces of the prosthesis articulations, this deformations are still produced, growing the total dept of penetration and consequently, the volume of wear material.

As a medical suggestion for the patient with a prosthesis is not only avoiding the excessive loading of the articulation by a big mass of the patient – it is contraindicated the obesity but also the reduction of the walking activity, as also avoiding standing very much for a long period of time. It is very important the professional reconversion, which costs, is smaller than a revision surgery (prosthesis reimplantation).

Received March 5<sup>th</sup> 2005

\* Technical University of Iassy

Faculty of Mechanics

\*\* University of Medicine and

Pharmacy „Gr. T. Popa” Iassy

Faculty of Medical Bioengineering

## REFERENCES

1. Abrahams N., Goldsmith A. A., Nicol A. C. *An investigation into the permanent deformation of UHMWPE acetabular cups* **12<sup>th</sup> Conference of the European Society of Biomechanics**, Dublin, 2000, 226;
2. Atkinson J. R. et. al. *Laboratory Wear Tests and Clinical Observation of the Penetration of Femoral Heads into Acetabular Cups in Total Replacement Hip II: A Microscopical Study of the Surfaces of Chamley Polyethylene Acetabular Sockets* – **WEAR** No. 104, 1995, 217-224;
3. Atkinson J. R. et. al. *Laboratory Wear Tests and Clinical Observation of the Penetration of Femoral Heads into Acetabular Cups in Total Replacement Hip III: The Measurements of Intemal Volume Changes in Explanted Charnley Sockets after 2 - 16 Years in Vivo and the Determination of Wear Factors* **WEAR** No. 104, 1995 225-244;
4. Moore F. D. *Viscoelastic Machine Elements, Elastomers and Lubricants in Machine Systems* **Butterworth-Heinemman Ltd. Linacre House OXFORD-0X2 8DP** 1993;
5. Wang A., Essner A., Polineni V. K., Sun D., Stark C., Dumbleton J. H. - *Lubrication and wear of ultra-high weight polyethylene in total joint replacements* - **Plenary and Invited Papers from The First World Tribology Congress** - London - 8 ÷ 12 sept. – 1997;
6. Pavelescu D. - *Tribotehnica* - **Editura Tehnica** - București – 1983;
7. Tudor A. - *Contactul real al suprafețelor de frecare* - **Editura Academiei** – 1990;
8. Jin Z. M., Dowson D. – *Analysis of fluid lubrication in artificial hip joint replacements* – **Proc. Instn. Mech. Engrs.** 1997, Vol. 211, Part II, (p 247 - 256);
9. Barbour P. M., Stone M. H., Fisher J. – *A hip joint simulator study, using simplified loading and motion cycles generating physiological wear paths and rates* – **Journal of Engineering in Medicine**, 213, 1999, (p 455 - 467);
10. Franek F, Pauschitz A., Kelman P. - *Tribologiscles System des Huftgelenkes Simulationsversuche und Ubertragungsmaglichkeiten* - **Proc. of 10<sup>th</sup> Intemational Colloquim, Technische Akademie Esslingen** - 1996 (p. 1495 - 1504);
11. Teoh S. H., Chan W. H., Thampuran R. – *An elasto-plastic finite element for polyethylene wear in total hip arthroplasty* – **Journal of Biomechanics**, issue 35, 2002, (p 323 - 330);
12. Wilmann G. - *Reibungs und Verschlei fragen Keramischer Werkstoffe fur Kunstliche Gelenke* - **Proc. of 10<sup>th</sup> Intemational Colloquim, Technische Akademie Esslingen** -1996 (p. 1505 - 1518);
13. Cates H. E., Faris P. M., Keating E. M. – *Polyethylene wear in cemented metal backed acetabular cups* – **Journal of bone and Joint Surgery**, 75B, 1999, (p 249 - 253);
14. Bajaria H., Bellare A. – *Deformation, Morphology and Wear Behaviour of polyethylene Used in Orthopaedic Implants* – **Medical Plastics and Biomaterials**, March, 1998, (p 132 - 141);

**UZURA PRIN DEFORMARE VÂSCO-ELASTO-PLASTICĂ A UNEI CUPE COTILOIDE DIN UHMWPE DE LA NIVELUL UNEI ENDOPROTEZE TOTALE DE ȘOLD**

**Rezumat:** Din observațiile experimentale ale lui Atkinson (1995), rezultă faptul că nu există o corelație directă între masa și volumul de material îndepărtat prin uzură. Altfel spus, conform masei de material îndepărtat rezultă un volum și, implicit, o adâncime de penetrare mai mici decât volumul măsurat. Studiile de la nivel mondial iau, în ultimul timp, în considerație faptul că UHMWPE are o comportare vâscoelastoplastică fiind amintit, numai, comportamentul la fluaj al polietilenei fără însă a se face o evaluare a importanței acestui comportament de elasticitate întârziată în calculul adâncimii de penetrare. În această lucrare se încearcă demonstrarea existenței unei componente a uzurii prin deformare, ce este strâns legată de comportamentul vâscoelastoplastic al polietilenei cu greutate moleculară mare.

## REJECTION POTENTIALLY DEFECTIVE KMOS CJ.

BY

POPO R.A

**Abstract:** In work some measures of increase of operational reliability of microcircuits at stages of manufacture and operation are considered {examined}.

**Keywords:**

### *1. Influence of gamma irradiation and annealing on criterial parameters CJ 564JE5.*

On the algorithm submitted on fig. 1. Results on change criterials parameters have shown, that the most changing parameter at an irradiation is the current of consumption, and, it {he} grows almost by the order more at potentially defective and defective CJ. However, at room temperature there is a fast recession of values with gradual returning to reference values after an exhibitor. From the analysis of experimental results it is possible to draw the following conclusions:

1) Measurement of values of a current of consumption CJ 564JE5 during 1 ч after an irradiation a doze 105 P allows to classify them on suitable and a marriage {spoilage} (to suitable CJ at what the current of consumption does not exceed shop norm - 60HA concern);

2) Relative changes on other parameters it is less, than on a current of consumption (though values are higher);

3) At room temperature in day of return to reference values of parameters it is not observed;

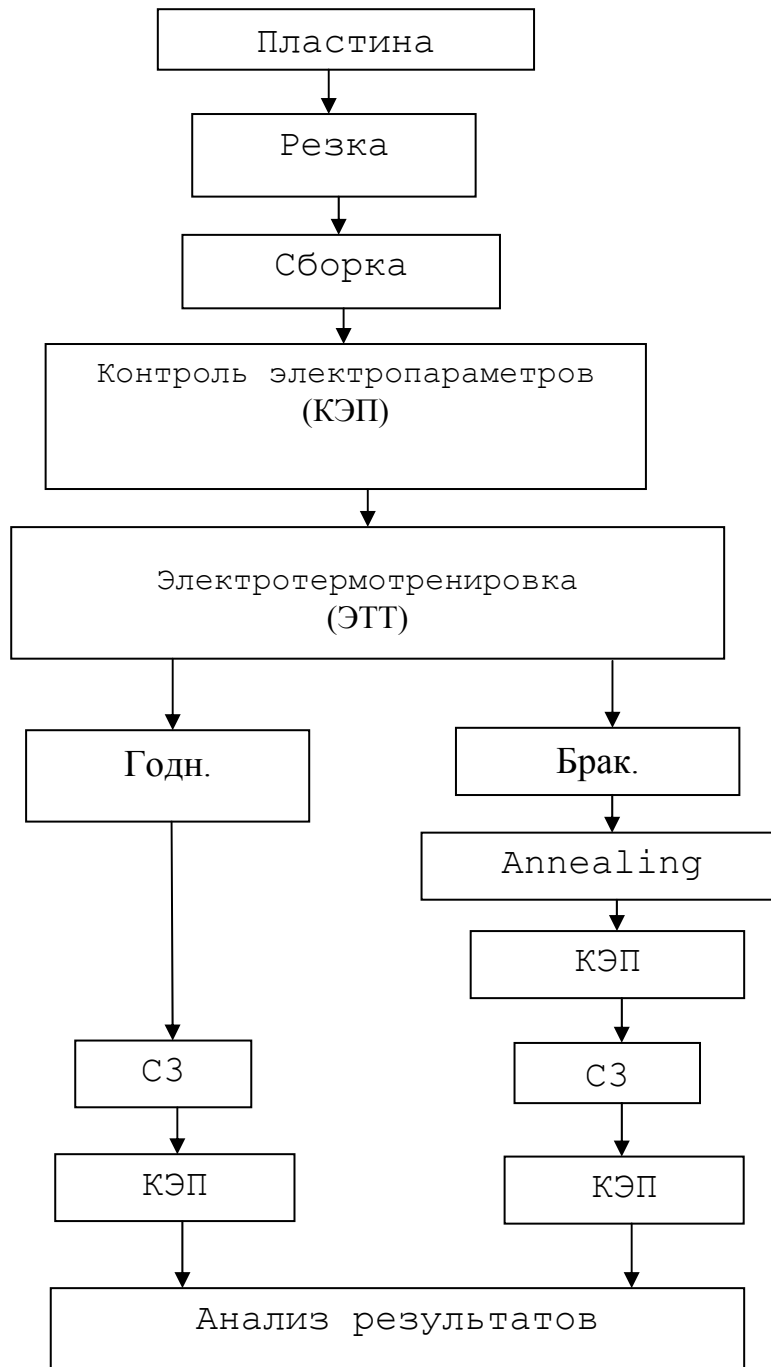
4) annealing at temperature 150□1800C within several hours does not return all parameters to reference values while annealing at 3500 With during 0,5-1 ч returns all parameters to reference values (including at defective).

The accelerated tests investigated CJ at temperature 1250 With and a pulse feed {meal} within 1 month have shown, that their parameters have remained within the limits of norms THAT.

### *2. Rejection potentially defective CJ on plates.*

Rejection potentially defective CJ on plates after an irradiation is more expedient. However, it for today represents some industrial difficulties connected to necessity of the control of parameters of structures within several hours - day. At a plenty of plates it is possible to use the express train of sample, but it reduces reliability of rejection.

Fig 1. Algorithm of carrying out of research on influence of an irradiation on electro parameters CJ.



The researches which have been lead{which have been carried out} on algorithm, submitted on fig. 2, have shown, that after ЭТТ and the subsequent gamma irradiation relative changes of a current of consumption are much higher (2118 % - 1 part, 1192 % - 2 part, 1290 than % - 3 part), than without carrying out ЭТТ (parts 2 and 3) while relative changes of a target current of a high level differ on 3,3 % (45,9 % - for 1 part, 49,2 % - for 3 parts). annealing CJ within 0,5-1 hours at temperature 3500C returns parameters to reference values, but after carrying out again ЭТТ the current of consumption grows at potentially defective CJ more.



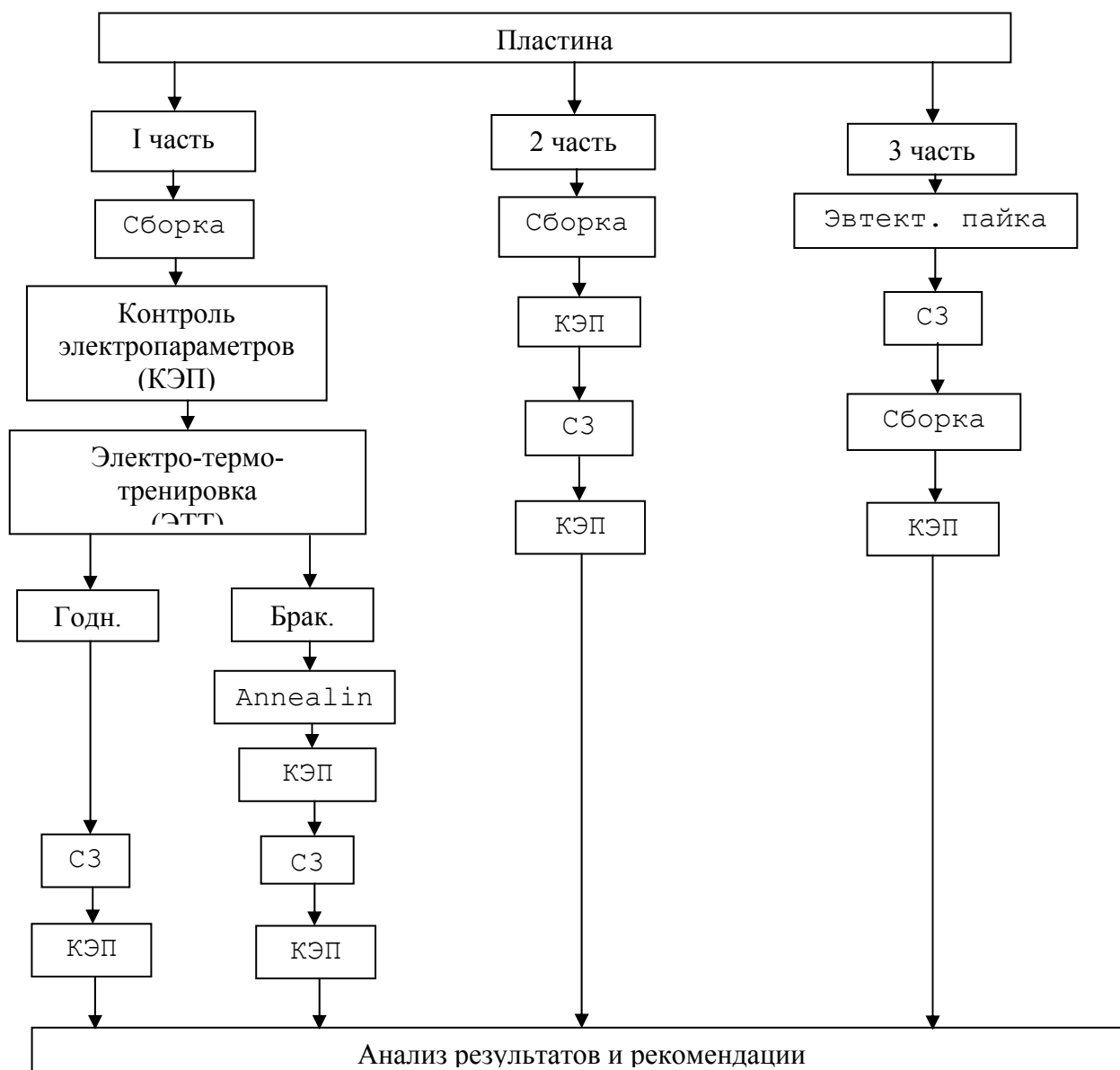


Fig. 2. Algorithm of carrying out of the comparative researches CJ made of one plate

Annealing within 3 day at temperature 1500C reduces values of a current of consumption (after ЭТТ were checked once again) up to reference values of effective articles. It means, that hour annealinga at temperature 3500C for investigated CJ was insufficiently for full restoration of parameters (system oxide - silicon remains unstable). It is possible to assume, that assembly CJ (landing {planting} on эвтектику in the investigated case, hermetic sealing) results in mechanical pressure {voltage} of a crystal which are added to internal pressure {voltage} in oxide and on border oxide silicon.

These pressure {voltage} are shown at temperature processings and gamma irradiation on changes of parameters. Gamma irradiation promotes display and deeper levels, and temperature annealing-to display and finer.

As a result of gamma irradiation and annealing there is an improvement of structure for one part of crystals and deterioration - for another which is potentially defective.

So:

1) Rejection potentially defective CJ can be carried out {be spent} with the help of gamma irradiation and annealing and better her {it} to do {make} on plates;

2) The temperature mode of manufacturing подзатворного oxide and the subsequent operations of manufacturing CJ should be supervised well that it was as small as possible formed internal and mechanical pressure {voltage}.

### ***3. Rejection potentially defective CJ a method of rise in temperature and submission of an exceeding pulse pressure {voltage} on the trunk of a feed {meal}.***

In this section accelerated tests CJ of memory 565PY1 and 556PT5 are considered {examined}. The problem of accelerated tests (УИ) CJ for developers ЭА is essential as refusals CJ can do without and millions roubles of losses (for example, in space objects).

Let's consider results of research CJ of memory with the help of the forced tests heat aging with applying the raised {increased} electric loadings and the subsequent check of functioning in conformity about THAT.

At a choice of temperature of tests it is necessary to take into account the physical phenomena occurring in concrete tested CJ, opportunities of the test equipment. The size of an exceeding pressure {voltage} got out so that there was no breakdown Ó-» - transitions, подзатворных oxides and oxides of remembering elements. The conclusion has been made of the analysis of work CJ 565PY1, that a mode at which all elements 565PY1 work practically, the mode of record is. Time of submission of an exceeding pulse {voltage} is defined {determined} by the diagram of conditions (for 565PY1 on an input {entrance} it should be equal  $60 \square 150$  nanosecond, beginning from the moment of submission on input {entrance} "CE" 12 В). Thus have been picked up a pressure {voltage} (up to 20 В), temperature (700C), duration of an exceeding pulse (up to 700 nanoseconds). During tests it was supervised ОУР CJ 565PY1.

Displacement of bottom border ОУР is typical of the majority investigated CJ on  $U_{DD}$  aside increases on 0,8-2 In, and on  $U_{BB}$  changes are insignificant. At action of temperature 700 With within 8 hours and amplitude 4 In from 70 investigated CJ five did not begin to store {keep} an exceeding pulse "1", one - "0", one "0" and "1", one - was restored. At action of the same temperature and an exceeding pulse amplitude 8 In within 24 hours 10 %, as well as in the first case have broken down 7 CJ from 70, that is. The conclusion arises, that over 8 hours to maintain CJ at 700C is inexpedient, that size of an exceeding pulse in 4 In and 8 In on influence do not differ. From investigated CJ the party {set} in 70 pieces which was exposed to temperature and electric influence within 140 hours per the same modes has been made. Any of them has not broken down, while from untried 70 CJ for same time 6 pieces have broken down. The analysis failed CJ has shown, that at the majority of them is punched диэлектрик.

In conformity about OST CJ of 556 series are tested at temperature 700C in a nominal mode 5 In within 168 hours. ЭТТ it is carried out {is spent} after "burn" smooth crosspieces and it is directed on revealing restored the ENCORE. Features of construction of internal structures and programming ENCORE ППЗУ allow to apply to them the following technique which essence is considered on an example 556PT5.

Principal cause "зараствания" smooth crosspieces in ППЗУ after programming is diffusion, ускоряемая at ЭТТ in temperature and an electric field. If in a mode "reading" to submit exceeding pulses on the trunk of a feed{meal} 5В (duration of pulses is compared to duration of pulses of programming and frequency of their submission is defined{determined} by the diagram of conditions) the percent{interest} "зараствания" crosspieces considerably decreases. These ways of the accelerated tests are introduced in НИЦЭВТ, НПО "Cascade", МНИИПА. For ways of the accelerated tests »-МОП CJ and bipolar ППЗУ it is received two copyright certificates.

From told it is possible to draw the following conclusions:

- 1) The accelerated tests 565PY1 allow to assert{approve}, that under certain conditions ЭТТ it is possible to speed up rejection potentially unreliable CJ;
- 2) Selection of temperature of the accelerated tests and exceeding pressure{voltage} should be carried out{be spent} in view of manufacturing techniques, design features and functioning CJ;
- 3) Failure CJ at the accelerated tests is connected, basically, with breakdown of poor made oxide.

#### **4. Conclusions.**

1. Gamma irradiation can be used for rejection potentially defective КМОП CJ with the help such criterials parameters as a current of consumption, a target current of a high level, etc.

2. As for restoration of parameters after gamma irradiation it is necessary to use annealing at temperature 3500C for reduction of the formed volumetric and superficial defects and as this temperature promotes formation{education} intermediate it is better to carry out{spend} rejection on plates. Besides rejection CJ on plates allows to save a significant amount of cases.

3. Used gamma irradiations for rejection of potentially defective crystals on plates it is economically justified and does not worsen reliability CJ the ambassador a plates.

4. Forced tests CJ (with the help of rise in temperature and submission of an exceeding pulse pressure{voltage}) can be used as a method of the accelerated rejection potentially defective CJ, and, time of tests in comparison with ЭТТ is reduced till 2-8 o'clock.

*Received: May 17 2005*



## THE STUDY OF THE SANDS OF CĂPUȘ (CLUJ COUNTY) WITH THE VIEW TO USING IN FOUNDRIES

BY

NASTACA TIMOFTE and BOGDAN NICOLAU

**Abstract:** The purpose of this work is to research the properties of the sand of Căpuș in order to use it in the foundries, because the different sandy varieties might be the basic staple in the material area for blends.

Analyzing the determinations made on the sand of Căpuș and the blends made by these sands, we consider that this might enter into the economic circuit, in the component of the molding blends from the foundries of nonferrous.

**Key words:** sand, molding blends

### 1. General considerations

An elevated weight in the area of raw material in the metallurgical industry is hold by the molding materials necessary in foundries.

The basic raw material in this area constitutes different sands varieties. Currently, most used-up sands, in foundries, are the one with an elevated content of quartz, and these facts confer them high property of refractoriness, being thus capable to support high temperatures whereat they are constrained during the casting.

The amount of the quartz from these sands touches the values of as far as 99% quartz's, and the minimum amount admitted depends on materials which were casted.

Thus, for the casting of steel or a cast-iron, the high temperature enforces us to use sand that contains a percent over 90-92% quartz to prepare the molding sand.

For castings of nonferrous alloys the percent of quartz from sand might recede up to 80-85.

Generally speaking, in industry, sands are used with elevated contents of quartz in order not to create problems to the casting of different parts.

On the basis of the previous mentioned, the present work propose to analyze the properties of sand with a feldspat.... nature, so it can be used in foundries.

The sand comes from Căpuș zone, Cluj County, and results from the extract of feldspats from the pegmatites from the exploitation Muntele Rece.

The sand of Căpuș is the residue abaft the flotation in average HF pegmatitului feldspatic.

We shall establish, on the strength of a determinations and analyses, if these sands may be used in foundries, especially for the fount of nonferrous alloys.

## 2. The chemical and mineralogical composition of the sand of Căpuș

As a result of the chemical analyses, we may establish the next chemical composition for the analyzed sandy samples .

Table 1. The chemical composition of the sand of Căpuș

SiO <sub>2</sub>	Na <sub>2</sub> O + K <sub>2</sub> O	Al <sub>2</sub> O <sub>3</sub>	MgO + CaO	Fe <sub>2</sub> O <sub>3</sub>
min. 88%	max 5%	max 7%	max 2%	max 0.22%

The mineralogical analyses of the sandy samples taken into consideration were made through the diffractometrical method using DRON type machine.

The results of the X rays analyze are presented in the table 2.

Table 2. The mineralogical composition of the sand from Căpuș

Feldspats	Quartz	Hornblend	Biotit	Illit
10 – 15 %	65 – 70 %	10 %	5 %	5 %

We may notice that 10-15 feldspats remain in the sand, as a result of extracting them by using the method of pegmatite flotation and these feldspats affect the refractoriness of the sand.

## 3. Granular analysis

For the granular analysis of the prelevated samples, we have used the next set of the sieves: 1, 00; 0, 630; 0, 500; 0, 400; 0, 315; 0, 250; 0, 200; 0, 160; 0, 100; 0, 090; 0, 063 mm.

The results obtained through the method of sifting are presented in the table 3. Interpreting the results we can establish which indexes characterize the granulation: The basic fraction (Fb), the average granulation ( M<sub>50</sub>) and the degree of uniformity (G.U.) Both the average granulation and the degree of uniformity may be established by using the cumulative curve shown in granular type-plug. The results obtained for the granular indexes are presented in the table 4.

Table 3. The granular analysis of the sand of Căpuș

Diameter of granules [mm]	Type of test	Rest of screen		Fraction with the diameter < d [%]
		g	%	
1,00	s	5,14	0,28	99,72
0,630	s	0,44	0,88	98,84
0,500	s	1,1	2,2	96,64
0,400	s	1,28	2,56	94,08
0,315	s	4,94	9,88	84,20
0,250	s	5,40	10,80	73,40
0,200	s	8,32	16,64	56,76
0,160	s	5,77	11,54	45,22
0,100	s	13,30	28,60	16,62
0,009	s	1,40	2,80	13,82
0,063	s	3,44	6,88	6,94
0,063	s	3,47	6,94	0,00
sum	-	50,00	100,00	-

Table 4. Granular coefficient

Basic fraction Fb	Average granulation M <sub>50</sub>	Degree of uniformity GU
0,2 – 0,1	0,185	51%

$$GU = 4/3 M_{50} - 2/3 M_{50} \%$$

#### 4. Molding blends

The molding blending consists of granular material (quartos sand, usually) and of a component which generates the property of formability.

In principle, the preparation of the molding blending consists in the achievement of binder films around the sandy granules during the process of liaison.

Regarding the quality conditions for the molding blends and taking into account the achievement of some little-rugosited and without defect castings, we used for our attempts a number of 5 recipes of preparing the molding blends, presented in the table 5. The bonding agents used was bentonite, natrium silicate and the urelite.

Table 5. Used molding blend formulas

Symbol of mixture	Components	Content
I	Sand	87
	Bentonite	8
	Water	5
II	Sand	77
	Bentonite	13
	Wooden flour	4
	Water	6
III	Sand	76
	Bentonite	16
	Water	8
IV	Sand	94
	Natrium silicate	6
V	Sand	97
	Urelite	2.2
	Benzo-sulfonic acid	0.8

For determining the properties of suggested blends we have preceded according to STAS 942-73. The attempts have been accomplished on crudeness test-pieces.

Concerning the test-pieces made of the suggested blends, it has been effectuated some determinations of the resistor to pressure detrusion traction and bending through the submission of the standard test-pieces to the respective sollicitations. The resistor to pressure has been determined on the type A cylindrical test-pieces, in accordance with STAS 9412-73 stipulations.

The determination of the bending resistance has been executed on parallelepipedical round-headed test pieces. Resistance to traction has been determined by using standard test-pieces with section of rupture of 5 cm<sup>2</sup>.

The determinations concerning the resistor to detrusion of different blends have been made on cylindrical type A test-pieces, STAS 9412-73.

The results of the determinations are shown in the table 6.

Table 6. Mechanical resistances

Symbol of mixture Mechanical tests	I	II	III	IV	V
0	1	2	3	4	5
Compression daN/cm <sup>2</sup>	0.25	0.32	0.64	8.3	8.6
	0.23	0.26	0.50	8.6	8.8
	0.25	0.28	0.58	8.4	8.6
Average	0.24	0.28	0.57	8.43	8.66
Bending daN/cm <sup>2</sup>	0.05	0.07	0.09	0.01	0.8
	Very small	0	0.07	0.09	0.9
	Very small	0.05	0.07	0.09	0.9
Average	-	0.04	0.096	0.093	0.86
Stretching daN/cm <sup>2</sup>	Very small	0.28	0.4	1.5	3.6
		0.2	0.25	1.2	4.4
		0.24	0.3	1.4	4.2
Average	-	0.24	0.31	1.36	4.06
Shearing daN/cm <sup>2</sup>	Very small	0.15	0.16	4.4	1.2
		0.15	0.16	3.8	1.6
		0.17	0.25	4.2	1.5
Average	-	0.15	0.19	4.13	1.43

Beside the nameable mechanic resistors the, about the suggested blends some extra-determinations have been made, such as: the penetrability, degree of shove, temperature of vitrification.

Beside the studied properties of the moulding blends it is necessary to know the behavior of the blend at high temperature, because in the process of casting both the form and the core are requested from the thermal point of view. Therefore, it is necessary to research refractoriness, which is influenced by the chemical composition, the mineralogical composition and by the size of sandy granules.

In practice, the refractoriness of the sand is influenced by two factors: the temperature of soak and the temperature of vitrification, the latest being very important.

It is preferable that the material's molten casting temperature not to exceed the temperature of vitrify of the blend.

The result of the effectuated determinations is presented in the tables 7, 8 and 9.

Table 7. Permeability

Symbol of mixture	Molding blend formulas	Permeability PU
I	Sand 87%, bentonite 8%, water 5%	75
II	Sand 77%, bentonite 13%, wooden flour 4%, water 6%	96
III	Sand 76%, bentonite 16%, water 8%	50
IV	Sand 94%, natrium silicate 6%	85
V	Sand 97%, urelite 2.2%, benzo-sulfonic acid 0.8% (A.B.s)	70



Table 8. The ramming degree

Symbol of mixture	Type of test	Number of the strokes applied	The ramming degree	
			Dietert units	
I	underdone	3	72	High ramming degree
		5	79	
		Average	75.5	
II	underdone	3	75	High ramming degree
		5	80	
		Average	77.5	
III	underdone	3	74	High ramming degree
		5	80	
		Average	77	
IV	Treated CO <sub>2</sub> (hardening)	3	80	High ramming degree
		5	82	
		Average	81	
V	Hardened with ABs	3	78	High ramming degree
		5	80	
		Average	79	

Table 9. Vitrification temperature

Number of test	Blends formula	Vitrification temperature °C
1	Căpuș sand	1200
2	Sand 77%, bentonite 13%	1100
3	Sand 94 %, natrium silicate 6%	1050 - 1100

### Conclusions

As a result of the analyses and research accomplished at Capus concerning the sand and the mixtures prepared with this sand it can be ascertained that the studied sand is feldspar sand with a relatively fine granulation, the permeability of the mixtures prepared with this sand and with various binding agents is relatively small, but using auxiliary materials as wood powder, coal dust, etc., that would be inserted into the mixture content, this fact doesn't represent any hindrance in the using of this sand in foundries. Because the mixed substances have good physical-mechanical properties this constitutes another sign in favor of exploitation of this sand although it has a relatively high percentage of feldspar in its mineralized structure.

The presence of the feldspars influences only the vitrifying temperature and for this part is a hindrance only concerning when using the sands in the preparation of the mixtures from the cast iron and steel foundries where the casting temperatures are high.

Where there is taking place casting of alloys and non-ferrous materials the utilization of the Capus sand in the mixing of the formation structures is imposed, as the quartz sands that can be replaced with the Capus sands can be exploited much more profitable in other purposes.

Analyzing the research accomplished concerning the vitrifying temperature it can be stated with certainty that this sand can be used in the non-ferrous foundries.

As regarding the proposed formation mixtures the ones that impose themselves are II, IV, V, because they show physical-mechanical properties that are good fit for a minimum binding agent consumption.

For proving the veracity of the conclusions resulted as regarding the possibility of utilization of the Capus sand in foundries we used the mixture of type II that has a higher permeability for casting some aluminum and steel parts.

Based on the results of the present study and on the casting experiments for some non-ferrous parts it was established without any doubt that the Capus sand can enter the economic circuit in the constitution of the formation mixtures from the non-ferrous foundries.

Received, 2005

Technical University „Gh. Asachi”

#### References

1. Cosneanu C. Cl. Ștefănescu (1989) – *Sisteme de amestecuri de formare pentru turnătorii*, Ed Tehnică, București.
2. Gianei A. F. , E. J. Freise (1967) – *Oportunisation of X-ray diffraction quantitative analysis*, Trans. Metallurg. Soc. Aime, no 239, p. 1676.
3. Petreuş I., L. Suciu (1983) – *Determinarea cantitativă a cuarțului din amestecuri de formare*, Creația Tehn. și Fiabil. în Construcții de Mașini, 22 – 23 nov, Iași.
4. Petreuş I. (1977) – *Petrologia rocilor sedimentare*, Curs litografiat , Univ. “Al. I. Cuza”, Iași.

Nastaca Timofte, Technical University „Gh. Asachi”, Bv. Mangeron, nr. 61, Iași, Romania

#### STUDIUL NISIPURILOR DE CAPUS (JUDETUL CLUJ) IN VEDEREA UTILIZARII IN TURNATORIE

**REZUMAT:** Scopul lucrării prezentate este acela de studiere a proprietăților nisipurilor de Căpuș în vederea utilizării lor în turnătorii, deoarece materia primă de bază în domeniul materialelor de formare o constituie diferitele varietăți de nisipuri.

Analizând determinările efectuate asupra nisipurilor de Căpuș și a amestecurilor preparate cu acest nisip, constatăm că acesta poate intra în circuitul economic în componenta amestecurilor de formare din turnătoriile de neferoase.

## COMPARATIVE STUDY ON MICROSTRUCTURAL AND MAGNETIC PROPERTIES OF FePt AND Fe/FePt THIN FILMS

BY

URSE MARIA\*, CHIRIAC HORIA\*, GRIGORAS MARIAN\*\* and MOGA ANCA –  
EUGENIA\*

**Abstract:** Thin magnetic layers are widely used as functional materials for different applications. In recent years, the (Fe,Co)Pt alloys have attracted growing interest as hard magnetic materials competing with the well-established NdFeB. FePt are promising hard thin film materials due to their high magnetocrystalline anisotropy and magnetic saturation. This paper reports some results concerning the effects of the composition and thermal treatment conditions on the structural and magnetic properties of FePt and Fe/FePt films. Samples of varying thickness (50 - 60 nm) were prepared by R.F. sputtering from composite target (disc of Fe with Pt pieces disposed on their surface) for FePt films and two elemental targets (disc of Fe and disc of Fe with Pt pieces disposed on their surface) for Fe/FePt films. The samples were subsequently annealed, in vacuum, at temperatures between 450°C and 700°C and a comparison between FePt and Fe/FePt films is presented. The polycrystalline thin films exhibited a coercivity of 7.6 kOe. This high coercivity is attributed to the magnetic domain pinning at the grain boundaries. By depositing Fe layers on the FePt films, an increase of remanence was observed as a result of the exchange coupling of the Fe and FePt layers.

**Keywords:** thin films, multilayer, hard magnetic, magnetocrystalline anisotropy, coercive field

### 1. Introduction

The nanocomposite magnetic thin films are widely used as functional materials for different applications such as high-density magnetic memory systems and MEMS (Micro Electro Mechanical Systems). In recent years, the FePt alloys have attracted growing interest as hard magnetic materials competing with the well-established NdFeB. Owing to its high magnetic anisotropy, high coercivity, and good corrosion resistance properties,  $L_{10}$  phase Fe-Pt is a strong candidate for ultrahigh density perpendicular recording media and as magnetic bias films [1,2]. The source of high coercivity in this alloy has been of great interest [3].

This paper report some results concerning the effects of the composition and thermal treatment conditions on the microstructure and magnetic properties of FePt and Fe/FePt thin films. A comparison between the magnetic properties of FePt and Fe/FePt thin films is also reported.

### 2. Experimental

The FePt and Fe/FePt multilayer films were prepared using a conventional R.F. diode sputtering system (Laboratory Sputtering Plant Z-400) using composite and simple targets. For FePt thin films was used a composite target which was made of a

Fe disc having 7.5 cm in diameter, on which Pt discs having 0.5 cm in diameter, were disposed.

The Fe/FePt multilayer films were prepared by sequential deposition in vacuum from two elemental targets, disc of FePt and disc of Fe. The thickness of layers was controlled by sputtering time and measured by using a Film Thickness Monitor (resolution 0.1 nm) during deposition process. The Pt content in FePt thin films was changed by modifying the number of Pt discs disposed on the surface of the target.

The samples were deposited on various substrates, depending on the intended measurements. The substrates were cooled during deposition.

For structural analysis and magnetic measurements, the FePt and Fe/FePt multilayer thin films were deposited on Si substrates. The structure of the samples was investigated by X-ray diffraction (XRD) analysis. An X-ray diffractometer with a monochromatized Cu-K  $\alpha$  radiation was used, in a Bragg-Brentano arrangement. Room temperature magnetic properties were measured by vibrating sample magnetometer (VSM) with the maximum applied field of 1500 kA/m.

The film composition was determined by electron probe analysis on Fe-Pt thin films that were deposited on molybdenum substrates.

The microstructure of FePt thin films was analysed by transmission electron microscopy (TEM), using Mo 'microscope grids' coated with an evaporated carbon (8 – 10 nm) thin films as substrates. FePt thin films with a total thickness of about 80 nm were used for TEM analysis. The electron microscopy studies were carried out with a JEOL –200 CX microscope.

The as – deposited FePt and Fe/FePt multilayer thin films were subsequently annealed, in vacuum, for different periods of time, at temperatures between 450°C and 700°C, in order to obtain the L1<sub>0</sub> ordered phase.

### 3. Results and discussion

We have prepared two types of samples on Si substrates: FePt with a thickness of about 50 nm and multilayer [Fe (2nm)/FePt (10nm)]x5 thin films with a total thickness of about 60 nm (Fe 10 nm and FePt 50 nm).

The optimal chemical composition for FePt thin films was found to be close to Fe<sub>55</sub>Pt<sub>45</sub> for a ratio 54/46 (%) of surfaces occupied by the Fe and Pt components on the surface of the sputtering target.

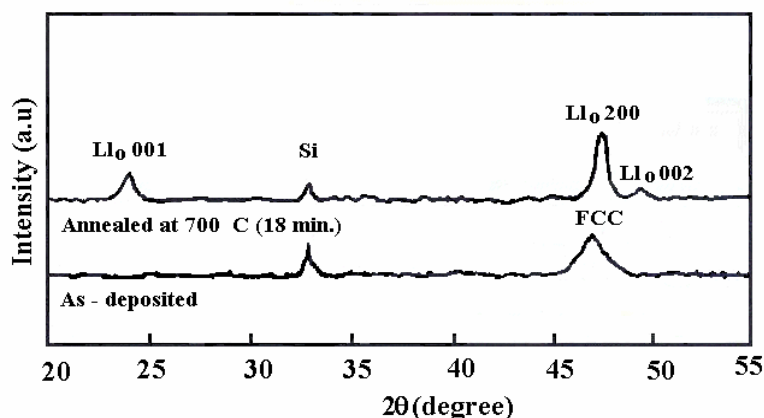


Fig.1. X- ray diffraction patterns for as – deposited and annealed FePt thin films

In Fig. 1 are presented the X-ray diffraction patterns for as – deposited and after rapid thermal annealing at 700°C for 18 minutes for FePt thin films with a thickness of about 50 nm. The XRD pattern for as – deposited sample indicates a (100) FCC phase. After the annealing process, the 50 nm thick FePt films exhibited a small X-ray diffraction intensity of the  $L_{10}$  (001) and  $L_{10}$  (002) peaks and a high intensity of  $L_{10}$  (200) reflection.

The X-ray diffraction patterns corresponding to  $[\text{Fe} (2 \text{ nm})/\text{FePt} (10 \text{ nm})] \times 5$  thin films do not exhibit evident changes as compared to the XRD patterns for FePt (50 nm) which are presented in Fig.1, indicating that no major structural changes were produced.

Fig.2 presents the dependence of the saturation magnetization and coercive field of the annealing temperature for FePt and multilayer Fe/FePt thin films.

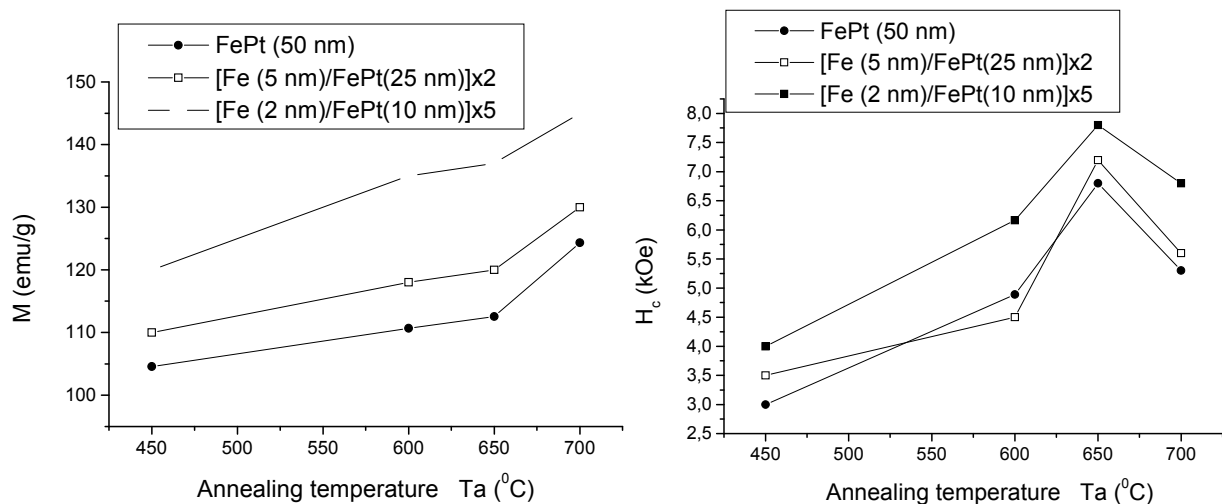


Fig.2. The dependence of the saturation magnetization and coercive field of the annealing temperature for FePt and multilayer Fe/FePt thin films.

One can see that the saturation magnetization values for multilayer Fe/FePt thin films are more as compared with FePt thin films. For all the samples, there is a gradual increase of the saturation magnetization values with increasing the annealing temperature up to 650°C, followed by an abruptly increase after annealing at 700°C. It can also be observed from Fig. 2 that, for all the samples, the coercive field values increase when increasing the annealing temperature up to 650°C and then decrease when increasing the annealing temperature up to 700°C. The Fe/FePt multilayer thin films present an enhanced coercivity as compared to the FePt thin films. The coercive field increases to about 7.6 kOe due to the domain wall pinning effect within the intergranular region.

For annealing temperatures around 650°C, the grains reach an optimum size of about 20 nm, fact suggested by the TEM image. After annealing at temperature of 700°C the grains have a size of about 30 nm and the coercive field values, for all the samples decrease.

Fig.3 shows the hysteresis loops at room temperature for FePt (50 nm) and  $[\text{Fe}(2\text{nm})/\text{FePt}(10\text{nm})] \times 5$  thin films, annealed at 600°C, with the applied magnetic

field parallel to the sample plane. One can see that the values of the remanence for Fe/FePt thin films are more as compared with FePt thin films

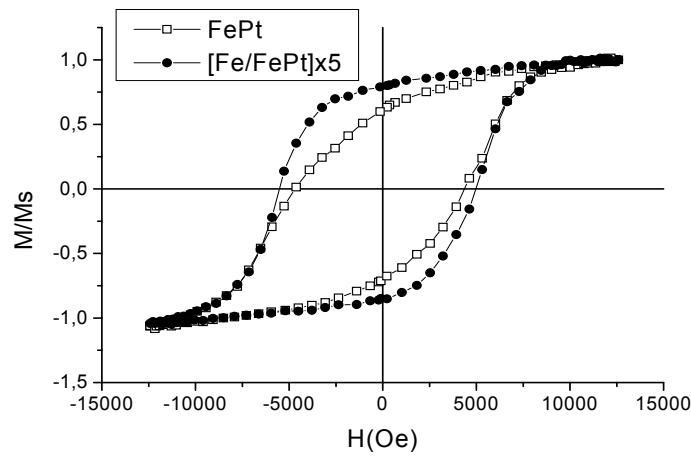


Fig. 3. The hysteresis loops at for FePt (50 nm) and  $[\text{Fe}(2\text{nm})/\text{FePt}(10\text{nm})] \times 5$  thin films

Fig.4 shows the electron micrograph of  $[\text{Fe}(2\text{nm})/\text{Fe}_{52}\text{Pt}_{48}(10\text{nm})] \times 2$  thin film after annealing at  $650^\circ\text{C}$ .

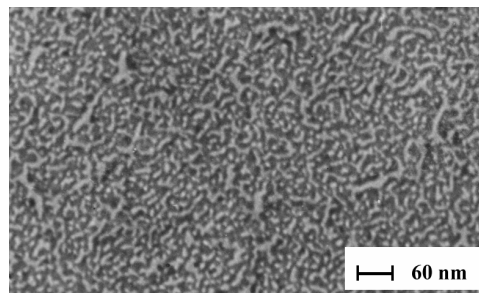


Fig.4. TEM micrograph of annealed  $[\text{Fe}(2\text{nm})/\text{Fe}_{52}\text{Pt}_{48}(10\text{nm})] \times 2$  thin film

TEM image for annealed Fe/FePt films display spherical particles, with the average sizes are about 20 nm. Most of the particles are discontinuous, but a significant fraction exists as small chains.

By controlling the experimental conditions of thermally treatment and layers thickness in multilayer systems, the nanogranular Fe/FePt thin films with good hard magnetic properties were obtained.

#### 4. Conclusions

The magnetic and microstructural properties of FePt and Fe/FePt thin films depend on the annealing temperature. An optimum of these characteristics was obtained for annealing temperature of  $650^\circ\text{C}$ .

As compared to FePt thin films, the multilayer Fe/FePt thin films, which have same thickness for FePt, exhibit a coercive field  $H_c$  about 7.6 kOe, saturation magnetization of about 135 emu/g and remanence of 0.75, after annealing at  $650^\circ\text{C}$ .

By analyzing these preliminary results it can be seen that the Fe/FePt thin films are interesting as permanent magnet for MEMS applications.

### References

- [1] Y.K.Takahashi, M.Ohnuma and K. Hono, - *Ordering process of sputtered FePt*, **J.Appl.Phys.****93**, (2003) **7580-7582**.
- [2] Y.K.Takahashi, T. Ohkubo, M.Ohnuma and K. Hono, - *Size effect on the ordering of FePt granular films*, **J.Appl.Phys.****93**, (2003) **7166-7168**.
- [3] J. Zhou, R. Skomski, X. Li, W. Tang, G.C. Hadjipanayis, and D.J. Sellmyer, - *Permanent – magnet properties of thermally processed FePt and FePt/Fe multilayer films*, **IEEE-Trans. Mag.** **38**, No. 5, (2002) **2802-2804**.

\* National Institute of Research Development for technical Physics Iasi

\*\* Faculty of Physics, University “Al.I.Cuza” Iasi

### STUDIUL COMPARATIV PRIVIND PROPRIETĂȚILE MICROSTRUCTURALE ȘI MAGNETICE ALE STRATURILOR SUBȚIRI FePt ȘI Fe/FePt

**Abstract.** *Straturile subțiri magnetice sunt foarte mult utilizate ca materiale funcționale pentru diferite aplicații. În ultimii ani, aliajele (Fe,Co)Pt au fost intens studiate ca materiale magnetice dure, în competiție cu binecunoscutul material NdFeB. Straturile subțiri FePt sunt materiale magnetice dure convenabile pentru o serie de aplicații specifice, datorită valorilor mari ale magnetizării de saturație și anizotropiei magnetocristaline. În această lucrare prezentăm o serie de rezultate privind efectele compoziției și tratamentelor termice realizate după depunere asupra proprietăților structurale și magnetice ale straturilor subțiri FePt și Fe/FePt. Probele, cu grosimi variind între 50 și 60 nm, au fost preparate prin pulverizare R.F. din 2 tipuri de ținte de pulverizare: țintă compusă formată dintr-un disc de Fe (diametru 7,5 cm) cu discuri de Pt (diametru 0,5 cm) dispuse pe suprafață, pentru straturile subțiri FePt; 2 ținte, una compusă din FePt și una simplă din Fe, pentru straturile subțiri Fe/FePt. Probele au fost succesiv tratate, în vid, la temperaturi cuprinse între 450 și 700°C. Rezultatele experimentale privind probele FePt și Fe/FePt sunt prezentate comparativ. Straturile subțiri policristaline FePt prezintă valori ale câmpului coercitiv de aproximativ 7.6 kOe. Această valoare mare a câmpului coercitiv este posibil să fie datorată procesului de fixare a domeniilor magnetice la granițele grăunților cristalini. În cazul straturilor subțiri multiple Fe/FePt se constată o creștere a remanenței, comparativ cu straturile subțiri FePt, ca efect al cuplajului de schimb dintre straturile de Fe și FePt.*





## **PARTICULAR ASPECTS ON THE DEFORMATION AND FRACTURE OF NOVEL DIBENZYL POLYURETHANE ELASTOMERS OF VARIABLE CRYSTALLINITY**

BY

**CRISTINA PRISACARIU, PAUL C. BUCKLEY and VICTOR ADRIAN  
PRISACARIU**

**Abstract:** New polymers were achieved, with a controlled ordering of copolymer hard segment blocks on the macromolecular chain. They derive from either one single type of diisocyanate of rigid or variable geometry, or from mixtures of isocyanates. Wide angle X-ray diffraction of the as-moulded polymers revealed the presence of crystallinity in a series of PU materials based on a flexible isocyanate, 4,4'-dibenzyl diisocyanate (DBDI). Mechanical tests included load-unload cycles at constant rate of extension, with measurement of hysteresis and strain recovery, and stress relaxation tests. The presence of DBDI hard segments instead of 4,4'-methylene bis(phenyl isocyanate (MDI) led systematically to increases in: the input strain energy to a given elongation, hysteresis and residual strain under cyclic loading, and stress relaxation. The influence of the PU hard segment nature on the stress-strain data was followed for different PU of variable phase segregation.

**Key words:** flexible isocyanates, polyurethane elastomers, hysteresis, stress relaxation.

### **1. Introduction**

Casting polyurethane elastomers (PU) have a segmented structure which gives rise to a heterophase morphology that is responsible for the “virtually crosslinked” state of the polymer and determines remarkable values of the polymer mechanical properties. The structure of PU consists of linear polymer primary chains which are segmented in composition and are specifically made up of alternating hard and soft segments which are joined end to end through strong covalent chemical linkages [1].

A series of PU based on new dibenzyl (DBDI) monomers were obtained. These monomers belong to a large category of diaromatic compounds with a variable geometry which induces significant effects in the macromolecular chains, especially those in connection to the rearranging capacity of the molecular fragments and thus to the increase in the degree of crystallinity [1-5]. The present paper deals with the presentation of a series of physical/mechanical and chemical aspects of PU block copolymers derived from diisocyanates 4,4'-dibenzyl diisocyanate (DBDI), 4,4'-methylene bis(phenyl isocyanate (MDI), or combinations of those, giving rise to PU consisting of different chemical, physical and consequently mechanical properties.

Particular aspects of the mechanical response for a series of PU with diol chain extenders were followed. A systematic investigation was made of the effects of varying hard and soft segment chemistry, crosslinking and preparation procedures, on the mechanical response of melt-cast polyurethane elastomers. Rotation around the central  $-\text{CH}_2-\text{CH}_2-$  bridge in DBDI allows alignment of aromatic rings and hence

crystallization within the hard phase, which is not available with MDI in melt-cast polyurethanes.

## 2. Experimental procedure

A family of polyurethane elastomers was synthesised in the Romanian laboratory. They were all three-component systems combined in stoichiometric proportions, and consisting of: (1) a diisocyanate (DI) generating hard segment HS (MDI or DBDI); (2) a soft segment macrodiol MD - poly(ethylene adipate) PEA, polytetrahydrofuran PTHF, or poly(butylene adipate) PBA; and (3) a small molecule diol as chain extender CE - anhydrous ethylene glycol EG, diethylene glycol DEG, or butylene glycol BG. The macrodiols were all of molar mass  $M_w = 2000 \pm 50 \text{ g mol}^{-1}$ . The three components were always mixed in the proportions HS:CE:MD = 4:3:1, giving hard segment mass fractions in the region of 30%, and isocyanic index  $I = 100$ . The synthesis procedure followed was the pre-polymer route described previously by Prisacariu et al. (2003). The HS and MD components were reacted together with vigorous mixing under vacuum at  $100^\circ\text{C}$ , to give prepolymer terminated by HS. This was then thoroughly mixed with the CE at  $90^\circ\text{C}$ , and cast into closed sheet moulds for curing at  $110^\circ\text{C}$  for 24 hours. The final result was polymer with  $M_w$  in the range 60-120  $\text{kg mol}^{-1}$ , in the form of sheets with thickness in the range 0.3-0.6 mm. The sheets were stored at room temperature for at least one month before testing. For PU with mixtures of DI (MDI DBDI), the synthesis was performed as previously reported elsewhere [5].

## 3. Results and Discussion

### 3.1. PU crystallinity

As shown [2] in all cases the more mobile DBDI structure leads to hard segments with a higher tendency to self associate evidenced by higher melting points and crystallization tendency (Figure 1.a) which is visible even when such structures are included in the polyurethane soft segment matrix [2].

The X-ray diffraction patterns of Fig.1.a show that crystallizability of DBDI based PU largely remains even after of inclusion of soft segments [2] The crystallinity is however, considerably reduced with the incorporation of MDI, [2,5].

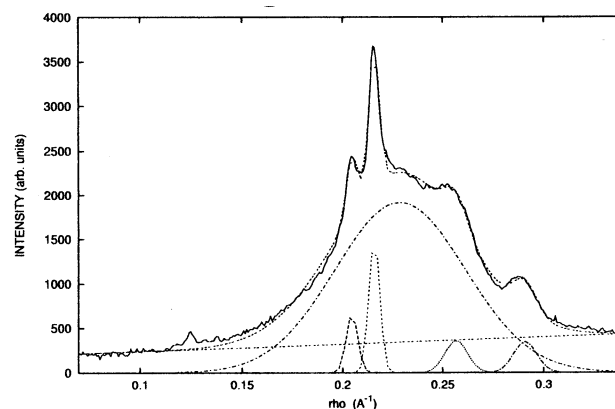


Fig. 1. PU materials - uniaxial stretch at nominal strain-rate = 0.0042/s; (a) Hard segments = DBDI  $\chi=0.14$ ;

### 2.2. PU stress-strain data and tensile strength properties

The characterization of different PU block copolymers consisting of different chemical, physical and consequently mechanical properties has been made by means of uniaxial tensile experiments.

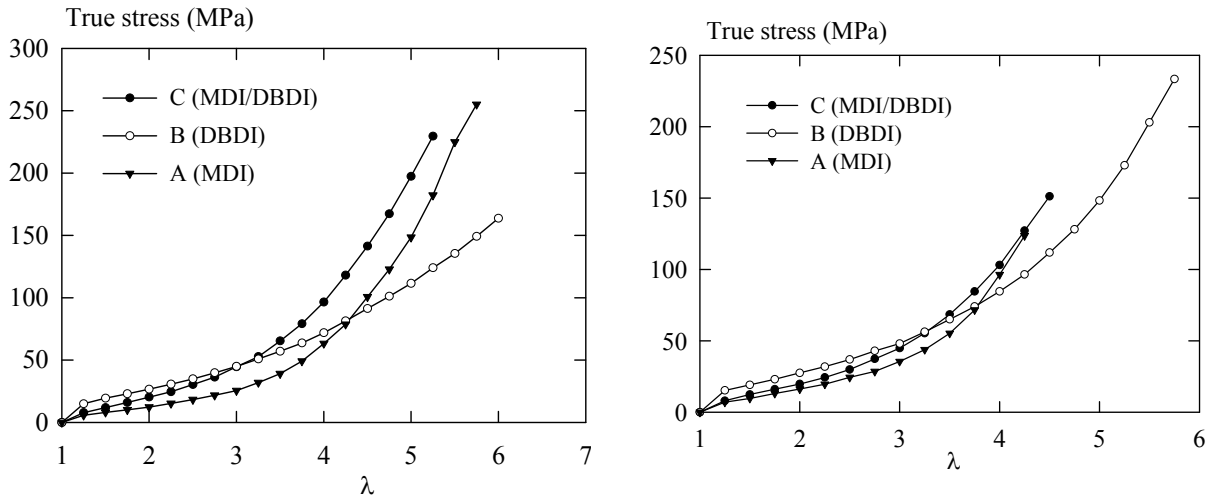
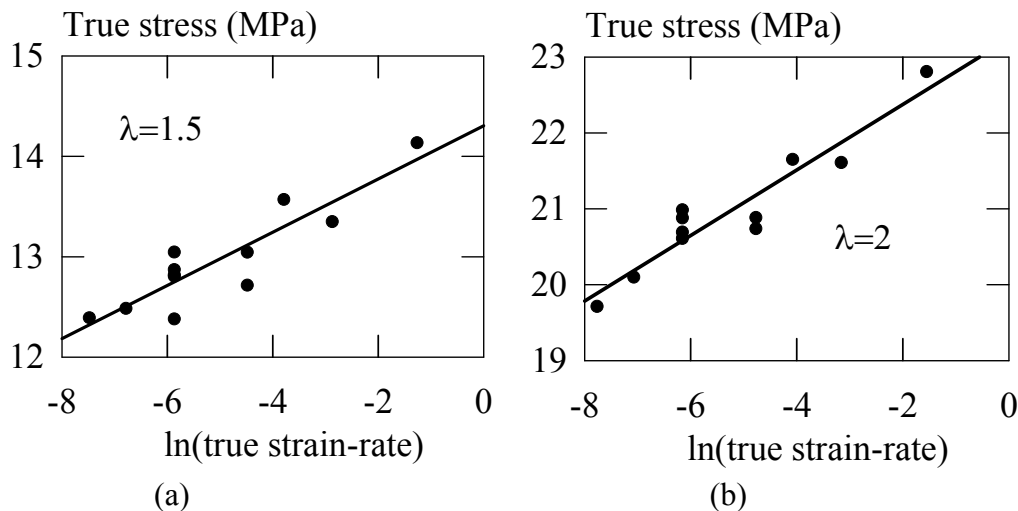


Fig. 2. Comparison between the PU stress-strain data of three PUs at nominal strain-rate = 0.0042/s. Polytetrahydrofuran (PTHF) was used as a soft phase; A=PU based on MDI; B=PU based on DBDI; C = PU based on mixtures of MDI/DBDI.

Fig. 3 As Fig.2 but for materials with poly(ethylene adipate(PEA) as soft phase

Stress-strain curves for three types of PU with PTHF or PEA are compared in Figs. 2 and 3, where systematic differences can be seen. Polymer B representing a PU based on DBDI has a higher flow stress than PU type A based on MDI and PU type C based on mixtures of MDI and DBDI. Yet PU derived from DBDI shows less pronounced strain stiffening. Polymer C shows more pronounced strain-stiffening than PU type A. All results shown here are for polymers A, B and C with polytetrahydrofuran (PTHF) as soft segment and ethylene glycol (EG) as a chain extender. The same pattern was observed in polymers where the adopted macrodiol (MD) was polyethylene adipate (PEA). The molar proportions used in the syntheses for these tests were diisocyanate D:MD:EG = 4:1:2.64.



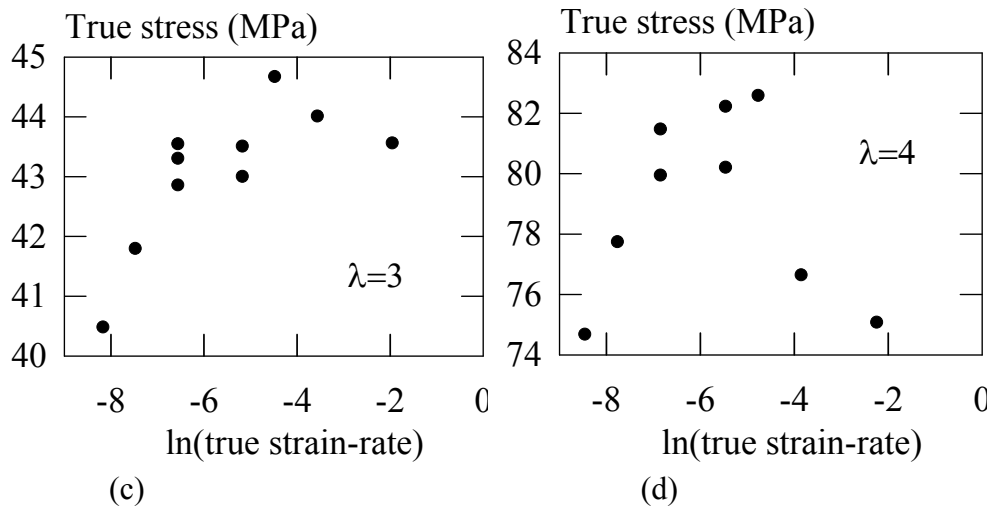


Fig. 4 Eyring plots for material C (MDI/DBDI).

Fig. 4 shows the dependence between the true stress and  $\ln$  (true strain-rate) when materials of type C based on mixtures of diisocyanates (MDI/DBDI) [5-8] were investigated. Different stretching levels of PU sample elongation ranging from 50% ( $\lambda = 1.5$ ) to 300% ( $\lambda = 4$ ) were approached. As expected (Fig. 4), the true stress when the PU sample is elongated between  $\lambda = 1.5$  to  $\lambda = 4$  depends strongly on the true strain-rate. The wider is the limit of elongation the higher is the true stress corresponding to equal values of the same true strain-rates.

### 2.3. PU Stress relaxation

Stress relaxation of PU derived from DBDI and from classical isocyanates was studied. In Fig. 5 the stress variation at a constant 300% elongation of a PU specimen is plotted as a function of time (100 hrs).

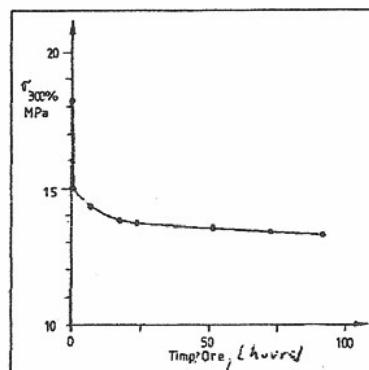


Fig.5. Stress relaxation curve (90 hrs) of a PU with DBDI based on BG, PEA, DBDI with  $I = 110$ .

As seen in Fig. 5, the main relaxation process occurs within the first 10 min. (70% of the relaxation value after 100 hrs) while the 24 hours relaxation is 95% of the relaxation value after 100 hours. The kinetics of the equation of relaxation proposed by Ferry [5] for other polymers was checked and it was found that eq (1) is valid also in the case of polyurethane elastomers, both in general as well as in the particular family of PU derived from dibenzyl structures.

$$\sigma_t = \sigma_o - a \cdot \log t \quad (1)$$

where  $\sigma_0$  is the stress corresponding to a given 300% elongation and  $\sigma_t$  is the reduced stress for a certain deformation at time  $t$ . In our case the  $a$  constant value was experimentally determined as the respective straight line slope of the  $\sigma - \log t$  dependence, for example  $15 / 2.1 = 7.14$  for a DBDI based PU, [2].

## 2.4. PU Cycling Tensile Tests

To investigate how the PU structure determines the mechanical performance of the materials as elastomers, a programme of cyclic tensile tests was carried out on the whole range of polymers synthesized [6-9]. Properties of particular interest were the strain energy input, and the strain energy recovery and strain recovery on unloading. In some cases these experiments were supplemented by stress relaxation tests. Wide angle X-ray diffraction (WAXD) was employed to compare the levels of hard segment crystallinity.

The sheet materials were cut into rectangular strips of dimensions  $6 \text{ mm} \times 0.3\text{-}0.6 \text{ mm}$ , and tested in tension at ambient temperature ( $23 \pm 1^\circ\text{C}$ ) and humidity ( $41 \pm \text{RH}$ ) using an Instron model 4204 testing machine, with 50 mm between the grips. Extension was measured using an Instron extensometer, with a gauge length of 20 mm. All the tests reported here were conducted at a nominal extension-rate of  $\pm 3 \times 10^{-2} \text{ s}^{-1}$ . This was chosen for consistency with preliminary studies of the same materials [8].

In the first phase of the study, the materials were cycled between an extension of 3, and zero load, for 3 cycles. An examples PU curve of nominal stress versus nominal strain is shown in Fig. 6.

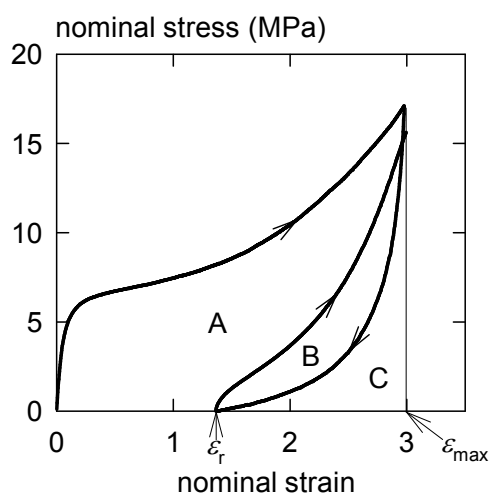


Fig. 6. Loading-unloading-reloading cycle for a PU with MDI/DBDI, with definitions of zones A, B, C of the diagram, maximum nominal strain  $\epsilon_{max}$  and residual nominal strain  $\epsilon_r$ .

It observes notable pronounced hysteresis, unrecovered strain and Mullins effect (whereby re-loading follows a stress-strain path closer to the unloading path than the original loading path). This is a specific feature for the DBDI/MDI and solely DBDI based PU with DI of variable crystallinity. From curves such as these several quantifiers of the inelasticity were calculated as reported elsewhere [9] in function of the defined three zones A, B and C in the stress-strain diagram denoting the energy density expended on first loading to a nominal strain of 3.

### 2.3. Interpretation in terms of a constitutive model

PU hysteresis and stress-strain curves in Figures 7 and 8 have the characteristic shape for elastomers containing reinforcing particles. There is a rate-dependent flow stress associated with stress-activated segmental diffusion at the surface or interior of reinforcing particles, superimposed on the strain-stiffening hyperelastic stress response of the elastomeric matrix. Such a system is amenable to a quantitative description in terms of the Glass-Rubber (GR) constitutive model framework which has been described elsewhere [6-8]. Hard and soft phases were assumed subject to the same deformation. PU hard phase contribution to the stress for polymers A, B and C, at a nominal strain rate of  $0.0042 \text{ s}^{-1}$  is shown in Figure 7 (data points).

Explanation for the differences between polymers A, B and C may be found in the structure of the hard phase, and structure of the soft phase. Structural information indicates the direction of increasing hard phase crystallinity is  $A \rightarrow C \rightarrow B$ , and suggests the direction of increasing phase separation is also  $A \rightarrow C \rightarrow B$ .

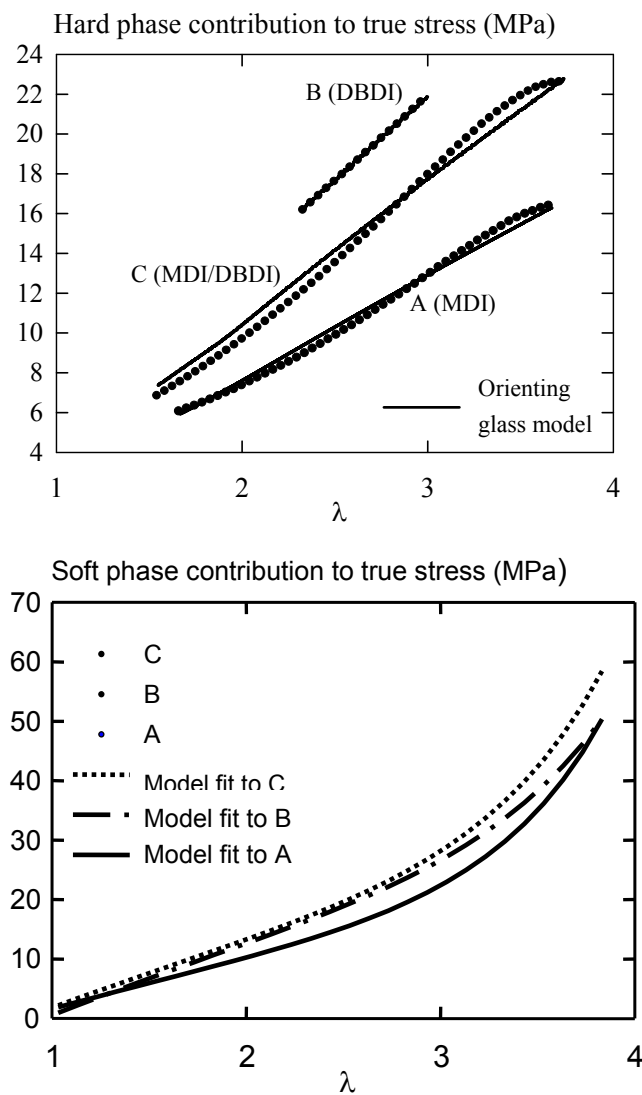


Fig.7. PU hard phase contribution to the stress for nominal strain-rate  $0.0042 \text{ s}^{-1}$ .

Fig.8. PU soft phase contribution to the stress at same nominal rate.

With regard to the PTHF based contribution of the hard phase (Fig.7), comparing A and B, the higher flow stress of polymer B is readily explained in terms of the higher level of hard phase crystallinity, and better phase segregation. Similarly, poorer phase segregation in A explains a lower density of flexible chains and chains with lower flexibility in the soft phase, (Fig.8). In both respects, polymer C is intermediate in structure and properties.

### 3. Conclusions

The characterization of different PU block copolymers consisting of different diisocyanates or combinations of them was made. PU phase separation tendency is significantly more pronounced in the case of polyurethanic materials based on dibenzyl structures than in the case of similar hard segments based on classical isocyanates of a rigid geometry as MDI. PU based on DBDI, display higher stiffness and strength than the conventional MDI-based PU, with lower strain recovery and strain energy recovery on cycling - a primary consideration for elastomers. Optimum response is obtained with mixed MDI/DBDI hard segments. The influence of the hard domain crystallinity in PU with DBDI structures is pronounced, leading to a significant increase in the stress in these experiments.

### 4. REFERENCES

1. C. Hepburn, **Iranian Journal of Polymers Science & Technology**, vol.1 No2, (1992), **84 -108**.
2. C. Prisacariu, Doctorate Thesis, Technical University "Gh. Asachi", Iasi, Romania, (1998).
3. A. Caraculacu, G. Caraculacu, **J. Macromol. Sci.-Chem**, A22 (5-7) (1985), **631-651**.
4. C. Prisacariu, I. Agherghinei, **J.M.S.-Pure Appl. Chem.**, **A37 (7)**, (2002), **785-806**.
5. C. Prisacariu C., R.H.Olley, A. Caraculacu A., D.C. Bassett and C.M. Martin, **Polymer** **44**, (2003), **5407-5421**.
6. C.P.Buckley C.P, C. Prisacariu C. and A. Caraculacu, **Euromech Colloquium and Workshop, Vienna, July 2002**, **96-99**.
7. C.P.Buckley, C.Prisacariu C. and A. Caraculacu A.A, **12th International Conference in Deformation, Yield and Fracture of Polymers**, 7-10 April, Cambridge, UK 2003, **349-352**.
8. C. Prisacariu, C.P. Buckley and A. Caraculacu, Mechanical response of dibenzyl based polyurethanes with diol chain extension – in the press, **Polymer**, 2005
9. C.P. Buckley, C. Prisacariu, A. Caraculacu, C.M. Martin, **ECCMR 2005**, Stockholm.

**CRISTINA PRISACARIU\***, **PAUL C. BUCKLEY\*\*** and **VICTOR ADRIAN PRISACARIU\*\*\***

\* The Romanian Academy, Institute of Macromolecular Chemistry „Petru Poni” Iasi, Aleea Grigore Ghica Voda, Nr.41 A, 700487, Iasi, Romania

\*\* The Department of Engineering Science, University of Oxford, Parks Road, Oxford, OX1 3PJ, Oxford, UK.

\*\*\* „Gh. Asachi” Technical University, Iasi, Faculty of Automatic Control and Computer Engineering, Department of Computer Engineering,  
Bdul. Dimitrie Mangeron, no. 53 A, IASI, cod 6600 ROMANIA

#### **ASPECTE PARTICULARE PRIVIND DEFORMAȚIA ȘI RUPEREA UNOR NOI ELASTOMERI POLIRETANICI CU STRUCTURI DIBENZILICE, DE CRISTALINITATE VARIABILĂ**

Au fost obținuți noi polimeri poliuretani (PU) ce prezintă ordonare controlată a blocurilor de segmente dure pe lanțul macromolecular. Acești polimeri au la bază fie un singur tip de izocianat cu geometrie fixă sau variabilă, fie combinații de izocianați. Studiile de difracții cu raze X au indicat prezența cristalinității în polimerii ce au la

bază izocianată cu geometrie variabilă. Încercările mecanice întreprinse asupra acestor polimeri au inclus studii histerezis prin efectuarea unor cicluri de întindere-revenire a polimerilor la o viteză constantă de alungire, precum și studii de relaxare mecanică. Prezența segmentelor dure dibenzilice (DBDI) cu geometrie variabilă ce înlocuiește izocianatul clasic MDI a determinat creșterea energiei de deformare și a histerezisului PU, ca și creșterea deformațiilor reziduale în cazul solicitărilor ciclice și de relaxare mecanică. Influența naturii de segment dur asupra curbelor caracteristice ale PU a fost urmărită pentru diferiți PU cu grade variabile de separare fazică.



## TUBING AND CASING THREAD JOINT. THEORETICAL RESEARCH AND EXPERIMENTAL TESTS

BY

STEFAN GRIGORAS and CRISTEL STIRBU

**Abstract** One of the modern constructive solutions for tubing and casing joint is the integral two steps threaded joint. The buttress thread assures the joint functioning. The sealing metal/metal zones are placed, one on the outer of the joint and the second on the inner zone of the box. A plastic material gasket may be used, like anticorrosive barrier, in the inner sealing zone. A central shoulder assures the final contact between the pin and the box and limits the make up torque. The value of the make up torque is the main parameter of well column mounting, because its influence on the contact deformations in the metal/metal contacts of the sealing. The stiffness of the two pieces determines the correct functioning of the joint. The material of the pin and box, the geometrical parameters and the load conditions influence the resistance of the joint. We have created a new method for stiffness evaluation and interconnection, based on the geometry of the joint and on the material parameters. We have determined the joint efficiency, the make up torque and the strength limits of the components by theoretical method. The experimental tests, which we have performed, confirm the theoretical functional parameters and the technological characteristics of the joint elements.

**Keywords:** tubing and casing joints; extractive industry; joint design

### 1. INTRODUCTION

The extractive industry uses many types of joints for tubing and casing. The integral joint is obtained of the pipes bodies. Figure 1 presents the aspect of an integral

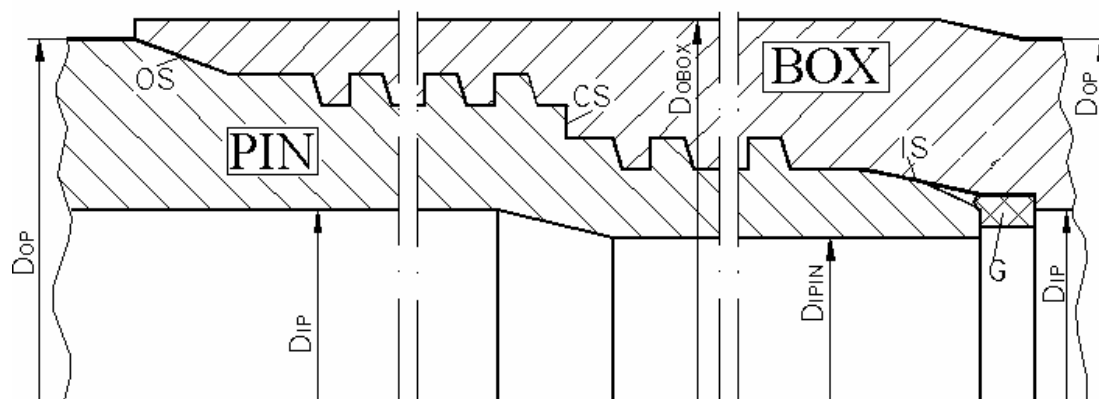


Fig. 1. The aspect of an integral joint.

two steps cylindrical thread joint ( $D_{OP}$  – the outer pipe diameter;  $D_{IP}$  – the inner pipe diameter;  $CS$  – central shoulder;  $OS$  – outer seal;  $IS$  – inner seal; plastic gasket). The

thread is paced on two cylindrical steps. The maximum outer diameter  $D_{OBOX}$  and the minimum diameter  $D_{IPIN}$  are limited by the bore and the drill diameter (the well technical conditions).

The widened box is obtained under cold technological conditions, like the compressed end of the pin. This process assures the necessary thickness for central shoulder materialization.

The aspect of a bended well column is presented by figure 2.

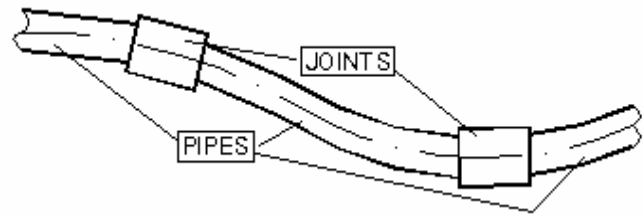


Fig. 2. A bended well column

## 2. THEORETICAL APPROACH

The joint functioning is assured by the thread (column montage), by the sealing zones (sealing efficiency), by the minimum area of the cross section (resistance to the traction loads), the wall thickness (inner and outer pressure and traction forces resistance), by the bending and combined resistance of the critical area and by the thread resistance and screwing capacity (figure 2). The main functional parameter of any joint is the make-up torque. The screwing of the pin produces local deformations in the metal/metal contacts of the joint and in the gasket, if that exists.

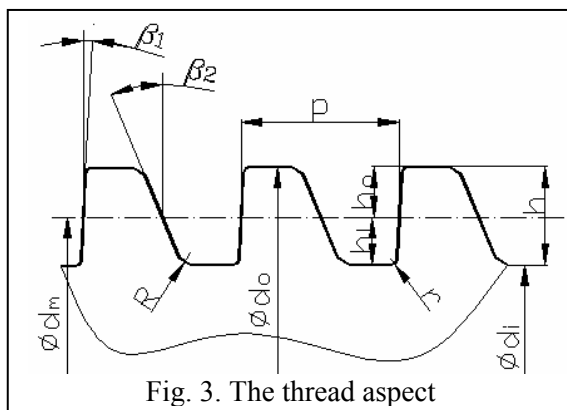


Fig. 3. The thread aspect

**The cylindrical thread** (figure 3) is placed on two steps. The two steps have pitch continuity, for manufacturing process assurance. The active angle  $\beta_1$  has small value (maximum  $3^\circ$ ) and  $\beta_2$  is greater ( $10-12^\circ$ ). In this case, the probability of pullout is inexistent. The thread assures the strength end the montage. The sealing functioning isn't the role of the thread. The two steps an uniform distribution of tensile forces on the column assures.

**The metal/metal contacts** represent the sealing zones, presented by figure 4. In

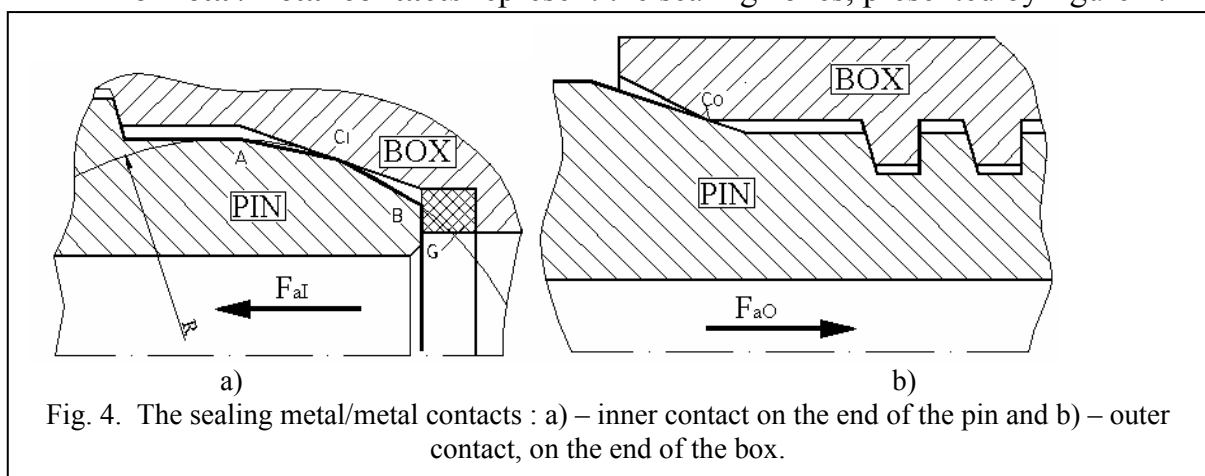


Fig. 4. The sealing metal/metal contacts : a) – inner contact on the end of the pin and b) – outer contact, on the end of the box.

the inner contact (fig. 4 a), the theoretical spherical end of the pin (radius  $R$ ) is replaced by two tapered zones,  $AC_1$  and  $C_1B$ . The box is tapered too. The stiffness of

the metal/metal linear contact, of the end of the pin, of the gasket and the elastic deformations of the contact, of the gasket and of the pin generates the axial load  $F_{aI}$ . This load must be produced by the thread (maximum value is limited by the plastic deformations appearing and the minimum value is dictated by the seals functioning). The outer seal (fig. 4 b) is a metal/metal linear contact too. The stiffness of the contact, of the end of the box and of the pin are the mains parameters of the axial load of this zone,  $F_{aO}$ . This load is produced by the screwing (column make up). The maximum value of  $F_{aO}$  is limited by the box resistance and the minimum value is shows by the sealing functioning.

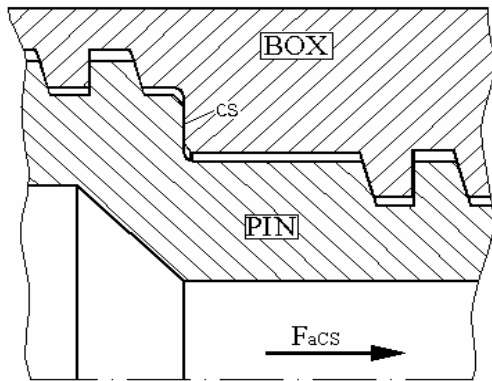


Fig.5. The central shoulder.

The contact between the pin and the box, on the central shoulder, shown in the figure 5 is the contact which limits the value of the make up torque. The contact pressure brings about to the axial load  $F_{aCS}$  determination, by limiting the pressure values to the material yield limit. The make-up torque is the functional parameter which assures the load on the contact.

The friction forces in all the described contacts, like the friction in the thread, produce the friction global torque, which is the make-up

torque:

$$T = T_I + T_O + T_{TH} + T_{CS} \tag{1}$$

were:  $T_I$ ,  $T_O$ ,  $T_{TH}$  and  $T_{CS}$  are the friction torques in the inner (index  $I$ ), outer (index  $O$ ) contacts; in the thread (index  $TH$ ) and on the contact shoulder, respectively. The make-up torque is  $T$ .

Another parameter of the joint functioning is his efficiency, defined by the ratio between the critical area of the joint,  $A_{crJ}$  (for traction) and the area of pipe section,  $A_p$ , [1]:

$$\varepsilon = \frac{A_{crJ}}{A_p} \cdot 100 \text{ [%]} \tag{2}$$

The efficiency -defined by (2)- is around 60...70%, for this joint type.

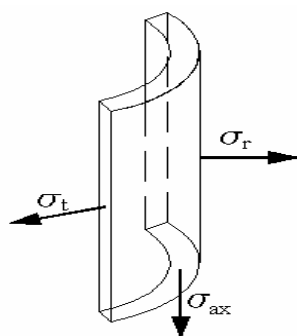


Fig.6. The stresses in the wall of pipe and joint

Other loads on the joint are the outer pressure, the inner pressure, the traction (column weight), the bending of the column and the thermal lengthen of the column (compression). The thread loads are the nonlinear distribution of traction load along the joint, the wear produced by the screwing and the bending and compression effects. An element of the wall of pipe or joint is represented in figure 6. The components of equivalent stress in the wall are:

- the normal axial stress:  $\sigma_{ax} = f(\sigma_t, \sigma_b)$ ;
- the normal radial stress:  $\sigma_r = f(p_i, p_o, p_c, p_s)$ ;
- the normal tangential stress:  $\sigma_t = f(p_i, p_o, p_c, p_s)$ ,

were:  $\sigma_t$  is the traction stress,  $\sigma_b$  is the bending stress,  $p_i$  - the inner pressure,  $p_o$  - the outer pressure,  $p_c$  - the equivalent compression pressure produced by the thread and  $p_s$  - the pressure produced by the screwing, [2]. The equivalent stress, calculated using these components limits the load of the pipe and joint, [3] and [4].

The make-up torque, considered as the main parameter of the joint assure the column montage and the, distribution on along the thread and the column resistance.

### 3. EXPERIMENTAL TESTS

Experimental tests have been developed on different lots of joint, for many sizes and for different materials too. The make-up torque was calculated by our theoretical method [1]. The aim was to determine the resistance of the joint (according to the pipe) and the sealing efficiency evaluation.

We have developed **tests under inner pure pressure**. For the initial tests,

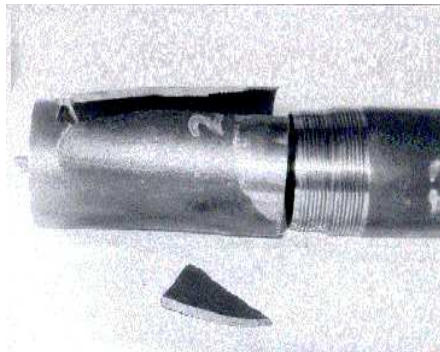
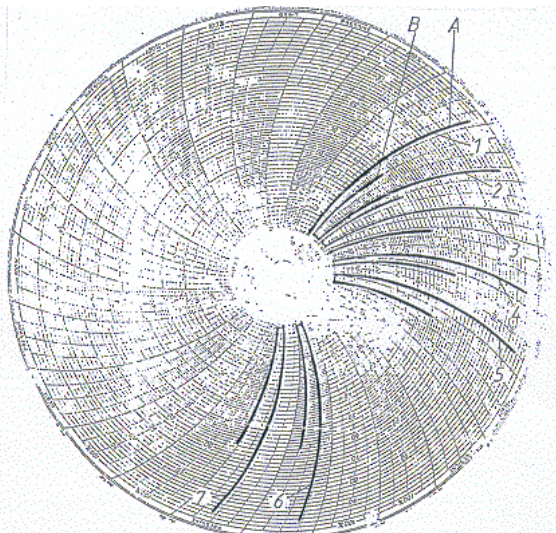


Fig. 7. The aspect of a destroyed joint under inner pure pressure

water and oil were the active fluids. The pressure can be considered as the normal radial stresses in the pipe and joint wall. They stop at the yield limit of the pipes steels (maximum values were 1000 bar). On can notice that the joint assures a strength limit greater then the medium yield of the steel. Other tests were performed to the strength of the joint body. Figure 7 presents the aspect of a joint, destroyed under inner pressure. The sealing functioning was perfect, if the tests keep the values of the make up torque and of the manufacturing precision.

The plastic material gasket can be used only as a free option of the well designer; the seal efficiency was perfect whether this gasket is used or not.



A - P<sub>int.</sub> values for the inner pressure tests

Fig. 8. The diagram of inner pressure evolution, for combined test: inner pressure and traction.

**The combined tests** represent the experimental evaluation of the functional and strength parameters of the joints, simultaneously for minimum two loads: **the inner pressure and the traction force**. The diagram of figure 8 presents the inner pressure evolution. Curve A refers only to the inner pressure and curve B shows the inner pressure which induces the traction load in the critical cross section of the joint. The 7 tested joints were of  $5\frac{1}{2}$  inches outer diameter of the pipe and 9.17 mm wall thickness of the pipe.

Table 1 presents the results of the tests, for 3 specimens of the joint.

The sealing efficiency is remarkable. The work fluid is the water under pressure.

Table 1. Tests parameter for combined load

Specimen	Inner pressure, [MPa]	Traction force, [N]	Sealing efficiency
1	70...71	$8 \cdot 10^5$	Losses=0 for 3.5 hours
2	71...73	$8.5 \cdot 10^5$	Losses=0 for 72 hours
3*	69	$7.8 \cdot 10^5$	Losses=0 for one hour

\* - test on joints without gasket.



Fig. 9. Test under inner pressure, traction force and bended column

The well column has the bending tendency, because of the different composition of the earth, along the column (fig. 2). We have created the condition **for the experimental tests developed under inner pressure, traction forces and bending of the column, taken over by the joints**. The testing fluid was the liquid nitrogen. The angle of the column bending was maximum  $10^0/20$  m column length, [1]. In this case, the axial stresses in the joint wall increase with 120 %, and the metal/metal seals lessen the normal loads on the contact surfaces. The minimum value of the make up torque assures the sealing efficiency, in perfect conditions and the resistance is perfect, too.

Figure 9 shows a test under bending, inner pressure and traction (the last load is produced by the inner pressure) on a column obtained of three joint pipes (outer pipe diameter is  $5 \frac{1}{2}$  inches and the pipe wall thickness is 9.17 mm). The maximum inner pressure was 40 MPa.

#### 4. RESULTS

Figure 9 presents the theoretical axial load repartition on the thread pitches, along a joint between two pipes with 139.7 mm outer nominal diameter and 9.17 mm wall thickness. The 1 curve represents the load produced by screwing and the curve number 2 is the repartition of the column weight. The superposition of the two component leads to a uniform load distribution.

The figure number 10 presents the evolution of make-up torque values for the same joint. Different materials for pipes were used in the theoretical determination. We present the minimum and the maximum value of the make – up torque for any used steel, according to [1].

The experimental tests show that the joint assure the sealing and resistance parameters for well column in the oil or gas extractive industry.

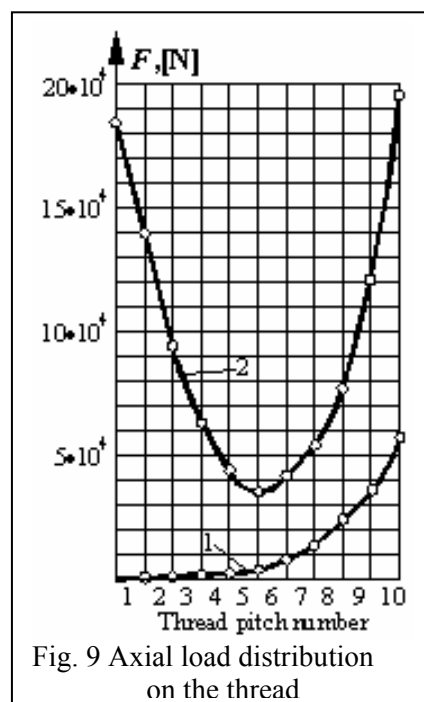


Fig. 9 Axial load distribution on the thread

#### 4. CONCLUSIONS

1. The presented joint is an original construction, because of its thread, sealing zones and manufacturing process.

The dimension of the joint are placed in the same domain like Hydril, Extrem Line, Vam and other companies. Joint performances are greater comparing with all the analyzed joints.

2. The experimental tests on pipes and joint confirm the choice of a type of joint (the technical solution) and the original algorithm of joints design. The tests developed under pure inner pressure shows the maximum efficiency of meta/metal seals, the role of anticorrosive barrier of the gasket and the resistance of the pipe and joint.

3. The combined tests (inner pressure and traction forces) determine the diminishing of contact stresses in the metal/metal seals. If the central shoulder is rationally placed and all the length dimensions depend on its position, the optimum functioning of the joint is assured. The manufacturing accuracy has a very important role in the joint evolution.

4. The main advantage of the new joint is the diminishing of thread stresses and the time of the screwing (reduced with 50%).

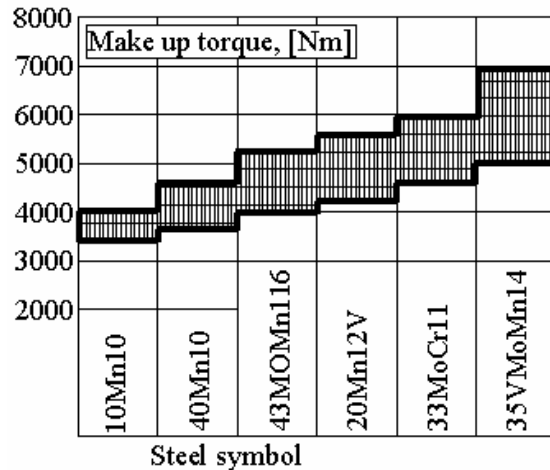


Fig.10. The make-up torque, for different steels

#### REFERENCES

1. American Petroleum Institute – Bulletin on Formulas and Calculations for Casing, TUBING, Drill Pipe, and Line Pipe Properties, ISO 10400/1993.
2. Gafitanu, M.D, Grigoras, St., Stirbu, C. - Original Joint for Casing And Tubing. Theoretical Analysis. Proceedings of The 26 – The Israel Conference on Mechanical Engineering, Haifa, 1996, 154 –156.
3. Gafitanu, M.D., Grigoras, S. and Stirbu C. - Functional Aspects of a Thread Joint for Tubing and Casing, Second WORLD TRYBOLOGY CONGRESS, Vienna, 2001, 693.
4. Stirbu, Cr.- Tubing and Casing Joints. Resistance and Functional Aspects, Meridian Engineering, ISSN 1683-853x, no.2, 2002, Edit. TEHNICA INFO, Chisinau, Rep. Moldova, 126-130.

#### IMBINARE PENTRU MATERIAL TUBULAR. CERCETARI TEORETICE SI EXPERIMENTALE

##### (Rezumat)

Lucrarea prezinta o solutie practica, originala de realizare a cuplarii tevelor de sonda. Sunt analizati parametrii functionali si de rezistenta necesari asigurarii competitivitatii si alinierii la normele API. De asemenea, sunt prezentate teste experimentale care confirma capacitatea imbinarii de a se adapta conditiilor oferite de exploatarea la sonda. Concluziile prezinta momentul de strangere, ca parametru essential, precum si capacitatea imbinarii de a asigura etansarea si rezistenta cerute.

## TECHNICAL SOLUTIONS FOR TUBING AND CASING THREADED JOINTS

BY

**CRISTEL STIRBU and STEFAN GRIGORAS**

**Abstract** The paper presents different aspects of tubing and casing joints. These technical solutions have a lot of similar theoretical, technological and dimensional aspects, like the dimensional correlation with the pipes, drill and other well elements, the mechanical strength of pipes and joints to the inner and outer pressure and to the proper weight of the column, the bending resistance of the column under different conditions of the ground properties, the resistance under high temperatures of the column, the perfect seal functioning, for extraction efficiency, the resistance under corrosive conditions of the different zones of the earth and the resistance to the mechanical wear and the possibility of the reutilization of the component elements. The results of a theoretical analysis of joint constructive solutions are the subject of the paper, according API standards and calculus methods for pipes. The technological considerations are a main role in the paper, according the precision and the functional conditions of the joints.

**Keywords:** tubing and casing joints; extractive industry; joint design

### 1. INTRODUCTION

A column of well represents many pipes and the joints between these pipes. The proper weight, the inner and the outer pressure, the chemical action of the medium, the bending of the pipes and the thermal compression are the main outer loads of the well column. The resistance of the pipes is assured by the material, the wall thickness and the execution technology.

The joints of pipes are the elements who assure the column continuation, the mechanical resistance, the sinuous way of the column, the possibilities of pipes dilatations and the sealing functioning, between the column components. The companies of extractive pipes produce the joints too. The theoretical analysis of these joints is the subject of the paper. In this respect, we present many constructive solutions, according to the pipes and joint strength, the technological criteria and the functioning parameters. The joints may be selected of a large lot of constructive solution, by the well designer. He has the tendency to assure the minimum outer diameter, the minimum wall thickness, the minimum length of joint and the maximum resistance.

The tendencies of the well designer activity are the main start point for the joint designer who can select the joint solution between the classic constructions or between many new integral joints or between the coupling connections.

## 2. CONSTRUCTIVE ASPECTS

The joints between the two pipes have many constructive aspects. The table 1 presents some solutions of joint produced by different companies.

**Table 1**

Constructive solutions of tubing and casing joint		
No	Type and characteristics	Constructive aspect
0	1	2
1	<p><b>Integral joint with tapered thread</b></p> <p>The pin and the box are realized in the pipes wall (outer diameter <math>\varnothing D</math> and inner diameter <math>\varnothing d</math>).</p> <p>The thread is generated on a tapered surface; he is the mounting element and a sealing zone too;</p> <p>OSH - outer metal/metal shoulder;</p> <p>G - plastic material gasket;</p>	
2	<p><b>Integral joint, with cylindrical thread</b></p> <p>The same parameters as the first position in the table.</p>	
3	<p><b>Integral joint</b></p> <p>Joint with box thickened wall (<math>t_0</math> value), for resistance increasing.</p> <p>ISH - inner blocking shoulder; on this shoulder can be considered and a sealing surface or a special plastic material rig.</p>	



**Table 1 (continuing)**

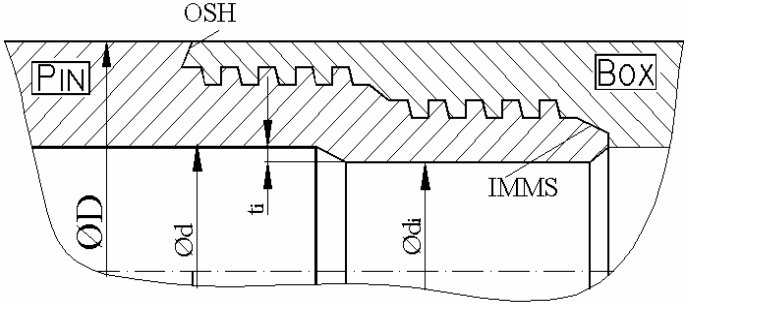
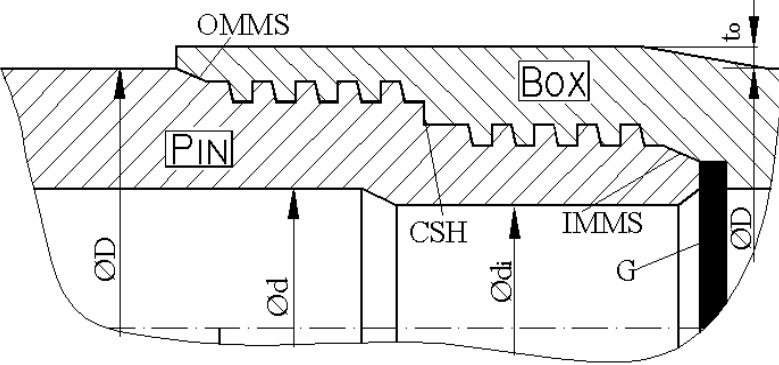
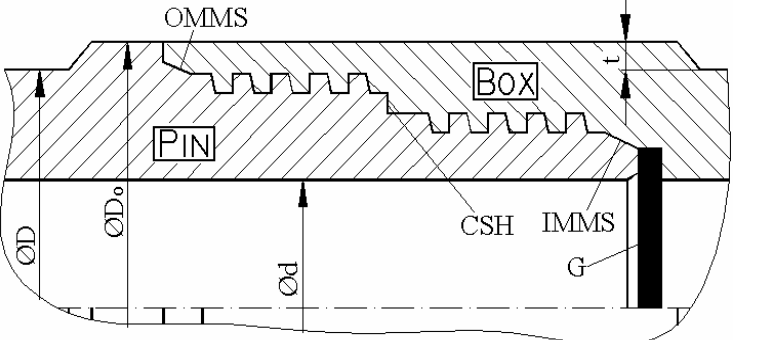
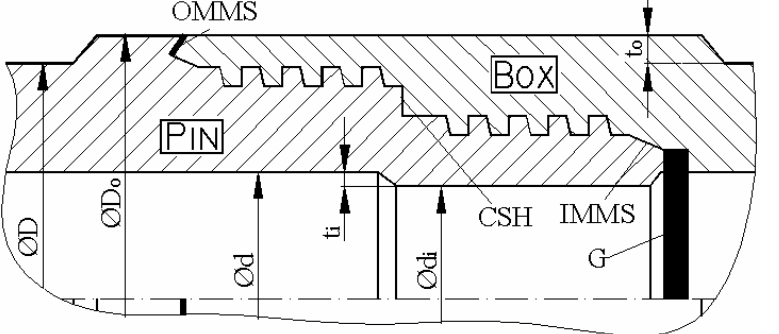
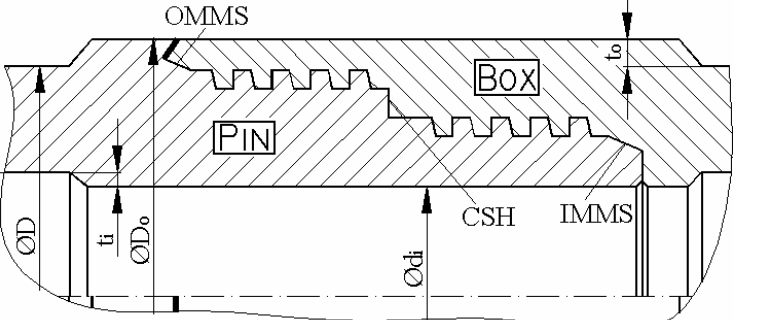
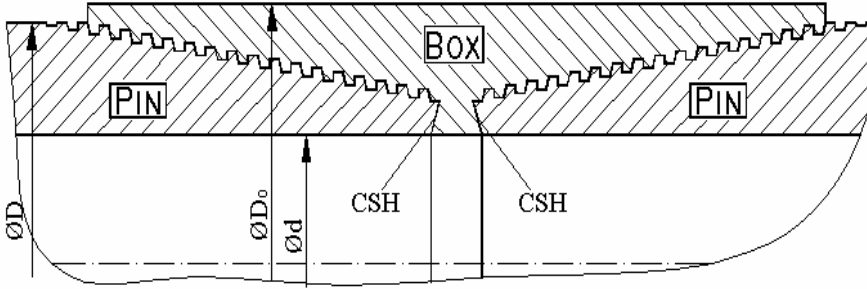
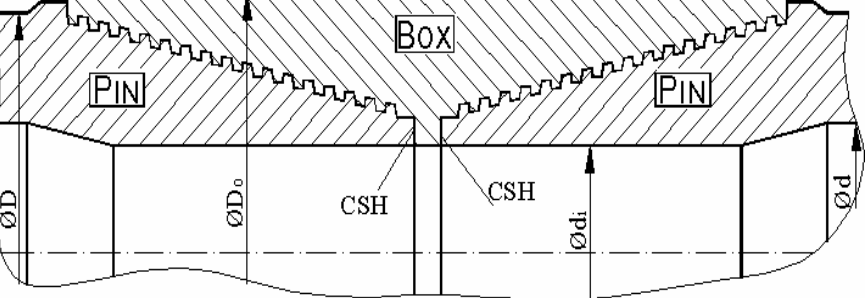
0	1	2
4	<p><b>Integral joint</b>                      The end of pipe is compressed (for two steps cylindrical thread realization).                      IMMS – inner metal/metal seal (linear elastic contact).</p>	
5	<p><b>Integral joint</b>                      The pin is compressed and the box is widened under cold conditions.                      OMMS – outer metal/metal seal (linear elastic contact).                      CSH – central shoulder</p>	
6	<p><b>Integral joint</b>                      Joint with both wall thickness of box and increased pin, under hot conditions.                      The noticed zones are the same</p>	
7	<p><b>Integral joint</b>                      Complex joint with box and pin wall thickened at the exterior and compressed pin.</p>	
8	<p><b>Integral joint</b>                      Joint with both pin and box thickened (on the outer and the inner diameters). High traction resistance. Long columns.</p>	

Table 1 (continuing)

0	1	2
9	<p><b>Coupling connection</b> Joint with detachable box. Tapered thread with sealing role. Small outer diameter.</p>	
10	<p><b>Coupling connection</b> High resistance joint with detachable box. Multiple make-up and brake use and torsion resistance. A special gasket can be used for sealing.</p>	

The table shows that the first 8 positions are integral threaded joints and the last two are by threaded and coupled joints. The 1 and 2 positions are realized only in the pipe body. For the joints 3, 4 and 5 the pipe is compressed or (and) widened for pin and box manufacturing. The variants 6, 7 and 8 have the wall thickness of the end of pipes grated both for pin and box. For the last two variants were utilized only detachable boxes.

### 3. THE FUNCTIONING PARAMETERS

Any joint type is characterized by many mounting, exploitation, technological and designing parameters. For exploitation, the resistance under pressure, temperature, corrosion and traction condition and the perfect sealing are the performance criteria. The manufacturing of the pin and of the box shows as main criteria the correct positioning of sealing metal/metal surfaces and the start and the end of thread. The time of manufacturing process and the dimensional precision are the technological parameter. The columns montage in the well shows the make-up torque and the time of screwing as the main parameters.

#### 2.1. The pipe and the connection resistance

The resistance under inner and outer pressure and the resistance under traction (column weight) are the subject of API standards, according to the material and to the pipe dimensions [10].

The internal pressure resistance is:

- internal yield pressure for pipe:

$$p = \frac{2 \cdot t \cdot \sigma_{0,2}}{D} \quad (1)$$

where:  $t$  and  $D$  are the nominal wall thickness and the nominal outside diameter of pipe, respectively and  $\sigma_{0,2}$  is the minimum yield strength.

- internal yield pressure for couplings:

$$p = \sigma_{0,2} \cdot \frac{W - d_1}{W} \quad (2)$$

with:  $W$  - nominal outside diameter of coupling,  $d_1$  - diameter at the root of the coupling thread at the end of the pipe in the power-tight position and  $\sigma_{0,2}$  refers to the coupling.

- pressure resistance for buttress thread casing joint strength:  
-for pipe thread strength:

$$P = 0.95 A_p U_p [1.008 - 0.0396(1.083 - \sigma_{0,2} / U_p) D] \quad (3)$$

- for coupling thread strength:

$$P = 0.95 A_c \cdot U_c \quad (4)$$

with:  $A_p$  - cross-sectional area of plain-end pipe;  $A_c$  - cross-section area of coupling;  $U_p$  - minimum ultimate strength of pipe;  $U_c$  - minimum ultimate strength of coupling and  $\sigma_{0,2}$  refers to the pipe;

- integral casing joint strength:

$$P = A_{cr} \cdot U_p \quad (5)$$

where  $A_{cr}$  is critical section area of box, pin or pipe, whichever is least and  $U_p$  is specified minimum ultimate strength.

The thrust load  $P$  depends to the  $A_{cr}$ , defined by the joint efficiency, imposed by the design conditions and by the API standards. The critical area of the joint may be lees to the cross section of the pipe (1...5 variants in the table 1).

- bending load failure strength:

$$P_b = 0.95 A_{jp} [U_p - (\frac{140,5BD}{(U_p - \sigma_{0,2})^{0,8}})^5] \quad (6)$$

where:  $A_{jp}$  is cross sectional area of the pipe wall, under the last perfect thread, or, for integral joint,  $A_{jp} = A_{cr}$ ;  $B$  bending angle, [ $^{\circ}$ /10 m column length],  $D$  - nominal outside diameter of pipe.

## 2.2. The sealing efficiency

The joint functioning depends to the sealing types, according to the column resistance. The metal/metal seals produce important axial loads in the joint thread. The local deformation of contact zones (theoretical linear contacts) and the limitation of this deformation to reduce the joint fracture or plastic deformation are the main functional conditions. The stiffness determination and the dimensional correlation between different sealing zones are the designing tendencies. The plastic material gaskets can be used only like a role of anticorrosive barrier.

### 2.3. Technological considerations

The axial dimensions of the pin and of the box assure the correct positions of the sealing zones and the screwing of the pin. In the variants 4...8 of the table 1, the central shoulder is the dimensioning base for metal/metal sealing surfaces. The measurement of axial dimensions, like the thread and sealing diameters assure the precision and the functioning conditions for the joints.

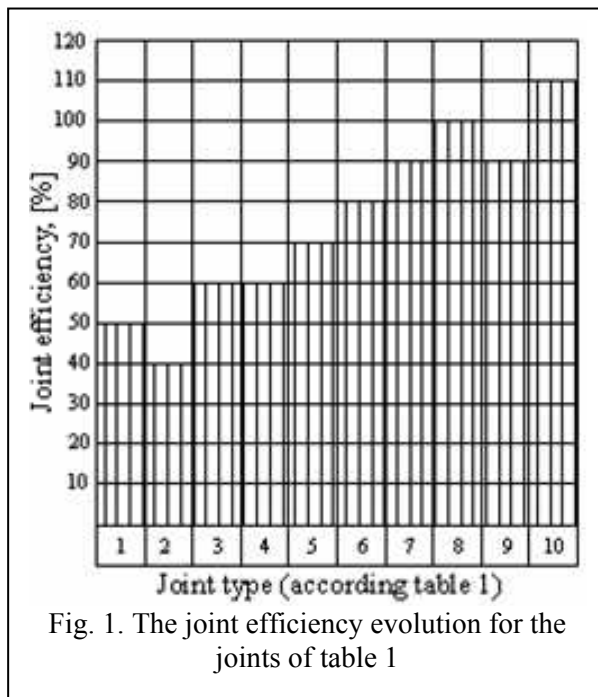
### 2.4. The column montage

The screwing of the pin is realized by special tools, to the well. The make-up torque is the main mounting parameter. His value (imposed by the designer and measured to the well) assures the sealing functioning and the column continuity and stiffness. The time of screwing is very important too, because the great price of mounting operation.

The make-up torque is obtained by summing the friction torques in whole the sealing surfaces, the torques who determines the elastic deformations in the metal/metal contacts and the thread friction torque.

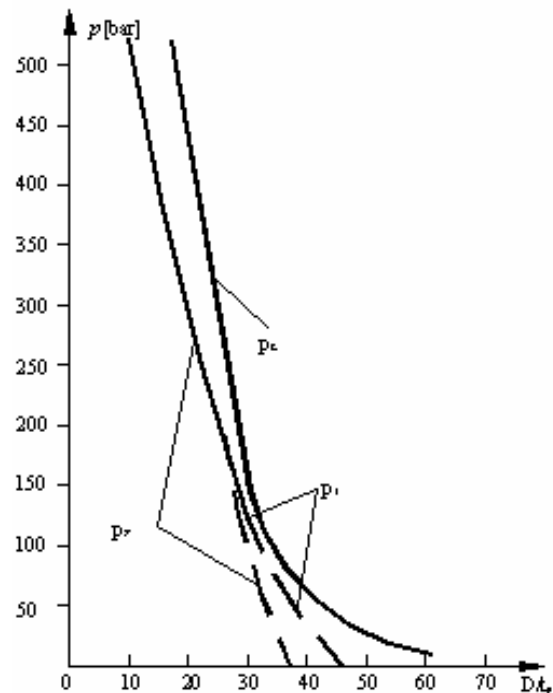
## 4. THEORETICAL RESULTS

Figure 1 presents the middle designed joint efficiency for the constructive cases



presented by table 1. The calculus has developed for the same pipe sizes (5.5 inches – outside diameter and 9 mm nominal wall thickness).

Fig. no.2 shows the limit collapse pressure for pipes, calculated according API recommendations and [2]. The joint has a great resistance under outer pressure, because his greater sizes. The main resistance problems refer to the pipe. The resistance under bending stresses is the main problem for the joint. The traction efficiency, presented by figure 1 diminishes with maximum 50% if the column is bended.



## 5. CONCLUSIONS

1. We present more constructive solution for tubing and casing joints, for theoretical comparisons and optimum design criteria establishing.
2. The integral joints represent the modern solution. The coupling connections refer primordially to the casing.
3. The joint resistance is superior to the pipe, except the bending resistance.
4. The traction forces, the dilatation, the bending and the torsion torques induce complex stresses in the pipe and in the joint walls. The evaluation and the minimization of the stresses are a designing procedure.
5. The technological process is based on linear sizes precision and on thread technology and start geometrical precision, to assure the mounting conditions.
6. The sealing metal surfaces are the main role for joint functioning. The local deformations are dictated by the stiffness and the resistance of the components.

*Received: May 19 2005*

*The "Gh.Asachi" Technical University from Iasi*

## REFERENCES

1. American Petroleum Institute – Bulletin on Formulas and Calculations for Casing, TUBING, Drill Pipe, and Line Pipe Properties, ISO 10400/1993.
2. Stirbu, Cr.- Tubing and Casing Joints. Resistance and Functional Aspects, Meridian Engineering, ISSN 1683-853x, no.2, 2002, Edit. TEHNICA INFO, Chisinau, Rep. Moldova, 126-130.

## **SOLUTII TEHNICE PENTRU IMBINARI FILETATE ALE TEVILOR DE EXTRACTIE SI BURLANELE DE TUBAJ**

(Rezumat)

Lucrarea prezinta cateva solutii tehnice de imbinari ale tevilor de extractie si burlanelor de tubaj. Criteriile de selectie a fost cele ale frecventei utilizarii si al evolutiei tehnologice. Imbinarile de tip "integral", la care mufele si cepurile sunt realizate direct din corpul tevii au avantajul simplitatii si unei elasticitati superioare. In schimb, rezistenta la tractiune nu este atuul lor esential. Etansarile functioneaza perfect in aceasta situatie. Imbinarile cu mufa detasabila, care folosesc filet conic prezinta avantajul unei rezistente superioare la incovoiere, dar timpul de realizare a montajului la sonda este mai mare. Eficienta la tractiune este, de regula superioara. Etansarea este asigurata de zonele speciale, dar si de filetul plasat pe generatoare conica. Solicitarile conduc la analiza starii spatiale de tensiuni si la comparatii intre modul de raspuns al tevariei si al imbinarilor. Pe baza aprecierilor comparative, au fost stabilite principalele criterii de proiectare. Momentul de strangere este considerat ca parametrul functional principal, data fiind importanta sa pentru portanta, etansare si reutilizarea elementelor imbinarilor.



## TEMPERING EFFECTS ON THE MICROSTRUCTURE AND TENSILE BEHAVIOUR OF A Cu-Zn-Al SHAPE MEMORY ALLOY

BY

LEANDRU-GHEORGHE BUJOREANU, VASILE DIA, VIORICA DAVID  
CORNELIU MUNTEANU and FLORIN MAXIM

**Abstract** The paper presents some experimental results concerning the effects of the tempering heat treatment applied to a quenched Cu-Zn-Al shape memory alloy. The alloy was quenched (800°C/ 5 hours/ water) and tempered (300°C/5, 10, 15, 20, 25 min/ water). The effects of tempering are investigated by optical microscopy and tensile testing. The results shown that with increasing the tempering time the initial martensitic phase is gradually transformed into a martensite +  $\alpha$  phase structure. Owing to the  $\alpha$ -phase occurrence, which is maintained within the elastic field during loading, the alloy becomes stiffer and presents a work hardening tendency.

**Keywords:** shape memory alloy; martensite; optical microscopy, tensile testing

### 1. INTRODUCTION

Cu-Zn-Al Shape Memory Alloys (SMAs) are ranked on the second place among commercially available materials that present Shape Memory Phenomena [1]. However, during functioning a marked tendency has been reported for thermomechanical fatigue which induces important changes of the critical transformation temperatures [2].

The temperature-transformation-time (TTT) diagram for Cu-Zn-Al SMAs with the typical chemical composition is shown in Fig.1

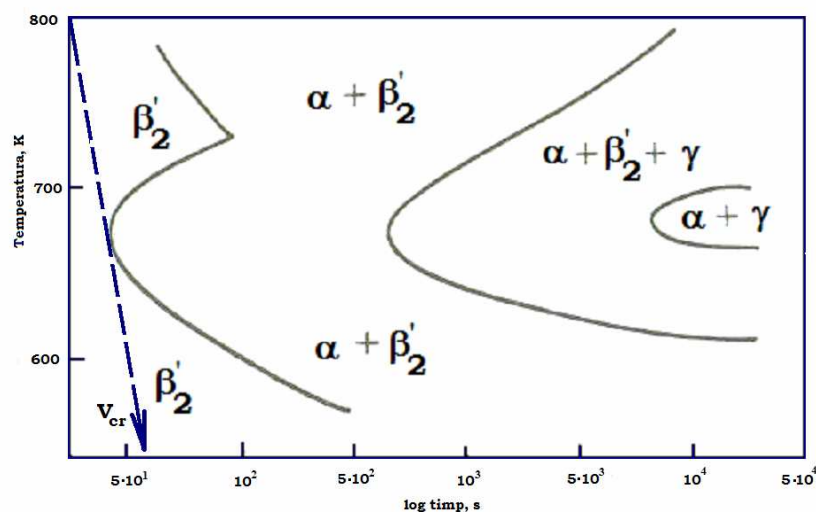


Fig.1 TTT diagram for a Cu-20 Zn-5 Al SMA [3]

From the diagram it is noticeable that the transformation curves are not clearly defined below 600 K (327<sup>0</sup>C), especially for isothermal maintaining times longer than 500 seconds (about 8 minutes) [3].

The purpose of the present paper is to report the effects of increasing the maintaining time at the tempering heat treatment applied to a quenched Cu-Zn-Al SMA.

## 2. EXPERIMENTAL DETAILS

The experiments were performed using a Cu-21.57 Zn-7 Al (wt. %) SMA which was subjected to optical microscopy observations and tensile tests. All the details concerning specimen preparation and the experimental devices employed were given in a previous paper [4].

## 3. RESULTS AND DISCUSSION

The optical micrographs are summarized in Fig.2.

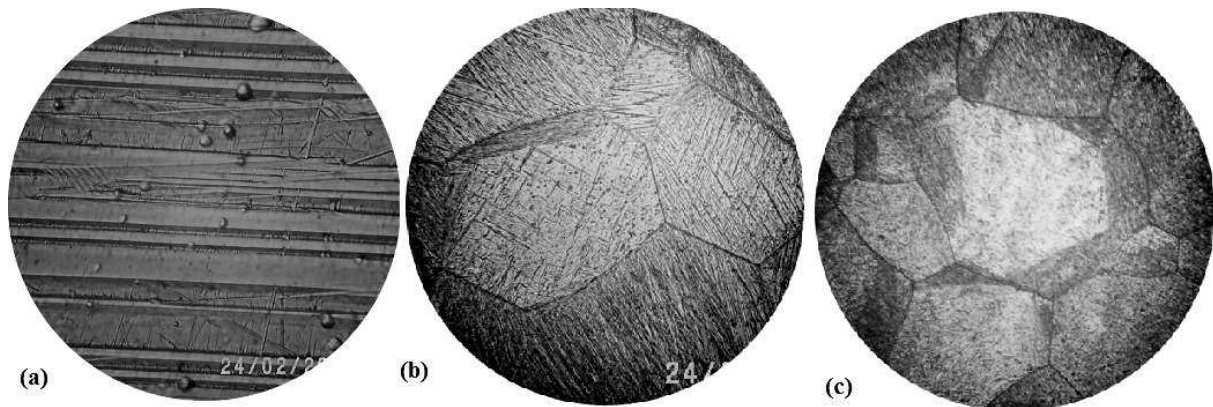


Fig.2 Summary of the optical micrographs recorded on the Cu-21.57 Zn-7 Al (wt. %) SMA: (a) in quenched state (2000:1); (b) after 10 minutes maintaining at 300<sup>0</sup>C (250:1); (c) after 25 minutes maintaining at 300<sup>0</sup>C (250:1)

In Fig.2(a) the disposal mode of the martensite plates, of the quenched specimen is noticeable. The plates crossed during their growth the entire former austenite grains. Their substructure has perfectly parallel sides as an effect of the complete crossing of the grains. A part of the plates have a substructure with internal faults. However one should have in mind that, in spite of the presence of internal faults, the martensite plates are accommodated by twinning.

In Fig.2(b) the coexistence of martensite with  $\alpha$ -phase is noticeable, after 10 minute maintaining at 300<sup>0</sup>C.

In Fig.2(c) the complete disappearance of martensite is revealed, therefore the initial martensite structure decomposed into the  $\alpha$ -phase the amount of which increases with the tempering time.

The effects of increasing the tempering time on the tensile behaviour are summarized in Fig.3.



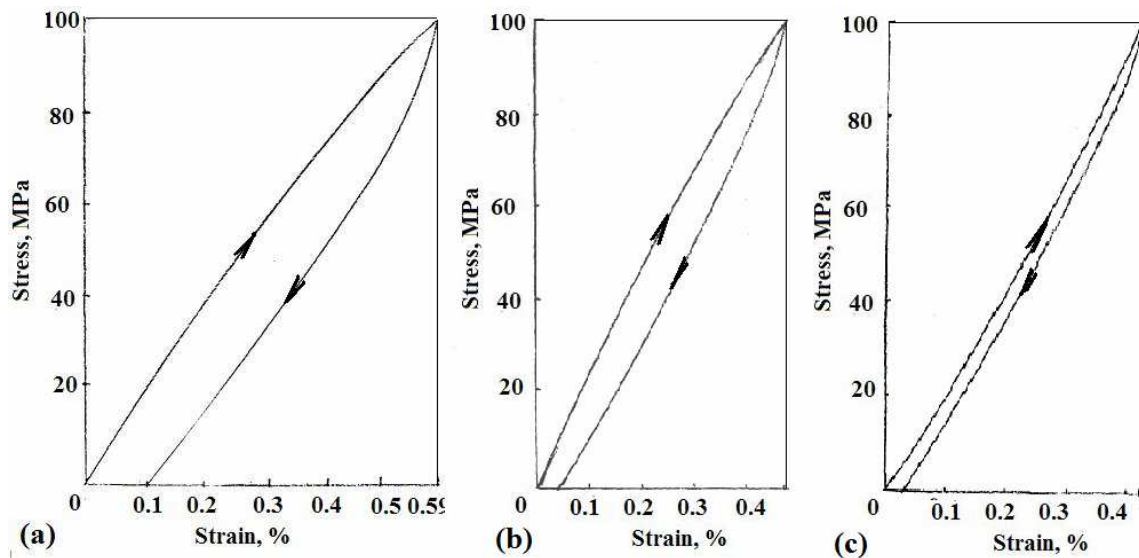


Fig.3 Tensile loading-unloading curves, recoded on the Cu-21.57 Zn-7 Al (wt. %) SMA: (a) in quenched state; (b) after 10 minutes maintaining at 300<sup>0</sup>C; (c) after 25 minutes maintaining at 300<sup>0</sup>C

In this case, increasing tempering time cause the reduction of the loop area the decrease of total strain and a slight work hardening tendency illustrated by the gradual increase of the Young modulus on loading, in Fig.3(c), corresponding to the specimen tempered for 25 minutes at 300<sup>0</sup>C.

#### 4. CONCLUSIONS

In the case of a quenched Cu-21.57 Zn-7 Al (wt. %) SMA the effects of increasing the maintaining time at 300<sup>0</sup>C were emphasized under the form of  $\alpha$ -phase formation from thermally induced martensite. As an effect of  $\alpha$ -phase formation, the alloy became stiffer and presented a slight work hardening tendency. This effect was caused by the fact that the  $\alpha$ -phase did not reach its yield limit on loading up to 100 MPa.

#### ACKNOWLEDGEMENTS

This paper was financially supported by the the Romanian Ministry of Education and Research, under CNCSIS Grant No.476/ 2005

Received: May 19 2005

The "Gh.Asachi" Technical University from Iasi

#### REFERENCES

1. Wu, M.H. – *Cu-based shape memory alloys*, **Eng.Asp.Shape Mem.All.** (Duerig, T.W. *et al.* eds.) Butterworth-Heinemann, 1990, **69-88**
2. Hornbogen, E. – *Fatigue of copper based shape memory alloys*, **Eng.Asp.Shape Mem.All.** (Duerig, T.W. *et al.* eds.) Butterworth-Heinemann, 1990, **267-280**.
3. Van Humbeeck, J. and Stalmans, R. – *Characteristics of shape memory alloys*, **Shape Memory Materials**, (Otsuka, K. and Wayman, C.M., eds.), Cambridge University Press, 1998, **149-183**

4. Leandru-Gheorghe Bujoreanu, Corneliu Munteanu, Iulian Ioniță, Mitică Temneanu And Viorel Kogăniceanu - *On the shape memory behaviour of Cu-based alloys and polyethylene terephthalate (PET)*, Buletinul Institutului Politehnic Din Iași, Tomul LI(LV), Fasc.4, 2005, Secția ȘTIINȚA ȘI INGINERIA MATERIALELOR, **43-50**

## **EFECTELE REVENIRII ASUPRA MICROSTRUCTURII ȘI COMPORTĂRII LA TRACȚIUNE A UNUI ALIAJ Cu-Zn-Al CU MEMORIA FORMEI**

**(Rezumat)**

**Abstract** Lucrarea prezintă unele rezultate experimentale referitoare la efectele tratamentului termic de revenire aplicat unui aliaj Cu-Zn-Al, călit, cu memoria formei. Aliajul a fost călit ( $800^{\circ}\text{C}/5$  ore/ apă) și revenit ( $300^{\circ}\text{C}/5, 10, 15, 20, 25$  min/ apă). Efectele revenirii sunt cercetate prin microscopie optică și încercări la tracțiune. Rezultatele arată că, odată cu creșterea duratei de revenire, faza martensită inițială se transformă treptat într-o structură de martensită + fază  $\alpha$ . Din cauza apariției fazei  $\alpha$ , care în timpul încărcării este menținută în domeniul elastic, aliajul devine mai rigid și prezintă o tendință de ecruisare.

## DES RECHES CONCERNANT L'INFLUENCE DE LA TEMPÉRATURE DE CHAUFFAGE PRÉALABLE DE LA COQUILLE SUR LES PROPRIÉTÉS MÉCANIQUES D'UN BRONZE ANTIFRICTION COULÉ PAR CENTRIFUGATION

FLORIN DIACONESCU, IOAN ALEXANDRU et IOAN CARCEA

*Resumé:* À la coulée centrifuge on utilise des moules permanents qui sont chauffés pour éviter le choc thermique et pour l'acrosissement de la résistance en exploitation. La température de chauffage préalable doit être choisie avec discernement parce qu'elle a une influence sur l'échange de chaleur entre l'alliage liquide et la coquille en déterminant une certaine structure du matériel de la pièce coulée.

*Dans la présente on étudie l'influence de la température de chauffage préalable sur les propriétés mécaniques d'un bronze antifricion, en suivant la limitation de la tendance de ségrégation du plomb.*

*Mots clef:* la température de chauffage préalable de la coquille, l'échange de chaleur, microstructure, les propriétés mécaniques de la pièce coulée.

### 1. Introduction

L'acrosissement de la résistance des coquilles est une préoccupation permanente parce qu'il assure la diminution des frais de fabrication, des durées de stationnement et croît la productivité du travail.[1]

Bien que les moules permanents sont protégés avec une peinture réfractaire d'isolation, la température de chauffage préalable est importante parce qu'elle influence le champ des températures du système alliage liquide-moule et la transmission du chaleur en déterminant la finesse de la structure et les propriétés de la pièce coulée. Plus que la température de chauffage préalable est plus haute, plus l'échange du chaleur entre l'alliage liquide et la coquille est plus lent et la structure est plus grossière[3]

Par d'ailleurs, une température de chauffage plus baissée détermine la réduction de la résistance de la coquille et l'augmentation des frais de fabrication.

### 2. La méthodologie de la recherche

En vue des recherches ont coulé par centrifugation en bronze antifricion CuPb10Sn10 des manchons avec les dimensions Ø120/Ø30/120 mm en utilisant une machine avec l'axe verticale de rotation.

La coquille a eu la rotation  $n = 900$  rot/min et différentes températures de chauffage:  $60^{\circ}\text{C}$ ;  $220^{\circ}\text{C}$ ;  $280^{\circ}\text{C}$  et  $300^{\circ}\text{C}$ . La température de la coquille a été mesurée par un thermomètre digital type TM 1300 fabriqué par BEHA (Allemagne). La température de coulée de l'alliage a été constante ( $1180^{\circ}\text{C}$ ) pour éliminer l'influence de ce facteur technologique sur les propriétés des pièces.

Dès manchons, de cette façon obtenus, ont confectionné des échantillons, pour essais à traction, prélevés de zone extérieure (e), moyenne (m) et intérieure (i).

Les essais à traction ont été effectués à une machine type MTS 810 (Material Test System) avec un système de traçage de la diagramme force-allongement et un extensomètre pour la détermination d'allongement. Ont utilisé des échantillons *proportionnel-normales*, avec le facteur dimensionnel  $n = L_0/d_0 = 5$  et le diamètre  $d_0 = 5$  mm.

La méthodologie d'essai a observé les prévisions de SR EN 10 002 – 1 : 1995

### 3. Les résultats expérimentaux et leur interprétation

Dans le tableau 1 sont présentés les propriétés mécaniques des pièces coulées par centrifugation en bronze antifriction CuPb10Sn10 en dépendance de différentes températures de chauffage préalable de la coquille.

La littérature de spécialité recommande, à la coulée centrifuge des bronzes en Sn et Pb, l'utilisation des températures de chauffage préalable sous  $100^{\circ}\text{C}$  pour prévenir la ségrégation "à rayures" du plomb [2]. Cependant, dans la pratique, ont utilisent des températures de chauffage préalable plus hautes [4] et voilà pourquoi nous avons employé des températures de  $220^{\circ}\text{C}$ ;  $280^{\circ}\text{C}$  et  $300^{\circ}\text{C}$  pour observer leur influence sur les propriétés des pièces coulées par centrifugation.

Pour la zone extérieure (e) on observe que la résistance à la rupture baisse avec la température de chauffage préalable de  $301,83\text{ N/mm}^2$  jusqu'à  $240,51\text{ N/mm}^2$ . Cette diminution s'explique par l'intensité réduite de l'échange de chaleur entre l'alliage et le moule, qui a déterminé la diminution du degré de finissage de la structure.

Tableau 1. Les propriétés mécaniques des pièces coulées à différentes températures de chauffage préalable

Symbol de l'échantillon	Température de la coquille [ $^{\circ}\text{C}$ ]	La zone de prélèvement	La résistance à la rupture, $R_m$ [ $\text{N/mm}^2$ ]	La limite d'écoulement, $R_e$ [ $\text{N/mm}^2$ ]	L'allongement à la rupture, $A_5$ [%]
PM T <sub>f</sub> 1	60	e	301,83	111,98	12,40
		m	286,60	110,62	12,82
		i	273,46	103,09	13,40
Pm T <sub>f</sub> 2	220	e	299,10	115,15	12,45
		m	282,11	104,38	12,93
		i	247,17	93,67	14,65
PM T <sub>f</sub> 3	280	e	256,17	87,35	13,83
		m	260,11	84,33	13,62
		i	238,34	77,46	16,47
PM T <sub>f</sub> 4	300	e	240,51	84,18	15,11
		m	243,90	81,35	15,23
		i	214,35	69,07	17,56

Ainsi, à la coulée dans la coquille chauffée à 60 °C la solution solide  $\alpha$  a un aspect dendritique estompé en présentant des petites dendrites isolées, mais avec la croissance de la température l'aspect dendritique est graduellement prononcé. Quand la température de chauffage de la coquille croît, les dendrites se ramifient et les dimensions des axes primaires et secondaires croissent et à la température de 300 °C croît et leur épaisseur. L'eutectoïde ( $\alpha+\delta$ ) est plus uniformément distribué pour la pièce coulée dans le moule chauffé à 60 °C et aux températures plus élevées les zones ( $\alpha+\delta$ ) sont plus étendues et plus rares.

L'analyse d'image, effectuée à la ligne d'analyse assistée par ordinateur, a montré que les séparations de Pb occupent individuellement des aires sous 50  $\mu\text{m}^2$  (60,9% du nombre total) et de 50-100  $\mu\text{m}^2$  (35%) pour la pièce coulée dans la coquille chauffée à 60 °C, mais à 300 °C la surface occupée individuellement croît jusqu'à 50-100  $\mu\text{m}^2$  pour 89,4 % du nombre total de séparations et justement à 100-400  $\mu\text{m}^2$  pour 11,6 % du nombre total de séparations.

Le degré de sphéroïdisation (GS) des séparations de Pb a été 0,5-0,7 pour 48,7% du nombre total des séparations et 0,7-0,9 (30,44% des séparations) pour la pièce coulée dans la coquille chauffée à 60 °C et dans le cas de la pièce coulée dans la coquille chauffée à 300 °C, GS = 0,5-0,7 pour 34,4% du nombre total de séparations, GS = 0,7-0,8 pour 20,6%, mais on a constaté que 21% du nombre total de séparations ont eu GS=0,36-0,52. Donc GS c'est différent avec la croissance de la température de chauffage préalable de la coquille.

Vis-à-vis de la zone extérieure, la zone moyenne (m) a présenté une microstructure avec un aspect dendritique plus prononcé, mais on a constaté une diminution du degré de finissage de la structure avec l'acroissement de la température de chauffage de la coquille. La pièce coulée dans la coquille chauffée préalable à 60 °C a présenté dans la microstructure des dendrites de solution solide  $\alpha$  et des zones fines d'eutectoïde ( $\alpha+\delta$ ). Les dimensions des axes primaires ont crû de 200-300  $\mu\text{m}$  ( $t=220^\circ\text{C}$ ) jusqu'à 300-500  $\mu\text{m}$  ( $t=280^\circ\text{C}$ ) et jusqu'à 400  $\mu\text{m}$  pour la température de chauffage de 300 °C. De même, ont crû les dimensions des axes secondaires et tertiaires qui ont devenu graduellement plus épaisses, en ferment entre elles des zones plus étendues d'eutectoïde ( $\alpha+\delta$ ).

L'analyse d'image a montré que l'aire occupée individuellement par les séparations de Pb a crû, avec la température de chauffage de la coquille, de 0-70  $\mu\text{m}^2$  pour 62,5% du nombre total de séparations ( $t = 220^\circ\text{C}$ ), jusqu'à 0-175  $\mu\text{m}^2$  pour 94,2% du nombre total de séparations ( $t = 300^\circ\text{C}$ ).

En même temps le degré de sphéroïdisation des séparations de Pb c'est diversifié avec l'augmentation de la température de chauffage, la quantité des séparations avec GS = 0,7-0,9 a crû de 28,7% ( $t = 60^\circ\text{C}$ ) jusqu'à 48,93% ( $t = 280^\circ\text{C}$ ) et puis a baissé jusqu'à 14,5% du nombre total de séparations ( $t = 300^\circ\text{C}$ ).

Les modifications structurales et la distribution du Pb expliquent l'acroissement de l'allongement à la rupture avec l'augmentation de la température de chauffage de la coquille.

La résistance à la rupture des échantillons prélevés de zone intérieure (i) des pièces a baissé de 273,46 N/mm<sup>2</sup> jusqu'à 214,35 N/mm<sup>2</sup> avec l'acroissement de la

température de chauffage préalable de 60<sup>0</sup>C jusqu'à 300<sup>0</sup>C, mais l'allongement à la rupture a crû de 13,40% jusqu'à 17,56%.

L'étude microscopique a relevé le fait que la microstructure a présenté des dendrites de solution solide  $\alpha$  ayant dimensions en peu réduits que celles de zone moyenne. À la température de chauffage de 280-300<sup>0</sup>C on a constaté l'accroissement de la grosseur des axes dendritiques et une ramification diminuée, ce qui a déterminé l'apparition des zones étendues et isolées d'eutectoïde ( $\alpha+\delta$ ).

L'analyse d'image a montré que l'aire occupée individuellement par les séparations de Pb a crû, avec la température de chauffage, de 0-250  $\mu\text{m}^2$  pour 95-99% du nombre total ( $t = 60^0 \text{ C}$ ), jusqu'à 0-375  $\mu\text{m}^2$  ( $t = 220^0 \text{ C}$ ) et puis a baissé à 0-300  $\mu\text{m}^2$  ( $t = 280^0 \text{ C}$ ) et à 0-200 $\mu\text{m}^2$  ( $t = 300^0 \text{ C}$ ).

La quantité de séparations de Pb avec GS=0,3-0,7 a baissé de 67,7% ( $t = 60^0 \text{ C}$ ), jusqu'à 54,6% ( $t = 300^0 \text{ C}$ ), mais à la température de chauffage  $t = 300^0 \text{ C}$  ont apparu encore 25,4% séparations avec GS = 0,2-0,3 et séparations avec GS = 0,7-0,9.

Les propriétés plastiques des pièces coulées par centrifugation en bronze antifriction, ont crû avec l'augmentation de la température de chauffage préalable de la coquille.

#### 4. Conclusions

L'accroissement de la température de chauffage préalable de la coquille à la coulée centrifuge du bronze CuPb10Sn10 détermine la réduction de la résistance à la rupture et l'augmentation d'allongement à la rupture.

Quand la température de chauffage de la coquille croît, l'intensité de l'échange de chaleur entre l'alliage liquide et le moule se réduit, ce qui détermine une diminution du degré de finissage de la structure. Toutefois, la structure de la zone extérieure (e) et intérieure (i) est un peu plus fine comme celle de la zone moyenne (m), ce qui détermine l'obtention d'une résistance à la rupture plus grande et un allongement à la rupture plus réduit.

Le degré de dispersion d'eutectoïde ( $\alpha+\delta$ ) baisse avec l'accroissement de la température de chauffage et croît l'aire occupée individuellement par les séparations de Pb.

Les recherches ont confirmé que la coulée centrifuge du bronze CuPb10Sn10, dans les coquilles chauffées jusqu'à 100<sup>0</sup>C, assure une bonne résistance mécanique et des propriétés antifriction correspondantes, données par le grand degré de dispersion des constituants métallographiques.

#### BIBLIOGRAPHIE

1. Alexandru, I. ș.a. – *Alegerea și utilizarea materialelor metalice*, Editura Didactică și Pedagogică, București, 1997.
2. Colan, H., Tudoran, P., Ailincăi, G., Marcu, M., Drugescu, E. – *Studiul metalelor*, Editura Didactică și Pedagogică, București, 1983.
3. Sofroni, L., Brabie, V., Bratu, C – *Bazele teoretice ale turnării*, Editura Didactică și Pedagogică, București, 1980.
4. Ștefănescu Claudiu ș.a. – *Îndrumătorul proiectantului de tehnologii în turnătorii*, Editura Tehnică, București, 1986.

*Reçue le 15 Avril 2005*

Université Tehnique " Gh. Asachi" Jassy

FLORIN DIACONESCU, Université Tehnique " Gh. Asachi" Jassy  
IOAN ALEXANDRU, Université Tehnique " Gh. Asachi" Jassy  
IOAN CARCEA, Université Tehnique " Gh. Asachi" Jassy

**CERCETĂRI PRIVIND INFLUENȚA TEMPERATURII DE PREÎNCĂLZIRE A COCHILEI  
ASUPRA PROPRIETĂȚILOR MECANICE ALE UNUI BRONZ ANTIFRICȚIUNE TURNAT  
CENTRIFUGAL**

**Rezumat:** La turnarea centrifugă se folosesc forme permanente care se preîncălzesc pentru evitarea șocului termic și pentru creșterea durabilității. Temperatura de preîncălzire trebuie aleasă cu mult discernământ, deoarece ea influențează asupra schimbului de căldură dintre aliajul lichid și formă, determinând o anumită structură a materialului piesei turnate. În lucrare se studiază influența temperaturii de preîncălzire asupra proprietăților mecanice ale unui bronz antifricțiune, urmărindu-se limitarea tendinței de segregare a plumbului.





## DES RECHERCHES CONCERNANT L'INFLUENCE DE LA TEMPÉRATURE DE CHAUFFAGE PRÉALABLE SUR LA DISTRIBUTION DU Pb DANS LES PIÈCES COULÉES PAR CENTRIFUGATION EN BRONZE CuPb10Sn10

FLORIN DIACONESCU et ROMEU CHELARIU

**Résumé:** Les coquilles se chauffent en préalable pour prévenir le choc thermique et, par conséquence, la diminution de la résistance en exploitation. La température de chauffage préalable influence sur l'échange de chaleur entre l'alliage liquide et la coquille, donc sur la vitesse de solidification. À son tour, la vitesse de solidification détermine une certaine finesse de la structure et voilà pourquoi dans le présent ouvrage on suit le choix d'une température de chauffage qui peut assurer une ségrégation minimale du Pb et sa distribution plus uniforme, pour augmenter la qualité des pièces coulées.

**Mots clef:** la température de chauffage préalable, l'échange de chaleur, la ségrégation minimale du Pb, la distribution uniforme.

### 1. Introduction

La température de chauffage préalable des coquilles doit être choisie avec discernement parce qu'elle présume un compromis entre la consommation d'énergie thermique nécessaire pour chauffage et la résistance en exploitation. Quand ces deux aspects économiques ne conduisent pas à une solution, le facteur décisif devient l'assurance de la qualité du produit.

La température de chauffage préalable influence le champ des températures, l'intensité d'échange de chaleur, la vitesse de solidification, la structure et le degré de finissage des constituants métallographiques.

Dans les alliages antifriction Cu-Pb-Sn utilisés pour les coussinets, le plomb a la tendance de ségrégation selon le poids spécifique, ce qui détermine une hétérogénéité de la structure et des propriétés des pièces coulées.

À la même épaisseur de paroi, la ségrégation croît avec la diminution de la vitesse de solidification, parce qu'on produit une stratification du liquide selon le poids spécifique. C'est pourquoi la littérature de spécialité recommande au coulage des alliages Cu-Pb que la température de chauffage préalable des coquilles être sous 100<sup>0</sup>C [2]. Toutefois, dans la pratique, on utilise des températures plus hautes, jusqu'à 300<sup>0</sup>C, parce que aux coulages répétés les moules métalliques accumulent la chaleur de l'alliage liquide.

Puisque les alliages Cu-Pb-Sn se distinguent du point de vue structural, dans le

présent ouvrage on étudie et l'influence des autres températures, plus hautes que celles recommandées par la littérature de spécialité, sur la distribution du Pb.

## 2. La méthodologie de recherche

En vue des recherches ont coulé par centrifugation en bronze antifriction CuPb10Sn10 des manchons avec les dimensions  $\varnothing 120/\varnothing 30/120$  mm en utilisant une machine avec l'axe verticale de rotation. Les pièces ont coulé à la même rotation  $n=900$  rot/min et la température de coulée a été dans tous les cas de  $1180^{\circ}\text{C}$  pour éliminer l'influence de ces facteurs sur la structure.

Les températures de chauffage préalable, mesurées par un thermomètre type TM 1300 fabriqué par BEHA (Allemagne), ont été de  $60^{\circ}\text{C}$ ,  $220^{\circ}\text{C}$ ,  $280^{\circ}\text{C}$  et  $300^{\circ}\text{C}$  [1]. Dès pièces coulées par centrifugation ont prélevé des échantillons de trois places différentes et puis ont effectué des analyses chimiques des divers points situés à direction du rayon, dans les zones extérieures (e), moyennes (m) et intérieures (I), ainsi que sur l'hauteur de la pièce, dans les zones supérieures (I), centrales (II) et inférieures (III). Avec les valeurs obtenues ont été construit des diagrammes de la distribution du Pb sur la surface des échantillons (figure 1). Pour étudier la distribution et la forme des séparations de Pb, ont effectué des analyses d'image à la ligne d'analyse assistée par ordinateur de la Faculté de Science et Génie de Matériaux de Bucarest.

## 2. Les resultants expérimentaux et discussions

Dans le cas de la pièce coulé dans la coquille chauffé à  $60^{\circ}\text{C}$  (figure 1.a) on constate un contenu plus grand de Pb dans la zone extérieure-supérieure (I e) fait expliqué par la grande vitesse de refroidissement qui a déterminé la solidification rapide de la solution solide  $\alpha$  et l'inclusion du Pb expulsé vers l'extérieur par la force centrifuge. Sur l'hauteur de la pièce le plomb est distribué inégal, c'est-à-dire à la partie supérieure (I) et centrale (II) le contenu de Pb est de 9,05% , mais à la partie inférieure baisse de 8,95% jusqu'à 8,65%. Dans la zone intérieure (i) on constate que le contenu de Pb croît graduellement de 8,45% jusqu'à 8,85% tandis que les lignes de distribution sont presque parallèles à la partie supérieure (I) et centrale (II).

De l'analyse d'image a résulté que dans la zone extérieure (e) l'aire occupée individuellement par les séparations de Pb a été sous  $100 \mu\text{m}^2$  pour 91,4% du nombre total, dans la zone moyenne (m) de  $500 - 1000 \mu\text{m}^2$  pour 96% du nombre total et pour la zone intérieure (i) l'aire a baissé sous  $250 \mu\text{m}^2$  pour 94% du nombre des séparations, parce que la vitesse du refroidissement à la surface intérieure a été plus grande.

Dans la zone extérieure 48,7% du nombre total des séparations de Pb ont eu le degré de sphéroïdisation  $GS = 0,5-0,7$ , dans la zone moyenne 48,83% et dans la zone intérieure 31,9%.

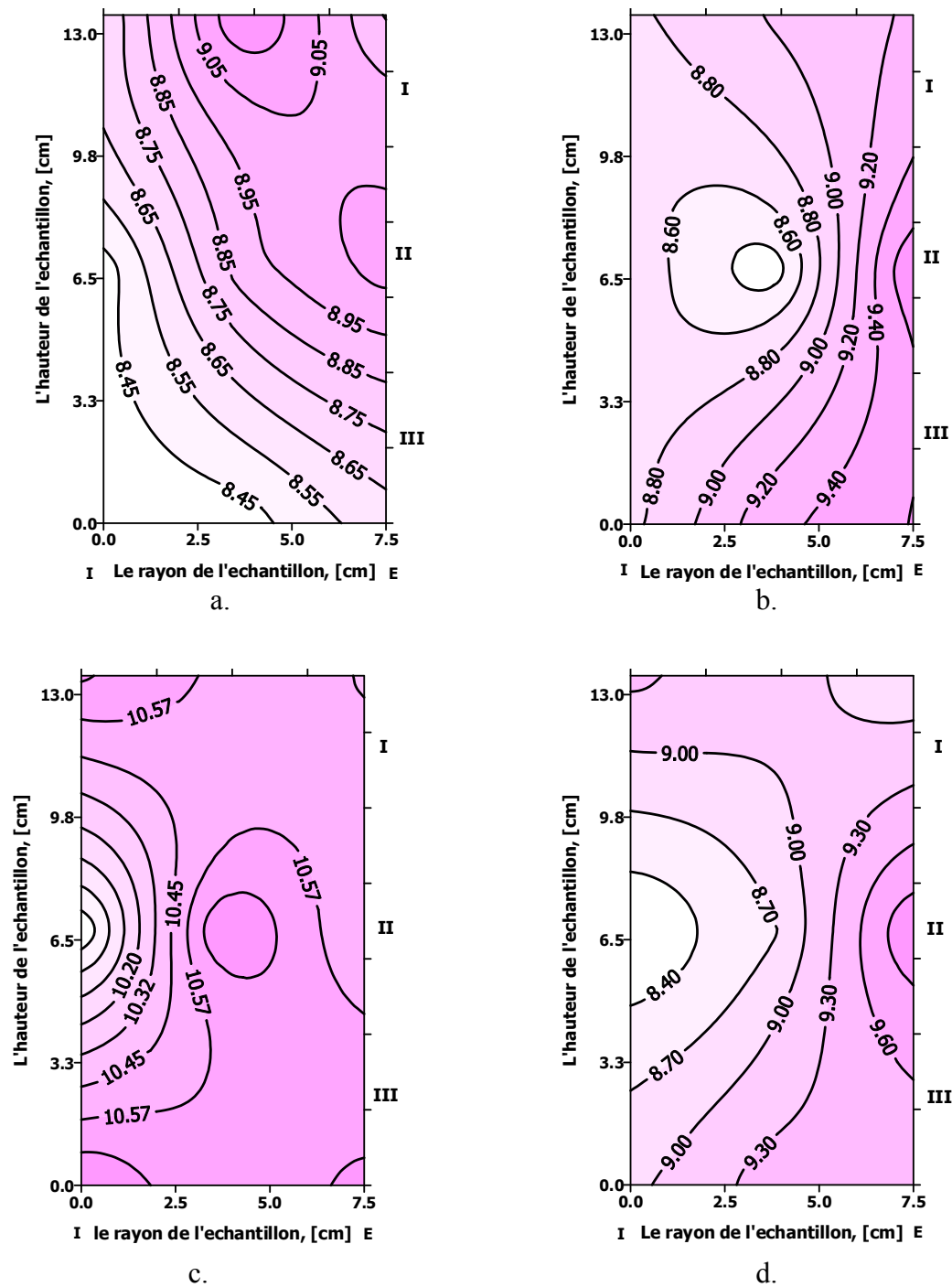


Figure 1. Les diagrammes de variation du contenu de Pb sur la section longitudinale des pièces coulées par centrifugation à différentes températures de chauffage de la coquille:

a)  $t = 60^{\circ}\text{C}$ ; b)  $t = 220^{\circ}\text{C}$ ; c)  $t = 280^{\circ}\text{C}$ ; d)  $t = 300^{\circ}\text{C}$

En même temps dans la zone extérieure 33,44% du nombre total des séparations de Pb ont eu  $GS = 0,7 - 0,9$  tandis que dans la zone moyenne et intérieure le degré de sphéroïdisation a baissé jusqu'à 0,3 - 0,5 pour 43% respectivement 36,7% du nombre

des séparations, parce que les dendrites de solution solide  $\alpha$  ont eu des ramifications plus grands que dans la zone extérieure.

Pour la pièce coulée par centrifugation dans la coquille chauffée à 220°C (figure 1.b) on a constaté que dans la zone extérieure le contenu de Pb est plus grand, mais constant sur l'hauteur de la pièce. Dans la zone moyenne (m) le contenu de Pb est en peu élevé dans la partie supérieure (I m) et inférieure (III m), mais dans la zone centrale (II m) on constate un contenu minimal qui ne peut pas diminuer les propriétés antifriction de la pièce.

Dans la zone intérieure (i) le contenu de Pb est de même plus grand à la zone supérieure (I i) et inférieure (III i). L'accroissement de la température de chauffage a réduit l'intensité de l'échange de chaleur et a permis une petite ségrégation du Pb vers l'extérieur de la pièce.

L'analyse d'image a montré que dans la zone extérieure les aires occupées par les séparations de Pb sont différentes: sous 80  $\mu\text{m}^2$  (84,3% du nombre total des séparations), de 80 – 160  $\mu\text{m}^2$  (10,5%) et de 160 – 750  $\mu\text{m}^2$  (5%). Dans la zone moyenne (m) 62,5% du nombre total des séparations de Pb ont l'aire occupée sous 70  $\mu\text{m}^2$ , 22,3% ont l'aire de 70 – 130  $\mu\text{m}^2$  et le reste ont l'aire de 130 – 600  $\mu\text{m}^2$ . Dans la zone intérieure 96,5% du nombre total des séparations ont eu l'aire sous 375  $\mu\text{m}^2$  et 3,5% ont eu l'aire de 375 - 700  $\mu\text{m}^2$ .

L'accroissement de la température de chauffage a déterminé l'extension des aires occupées individuellement par les séparations de Pb.

Le degré de sphéroïdisation a été  $G_s = 0,4 - 0,9$  pour 52,97% du nombre total des séparations de Pb à l'extérieur, dans la zone moyenne (m) pour 66,35% et dans la zone intérieure (i) a baissé jusqu'à  $G_s = 0,3 - 0,7$  pour 66,3% du nombre total des séparations.

Dans le cas de la pièce coulée dans la coquille chauffée à 280°C (figure 1.c), on a constaté un contenu de Pb plus grand (10,57%) dans la zone extérieure (e) et moyenne (m) et une distribution uniforme sur l'hauteur de la pièce. Dans la zone intérieure (i) on observe une distribution inégale du contenu de Pb sur l'hauteur de la pièce ce qui réduit les propriétés antifriction.

L'analyse d'image a montré que l'aire occupée individuellement par les séparations de Pb a crû jusqu'à 120  $\mu\text{m}^2$  pour 83,4% du nombre total dans la zone extérieure, jusqu'à 130  $\mu\text{m}^2$  pour 87,1% dans la zone moyenne et jusqu'à 300  $\mu\text{m}^2$  dans la zone intérieure.

Dans la zone extérieure  $G_s$  a été différent:  $G_s = 0,26 - 0,33$  (pour 30% du nombre total),  $G_s = 0,55 - 0,8$  (pour 33,38%) et  $G_s = 0,55 - 0,8$  (pour 35,1%). Dans la zone moyenne  $G_s = 0,4 - 0,7$  pour 55,4% du nombre total des séparations de Pb et  $G_s = 0,7 - 0,9$  pour 36,5% des séparations. Dans la zone intérieure 28,95% des séparations ont eu  $G_s = 0,3 - 0,53$  et 26,68% ont eu  $G_s = 0,53 - 0,76$ .

L'accroissement de la température de chauffage a réduit l'intensité de l'échange de chaleur et a déterminé une ramification plus puissante des dendrites de solution solide  $\alpha$  et la diversification du  $G_s$  à l'extérieur.

À la pièce coulée par centrifugation dans la coquille chauffée à 300°C (figure 1.d), on a constaté un contenu de Pb plus grand dans la zone centrale-extérieure (II e), mais dans la zone moyenne le contenu de Pb a été approximativement constant sur

l'hauteur de la pièce et dans la zone intérieure c'est enregistré un contenu minimal dans la zone centrale (II i).

L'analyse d'image a montré que dans la zone extérieure l'aire occupée individuellement par les séparations de Pb a baissé sous  $100 \mu\text{m}^2$  pour 89,4% du nombre total des séparations, mais ont apparu des séparations avec l'aire de  $100 - 200 \mu\text{m}^2$  (7%) et même de  $200 - 400 \mu\text{m}^2$  (4,6%). Vis-à-vis d'échantillon précédent dans la zone moyenne l'aire occupée a crû jusqu'à  $175 \mu\text{m}^2$  pour 94,2% du nombre des séparations et dans la zone intérieure a baissé jusqu'à  $200 \mu\text{m}^2$ , mais a crû le nombre des séparations avec l'aire de  $200 - 600 \mu\text{m}^2$ .

Le degré de sphéroïdisation (GS) est très différent dans toutes les zones. La majorité des séparations avec  $GS = 0,5 - 0,75$  représentaient 33% du nombre total dans la zone extérieure, 51,8% dans la zone moyenne et 29,8% dans la zone intérieure. La ramification prononcée des dendrites et la vitesse réduite de solidification ont produit une différenciation du degré de sphéroïdisation sur la section de la pièce et une grande hétérogénéité structurale.

#### 4. Conclusions

L'accroissement de la température de chauffage préalable de la coquille produit une distribution hétérogène du contenu de Pb sur la section de la pièce coulée par centrifugation, c'est - à - dire croît graduellement le contenu de plomb vers l'extérieur ce qui conduit à une légère diminution de la dureté, mais qui n'affecte pas les propriétés antifriction.

Avec la croissance de la température de chauffage l'hétérogénéité chimique s'intensifie en enregistrant la diminution du contenu de Pb dans la zone centrale-intérieure (II i) ce qui peut réduire les propriétés antifriction.

L'aire occupée individuellement par les séparations de Pb croît avec la température de chauffage dans toutes les zones, donc baisse le degré de finissage des séparations de plomb et se diversifie le degré de sphéroïdisation.

Donc à la coulée par centrifugation des bronzes Cu-Pb-Sn on recommande d'employer une température de chauffage préalable de  $60-100^{\circ}\text{C}$  pour limiter la ségrégation du Pb vers l'extérieur des manchons.

#### BIBLIOGRAPHIE

1. Diaconescu Florin, Carcea Ioan – *Experimental research concerning the influence of mould preheating temperature on the hardness of centrifuge cast parts from antifriction Cu-Pb-Sn bronze*, Buletinul Institutului Politehnic Iași, Tomul L (LIV) Fasc.1, 2004, p.83-88.
2. Iudin, S.B., Levin M.M., Rozenfeld S.E. – *Turnarea centrifugă*, Editura Tehnică, București, 1973

Reçue le 20 Avril 2005

Université Technique "Gh. Asachi" Jassy

FLORIN DIACONESCU, Université Technique "Gh. Asachi" Jassy  
ROMEU CHELARIU, Université Technique "Gh. Asachi" Jassy

**CERCETĂRI PRIVIND INFLUENȚA TEMPERATURII DE PREÎNCĂLZIRE A COCHILEI  
ASUPRA DISTRIBUȚIEI Pb ÎN PIESELE TURNATE CENTRIFUGAL DIN BRONZ Cu-Pb10-Sn10.**

**Rezumat:** Cochilele se preîncălzesc pentru a se preveni șocul termic și, în consecință, scăderea durabilității lor în exploatare. Temperatura de preîncălzire influențează asupra schimbului de căldură dintre aliajul lichid și formă și deci asupra vitezei de solidificare. La rândul ei viteza de solidificare determină o anumită finețe a structurii și de aceea în lucrare se urmărește alegerea unei temperaturi de preîncălzire care poate asigura o segregare minimă a Pb și distribuția sa cât mai uniformă, pentru a crește calitatea pieselor turnate.

## DES RECHERCHES CONCERNANT L'INFLUENCE DE LA ROTATION DE LA COQUILLE SUR LA DISTRIBUTION DU Pb DANS LES PIÈCES COULÉES PAR CENTRIFUGATION EN BRONZE CuPb10Sn10

FLORIN DIACONESCU et ROMEU CHELARIU

*Résumé: Les pièces coulées par centrifugation présentent une hétérogénéité chimique et structurale causée par la solidification dans le champ centrifuge. Dans les alliages antifriction Cu-Pb-Sn le plomb est introduit pour améliorer l'usinage et les propriétés antifriction. Sous l'action de la force centrifuge, Pb a une tendance de ségrégation et voilà pourquoi dans le présent ouvrage on suit la détermination d'une rotation optimale qui peut assurer une distribution plus uniforme du Pb sur la section de la pièce.*

*Mots clef: la hétérogénéité chimique et structurale, la solidification en champ centrifuge, la limitation de la ségrégation du Pb.*

### 1. Introduction

Les matériaux antifriction doivent avoir des structures hétérogènes justement pour satisfaire les nécessités d'exploitation. Ainsi elles doivent contenir des phases malléables en jouant un rôle antigrippaux et des dures phases qui donnent la résistance à l'usure de la matrice.

Dans le cas du bronze CuPb10Sn10 la dureté nécessaire est donnée par la matrice formée de solution solide  $\alpha$  et surtout d'eutectoïde ( $\alpha+\delta$ ) dure mais fragile, parce que la dureté du Pb ( $HB \cong 8$ ) est non significative. Pour obtenir des bonnes propriétés antifriction, il est nécessaire que le plomb être uniformément distribué sur la surface de travail (intérieure) des coussinets, mais par suite de la force centrifuge, qui croît avec la rotation, il a une tendance de ségrégation. C'est pourquoi il est nécessaire à déterminer une rotation optimale qui peut assurer une uniforme distribution du Pb sur la surface de travail et sur la section transversale pour ne diminuer pas la dureté et la résistance à l'usure.

### 2. La méthodologie de recherché

Pour étudier l'influence de la rotation de la coquille sur la distribution du Pb dans les pièces coulées par centrifugation en bronze CuPb10Sn10, ont coulé des manchons ayant les dimensions  $\varnothing 120/\varnothing 30/120$  mm, en utilisant une machine centrifuge avec l'axe verticale de rotation et rotations variables, en employant rotations de 700 rot/min, 800 rot/min, 880 rot/min et 900 rot/min. La gamme restreinte de rotations a été imposée d'un part par la réalisation de la géométrie intérieure des pièces et d'autre part

par la limitation de ségrégation du Pb qui apparaît à rotations plus agrandis que 1000 rot/min.

La température de la coquille a été dans tous les cases de 100<sup>0</sup>C, tandis que la température de coulée d'alliage a été de 1180<sup>0</sup>C.

La composition du bronze CuPb10Sn10 a été celle prévue en STAS 1512-80.

Dès pièces coulées par centrifugation ont prélevé des échantillons de trois places différentes de la pièce et puis ont effectué les analyses chimiques des différents points situés à direction du rayon, dans les zones extérieures (e), moyennes (m) et intérieures (i), ainsi que sur l'hauteur de la pièce, dans les zones supérieures (I), centrales (II) et inférieures (III). Avec les valeurs obtenues ont été construit des diagrammes de la distribution du Pb sur la surface des échantillons prélevés des pièces coulées à différentes rotations. Pour étudier la distribution et la forme des séparations de Pb, ont effectué des analyses d'image à la ligne d'analyse assistée par ordinateur de la Faculté de Science et Génie de Matériaux de Bucarest.

### 3. Les résultats expérimentaux et discussions

Dans la figure 1 sont représentées les diagrammes de variation du contenu de Pb sur la section longitudinale des pièces coulées en bronze CuPb10Sn10 à différentes rotations de la coquille.

Pour la pièce coulée à 700 rot/min (figure 1.a) on observe un contenu plus grand de Pb (10,43%) dans la zone inférieure-extérieure (IIIe) et inférieure – moyenne (III m) par suite de la rotation diminuée qui a permis une petite ségrégation du liquide selon le poids spécifique. Pourtant les valeurs du contenu de Pb sont plus grandes à l'extérieur que l'intérieur.

L'analyse d'image a montré que dans la zone extérieure (e) l'aire occupée individuellement par les séparations de Pb a été sous 250  $\mu\text{m}^2$  pour 95% du nombre total, dans la zone moyenne (m) l'aire occupée a crû jusqu'à 250 – 500  $\mu\text{m}^2$  par suite d'un échange lent de chaleur, mais dans la zone intérieure bien que le contenu de Pb a baissé un peu, l'aire occupée individuellement a crû jusqu'à 500  $\mu\text{m}^2$ . Donc à la rotation réduite la distribution du Pb est inégale.

Les séparations de Pb avec le degré de sphéroïdisation  $GS = 0,3-0,7$  ont représenté à l'extérieur 59,7% du nombre total des séparations, à la zone moyenne a été de 66,65% et dans la zone intérieure de 71,63%.

Dans le cas de la pièce coulée à rotation  $n = 800$  rot/min, la distribution du Pb est plus uniforme que celle du premier cas (figure 1.b). On a constaté l'accroissement du contenu de Pb dans la zone supérieure-extérieure (Ie) et une diminution jusqu'à 9,50% Pb dans la zone centrale-intérieure (II i).

L'analyse d'image a montré que l'aire occupée individuellement par les séparations de Pb est plus réduite à l'extérieur en étant sous 100  $\mu\text{m}^2$  pour 90% du nombre total des séparations et à l'intérieur sous 2500  $\mu\text{m}^2$  pour 98% du nombre total, ce qui s'explique par l'intensification d'échange de chaleur à la croissance de la rotation. En conséquence, ont produit plusieurs cristaux de solution solide  $\alpha$  qui ont été expulsé vers l'extérieur par la force centrifuge, en laissant pour le Pb liquide seulement des petites micro volumes qui n'ont pas permis aux séparations une importante extension.



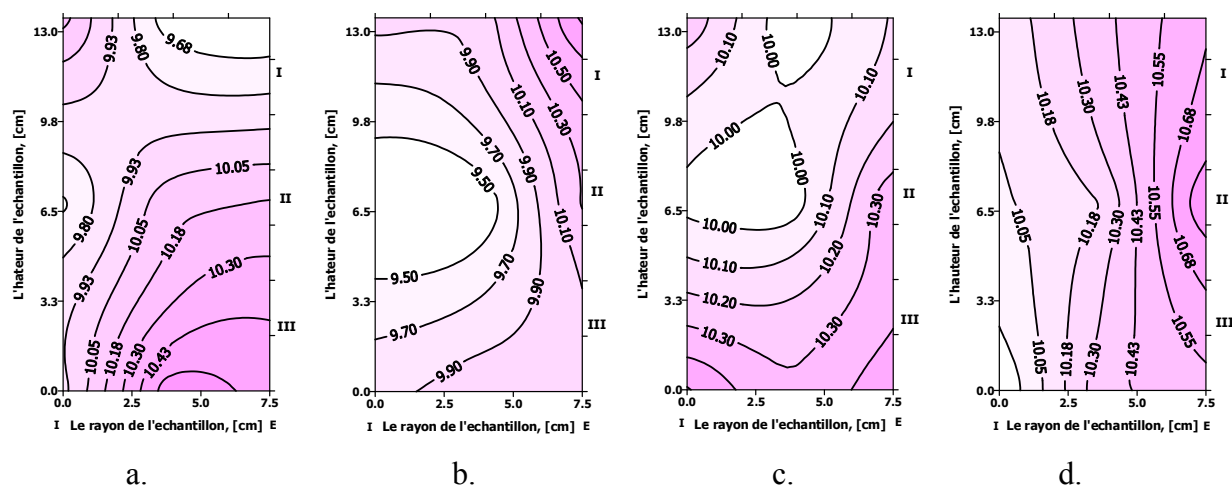


Figure 1. Les diagrammes de variation du contenu de Pb sur la section longitudinale des pièces coulées par centrifugation, à différentes rotations: a)  $n = 700$  rot/min; b)  $n = 800$  rot/min; c)  $n = 880$  rot/min; d)  $n = 900$  rot/min

Les séparations de Pb avec  $GS = 0,3-0,7$  ont représenté à l'extérieur 51,69% du nombre total des séparations, dans la zone moyenne a été de 61,3% et dans la zone intérieure de 66,34%. En même temps ils ont apparu des séparations de Pb avec  $GS = 0,7-0,9$  en quantité de 20% dans la zone extérieure, de 32,1% dans la zone moyenne et de 12,1% dans la zone intérieure. Ce fait s'explique par l'apparition des dendrites ramifiées de solution solide  $\alpha$  dans la zone moyenne.

La pièce coulée à rotation  $n = 880$  rot/min présente une distribution préférable du Pb vers la zone inférieure (III) de l'éprouve, expliquée par la ségrégation selon le poids spécifique puis un contenu de 10% Pb dans la zone centrale-intérieure (II.i) et dans la zone moyenne-supérieure (I.m) comme l'on voit dans la figure 1.c.

L'analyse d'image a montré que l'aire occupée individuellement par les séparations de Pb a été à l'extérieur sous  $100 \mu\text{m}^2$  pour 95% des séparations et à l'intérieur sous  $200 \mu\text{m}^2$  pour 88% des séparations, mais aussi à l'intérieur ils ont apparu des grandes séparations de  $200 - 400 \mu\text{m}^2$  pour 8% du nombre total et justement très grandes ( $400 - 800 \mu\text{m}^2$ ) pour 2,3% des séparations. L'aire des séparations de Pb a baissé vis-à-vis des cases antérieures, ainsi que leur distribution c'est améliorée avec la croissance du degré de finissage de la structure de la matrice. Les séparations de Pb avec  $GS = 0,3 - 0,7$  ont représenté à l'extérieur 67,33% du nombre total, mais dans la zone moyenne et celle intérieure a été 71,78% respectivement 71,42%. Des séparations avec  $GS = 0,7 - 0,8$  ont apparu en quantité de 10,88% dans la zone extérieure (e) et de 12,4% dans la zone intérieure (i).

Enfin, pour la pièce coulée à rotation  $n = 900$  rot/min apparaît une distribution graduelle du Pb, en enregistrant des contenus plus grands à l'extérieur (10,68% Pb) et de plus en plus petits vers l'intérieur (10,05% Pb)

Sur l'hauteur de l'échantillon la distribution du contenu de Pb est presque uniforme (figure 1.d), mais apparaissent les prémisses d'une ségrégation "à rayures".

L'analyse d'image a montré que vis-à-vis des autres échantillons, à la rotation de 900 rot/min l'aire occupée individuellement par les séparations de Pb est sous  $100 \mu\text{m}^2$  pour 85,4% du nombre total dans la zone extérieure et de 85,6% pour la zone moyenne, mais dans la zone intérieure l'aire croît jusqu'à  $200 \mu\text{m}^2$  pour 91,8% du nombre total des séparations.

Les séparations avec  $GS = 0,3 - 0,7$  représentent 65,58% du nombre total dans la zone extérieure, 64,96% dans la zone moyenne et 63,44% dans la zone intérieure. En même mesure les séparations avec  $GS = 0,3 - 0,7$  représentent 23,75% du nombre total dans la zone extérieure et 17% dans la zone moyenne, mais dans la zone intérieure apparaissent des séparations avec  $GS = 0,7 - 0,9$  en représentant 25,2% du nombre total. L'explication est donnée par la fragmentation des dendrites de solution solide  $\alpha$ , par suite de la croissance de la pression du métal liquide avec la rotation. L'apparition de la structure dendritique fine avec l'agrandissement de la rotation, a déterminé la diminution de l'aire occupée individuellement par les séparations de Pb et la croissance du degré de sphéroïdisation (GS).

### 3. Conclusions

L'accroissement de la rotation de la coquille détermine l'apparition d'un échange de chaleur de plus en plus intense dans l'intérieur de la pièce en train de solidification. En conséquence la structure de la matrice se finisse, mais la distribution du Pb est plus uniforme.

Avec l'agrandissement de la rotation baisse l'aire occupée individuellement par les séparations de Pb dans la zone intérieure et se diversifie le degré de sphéroïdisation, c'est-à-dire à rotations de 880 – 900 rot/min apparaissent des séparations avec  $GS = 0,7 - 0,9$ , donc la structure se finisse.

À rotation  $n = 900$  rot/min apparaissent les prémisses d'une "ségrégation à rayures", donc le dépassement de cette rotation peut conduire à une plus grande hétérogénéité chimique et structurale qui peut diminuer les propriétés antifriction des pièces coulées par centrifugation en bronze CuPb10Sn10.

### BIBLIOGRAPHIE

1. Diaconescu Florin, Carcea Ioan – *Des recherches experimentales concernant l'influence de la rotation de la coquille sur la dureté des pièces coulées par centrifugation en alliages Cu-Pb-Sn*, Buletinul Institutului Politehnic din Iași, Tomul L (LIV), Fasc. 1, 2004, p.89-94
2. Domșa Șerban, Miron Zeno – *Îndrumător pentru utilizarea fontelor, oțelurilor și aliajelor neferoase*, Editura tehnică, București, 1985

Reçue le 20 Avril 2005

Université Technique "Gh. Asachi" Jassy

FLORIN DIACONESCU, Université Technique "Gh. Asachi" Jassy  
ROMEO CHELARIU, Université Technique "Gh. Asachi" Jassy

### CERCETĂRI PRIVIND INFLUENȚA TURAȚIEI COCHILEI ASUPRA DISTRIBUȚIEI Pb ÎN PIESELE TURNATE CENTRIFUGAL DIN BRONZ CuPb10Sn10

**Rezumat :** Piesele turnate centrifugal prezintă o neomogenitate chimică și structurală cauzată de solidificarea în câmp centrifug. În aliajele antifricțiune Cu-Pb-Sn, plumbul este introdus pentru îmbunătățirea prelucrabilității și a proprietăților antifricțiune. Sub acțiunea forței centrifuge Pb are tendința de a segrega și de aceea în lucrare se urmărește determinarea unei turații optime care să asigure o distribuție cât mai uniformă a Pb pe secțiunea piesei.

## DES RECHERCHES CONCERNANT L'INFLUENCE DE LA ROTATION DE LA COQUILLE SUR LES PROPRIÉTÉS MÉCANIQUES D'UN BRONZE COULÉ PAR CENTRIFUGATION

DIACONESCU FLORIN, ALEXANDRU IOAN et CARCEA IOAN

**Résumé:** Les pièces coulées par centrifugation en bronze ont les propriétés mécaniques plus élevées que celles coulées en moules stationnaires parce que la force centrifuge détermine une meilleure séparation des inclusions oxydiques et gazeuses vers la surface libre des manchons.

L'agrandissement de la rotation de la coquille détermine l'intensification de l'échange convectif de chaleur dans l'alliage qui se solidifie et, par conséquence, croît le degré de la structure.

Dans la présente on étudie l'influence de la rotation de la coquille sur les modifications structurelles et sur les propriétés mécaniques des pièces coulées par centrifugation en bronze CuPbSn10.

**Mots clef:** rotation de la coquille, la séparation des inclusions, le finissage de la structure, l'agrandissement des propriétés mécaniques.

### 1. Introduction

La coulée centrifuge présente l'avantage d'une séparation avancée des inclusions oxydiques et gazeuses. Cette séparation est donnée de la différence entre le poids spécifique du métal coulé et celle des inclusions oxydiques et gazeuses.

Dans un liquide en rotation à la vitesse angulaire  $\omega$  et que contient des inclusions, la force centrifuge qui actionne sur une particule est :

$$F_c = m \cdot \omega^2 \cdot r = \omega^2 \cdot v \cdot (\rho_i \cdot r_1 - \rho_m \cdot r_2) \quad (1)$$

dans laquelle :

$v$  est le volume de la particule d'inclusion ;

$\rho_m$  – la densité du métal ;

$\rho_i$  – la densité de l'inclusion ;

$\omega$  – vitesse angulaire ;

$r_1$  – le rayon du centre de la force d'inertie de la inclusion ;

$r_2$  – le rayon du centre de la force d'inertie du volume de métal disloqué par inclusion.

Quand l'inclusion a une densité uniforme, l'équation (1) a l'expression :

$$F_c = v \cdot \omega \cdot r (\rho_i - \rho_m) = \frac{\omega^2 \cdot v \cdot r}{g} (\gamma_i - \gamma_m) \quad (2)$$

dans laquelle:

$\gamma_i$  est le poids spécifique de l'inclusion;  
 $\gamma_m$  – le poids spécifique du métal;  
 $g$  – la accélération de la gravité.

Comparativement avec la coulée en moules stationnaires, quand les inclusions sont soumises à une force d'ascension :

$$F_a = v \cdot g \cdot (\rho_i - \rho_m), \quad (3)$$

à la coulée centrifuge des forces qui actionnent sur une inclusion plongée dans le liquide en rotation, croissent de  $k$  fois, selon l'équation:

$$\frac{F_c}{F_a} = \frac{v \cdot \omega^2 \cdot r (\rho_i - \rho_m)}{v \cdot g (\rho_i - \rho_m)} = \frac{\omega^2 \cdot r}{g} = k \quad (4)$$

Quand  $\rho_i < \rho_m$ , la force centrifuge est négative et est orientée vers la surface libre, en favorisant la séparation des inclusions. Cette force dépend comme l'on voit, du carré de la vitesse angulaire.

## 2. La méthodologie de la recherche

Pour étudier l'influence de la rotation de la coquille sur les propriétés mécaniques des pièces coulées par centrifugation en bronze CuPb10Sn10, ont coulé des manchons à diamètre extérieur 120 mm, diamètre intérieur 30 mm et l'hauteur de 120 mm, en utilisant une machine avec l'axe verticale de rotation vitesses variables. La gamme de rotations (700, 800, 880 et 900 rot/min) a été imposée soit de réalisation de la configuration intérieure des manchons, soit de limitation du phénomène de ségrégation "à rayures" du plomb.

La température du coulée a été dans les cases 1170°C, et la température de chauffage préalable de la coquille de 160°C, pour éliminer l'influence des autres paramètres de coulée centrifuge.

Dès manchons, de cette façon obtenus, ont confectionné des échantillons, pour essais à traction, prélèvements de zone extérieure (e), moyenne (m) et intérieure (i) qui ont des structures différentes produites par l'échange de chaleur entre la pièce et la coquille.

Les essais à traction ont été effectués à une machine type MTS 810 (Matériel Test System) prévue avec un système de traçage de la diagramme force – allongement et extensomètre pour la détermination d'allongement. Ont utilisé des échantillons proportionnel – normales, avec le facteur dimensionnel  $n = L_0 / d_0 = 5$  et le diamètre  $d_0 = 5$  mm.

La méthodologie d'essai a observé les prévisions de SR EN 10002 – 1 ÷ 1995.

### 3. Les résultats expérimentaux et leur interprétation :

Dans le tableau 1 sont présentés les propriétés mécaniques des pièces coulées par centrifugation en bronze antifriction, en dépendance de différentes rotations de la coquille.

Tableau 1. La variation des propriétés mécaniques des pièces coulées par centrifugation en dépendance de différentes rotations de la coquille

Symbole d'échantillon	Rotation [rot/min]	La zone de prélèvement	La résistance à la rupture $R_m$ [N/mm <sup>2</sup> ]	La limite d'écoulement $R_e$ [N/mm <sup>2</sup> ]	L'allongement à la rupture $A_5$ %
PM n 1	700	e	221.719	82.25	17.05
		m	237.717	91.76	16.48
		i	229.342	86.46	16.78
PM n 2	800	e	235.761	90.76	16.30
		m	260.454	89.19	13.50
		i	260.974	98.91	13.60
PM n 3	880	e	251.692	85.82	14.10
		m	268.863	90.33	13.40
		i	268.407	88.57	13.45
PM n 4	900	e	256.004	89.60	13.80
		m	276.069	92.76	13.30
		i	289.596	97.88	12.75

Pour la zone extérieure (e) on observe comme la résistance à la rupture croît avec la rotation de la coquille de 221,72 N/mm<sup>2</sup> jusqu'à 256,00 N/mm<sup>2</sup>. Ce fait s'explique par les modifications structurales qui apparaissent à la croissance de la rotation de la coquille. L'analyse microscopique a montré que la structure de la masse métallique principale des bronzes coulés expérimentalement est biphasique en étant constituée de solution solide  $\alpha$ , moins résistante mais plastique, et eutectoïde ( $\alpha + \delta$ ) dur et résistant mais fragile.

À la rotation de 700 rot /min la solution solide  $\alpha$  a un aspect dendritique peu prononcé, mais avec la croissance de la rotation cet aspect disparaît graduellement et croît la quantité d'eutectoïd ( $\alpha + \delta$ ) par la suite de l'intensification de l'échange convectif de chaleur dans l'intérieur de la pièce en train de solidification.

La résistance mécanique croît avec la quantité d'eutectoïd ( $\alpha + \delta$ ), tandis que l'allongement à la rupture ( $A_5$ ) baisse de 17.05% jusqu'à 13.80%.

Comparativement avec les bronzes Cu-Sn, la résistance à la rupture est plus basse par la suite du contenu de 10% Pb, introduit pour l'augmentation des propriétés antifricition.

L'analyse de l'image à la ligne assistée par computer (ordinateur) de la Faculté de Science et Génie de Matériaux de Bucarest, a montre que individuellement la surface occupée par les séparations de Pb baisse avec la croissance de la rotation. Donc à la rotation de 700 rot /min les séparations avec aire moins 250  $\mu\text{m}^2$  représentaient 95% du nombre total, ainsi qu'à la rotation de 900 rot /min 85.4% des séparations de Pb occupaient individuellement aires sous 90  $\mu\text{m}^2$ . La degré de sphéroïdisation (GS) des séparations de Pb s'est modifié en fonction de rotation. Les séparations avec GS = 0.3-0.7 s'ont été maintenues dans les limites 59.7-67.33 %, tandis que ont crû de 20% jusqu'à 23.75% et ainsi a baissé l'effet d'entaille.

Pour la zone moyenne (m) la résistance à la rupture a crû avec la rotation de 237,06N/mm<sup>2</sup> jusqu'à 276.06 N/mm<sup>2</sup>. Dans cette zone les microstructures ont présenté

un aspect dendritique plus prononcé vis-à-vis de la zone extérieure (e), parce que l'échange de chaleur entre alliage et le moule métallique a été plus lent. Cependant, par la comparaison des microstructures, ont constaté que la structure se finisse au fur et à mesure que la rotation de la coquille croît.

Donc à la rotation de 700 rot /min la microstructure a présenté des dendrites de solution solide  $\alpha$  de grands dimensions et des fragments dendritiques tandis que pour des rotations plus élevées ont observé la diminution des dimensions des axes primaires de  $300\mu\text{m}$  jusqu'à  $150\mu\text{m}$  et la présence d'un nombre croissant des fragments dendritiques avec différentes orientations. La vitesse de refroidissement plus réduite à détermine l'apparition des dendrites avec des minces ramification qui s'ont fragmenté plus facilement par la suite de la croissance de la rotation.

La rotation de plus en plus rapide a détermine l'augmentation de la pression métalostatique sur les dendrites de solution solide  $\alpha$ , en train de formation et leur rupture. Le degré de dispersion d'eutectoïd ( $\alpha + \delta$ ) a crû concomitant avec la ramification des dendrites et leur fragmentation ce qui a conduit à l'augmentation de la résistance à rupture, mais aussitôt à la diminution de l'allongement à la rupture de 16,48 % jusqu'à 13,30%.

La croissance de la rotation a détermine, par le même mécanisme de rupture des dendrites, la réduction de l'aire occupé individuellement par 90 - 95% du nombre total de séparations de Pb de  $250 - 500\mu\text{m}^2$  pour la rotation de 700 rot /min, jusqu'à  $0 - 175\mu\text{m}^2$  dans le cas de la pièce coulée à 800 rot /min et jusqu'à  $0 - 100\mu\text{m}^2$  pour les pièces coulées à 880 rot /min. Les séparations de Pb avec le degré de sphéroïdisation 0.3 - 0.7 ont représenté 61.3 - 71.78 % du nombre total, ainsi que celles avec GS = 0.7 - 0.9 ont crû avec la rotation de 34% jusqu'à 38 %.

Dans le cas de la zone intérieure (i) la résistance à la rupture croît avec la rotation de la coquille de 229.34 N/mm<sup>2</sup> jusqu'à 289.59 N/mm<sup>2</sup>, ainsi que l'allongement à la rupture baisse de 16.78 % jusqu'à 12.75 %.

Dans la zone intérieure s'ont manifesté deux phénomènes: un refroidissement plus intense que la zone moyenne à cause de la surface libre de la pièce et une séparation différente des inclusions en dépendance de rotation et de viscosité du alliage liquide.

Par la suite de l'augmentation de la rotation, dans cette zone la structure s'est modifiée, c'est-à-dire à la 700 rot /min ont apparaît des dendrites de solution solide  $\alpha$  un peu ramifiées, à 800 rot /min l'axe primaire des dendrites était de 200 - 300  $\mu\text{m}$  ainsi que à 880 et 900 rot /min les dendrites ont été les plus fines, ce qui explique la croissance de la résistance à rupture.

L'aire occupée individuellement par 88 - 98% des séparations de Pb a été plus grande que dans les zones extérieure et moyenne, mais elle est diminuée avec l'augmentation de la rotation de  $500\mu\text{m}^2$  jusqu'à  $200\mu\text{m}^2$ . Le degré de sphéroïdisation des séparations de Pb a été 0.3 - 0.7 pour 63.4 - 71.63 % du nombre total de séparation, mais le nombre total de séparation avec GS = 0.7 - 0.9 a crû avec la rotation de la coquille de 12.09% jusqu'à 25.2 %, fait expliqué par la fragmentation des dendrites, qui ont limité la croissance des dimensions des séparations de Pb sur une direction préférable.

Les essais a traction ont montré que la rupture a été ductile, les échantillons en présentant un "cône" et une "coupe".

Les valeurs obtenues à traction pour la résistance à la rupture et l'allongement à la rupture sont plus grandes que les minimaux recommandés dans la littérature de spécialité.

#### 4. Conclusions

L'augmentation de la rotation de la coquille à la coulée centrifuge de bronze en Sn et Pb détermine la croissance de la résistance à la rupture et la diminution des propriétés plastiques.

Le degré de finissage de la structure croît avec l'augmentation de la rotation, c'est-à-dire baissent les dimensions des dendrites, baisse la surface occupée individuellement par les séparations de Pb et croît le degré de sphéroïdisation de ces séparations.

La finition de la structure détermine un blocage d'un nombre de plus en plus grand de dislocations et la croissance de la résistance à la rupture.

Avec l'augmentation de la rotation de la coquille croît aussi le degré de dispersion d'eutectoïd ( $\alpha + \delta$ ), ce qui détermine la croissance de la résistance à la rupture et la diminution des propriétés plastiques.

La finition de la structure avec la croissance de la rotation se produit soit grâce à l'intensification de l'échange convectif de chaleur entre la pièce et la coquille, soit à cause de fragmentation des dendrites de solution solide  $\alpha$  par suite de l'augmentation de la pression d'alliage liquide sur les dendrites en train de formation.

DIACONESCU FLORIN, Université Technique " Gh. Asachi" Jassy  
ALEXANDRU IOAN, Université Technique " Gh. Asachi" Jassy  
CARCEA IOAN, Université Technique " Gh. Asachi" Jassy

Reçue le 15 Avril 2005

Université Technique de Jassy

#### Bibliographie :

1. Alexandru, I., et autres *Alegerea si utilizarea materialelor metalice*. Editura Didactica si Pedagogica, Bucuresti, 1997.
2. Bratu, C., Sofroni, L., Brabie, V. *Bazele teoretice ale turnarii*. Editura Didactica si Pedagogica, Bucuresti, 1981.
3. Colan, H., Tudoran, P., Ailincăi G., Marcu, M., Drugescu, E. *Studiul metalelor*. Editura Didactica si Pedagogica, Bucuresti, 1983.
4. Gâdea, S., Protopopescu, M. *Aliaje neferoase*. Editura Tehnica, Bucuresti, 1965.
5. Geru, N. *Metalurgie fizica*. Editura Didactica si Pedagogica, Bucuresti, 1981.

#### CERCETARI PRIVIND INFLUENTA TURATIEI COCHILEI ASUPRA PROPRIETATILOR MECANICE ALE UNUI BRONZ ANTIFRICTIUNE TURNAT CENTRIFUGAL

**Rezumat:** Piesele turnate centrifugale din bronz au proprietati mecanice numai ridicate decât cele turnate în forme stationare, deoarece forta centrifuga determina o mai buna separare a incluziunilor oxidice si gazease catre suprafata libera a bucselor.

Cresterea turatiei cochilei determina intensificarea schimbului convectiv de caldura in aliajul care se solidifica si in consecinta finisarea structurii .

In lucrare se studiaza influenta turatiei cochilei asupra modificatorilor structurale si mecanice ale pieselor turnate centrifugal din CuPb10Sn1.



## A SUITABLE METHOD FOR OBTAINING FUNCTIONAL POLYMER-METAL COMPOSITED MATERIALS BY ELECTRODEPOSITION

BY

FLORIN BRÎNZĂ, CRISTIAN PÎRGHIE and NICOLAE Sulițanu

**Abstract.** A functionalised, nanostructured polymer-metal composite material was obtained using technology of electrodeposition. Porous membrane of polyethylene or other thermoplastic polymers was electroactivated on one side. Using suitable bath, pure metals or alloys were deposited inside of membrane's pores. Obtained composite materials maintain the plastic properties of polymers and add new properties of nanostructured metal or alloy which is functionalized. Applications cover a wide area, such as magnetic polymers, functionalised catalytic membranes, electromagnetic shields with complicated shapes, medicine.

**Keywords:** composite materials, porous membranes, polymers, nanostructured metals

### 1. INTRODUCTION

Composite materials based on micro and nanoclusters of ferromagnetic metals are promising constituents for new-generation functional materials because of their unique physical and chemical properties with strong differences from some properties of bulk materials. Since the properties of clusters are size-dependent, the material functions may be tuned by specifying the size and shape of those. A key step for making it possible is to establish methods for manufacturing of size and shape-preselected clusters [1].

One of the most utilized technologies is embedding of desired materials in a nanostructured matrix with regular or irregular geometry. Magnetic materials, such as Fe [2], Co [3] or Ni [4] were embedded in nanoscale- and microscale-dimension holes of the membranes by electrodeposition, sol-gel or other techniques. Particularly, there is interest in Fe-Co alloys due to their high Curie temperature, high magnetization and low coercivity.

Two principal ways are used to build a micro and/or nanostructured composite material: the mixture of components is suitable for packaging in a short-range atomic order or the components are forced to be structured using a matrix at corresponding dimensions. The second way has been developed in various manners, e.g. lithographic and nanolithographic methods or filling the pores with nanoscale dimensions of various membranes, like  $\text{Al}_2\text{O}_3$  or other materials [1].

The aim of this paper is to present the preparation method and structural properties of clusters of Fe-Co alloy obtained by electrodeposition in a polymer-based matrix.

## 2. EXPERIMENTAL PROCEDURE

*Porous membranes obtaining.* Technology of those new classes of materials is a two-step type technology. First, the nano- and microporous membranes are obtained. Polyethylene (PE) foil with 0.01 to 0.1 mm in tick is obtained using co-lamination procedures of mixture polyethylene powder and high-temperature melting filler nano- and micro grains.

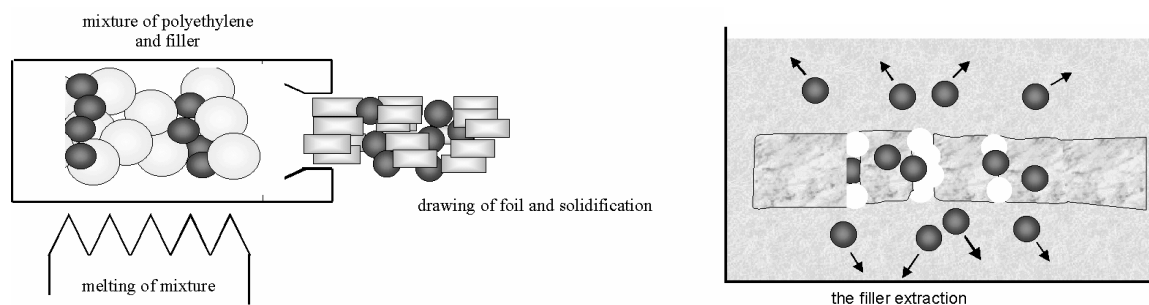


Fig. 1. Obtaining technology of porous membrane.

Primary obtained polyethylene powder are mixed with calculate quantities of filler with average diameter of grains dispersed in 40-2000 nm domain. The filler quantity and filler grains size depend of desired porosity and pores diameter. The both two types of grains are mixed in extrusion plant and mixture of melted PE and filler is laminated in order to obtain foil with various ticks. During lamination processes, the filler grains are surrounded by matrix of melted PE. The as-obtained foil having various ticks is washed in acetone bath in order to extract the filler. The washing time duration is 4 to 12 hours. After filler removal, obtained nanoporous membrane is dried using vacuum method. The obtaining technology is schematic depicted in Fig. 1.

*Electric activation.* On the one side of membrane, a thin film of conductive material, such Ag, In or Sn (in our experiment, Ag) is deposited using vacuum evaporation method. This thin film plays the role of the cathode for the electrodeposition processes. Membrane is placed in electrolytic bath, using precaution in order to avoid electrical contact between bath and Ag thin film or other parts of cathode's support. In this manner, ionic species are forced to penetrate by capillarity only the exposed side of membrane. Bath composition was 60 g/l  $\text{CoSO}_4 \cdot 7\text{H}_2\text{O}$ , 60 g/l  $\text{FeSO}_4 \cdot 7\text{H}_2\text{O}$ , 30 g/l  $\text{H}_3\text{BO}_3$  and 1.5 g/l ascorbic acid. Bath was continuous stirred and maintained at 30°C. Deposition was performed using DC power supply and chronoamperometry mode. The parameters was: starting current density- 20  $\text{mA}/\text{cm}^2$  and deposition time 240-600s.

*Structure and composition analysis.* Evaluation of pores-size and pores-filling distribution was performed using microphotographic method. Structure of filled membrane was relieved using SEM microscopy. The cross-section was obtained by breaking filled membrane in liquid nitrogen. The composition analysis was performed using EDS method. Structure of new material was determinate using X-ray diffraction (XRD) technique.

### 3. RESULTS AND DISCUSSIONS

Fig. 3 present a section of the composite material. PE membrane used as irregular matrix of new material has low porosity degree (6-8%) and 100  $\mu\text{m}$  thick. We can observe structure of composite material consisting in PE matrix surrounding Fe-Co clusters. The shape of reinforced material in a chain-like spherical nanodimensional and microdimensional clusters. Clusters form chains and are as follow of matrix structure. Dimensional dispersion of clusters is presented in diagram from Fig. 2b. The distribution is the similar of grain-size distribution of filler.

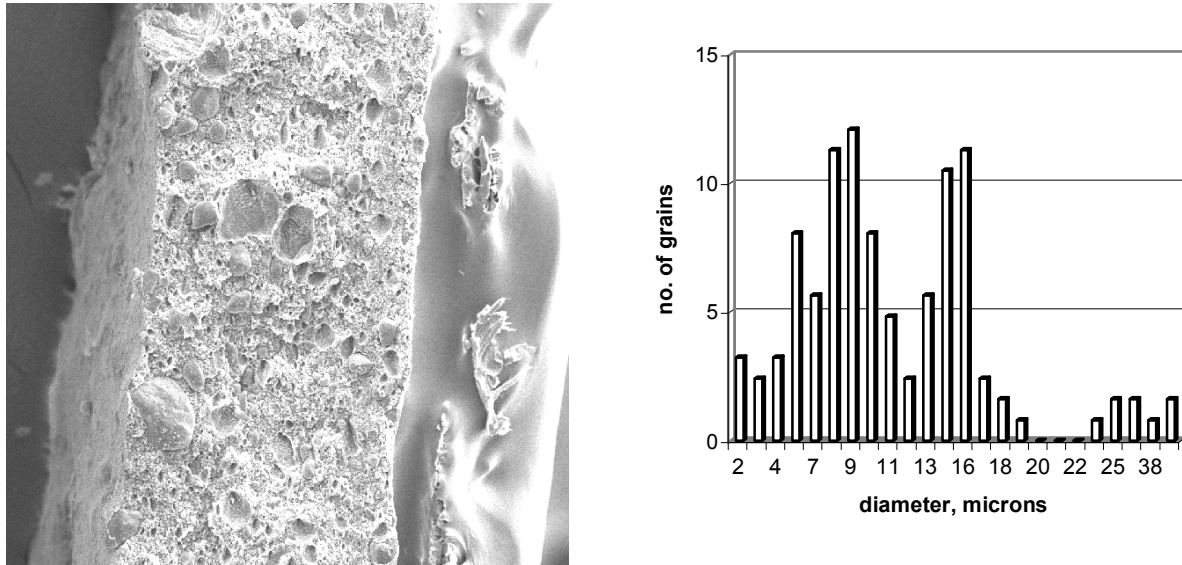


Fig. 2. a) SEM cross-section of PE membrane with Fe-Co clusters; b) distribution of average diameter of Fe-Co clusters.

Two maximum of average diameter distribution is centred on 9  $\mu\text{m}$  and 16  $\mu\text{m}$ . Those two values are similar to maximum of distribution of PE powder grains (9  $\mu\text{m}$ ) and filler grains (16  $\mu\text{m}$ ). Another small peak is presented at approximate value obtained by summing those two maximum average diameters, probably as result of spatial intermodulation processes. High-resolution TEM images presented elsewhere [13] reveal also presence of nanometric clusters, as result of internal nanometric spaces of macromolecular chains specific to PE membranes. XRD investigation of composite material confirm presence of micro- and nanoclusters.

Cluster composition have the same composition as thin films deposited from 50%-50% weight composition of Fe and Co precursors, respectively 47% atomic Co and 53% atomic Fe.

### 4. CONCLUSIONS

A possible two-step technology is presented for new composite materials obtaining, consisting in polyethylene or others polymers as matrix and ferromagnetic clusters or others metallic clusters as reinforced agent. In first step, micro- and nanoporous host membrane is obtained. In second step, one side electrical activated membrane is filled by electrodeposition technology. Cross-section of obtained material confirm the expected structure: chains of metallic clusters having average diameter

accorded with average diameter of host matrix polyethylene grains, internal spaces between polymeric chains and initial filler grains. This composite material has the mechanical properties of polyethylene foil. In this manner, can be obtained various functionalised membranes suitable for electromagnetic field absorbers, selective filters and other.

*Received May 24, 2005*

*“Al. I. Cuza” University Iasi*

#### REFERENCES

- /1/. L.W. Wang, Y. Liu, Z. Zhang, *Handbook of Nanophase and Nanostructured Materials*, Kluwers Academic Publishers, The Netherlands, Dordrecht, 2002.
- /2/. E. Rashba1, D. Gamota, J. Nanopartic. Res. 5 (2003) 401.
- /3/. K.K. Lew, J.M. Redwing, J. Crystal Growth 254 (2003) 14.
- /4/. K. Ouchi, IEEE Trans. Magn. 37 (2001) 1217.
- /5/. F. Brînză, N. Sulitanu, Bul. Inst. Polit. Iași 2005, *in press*.

#### O POSIBILĂ METODĂ DE OBȚINERE A MATERIALELOR COMPOZITE POLIMER-METAL PRIN DEPUNERE ELECTROLITICĂ

(Rezumat)

O nouă clasă de materiale compozite polimer-metal, funcționalizate, au fost obținute prin tehnologia electrodepunerii. Membrane micro- și nanoporoase de polietilenă sau alți polimeri termoplastici au fost electroactivate pe una din fețe. Utilizând băi electrolitice de compoziție adecvată, în porii membranei au fost depuse materiale metalice pure sau aliaje metalice. Materialul compozit obținut păstrează proprietățile plastice ale polimerului-matrice dar la acestea se adaugă proprietăți noi, dependente de materialul metalic nanostructurat depus în pori. Aplicațiile acestor materiale acoperă o arie largă de domenii, cum ar fi polimeri magnetici, membrane catalitice funcționalizate, ecrane electromagnetice de forme complicate, aplicații în medicină.

## HARDENING OPTIMIZING BY INDUCTION OF REVOLUTION SAMPLES

BY

MIHAI GRAMATICU AND SILVIU GABRIEL STROE

**Abstract.** Thermal treatments of fast heading steels, especially those applying to induction, develop themselves as surface localized treatments. This study carries on the experimental verification regarding the influence of specific power, displacement speed and rotational speed upon the surface hardness

**Keywords:** heat treatment, heading steels

### 1. INTRODUCTION

Thermal treatments of fast heating steels, especially those applying to induction, develop themselves as surface localized treatments, due to the advantages shown by this technique namely:

- it provides an optimum combination between hardness, mechanical stress and tenacity of the hardened steel, thus giving designers the possibility to decrease the dimension and mass of the hardened products;
- fast heating for austenitizing provides fine grained steel, lower dissolution of carbides and therefore higher resistance, hardness and increased resistance to wear and tiredness;
- compressive stress in the surface layer which results in the improvement of tiredness behaviour;
- minimal deformation;
- slight possibility of adjusting the hardness depth, by adjusting the electrical parameters, etc;

Induction heating generates a sufficiently intensive electromagnetic field to provide an optimum transmission of energy from the heating inductor into the treated sample(table 1).

Table 1. The transferable power by different heating techniques

Heating Type	Transmitted power (kW/cm <sup>2</sup> )
Convection	$5 \cdot 10^{-1}$
Radiation (electrical ovens)	8
Thermal conduction	20
Infrared emission	$2 \cdot 10^2$
Flame	$10^3$
Induction Heating	$10^4$
CO <sub>2</sub> - laser	$10^8$
Beam of electrons	$10^{10}$

The heating penetration  $v_i$  as well as the hardening penetration on current frequency and heating temperature. The supply sources have frequencies between 50 Hz to 3000 kHz, being of:

- low frequency: 50 Hz...500Hz;
- medium frequency: 500Hz...50kHz;
- high frequency: 50kHz...3MHz.

The pellicle effect is the basis of induction heating method, especially in surface hardening. It consists of non-uniform distribution of the current on section (fig.1):

The penetration of current [3]:

$$\delta = 503 \sqrt{\frac{\rho}{\mu \cdot f}} \quad [\text{m}] \quad (1)$$

$$\frac{I_m}{I_{me}}, \frac{E_m}{E_{me}}, \frac{H_m}{H_{me}}$$

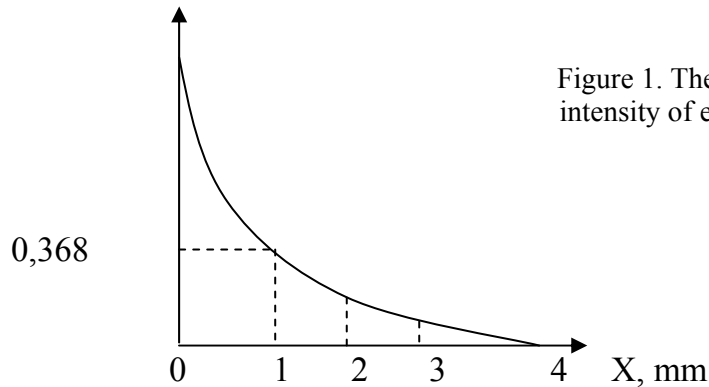


Figure 1. The dependence of current density and intensity of electric and magnetic fields on penetration.

The electric current density  $I_{me}$  on surface is given by the relation 2 [1]:

$$I_{me} = \sqrt{2} \cdot \frac{H_{me}}{\delta} \quad (2)$$

The current penetration into steel and copper depending on current frequency is given in table 2

Table 2. The current penetration in mm

Frequency, Hz	Penetration, $\delta$ , in mm		
	Cu la 15°C ( $\rho=1,8 \cdot 10^{-8} \Omega \cdot \text{m}$ , $\mu=1$ )	Steel 0,45%C	
		15°C ( $\rho=2 \cdot 10^{-7} \Omega \cdot \text{m}$ , $\mu=40$ )	800°C ( $\rho=10^{-6} \Omega \cdot \text{m}$ , $\mu=1$ )
50	10.0	5.0	70.0
500	3.0	1.5	22.0
2500	1.3	0.67	10.0
10000	0.7	0.34	5.0
100000	0.22	0.11	1.6
1000000	0.07	0.034	0.5

If heated, steel changes its magnetic resistivity and permeability, that is its resistivity increases to Curie point, and decreases afterwards. The resistivities of steel remain approximately constant at above 800°C temperature almost equal to  $10^{-6} \Omega \cdot m$ .

The non-uniform distribution of the induced current into the heated conductor generates a heating gradient depending on heating temperatures achieved and on cooling conditions, will lead to a succession of structures and specific properties as well.

The penetration of hardened layer in the case of some cylinder pieces is almost equal to relation 3 [2]:

$$\frac{X_k}{D_p} = 0.05 \dots 0.1 \quad (3)$$

where:  $X_k$  is hardening penetration, the distance from surface to semi-martensite;  $D_p$  is diameter of sample.

When choosing the hardening penetration, one should take into consideration the wearingness of the piece, the specific loads to which it is subjected, as well as the distribution of remanent tensions and of those resulted from external forces which influence greatly the resistance to tiredness.

The induction heating must be achieved in layer at temperatures of above  $A_{c3}$  to austenize the layer, thus obtaining the martensite structure inside the layer by energetic cooling (water, oil, emulsion shower) figure 2.

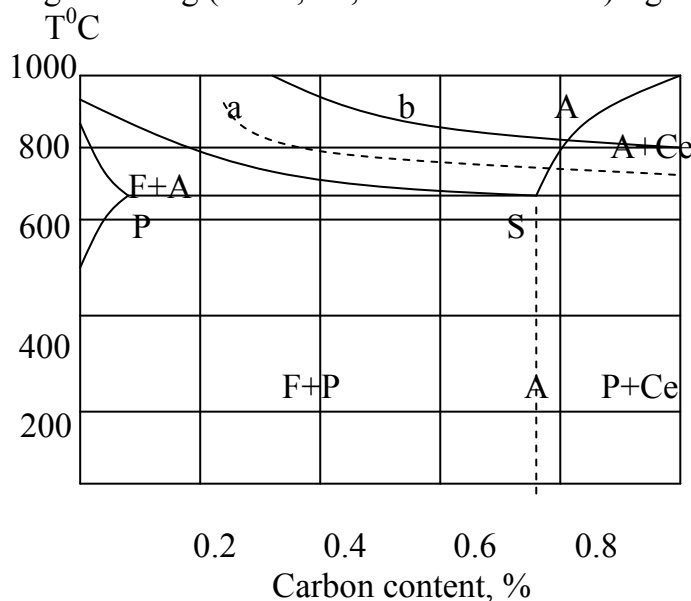


Fig. 2 Fragment of diagram Fe-C  
a) heating in oven; b) induction heating

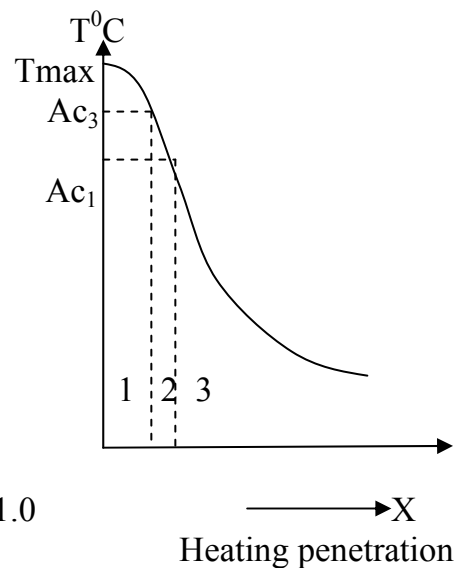


Fig. 3 Thermal gradient depending on heating penetration

At heating, a completely austenite structure results from layer 1 (figure 3) [4] which provides a martensite structure layer by energetic cooling, at a speed above  $v_{cr}$ . Layer 2 which is subjected to intercritical heating will have a mixt structure at heating A+F (austenite+ferrite). while at cooling a structure M+F (martensite+ferrite), whereas layer 3 does not display any physical transformation, its structure being of pellet type.

The heating temperatures achieved inside layer depend on specific consumed power while the hardening penetration depends on supply current frequency of the inductor.

The heating temperature and thermal gradient on section determine the structural gradient and properties, parameters as well, and they will be adjusted by specific power adjustment and by choosing the high frequency generator which supplies the heating inductor.

Due to fast heating, the austenizing temperature is higher with 100..200<sup>0</sup>C than that of common hardening and it is directly correlated to heating speed.

The following parameters must be established in order to apply the induction hardening method:

- current frequency; power of generator; heating penetration; heating temperature; heating time; overheating degree at given penetration; specific power at sample; yield of generator, displacement speed of inductor alongside sample, rotational speed of sample.

This research foccuses on the influence of specific power, displacement speed of inductor and rotational speed of the hardened sample on the hardness of hardened surface and on hardening penetration.

## II. RESEARCH METHODS.

The research focused on the effect of important technological parameters regarding surface hardening by induction (such as specific power  $p_{sp}$  in kW/cm<sup>2</sup>, displacement speed of inductor  $v_i$ , mm/min and rotational speed of sample,  $n$ , rot/min) on the surface hardness of steel alloys 40Cr10, 34MoCr11 and 60Si15A.

The chemical composition of alloys determined by a POLIVAC analyzer is shown in table 3.

Table 3. The chemical composition of hardened steels.

Type	Chemical composition, %											
	C	Si	Mn	P	S	Cr	Mo	Ni	Al	Cu	W	Sn
34MoCr11	0.365	0.31	0.540	0.006	0.03	0.89	0.101	0.181	0.038	0.31	0.002	0.016
40Cr10	0.448	0.27	0.63	0.015	0.041	1.05	0.08	0.108	0.027	0.32	0.002	0.017
60Si15A	0.616	1.83	0.826	0.005	0.207	0.273	0.093	0.129	0.026	0.283	0.003	0.008

The initial structure of these alloys is pearlite-ferrite, with lamellar grained pearlite, and uniformly distributed ferrite.

The hardness and resistance of these steels with pearlite-ferrite structure are given in table 4.

Table 4. The Mechanical properties of experimental steels

Type	Hardness, daN/mm <sup>2</sup>		Mechanical resistance to rupture, MPa	Structure
	Vickers	Brinell		
34Mocr11	231	219	740	P+F
40Cr10	348	333	1125	P+F
60Si15A	267	252	850	P+F

### II.1. Experiment planning.

The planned parameters are:

A - specific power, in kW/cm<sup>2</sup>



B - displacement speed of inductor alongside the hardened sample, in mm/min

C - rotational speed of sample, in rot/min.

For each factor, two levels noted with 1 and 2 are planned:

1 - inferior level and 2 - superior level

The experimental plan will be in this case of  $2^k$  type [4].(two levels and  $k=3$ , 3 planned factors respectively).

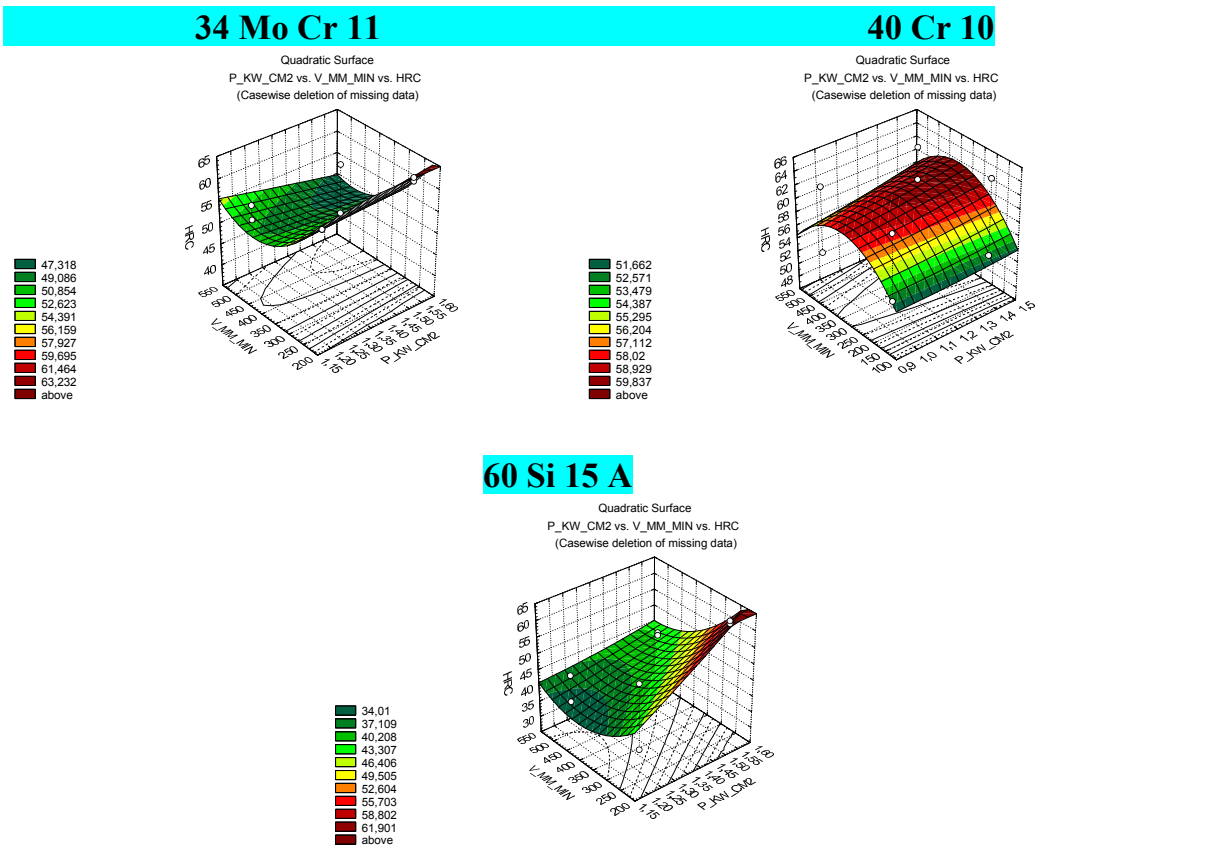
The experimental plan which was used is shown in table 5.

Table 5.

Experiment Number(No)	Factors			System answer Rockwell Hardness		
	A	B	C	34MoCr11	40Cr10	60Si15A
1	24	250	150	58	51	53
2	24	250	300	58	49	39
3	24	500	150	52	49	39
4	24	500	300	48	61	49
5	36	250	150	60	63	60
6	36	250	300	61	49	61
7	36	500	150	53	61	51
8	36	500	300	49	55	50

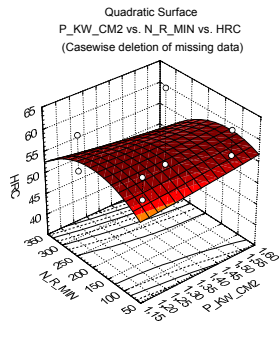
### III.GRAPHICS.

## HRC VS. SPECIFIC POWER AND DISPLACEMENT SPEED OF INDUCTOR ALONGSIDE THE HARDENED SAMPLE

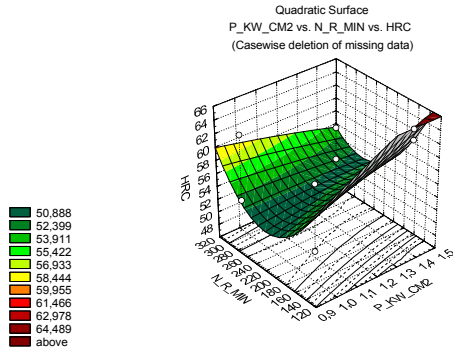


**HRC VS. SPECIFIC POWER AND ROTATIONAL SPEED OF SAMPLE**

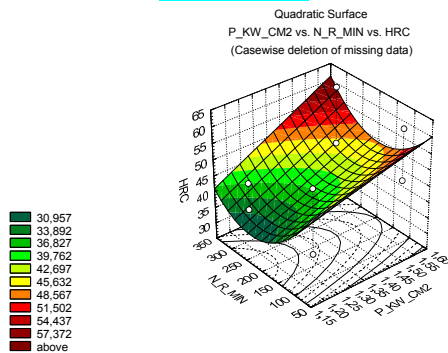
**34 Mo Cr 11**



**40 Cr 10**

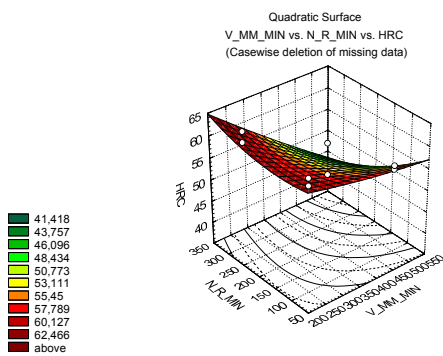


**60 Si 15 A**

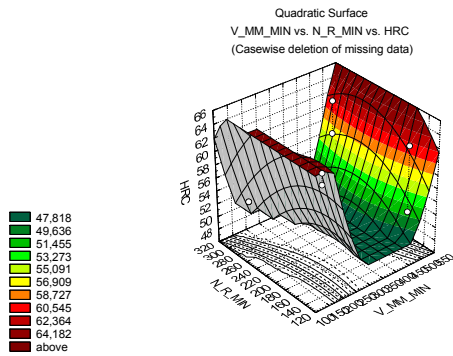


**HRC VS. DISPLACEMENT SPEED OF INDUCTOR ALONGSIDE THE HARDENED SAMPLE AND ROTATIONAL SPEED OF SAMPLE**

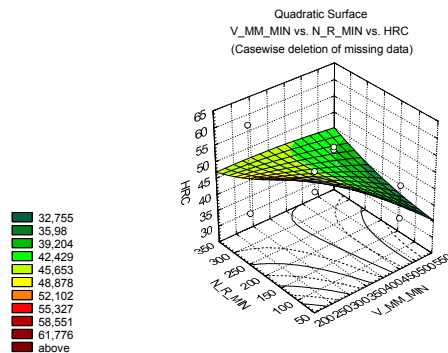
**34 Mo Cr 11**



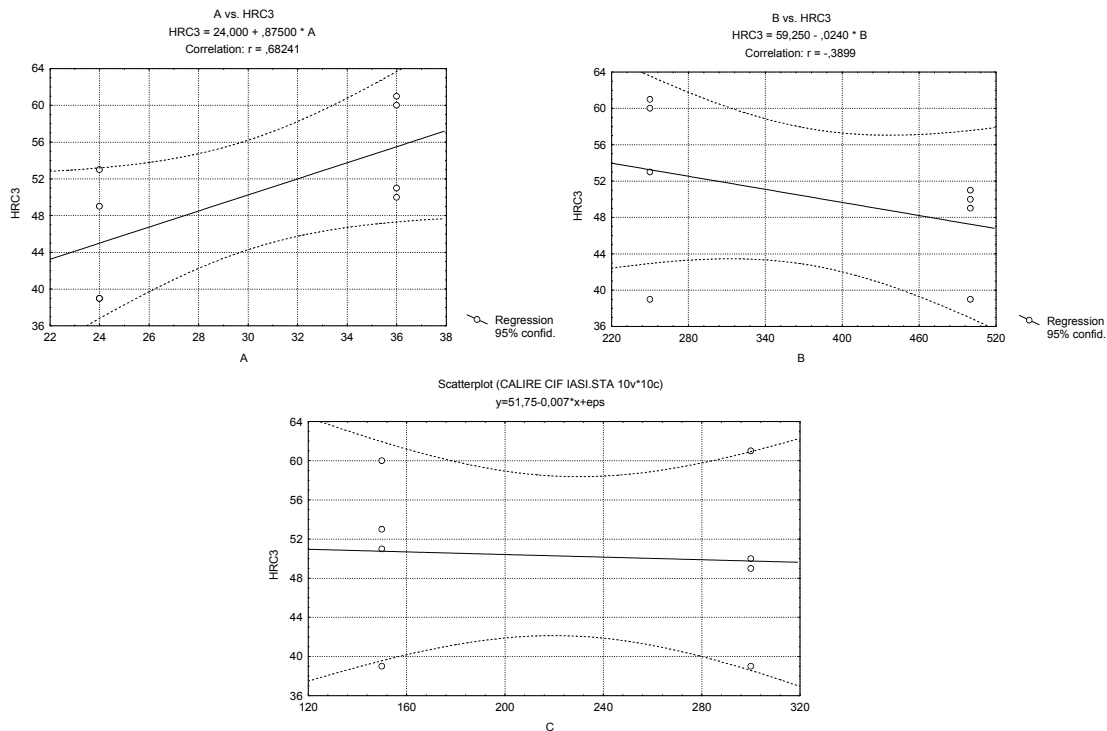
**40 Cr 10**



**60 Si 15 A**



## HRC vs. **A** - SPECIFIC POWER; **B** - DISPLACEMENT SPEED OF INDUCTOR ALONGSIDE THE HARDENED SAMPLE AND **C** - ROTATIONAL SPEED OF SAMPLE



### IV. CONCLUSIONS.

Surface hardening treatment provides an optimum combination between hardness, mechanical resistance and tenacity of hardened steels.

The penetration depends both on the material and the heating and cooling conditions for hardening.

From the analysis of variation graphics for hardness of the hardened surface layer, in the case of alloyed steels 34MoCr11, 40Cr10 and 60Si15A, we get to the conclusion that the optimum operating parameters of the hardening system must submit to the following:

- for 34MoCr11: - specific power: 1,45-1,6 kW/cm<sup>2</sup>  
 - displacement speed of inductor: 200-300 mm/min
- for 40Cr10: - specific power: 1,4-1,6 kW/cm<sup>2</sup>  
 - displacement speed of inductor: 200-400 mm/min
- for 60Si15A: - specific power: 1,45-1,6 kW/cm<sup>2</sup>  
 - displacement speed of inductor: 200-300 mm/min

From the hardness variation graphic of surface layer in hardened samples depending an rotational speed of sample we get to the conclusion that this factor does not have a significant influence on the final results, its important role focusing on the hardened layer thickness of uniformity.

**REFERENCES**

- /1/ Dulămiță T., Florian E., *Thermal and thermochemical treatment*, EDP, București,;
- /2/ Gâdea S., Petrescu M., *Physical Metallurgy and Metal Study*, EDP, București, 1981;
- /3/ Sluhoțkii A. E., Rîschin S.E, *Electric heating Inductors*, Ed. Tehnică, București, 1982;
- /4/ Ionescu R., Amarandei D., *Planning of efficient and qualitative experiments*, Ed. AGIR București,2004;
- /5/ Gramaticu M., Stroe S.G., *Surface hardening Optimization by induction of carbon steels*, Scientific Session TEHNOMUS XII, 6 - 7 mai 2005, Ed. Universității Suceava.

**OPTIMIZAREA DURIFICĂRII PISELOR DE REVOLUȚIE PRIN INDUCȚIE**

(Rezumat)

Tratamentele termice ale oțelurilor rapide, mai ales ale celor ce folosesc inducția, s-au dezvoltat ca tratamente termice localizate. Lucrarea prezintă verificarea experimentală a influenței puterii specifice, vitezei de deplasare și a celei de rotație asupra durității suprafeței.

## FATIGUE UNDER MULTIAXIAL STRESSES OF SOME STEELS

BY

MIHAI MIHALCUT, PAUL-DORU BARSANESCU and CONSTANTIN BITCA

**Abstract.** This study deals with simulations for cyclic stress/strain evolutions and redistributions, and evaluations of fatigue parameters suitable for estimating fatigue lives under proportional or non-proportional multiaxial loadings. The local cyclic elastic-plastic stress-strain responses were analysed using finite element program for both smooth and notched specimens made of three materials: a medium carbon steel in the normalized condition, an alloy steel quenched and tempered and a stainless steel, respectively. For experimental verifications, a series of tests of biaxial low-cycle fatigue composed of tension/compression with static or cyclic torsion were carried out on a biaxial servo-hydraulic testing machine. Different loading paths were carried out, in order to verify the effects of these loading paths in the additional cyclic hardening. The comparisons between numerical simulations and experimental observations show that the FEM simulations allow better understanding on the evolutions of the local cyclic stress-strain.

**Keywords:** simulation of stress/strain; redistribution of loading; multiaxial fatigue; non-proportional loading; low cycle fatigue; cyclic plasticity; fatigue life prediction

### 1. INTRODUCTION

Fatigue failure of mechanical components is a process of cyclic stress/strain evolutions and redistributions in the critical stressed volume. It may be imagined that due to stress concentration (notches, material defects or surface roughness) the local material yields firstly to redistribute the loading to the surrounding material, then follows with cyclic plastic deformation and finally crack initiates and the resistance is lost. Therefore, the simulations for cyclic stress/strain evolutions and redistributions are critical for predicting fatigue failure of mechanical components.

In this study, both numerical and experimental methods are applied to study the cyclic stress/strain evolutions under biaxial loading conditions. The local cyclic elastic-plastic stress-strain responses are analysed using Ansys finite element program for the notched specimens made of three materials: medium carbon steel in the normalized condition, an alloy steel quenched and tempered and a stainless steel, respectively.

Elastic-plastic FEM is used to predict the stabilized cyclic stress/strain state. The predicted stress relaxations are then compared with experimental observations. For experimental verifications, a series of tests of biaxial low-cycle fatigue composed of tension/compression with static or cyclic torsion were carried out on a biaxial servo-hydraulic testing machine (8800 Instron). Different loading paths were carried out, including proportional and non-proportional loading paths in order to verify the effects of these loading paths in the additional cyclic hardening [1, 2].

The FEM simulations allow better understanding on the evolutions of the local cyclic stress-strain. Based on the local cyclic elastic-plastic stress-strain responses, the energy-based multiaxial fatigue damage parameters are applied to correlating the experimentally obtained lives. A non-proportional parameter, based on the Minimum Circumscribed Ellipse to the shear stress path is proposed, which when applied to the ASME methodology for multiaxial loading improves correlation between the predicted and the experimental results.

## 2. EXPERIMENTS

In order to compare the sensitivity of materials to non-proportional loadings, three materials are studied in this research. The materials studied are: CK45 steel normalized, high strength steel 42CrMo4 and the stainless steel AISI 303. Some of the monotonic and cyclic mechanical properties of studied materials are shown in table 1.

**Table 1:** Mechanical properties of studied materials

Mechanical properties	CK45	42CrMo4	AISI 303
Tensile strength $\sigma_R$ (MPa)	660	1100	625
Yield $R_{p0.2}$ (MPa)	410	980	330
Young's modulus $E$ (GPa)	206	206	178
Elongation $A$ (%)	23	16	58

The geometries and dimensions of the specimens are shown in Fig. 1. To compare the cyclic stress/strain evolutions and redistributions in the critical stressed volume, both smooth specimen, Fig. 1(a), and notched specimen, Fig. 1(b), were used in experiments. Table 2 shows the biaxial loading paths applied in experiments carried out using a biaxial servo-hydraulic machine 8800 Instron (fig.2).

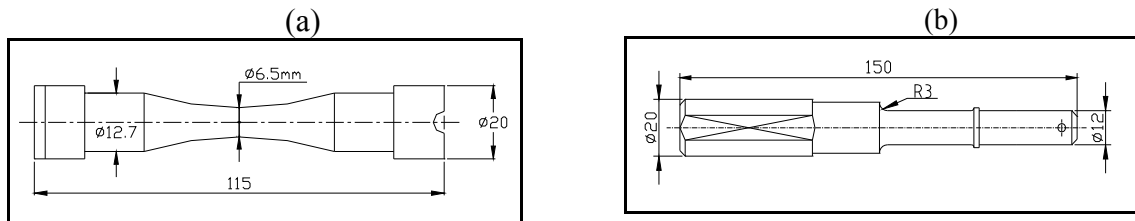


**Fig.1:** Specimens: (a) smooth, (b) notched

Axial stress  $\sigma$  and shear stress  $\tau$  were calculated from load and torque measured by a load cell. Equivalent stress  $\sigma_{eq}$  and equivalent plastic strain  $\varepsilon_{eq}^p$  were defined by von Mises equivalence for tension/torsion loading as:

$$\sigma_{eq} = \sqrt{\sigma^2 + 3\tau^2} \quad (1)$$

$$\varepsilon_{eq}^p = \sqrt{\varepsilon^p^2 + \frac{\gamma^p^2}{3}} \quad (2)$$

Equivalent total strain  $\sigma_{eq}$  was defined by analogy [3] as:

$$\varepsilon_{eq} = \sqrt{\varepsilon^2 + \frac{\gamma^2}{3}} \quad (3)$$

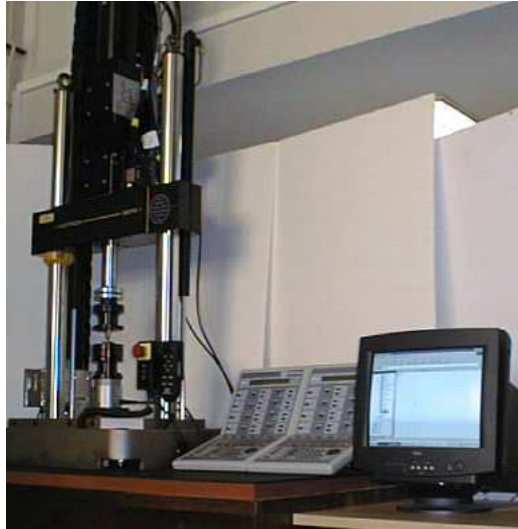


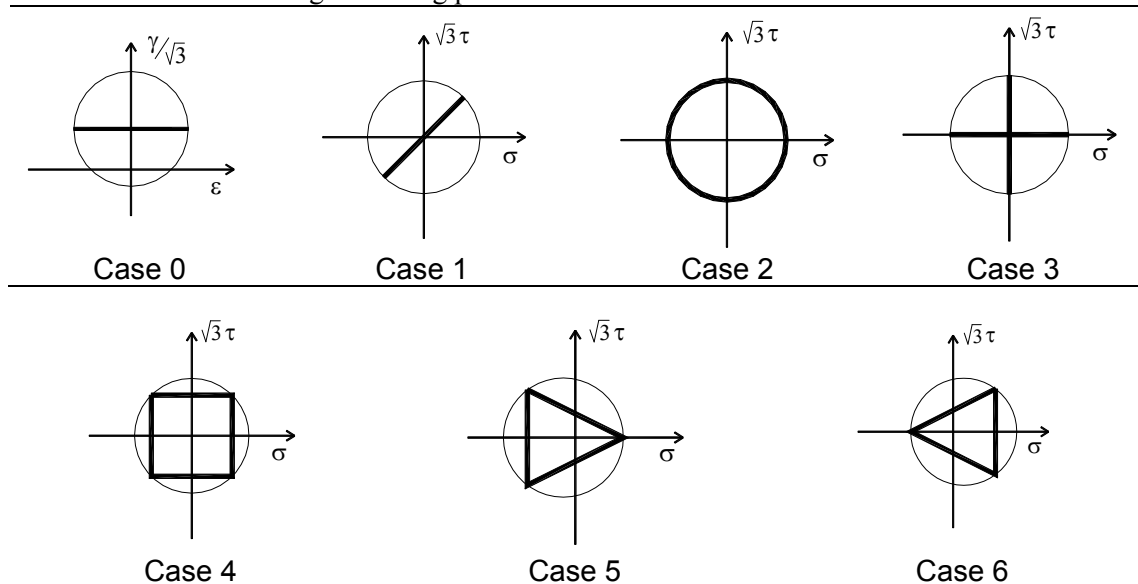
**Fig.2:** Biaxial testing machine 8800 Instron

The factor of non-proportionality of the loading paths can be characterized by the MCE (Minimum Circumscribed Ellipse) approach [4]:

$$F_{NP} = \frac{R_b}{R_a} \quad (4)$$

Where  $R_b$  and  $R_a$  are the minor and major radius of the Minimum Circumscribed Ellipse involving the loading path, as will be explained at the section of the MCE approach.

Table 2: Biaxial fatigue loading paths



### 3. NUMERICAL SIMULATIONS

The local cyclic elastic-plastic stress/strain responses are evaluated using Ansys finite element code. Isoparametric solid element C3D20R with 20 nodes and reduced integration points was used. Kinematic hardening model with von Mises yield criterion and associative flow rule was used for elastic-plastic FEA. The FEM analyses showed that the cyclic stress-strain responses are different under different loading paths. The

images of stress/strain distributions at different instant of the loading cycle are helpful to study the evolutions and redistributions of the cyclic stress/strain fields. Fig. 3 shows some cutting-view images of the notched specimen and Fig. 4 shows some cutting-view images of the smooth specimen under non-proportional loading.



Fig. 3: Some cutting-view images of the notched specimen



Fig. 4: Some cutting-view images of the smooth specimen

Fig. 5 shows the evolution histories of some local cyclic stress-strain responses, where it shows that the stabilized cycle differs from the initial cycle and the stress-strain ranges of the stabilized cycle are appropriate for life predictions.

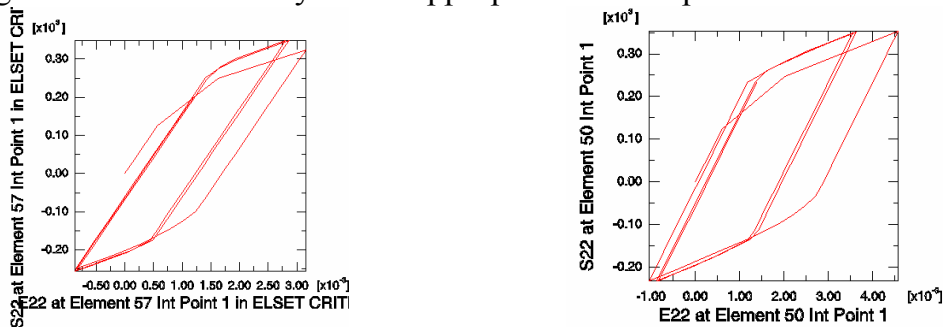


Fig. 5: Evolution histories of some local cyclic stress-strain responses

Fig. 6 shows the comparison between the shear stress relaxation during the first ten cycles for different levels of strain loading with loading path case 0, initial condition (see table 2). It is very interesting to note the similar way of the behaviour obtained.

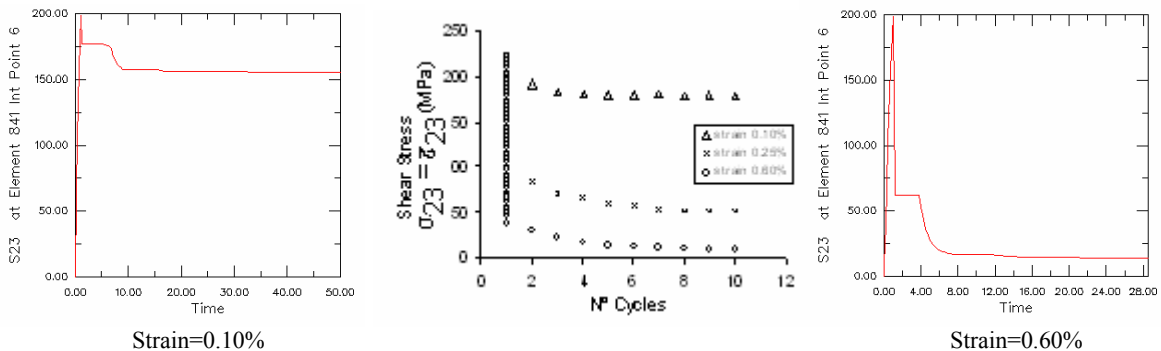


Fig.6: Comparison between FEA simulation and experimental evolution of the shear stress (CK45 steel)



## 5. RESULTS AND DISCUSSIONS

Fig. 7 shows the comparisons of the experimental fatigue life against the predicted results without and with modification for non-proportional effects, respectively. It can be seen that the predictions with the modified equivalent strain range of the ASME code (Fig. 7(b)) are more accurate when compared to the experimental results.

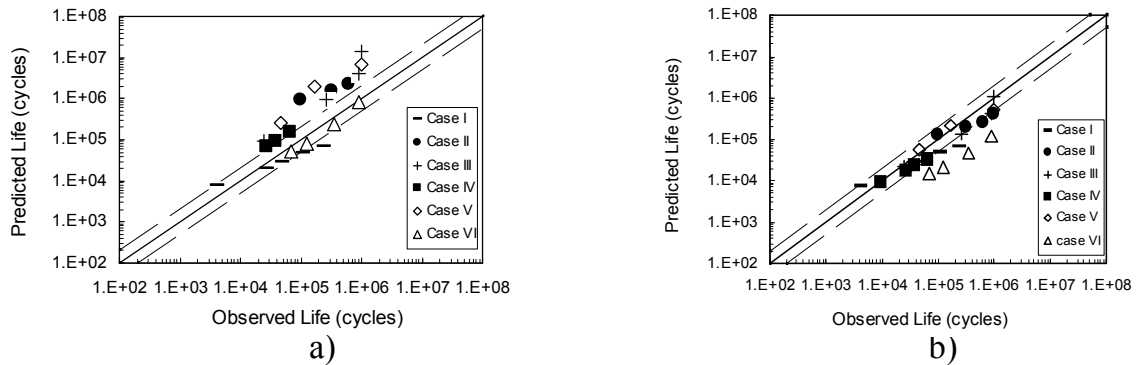


Fig. 7: Comparison between endurance experimental fatigue life of 42CrMo4 with predicted results by: (a) equivalent strain range of the ASME code, (b) modified equivalent strain range of the ASME code.

## 6. CONCLUSIONS

The local cyclic stress-strain states are influenced by the multiaxial loading paths, due to the interactions between the normal stress and shear stress during cyclic plastic deformation. The numerical simulations are very helpful to understand the evolutions and redistributions of the cyclic stress/strain field under multiaxial loading conditions.

The simple and easy of use approaches, such as the equivalent strain range of ASME code approach based on the distortion energy (6), can provide good predictions of fatigue life by taking into account some modifications for non-proportional effects.

Received May 30, 2005

The "Gh.Asachi" Technical University Iasi

## REFERENCES

- /1/. D. F. Socie and G. B. Marquis, *Multiaxial Fatigue*, Society of Automotive Engineers, Warrendale, 2000. PA 15096-0001.
- /2/. F. Ellyin, *Fatigue Damage, Crack Growth and Life Prediction*, Chapman & Hall, 1997.
- /3/. V. Aubin, P. Quaegebeur and S. Degallaix, *Cyclic Behaviour of a Duplex Stainless Steel under Multiaxial Loading: Experiments and Modelling*, Proceedings of the 6<sup>th</sup> International Conference on Biaxial/Multiaxial Fatigue & Fracture, Edited by M. de Freitas, Lisbon, Portugal, 2001, pp. 911-916.
- /4/. M.de Freitas, B. Li and J.L.T. Santos, A numerical approach for high-cycle fatigue life prediction with multiaxial loading *Multiaxial Fatigue and Deformation: Testing and Prediction*, ASTM STP 1387, S. Kaluri and P.J. Bonacuse, Eds., American Society for Testing and Materials, West Conshohocken, 2000, PA, pp.139-156.
- /5/. H. Zenner, A. Simburger and J. Liu, *On the fatigue limit of ductile metals under complex multiaxial loading*, Int. J. Fatigue, 22, (2000), pp.137-145.
- /6/. ASME Code Case N-47-23 (1988) Case of ASME Boiler and Pressure Vessel Code, American Society of Mechanical Engineers

**OBOSEALA LA SOLICITARI COMPUSE A UNOR OTELURI**

(Rezumat)

Acest studiu prezintă simulări privind evoluțiile și redistribuțiile tensiunilor și deformațiilor ciclice, și evaluarea parametrilor de oboseală necesari pentru aprecierea rezistenței la oboseală în cazul încărcărilor multiaxiale. Evoluția tensiunilor și deplasărilor la solicitările locale elasto-plastice au fost analizate utilizând un program de analiză cu element finit pentru ambele tipuri de epruvete lustruite și crestate, realizate din trei tipuri de materiale: un oțel carbon mediu obișnuit; un aliaj de oțel încălzit și revenit și un oțel inoxidabil. Pentru verificări experimentale sau efectuat o serie de teste la oboseală, compuse din tracțiune / compresiune cu torsiune statică sau ciclică pe o mașină servo-hidraulică de testat (Instron 8800). Comparațiile dintre simulările numerice și observațiile experimentale arată că simulările FEM permit înțelegerea mai bine a evoluției locale a tensiunilor și deformațiilor ciclice.

## **MODIFICATION AND GRAIN REFINING OF MULTIFUNCTIONAL MATERIALS IN Al-Si-Mg SYSTEM BY ADDITION OF Sr, Ti AND B**

**BY**

**PETRU MOLDOVAN, GABRIELA POPESCU, IOANA APOSTOLESCU  
and MARIANA ZSIGMOND**

**Abstract.** The aim of the paper is to present the influence of a new multifunctional material, a master alloy named Al-Sr-Ti-B, in aluminum foundry alloys. The Al-Sr-Ti-B master alloy represents a new combination of two master alloys, already known in aluminum industry, AlTiB and AlSr, used in treatment of aluminum alloys for grain refining and modification. The paper presents optic and electron microscopy studies realized on AlSi7Mg alloy treated with this new multifunctional material. The effect of nucleating particles (Al,Ti)B<sub>2</sub> together with the modification of structure obtained by SrAl<sub>4</sub> compounds was highlighted.

**Keywords:** master alloy, multifunctional materials, grain refining, modification

### **1. INTRODUCTION**

Great progresses have been achieved on aluminum alloys after the Crosley and Mondolfo work [1]. Since then, it is well known that AlTiB master alloy has normally been used as a grain refiner in aluminum foundry alloys, especially for Al-Si systems. As an alternative to this grain refining, Hydrelko and Aluminum Rheinfelden introduced TiBloy in 1993 [2], alloy which put in evidence a better grain refining qualities compared with AlTiB master alloy. TiBloy was designed especially for foundry industry and proved his better properties regarding grain refining efficiency, and also long holding time in this alloy system [3,4]. Now, TiBloy is a well-established grain refiner for aluminum foundry industry.

As a further development of this master alloy, Hydrelko tried to obtain another master alloy based on TiBloy but with strontium, named Strobloy. This new master alloy provides both grain refining of and modifies the Al-Si castings. The combined effect of this master alloy was studied by E.Bondhus and T.Sagstad [5]. They established that Strobloy had beneficial properties regarding grain refining and modification of A356 alloy.

In an effort to understand these remarks the authors tried to realize a multifunctional material Al-Sr-Ti-B, which have the benefits of both AlTiB as a grain refiner and AlSr as a modifier.

### **2. EXPERIMENTAL PROCEDURE**

Trials of grain refining and modification were realized in Department of Nonferrous Materials, Materials Science and Engineering Faculty, Polytechnic

University of Bucharest, on AlSi7Mg alloy. The chemical compositions of the AlSi7Mg alloy and also of the new master alloy Al-Sr-Ti-B used in experiments are presented in table 1.

Table 1. Chemical compositions of the used materials

Material	Chemical composition, wt. %							
	Al	Si	Mg	Mn	Fe	Ti	B	Sr
AlSi7Mg	Bal.	6.9	0.40	0.06	0.13	0.11	-	-
Al-Sr-Ti-B	Bal.	0.3	-	-	0.10	0.60	0.40	2.9

The Al-Sr-Ti-B master alloy was obtained by melting of AlSr10, AlTi10 and AlB8 master alloys in an electrical furnace with Khantal resistance, taking different percentages of master alloys, in the presence of argon gas as degassing agent and under refining and deoxidation protection fluxes. To realize this, first step was to allow Ti and B to react for obtaining  $(Al,Ti)B_2$  particles, these particles having a low solubility in molten aluminum. Secondly, by adding strontium after this reaction, a minimum of phases containing Ti, B and Sr will be created. Therefore, phases such as  $(Al,Ti)B_2$  and  $AlSr_4$  will be dominating phases in Al-Sr-Ti-B.

The EDS analysis of Al-Sr-Ti-B master alloy is presented in figure 1. We can remark the presence of Sr, Ti and B in the quaternary master alloy.

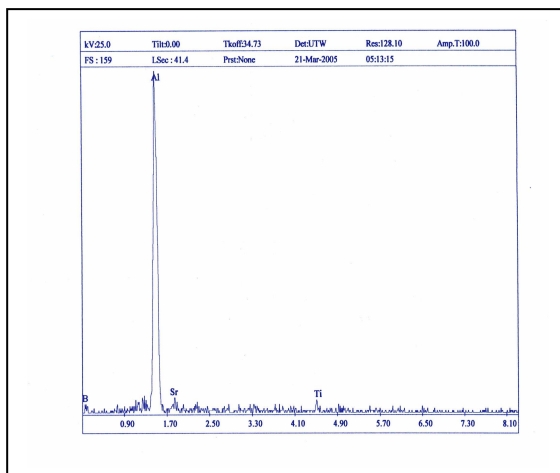


Fig. 1. EDS of multifunctional Al-Ti-Sr-B master alloy

The experiments were realized in graphite crucibles, starting with melts of 1kg, and taking samples of 200g from time to time.

The advantages of using Al-Sr-Ti-B multifunctional master alloy are:

- small addition, with low costs, because of cumulating of the two operations in one: grain refining and modification
- quick action of the grain refiners
- best quality of the cast parts surface because of the absence of microshrinkage and the absence of the hot cracking tendency
- high efficiency of modification and refining
- low contraction damages
- reducing of modifier/refiner addition error.

The treatment with this quaternary master alloy was realized on an AlSi7Mg alloy following the flowchart presented in figure 2.

The addition of Al-Sr-Ti-B master alloy was calculated for each sample at different strontium content: 50 ppm, 150 ppm, and respectively 250 ppm. Samples were taken from the molten melt at each 1 minute, 5, 30 and respectively 60 minutes.

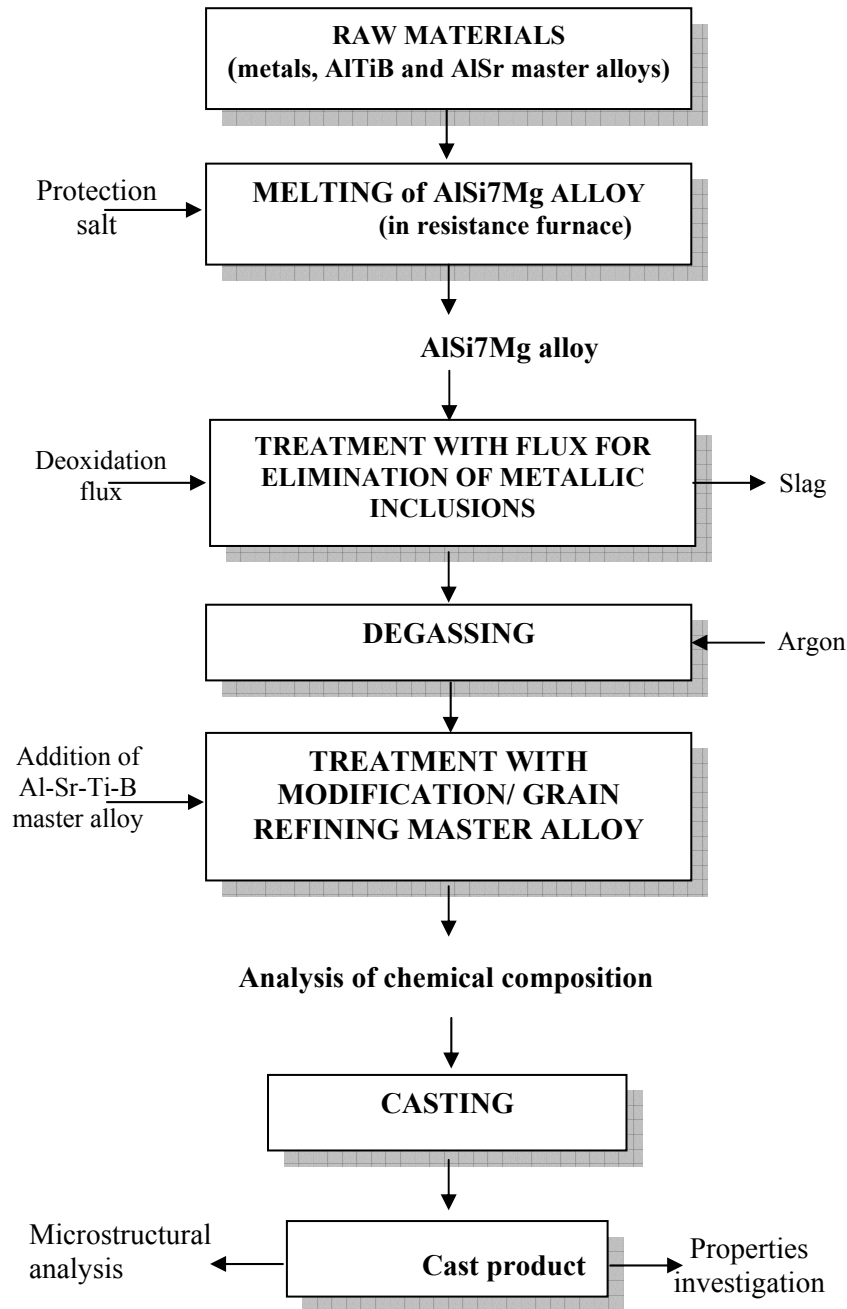


Fig. 2. Flow chart of AlSi7Mg multifunctional master alloy processing

### 3. Experimental results and discussion

The microstructure of an AlSi7Mg unrefined alloy is presented in figure 3.

The AlSi7Mg alloy was treated with Al-Sr-Ti-B master alloy introduced in the melt and stirred for 10 minutes. Due to the fact that the new master alloy contains a mixture of small boride particles,  $(Al,Ti)B_2$ , with lower density than aluminum, the experiments were done with low stirring rate.

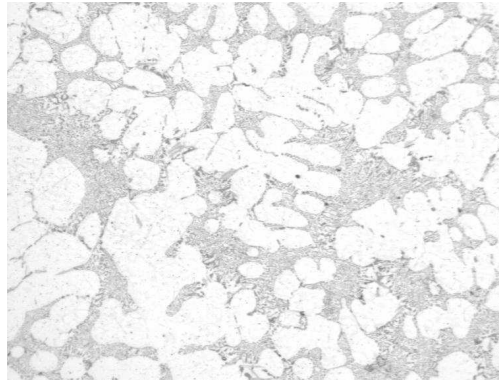


Figure 3. Microstructure of unrefined AlSi7Mg alloy; x200

The largest particles in Al-Sr-Ti-B were  $\text{AlSr}_4$  particles, which had fast-dissolving period then that are present in  $\text{AlSr}_{10}$  master alloy. The holding time before casting was increased in comparison with that used for refining only with Al-Ti-B master alloy. The microstructure of AlSi7Mg alloy treated with Al-Sr-Ti-B master alloy, containing 50 ppm Sr (noted sample 1), is presented in figure 4. We can observe the similarity of modification with that of the quaternary master alloy, which is almost the same or a better than the unmodified alloy but one cannot notice a significant improvement.

The microstructure of AlSi7Mg alloy treated with Al-Sr-Ti-B master alloy, containing 150 ppm Sr (noted sample 2), is presented in figure 5. We can remark a good modification and a good refining structure. We can say that this is the best content for the Al-Sr-Ti-B master alloy in order to obtain a very good structure.

The microstructure of AlSi7Mg alloy treated with Al-Sr-Ti-B master alloy, containing 250 ppm Sr (noted sample 3), is presented in figure 6. In this case, we remark a supermodification of the structure. So, we can stop with the strontium content at the level of 150 ppm, level in which we obtained a fine structure with fine dendrites. Also, we can remark the presence of  $\text{Al}_2\text{SrSi}_2$  ternary eutectic.

Figures 7 and 8 underline the modification index of AlSi7Mg0.3 and the grain size of this alloy in the case of Sr modification (at different content). We can easily notice that the modification with 50ppm Sr slightly improves the structure of the alloy. When Sr is added in a proportion of 150ppm we observe a good grain refining of the alloy. The grains become smaller and the effect of the grain refiner is clearly improved and the obtained structure has the correct granulation. In the case of modification with 250ppm Sr we can see an over modification of the alloy.

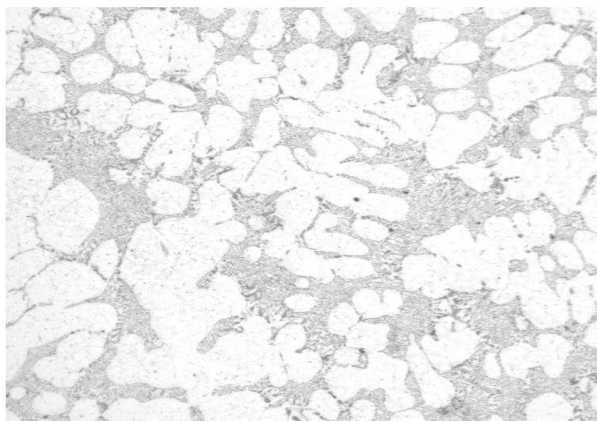


Figure 4. Microstructure of AlSi7Mg alloy treated with Al-Sr-Ti-B master alloy with 50 ppm Sr.

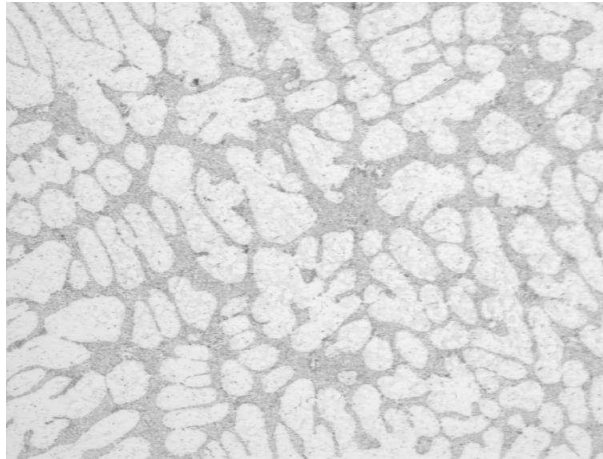


Figure 5. Microstructure of AlSi7Mg alloy treated with Al-Sr-Ti-B master alloy with 150 ppm Sr.

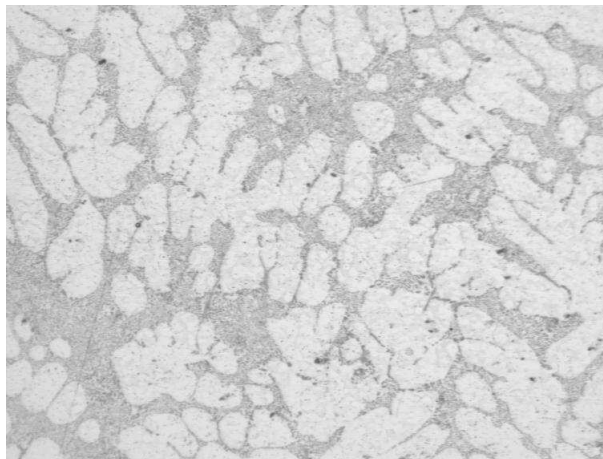


Figure 6. Microstructure of AlSi7Mg alloy treated with Al-Sr-Ti-B master alloy with 250 ppm Sr.

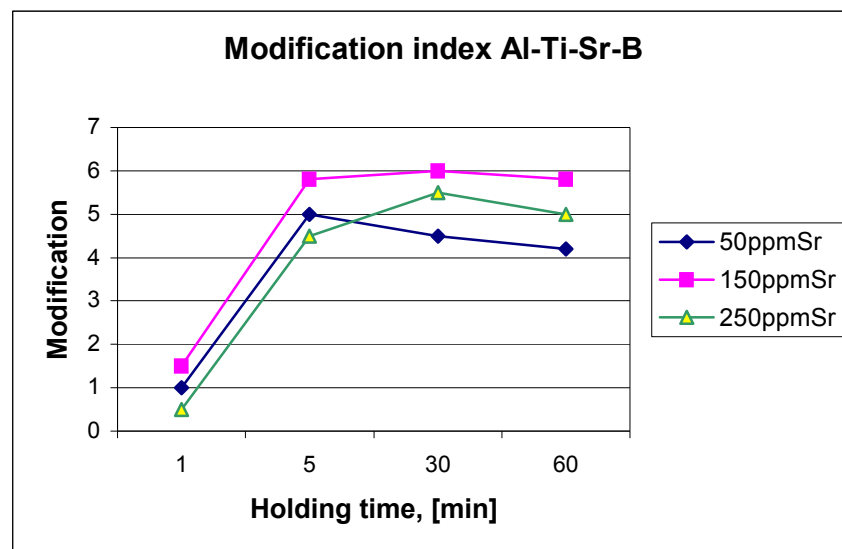


Fig.7 . Modification index of AlSi7Mg alloy with quaternary master alloy from Al-Ti-Sr-B system

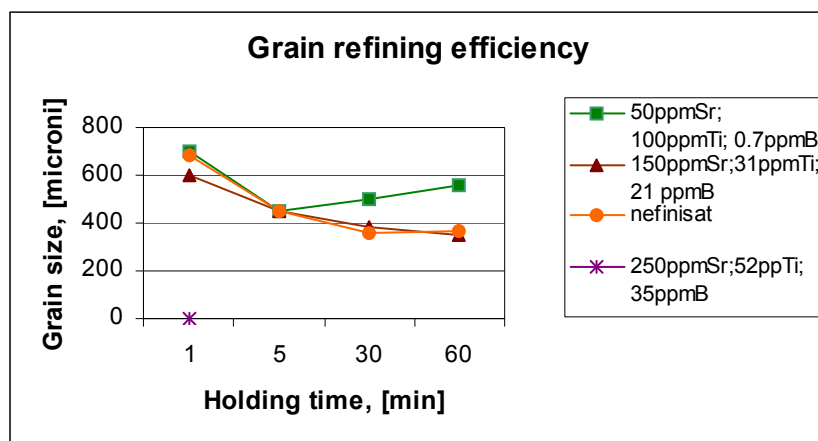


Fig. 8. Grain size of AlSi7Mg alloy in function of holding time of the Al-Sr-Ti-B master alloy

#### 4. CONCLUSIONS

1. Obtained results conclude that, it is important to combine two operations, modification and grain refining, in only one of treatment
2. Metallographic analysis showed a very good modification with the present of fine eutectic silicon in case of alloy treated with Al-Sr-Ti-B master alloy contain 150 ppm Sr.
3. Compared to separated additions of Al-Ti-B and Sr, the efficiency of quaternary master alloy is approximately the same.

Received May 30, 2005

"Politehnica" University București

#### REFERENCES

- /1/. P.E.Crosley, L.F.Mondolfo, AFS Transactions, vol.74, 1966, pp.53-64.
- /2/. H. Koch, U.Hielscher, A.Schaathum, a.o., "High effective permanent grain-refining for Al-Si foundry alloys", Rheinfelden, News from R&D Departement.
- /3/. E.Bondhus, T.Sagstad, "Grain refinement of hypoeutectic Al-Si foundry alloys with TiBloy", Light Metals 1999, pp.693-698.
- /4/. T.Sagstad, Nora Dahle, a.o., "Grain refining of hypoeutectic Aluminum-Silicon alloys with TiBloy", Molten Aluminum Processing, AFS-1998, pp.97-116.
- /5/. E.Bondhus, T.Sagstad, "Strobloy – The new combined grain refiner and modifier for hypoeutectic Al-Si foundry alloys", Light Metals 2000, pp.845-849.

#### MODIFICAREA SI FINISAREA GRANULATIEI MATERIALELOR MULTIFUNCTIONALE IN SISTEMUL Al-Si-Mg PRIN ADITIA DE Sr, Ti si B

(Rezumat)

Scopul acestei lucrări este de a prezenta influența unui material nou, multifuncțional, un prealiāj denumit Al-Sr-Ti-B, în aliajele de aluminiu de turnatorie. Prealiājul Al-Sr-Ti-B reprezintă o nouă combinație a două prealiāje deja cunoscute în industria de aluminiu, AlTiB și AlSr, folosite în tratarea aliajelor de aluminiu în vederea modificării și a finisării granulației. Lucrarea prezintă studii de microscopie optică și electronică realizate pe aliaj AlSi7Mg tratat cu acest material multifuncțional. Efectul particulelor multifuncționale (Al,Ti)Ti<sub>2</sub> împreună cu structura compusului SrAl<sub>4</sub> au fost evidențiate.



## THE TECHNOLOGY FOR HEAVY METALS FROM ELECTROPLATING SLUDGE VALORIFICATION, FOR ENVIRONMENT DEPOLLUTION

BY

ROMANIȚA TEODORESCU and \*MARIA GHEORGHE

*Abstract.* The paper presents the results of the researches performed into the RELANSIN program, for establish a new non-polluting technology, by total recovery of the some heavy metals from electroplating sludge resulted in the neutralization station of rinsing waters and spent solutions from the electroplating lines. This technology is non-producing of another noxious. The technology for recovery of the heavy metals from the sludge relies on chemical and hydro-metallurgical procedures, the final products being salts or pigments of the respective metals [ 1,2,3,4 ]. The technology for the irreversible immobilization of the heavy metals contained in the sludge or in the technological residues consists of their solidification/stabilization in siliceous matrix , the final products obtained in the immobilization process being used as building materials [ 5,6 ]. This paper presents: the technology for recovery of some metals which for the content in the sludge is very high 8-15%; the inertization of the technological residues resulted from the heavy metals recovery process by immobilization in different kinds of composites materials utilized like building materials. The leaching tests have proved the irreversible binding capacity of metals in the composites materials structure [ 7 ].

**Keywords:** electroplating sludge, wastes, technologies, L:L extraction, cementation, precipitation.

### 1. INTRODUCTION

Several industrial sectors especially those of surface treatment and electroplating lines, discharge waste solutions containing heavy metals such as zinc, copper, nickel, etc. These effluents are currently treated by conventional methods such as precipitation, ion exchange, evaporation, reverse osmosis, electro-dialysis , adsorption by activated carbon or clays, solvent extraction, cementation /1,2,3,4.../. The most popular is the neutralization/precipitation that generates sludge containing heavy metals. The resulting sludge, contain the metals like sparingly soluble hydroxides. Currently, these materials are stored in controlled waste disposals.

Nowadays we are facing an important decrease in natural raw materials. In the same time the concentration of useful non-ferrous metals in wastes is sometimes higher than that existing in ores.

Therefore, metals recovery from those polluting useless wastes, could be an important solution now and in the future. The use of wastes is also useful because of the necessity to eliminate the environmental pollution in the context of the integration of Romania in UE.

The available literature on this subject indicates that many specialists from all over the world are working to solve the pollution problems risen by the sludge containing toxic metal ions (Cr, Cu, Ni, Cd, Zn, Fe, Pb etc.). Chemical and hydro-

metallurgical processes and the immobilisation of the metals in siliceous matrixes are recommended for their recovery. These processes are based on metals leaching followed by their separation using different methods.

The immobilisation in siliceous matrix are realised by solidification/stabilisation of heavy metals from the sludge in hydraulic matrix with Portland cement, mixing with or without other supplements, or in ceramic matrix at the temp. over 1000<sup>0</sup>C / 5,6.

In the case of the immobilisation of heavy metals the most important is the study of the irreversible immobilisation capacity of the metals in siliceous matrix. These determinations were realised by the study of the heavy metals leaching in waters for long time in accordance with international norms by leaching tests / 7 /.

This work presents the experiments performed last years by our research group in the field of recovery of heavy metals from electroplating sludge with high content of the metals. These sludge resulted from collective neutralisation of washing waters and spent solutions arise from electroplating lines on two Romanian industrial platforms of machine building and electro-techniques industry.

## 2. EXPERIMENTAL

### Materials and the methods

The work presents the researches which was carried out for a new technology non-polluting and non producing of another noxious, stabilisation for some heavy metals from EL-CO and HIDROJET industrial sludge valorification.

Two work methods was utilised:

- chemical or hydro-metallurgical processing of the sludge, in acid medium at normal or high pressure and temperature, for quantitative leaching of the metals with high content,
- recovery of the metals from the leaching solutions by various methods.

The influence of the various work parameters like temperature, pH, L:S ratio, number of the extraction steps on leaching and recovery of the metals efficiency was studied.

The table nr.1 shows the compositions of the sludge which were utilised in the works.

In order to the recovery of the heavy metals, the electroplating sludge was processed by washing, re-washing, filtration, drying and crushing.

The studies were conducted in three works variant (fig.nr.1), as follows:

In the first variant the processing of the sludge include the following steps:

- the acid leaching in counter-current at high temperature and pressure
- the processing of the finale solutions by cementation for copper recovery

The washed Cu-Zn-Ni sludge was introduced by continuous stirring in leaching reactor (autoclave), in the first step over intermediate solution, resulted in the second step of the leaching. In the reactor the enriching in copper and zinc of the solution, the advanced separation of the impurities and bring the pH in 2-3 interval., take place. After separation of the phases, siphon off the clear solution and filtration, a final solution and a thickened was resulted. The thickened was re-introduced together sulphuric concentrate acid and washing and fresh water in autoclave in the second leaching step. In that step take place the finish of the leaching of the metals reaction and the partial purification of the solutions by re-precipitation of some impurities.

After filtration results:

- an intermediate solution which is re-circulate in the first step of the leaching
- a residue which comport washing, drying, and inertization in siliceous matrix

Table 1. Spectral and chemical composition of the EL-CO and HIDROJET sludge

Metals (in dry sludge) %	Spectral analyse	chemical analyse, %			
		EL-CO		HIDROJET	
		Sample 1	Sample 2	Sample 1	Sample 2
Cu	p	18,56	17,1	<0,005	10,46
Zn	p	14,21	17,3	9,33	0,18
Cr	0,5-1	1,46	0,56	-	0,01
Fe	0,5-1	1,38	2,13	22,62	0,54
Pb	0,5	0,06	0,042	0,09	<0,01
Si	0,1-0,5	0,62	1,48	0,25	0,016
Na	p	2,45	1,25	1,0	26,4
Al	$5 \cdot 10^{-2}$	0,048	0,16	-	0,009
Ni	0,5-1	1,48	4,3	0,08	0,007
Mg	0,1-0,5	0,54	0,84	-	-
Ag	$5 \cdot 10^{-2}$	0,062	0,054	-	-
Sn	$5 \cdot 10^{-3}$	0,008	0,2	-	-
P	$5 \cdot 10^{-2}$	0,01	0,04	12,55	-
Anions: $\text{NH}_4^+$		absence	absence	absence	absence
$\text{NO}_3$		7,56	2,85	1,0	4,5
$\text{SO}_4$		9,9	1,68	0,31	27,0
$\text{CO}_3$		8,41	10,97	0,84	30,07
Cl		0,76	0,22	0,01	14,87
$\text{H}_2\text{O}$		9,77	6,3	1,3	7,4
Lost of the burning:					
P.C. $800^\circ\text{C}$		30,66	30,72	15,42	26,89
P.C. $1000^\circ\text{C}$		30,75	31,08	15,45	42,33

The leaching efficiency of the sludge in that variant is about 85%.

In order to recover the copper from the final solutions the cementation technique with zinc metallic was applied. The Cu cement resulted was separated by filtration from Zn and Ni solutions, washed, dried and grind.

The total efficiency for cementation of the copper in that variant is over 97%.

In the second variant the processing of the sludge include the following steps:

- the acid leaching in counter-current at high temperature and pressure
- the processing of the finale solutions by L:L extraction for copper recovery
- the regeneration of organic phase
- alkaline precipitation in three steps
- the inertization of the residue in siliceous matrix

The recovery of the Cu from the final solutions was realised by extraction with organic solvents. Like extraction agent was utilised the agent ACORGA M 5640 in KEROSEN. The leaching solutions with 15 g/l Cu content - resulted by dilution with water - was introduced in extraction installation, in three steps, in counter-current. Cu was extracted in organic phase. The regeneration of organic phase and the recovery of

the Cu after quantitative separation of the phases take place in stripping installation, in three steps, in counter-current. Like stripping agent is utilised an acid solution of copper sulphate. Finally, after three re-circulation, a copper sulphate with 45 g/l concentration and a Zn and Ni sulphate solutions, resulted from this installation. The recovery of the copper from the sulphate solutions was realised in electrolytic installation.

The recovery of the metals from Zn and Ni sulphate solution was realised in three steps, in alkaline medium, by precipitation.

In the first stage, in the interval of the pH = 3-5,5, the metal impurities like Cr, Fe, residual Cu a.o. are taken away from the solutions and accumulate in solid phase.

Under continuous stripping the solutions with Zn and Ni content resulted at the cementation or at the L:L extraction was introduced in precipitation reactor together with the agent of precipitation (NaOH sau Na<sub>2</sub>CO<sub>3</sub>).

In the second stage of the precipitation, in the pH = 5,5-7,5 interval, take place the quantitative Zn precipitation. After washing, drying and burning of Zn precipitate a ZnO pigment possible to utilise in the tyre or construction industry, was obtained.

In the third stage of the precipitation, in the pH = 7,5-10,5 interval, take place the quantitative precipitation of the Ni and the complete release of metals from the solutions.

The salts of the nickel, carbonate or hydroxide, resulted from the precipitation were separated by filtration from the suspension, washed and dried. The washing waters, free of the heavy metals, were sanded in the neutralisation station.

## **Results and discussions**

In the following tables, the work parameters on the phases of the flow sheet, there are presented.

Table 1 shows that the sludge used for the experiments contain high quantities of heavy metals ions (Cu, Zn, Ni, Fe). In the experiments which were performed in the conditions presented in the table nr.2, 3... it was observed that :

Table nr.2 The work conditions utilised at the washing of the sludge

<b>washing of the sludge</b>	
washing agent	water
nr.of washing steps	4
work techniques	re-washing
temperature	20-30 <sup>0</sup> C
stirring times	30 min/ step
S:L ratio	1:4
The composition of the unwashed sludge: 3-8% SO <sub>4</sub> <sup>2-</sup> and 2 – 5 % Na	
The composition of the washed sludge: 0,5-1,3% SO <sub>4</sub> <sup>2-</sup> and 0,2 – 0,8 % Na	

Table nr.3 The work conditions utilised at the leaching of the sludge

<b>Leaching <i>in open system</i> / autoclave</b>	
washing agent	acid medium - H <sub>2</sub> SO <sub>4</sub>
acid concentration	20%
temperature	60 – 80 / 135-145 <sup>0</sup> C
pressure	Normal / 3-4 atm
consumption of the acid	Excess / stoichiometric
- S:L ratio	1 : 5 - 1 : 8
- reaction time	2h / 1h / step
- final pH	1,5 – 2 / 2,5 - 3
- technique of the work	counter-current
- density	1,1-1,2 / 1,2 – 1,3
Leaching efficiency	80% / 83-85%
The composition of the intermediate solution 11,55Cu, 10,82Zn, 1,44g/l Ni pH = 0,89	
The composition of finale solution: 26,6 / 35 Cu, 24,57 Zn, 1,59 Ni, 0,7 Fe, 0,59 Cr, 0,43 g/l Si, pH = 2,6	

The composition of the sludge before and after washing shows that after 4 washing steps in counter-current in the optimum conditions presented in the table nr 2, the removal efficiency of the  $\text{SO}_4^{2-}$  is over 95%

The analyse of the results obtained in the leaching experiments of the sludge in acid medium shows that

- for the sludge with high content of Cu and Zn, working in open system, at 70 - 80°C S:L ratio 1 : 6, time 2 h, at pH=1,5 - 2, the leaching efficiency for the Zn is over 90% but for Cu is lower, about 50%
- for pH=0,5-1,5 the leaching efficiency is highest but, impurities pass in the solutions
- for the leaching of the sludge in autoclave, at high temperature 135-140°C and 3-4 atm pressure, pH between 2,1-2,6 the content of the impurities in the solutions is minimum and the leaching efficiency of the copper is over 85 %
- the composition of the final solutions resulted in the second step of the leaching, in autoclave, in two counter-current steps, shows that the Cu and Zn contents, between 35-45 g/l, are with 25-30% over the same content from the solutions resulted in open system and the content of the impurities is under the content from the same solutions
- the leaching efficiency is higher in the counter-current system
- the consumption of the reactive are lower by re-circulation of the solution

Table nr.4 The work conditions utilised at Cu cementation

<b>Copper cementation</b>	
Cementation agent	metallic Zn
Consumption of Zn	stoichiometric+excess 20-30 %
time	105 minute
temperature	45°C
washing agent	water
Cementation efficiency	97%
Cu cement: Cu 92,3,Zn 0,28, Ni 0,006, Cr 0,14, Fe 0,01%	
sulphates solutions Zn 61,4, Ni 3,3 %	

- Working in the conditions presented in the table nr.4 the results show that:
- the cementation of the Cu is quantitative
  - the Cu cement has good qualities.

Table nr.5 The work conditions utilised at the L:L extraction of the Cu

<b>L: L Extraction in counter-current</b>	
extraction agent	ACORGA M 5640 in KEROSEN
FO : FA Ratio	1:1
nr. of extraction steps	3
stirring time	5 minute / step
temperature °C	23
pH	about 2
extraction efficiency	99 %
Composition of the sulphate solution Zn, Ni 14 Zn, 2,7 Ni, 1,56 g/l Cu	

The analyse of results obtained in the extraction experiments show that : from the solutions with 14,3 Cu, 14 g/l Zn content, at pH=1,8-2, working in counter-current in 3 extraction steps, the rapport Cu/Zn is modified from 1,02 at 0,1-0,12 by removal of the Cu. The extraction efficiency of copper is over 95%. Therefor, from the solution where the content of the copper is under 14 g/l the extraction efficiency of copper is maximum.

Table nr.6. The work conditions utilised at the regeneration of the organic phase

<b>OF Regeneration in counter-current</b>	
stripping agent	copper sulphate solution
OF: SA Ratio	1:1
nr. of re-extraction steps	3
stirring time	5 minute / step
temperature °C	ambient
re-extraction efficiency	99,9 %
initial solution : copper sulphate solution 18 g/l Cu , acidity ~180g/l H <sub>2</sub> SO <sub>4</sub>	
finale solution: copper sulphate solution 34 –37 g/l Cu and 1,1 –1,2 g/l Zn	

The experiments show that the Cu sulphate solution with 18 Cu, 180 g/l H<sub>2</sub>SO<sub>4</sub>, stripping agent , realised the quantitative retention of the copper from OF like Cu sulphate . After 3 re-extraction steps the content of the Cu in solution is 44-45 g/l . Cu is recovered from this solutions by electrolysis. The re-extraction efficiency of Cu is over 98%. The content of Cu and Zn in regenerated OF in 3 steps is under 0,1 g/l

Table nr.7. The work conditions utilised at precipitation

<b>Precipitation</b>	
medium	NaOH / Na <sub>2</sub> CO <sub>3</sub>
temperature	40-60°C
Nr.pp. steps	3
time	2h/ 1step, 3h/ 2 step 1h/ 3 step +1/2h at pH ct
pH	2,5 - 5,5 / 1step 5,5 - 7,5 / 2step 7,5 - 10,5 /3step

The purification of the solutions was realised by precipitation with a solution of NaOH or Na<sub>2</sub>CO<sub>3</sub> 355 g/l , in the interval of the pH 2,5-5,5. The precipitate of the impurities after washing and dried is possible to utilise in construction materials.

After the impurities separation, under continue stirring, at the pH between 5,5-7,5 zinc was precipitated from the solutions like hydroxide or carbonate. The Zn precipitation efficiency is over 95%. Over pH 7,7 from the solution was precipitated the salt of the Ni with very good efficiency. The technique of precipitation allow the release of all the metals from the solutions resulted after recovery of copper .

After separation of zinc salts by filtration, washing with water in 4 steps , dried and burning at 800-850°C for 2 hours, resulted ZnO for rubber industry or substitution pigment in construction materials.

Table nr.8 The work conditions utilised at burning

<b>Burning</b>	
Material	zinc precipitate (2 <sup>th</sup> step)
temperature	800 - 850 <sup>o</sup> C
Time	2 h
harden / washing agent	water

### **The immobilisation of the metals in the construction materials**

From the technology which was presented in the fig.nr.1 resulted next to the final products:

- a precipitate of the impurities in the first step of the precipitation
- the technological residues resulted at the leaching of the sludge.

Table nr.9. The medium composition of a finale residue

Metal / residue	Cu %	Fe %	Al% / P %	Cr %	Ni %	Na %	Si %	Zn %	Ca %	SO <sub>4</sub> <sup>2-</sup> %
EL-CO residue from autoclavization	2,08	7,16	0,44/	1,00	0,036	0,27	0,002	0,22	6,09	19,6
EL-CO residue from normale solubilisation	1,9	1,35	/0,02	0,03	0,056	0,086	3,47	0,16	5,24	3,6
HIDROJET rezidue normale solubilisation	0,004	29,0	/15,5	0,18	0,007	0,034	0,034	2,3	6,3	0,6

The ecological immobilisation in siliceous matrix was realised by solidification/stabilisation of heavy metals from the technological residues in hydraulic matrix, mixing Portland cement with 50% residue, or the immobilisation of heavy metals in a stable structure with 10-15% residue with or without other supplements, the resulted materials can be used like construction materials.

The study of the irreversible immobilisation capacity of the metals in siliceous matrix were realised by the study of the heavy metals leaching in waters for long time in accordance with international norms by leaching tests. The results show us that after 365 days the content of the metals in water was <0,001g/l , therefore all the metals was complete immobilised .

## **2. CONCLUSIONS**

The researches which was carried out ,allowed us to establish a complex technology which was patented and verified at pilot level .

The combinative process for the integral valorification of Cu, Zn, Ni, from the electroplating sludge consist in the leaching of the sludge in sulphuric acid , cementation or L:L extraction of the copper from the leaching solutions, the precipitation of the zinc and nickel from the solutions free of copper and the inertization of the technological residues in siliceous matrix .

Received April 19, 2005

*Institute for Non-Ferrous and Rare Metals, București*  
*\*Technical University of Civil Engineering, București*

**REFERENCES**

- /1/. Zadiranov A.N. *Recycling technologies of nickel metal – containing wastes recovery in electroplating industry*, Recycling and Waste Treatment in Mineral Processing: Technical and Economic Aspects 16-20 June 2002 , Lulea Sweden, Proceedings pg. 815-820.
- /2/. Serdar Aktaş, *Recovery of zinc from galvanized scraps*, Turkish Journal of Engineering & Environmental Science 2002, 26(5) 395-402.
- /3/. Gunter Subklew a.o., *Separation of heavy metals from industrial waste waters by reactive liquid/liquid extraction*, Models in chemistry 134 (6), 28 apr. 1997, pp 853-864.
- /4/. Albinas Pigaga, a.o, *Waste treatment of two electroplating solutions of Cu and Zn by mixing and precipitation*, Separation Science and Technology, 37(13), 3155-3168 (2002)
- /5/. R. Teodorescu , S. Martinez , J. MaNoguez Carulla , R. Mateuca, *Stabilisation of heavy toxic metals from electroplating sludges in siliceous matrixes* ,3rd International Conference of Balkan Environmental Association on Transboundary Pollution 23 – 26 nov.2000, Bucharest, Romania
- /6/. M. Gheorghe, R. Teodorescu, *Some aspects regarding the influence of the type concrete matrix on the s/s process of some industrial electroplating sludge*; International Congress , Dundee University 2002 ,proc.
- /7/. German Standard: DIN 38414 Tail 4

**TEHNOLOGIE DE VALORIFICARE A UNOR METALE GRELE DIN NAMOLURI GALVANICE ÎN  
VEDEREA DEPOLUĂRII MEDIULUI**

(Rezumat)

Lucrarea prezintă rezultatele cercetărilor efectuate în cadrul programului RELANSIN de stabilire a unei tehnologii noi, nepoluante și neproducătoare de alte noxe, prin recuperarea totală a unor metale grele din nămolurile galvanice rezultate în stațiile de neutralizare uzinale a apelor de spălare și a soluțiilor epuizate din liniile de acoperiri metalice. Tehnologiile pentru obținerea metalelor grele din nămoluri se bazează pe procedee chimice și hidro-metalurgice, produșii finiți fiind săruri sau pigmenți ai metalelor respective /1,2,3,4/. Tehnologiile de imobilizare ireversibilă a metalelor grele conținute în nămoluri sau în reziduurile tehnologice, constau în solidificarea/stabilizarea lor în matrice silicioase , produșii finiți obținuți în procesul de imobilizare fiind utilizați ca materiale de construcții /5,6/. Lucrarea prezintă: tehnologia de recuperare a unor metale pentru care conținutul în nămol este de peste 8-15 %; inertizarea reziduurilor tehnologice rezultate în procesul de recuperare a metalelor grele prin imobilizare în diverse tipuri de matrice silicioase cu obținere de materiale compozite cu utilizări în construcții. Testele de levigare ale acestor materiale evidențiază capacitatea blocării ireversibile a metalelor în structura matricei /7/.

**Mulțumiri**

Autorii mulțumesc Ministerului Educației și Cercetării pentru ajutorul financiar acordat pentru realizarea acestui proiect.



## PROCESSING EXAMPLE FOR SUSTAINABLE DEVELOPMENT CONCEPTON METALLURGICAL FIELD LEVEL

BY

MIRELA SOHACIU and AVRAM NICOLAE

**Abstract.** In this paper, the authors test concrete possibilities for applying sustainable development in case of recycling powder materials use (EAF dust, scale and slurry) for steelmaking in electric arc furnace. Using method for recycling powder materials is briquettes making. The authors research the briquettes behavior to transport and handling by experimental measurements concerning the fissure strength ( $R_f$ ), crushing strength ( $R_s$ ), crushing interval ( $R_{fs}$ ). It was establish the best field from technological point of view for using efficient briquettes. It makes recommendations concerning the best proportions of EAF dust, scale and slurry, which can be add in briquettes.

**Keywords:** sustainable development, recycling powder materials, EAF dust briquettes

### 1. INTRODUCTION

The metallurgical process is submitted compulsory to the leading activity, today. For this, it appeals to processing named process identification.

The identification experiment has 2 phases:

- the knowledge (acquisition) of input-output process;
- processing of acquisition data.

For processing of acquisition data, we will use numerical methods of linear and / or not linear regression in parameters.

The model obtained, which are afferent for a process for its identification on processing of acquisition data, represents, in essence, which in literature named experimental modeling, too.

Taking into consideration that, in prospect, the using of by-products (including powder materials) will have a very big extension, the authors consider that the identification of such processes has a big importance, in this way, on the basis of model obtained it can provide the technologies leading (automatic, possibly) for expanding EAF materials base by using of substitute for scrap.

### 2. INFORMATION CONCERNING THE BRIQUETTES MAKING.

For briquettes making it was collected, in the first stage, lots of 50 kg of by-products (EAF dust, slurry, scale) from industrial high tide, which is to CH. Chemical analysis of these materials lots made by 2 methods: damp chemical

analysis and atomic absorption spectrometric analysis. The average chemical composition of 3 by-products is presented in table 1 and table 2:

Table 1. Chemical composition of raw materials which was made by damp chemical analysis

Component	Amount [%]		
	EAF dust	Scale	Slurry
SiO <sub>2</sub>	5,36	0,8	1,29
CaO	9,33	0,49	0,77
MgO	5,93	0,36	0,58
Al <sub>2</sub> O <sub>3</sub>	0,66	0,14	0,21
Fe <sub>tot</sub>	35,15	73,08	63,61
FeO	3,82	66,1	42,52
Fe <sub>met</sub>	0,61	0,56	1,21
Fe <sub>2</sub> O <sub>3</sub>	45,15	30,33	42,03
MnO	3,49	0,42	0,57
Cr <sub>2</sub> O <sub>3</sub>	0,37	0,11	0,11
P <sub>2</sub> O <sub>5</sub>	0,22	0,14	0,05
S	0,14	0,02	0,05
Na <sub>2</sub> O	0,55	0,18	0,19
K <sub>2</sub> O	0,4	0,03	0,07
C	1,80	0,11	7,76
Calcinations loss	7,03	0	5,75

Table 2 Chemical composition of raw materials which was made by atomic absorption spectrometric analysis

Component	Amount [%]		
	EAF dust	Scale	Slurry
CuO	0,02	0,09	0,13
PbO	0,8	0,05	0,04
ZnO	8,1	0,06	0,04
CdO	0,03	0,001	0,001
NiO	0,02	0,03	0,02

The composition characteristics of using admixture materials are presented in table 3:

Table 3

Composition, %	Coke	Ash coke	Limestone	Lime	Bentonite
FeO	-	15,5	-	-	-
MnO	-	0,45	-	-	-
SiO <sub>2</sub>	-	46	3,74	4,8	38,8
CaO	-	4,6	51,25	93	17
Al <sub>2</sub> O <sub>3</sub>	-	19...22	1,47	1,8	16,5
MgO	-	2,4	0,85	1,3	3
Fe <sub>2</sub> O <sub>3</sub>	-	1,6	-	-	-
Na <sub>2</sub> O <sub>3</sub>	-	-	-	-	-
S	1,1	-	-	-	-
P	-	-	-	-	-
C	86,7	-	-	-	-
V	0,7	-	-	-	-
W	7...8	-	-	-	14,9
A	11,6	-	-	-	-

The recipes of briquettes making, which subdue experiments are presented in tables 4 – 6:

**Table 4.** The recipes of briquettes making with EAF dust, [%]

Component	The recipe							
	BP 1	BP 2	BP 3	BP 4	BP 5	BP 6	BP 7	BP 8
EAF dust	71,5	72,0	72,5	73,0	73,5	74,5	75,5	76
Bentonite	7	7	7	7	6,5	6,5	6,5	6,5
Lime	Constant							
	3,8	3,8	3,8	3,8	4	4	4	4
Limestone	0,5	0,5	0,5	0,5	1,0	1,0	1,0	1,0
Coke	17,2	16,7	16,2	15,7	15,0	14,0	13,0	12,5
<b>Total</b>	100	100	100	100	100	100	100	100

**Table 5.** The recipes of briquettes making with scale, [%]

Component	The recipe					
	BT 1	BT 2	BT 3	BT 4	BT 5	BT 6
Scale	59,5	60,5	61	62	63	63,5
Bentonite	7	7	7	6,5	6,5	6,5
Lime	Constant					
	5	5	5	4,7	4,7	4,7
Limestone	0,5	0,5	0,5	1,0	1,0	1,0
Coke	28	27	26,5	25,8	24,8	24,3
<b>Total</b>	100	100	100	100	100	100

**Table 6.** The recipes of briquettes making with slurry, [%]

Component	The recipe					
	BN 1	BN 2	BN 3	BN 4	BN 5	BN 6
Slurry	62,0	62,5	63	64	65	66,0
Bentonite	7	7	7	6,5	6,5	6,5
Lime	Constant					
	5	5	5	4,7	4,7	4,7
Limestone	0,3	0,3	0,3	0,6	0,6	0,6
Coke	25,7	25,2	24,7	24,2	23,2	22,2
<b>Total</b>	100	100	100	100	100	100

### 3. EXPERIMENTAL RESULTS. GRAPHICAL PROCESSING. EXPERIMENTAL MODELING.

The experimental results are presented in table 7.

Graphical processing of experimental data is presented in figures 1...4.

The experimental modeling, which was materialize in regression equations, is presented in figures 1 ... 4.

**Table 7.** The results of compression tests

Sample	$R_f$ , [kN/cm <sup>2</sup> ]	$R_s$ , [kN/cm <sup>2</sup> ]	$\Delta R_{fs}$ , [kN/cm <sup>2</sup> ]	Proba	$R_f$ , [kN/cm <sup>2</sup> ]	$R_s$ , [kN/cm <sup>2</sup> ]	$\Delta R_{fs}$ , [kN/cm <sup>2</sup> ]
BP 1	0,76	0,91	0,15	BP 5	0,42	0,72	0,30
BP 2	0,68	0,87	0,19	BP 6	0,46	0,71	0,25
BP 3	0,59	0,79	0,20	BP 7	0,48	0,78	0,30
BP 4	0,57	0,80	0,23	BP 8	0,45	0,76	0,31
BT 1	0,39	0,49	0,10	BT 4	0,30	0,40	0,10
BT 2	0,34	0,45	0,11	BT 5	0,31	0,41	0,13
BT 3	0,33	0,43	0,10	BT 6	0,29	0,43	0,14
BN 1	0,34	0,38	0,04	BN 4	0,26	0,28	0,02
BN 2	0,33	0,36	0,03	BN 5	0,24	0,30	0,06
BN 3	0,30	0,33	0,03	BN 6	0,26	0,31	0,05

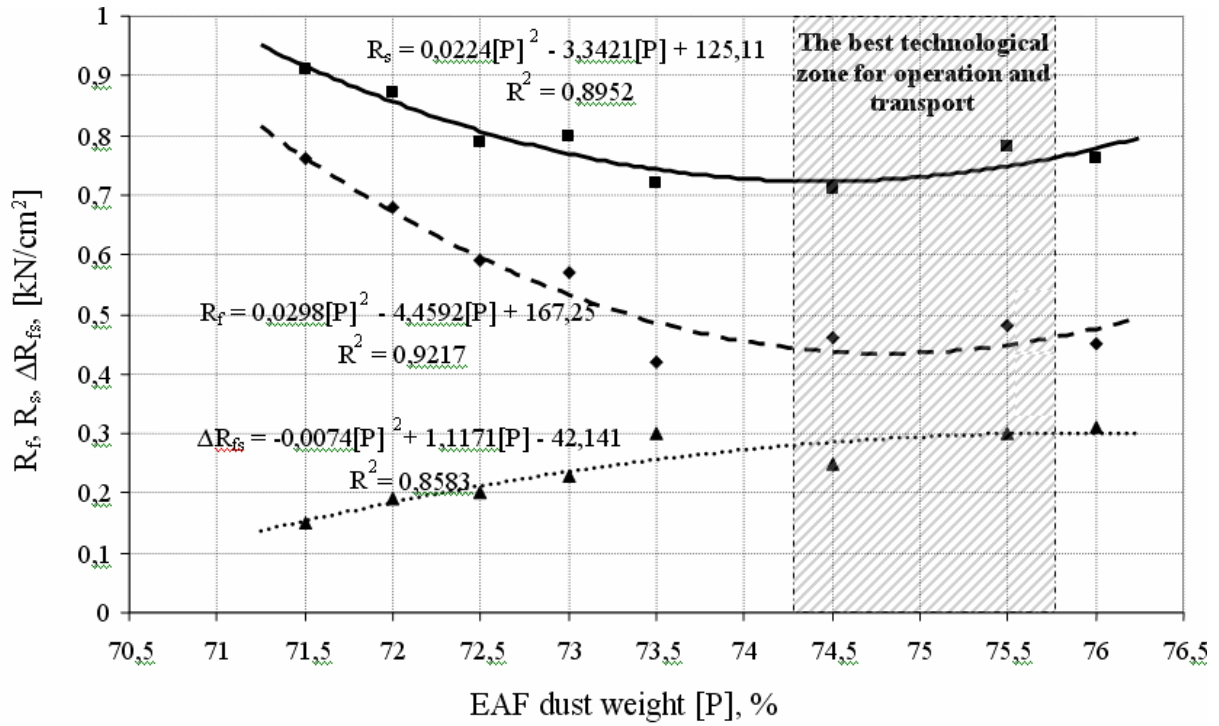


Fig. 1. The briquettes behaviour to operation and transport, function of EAF dust weight

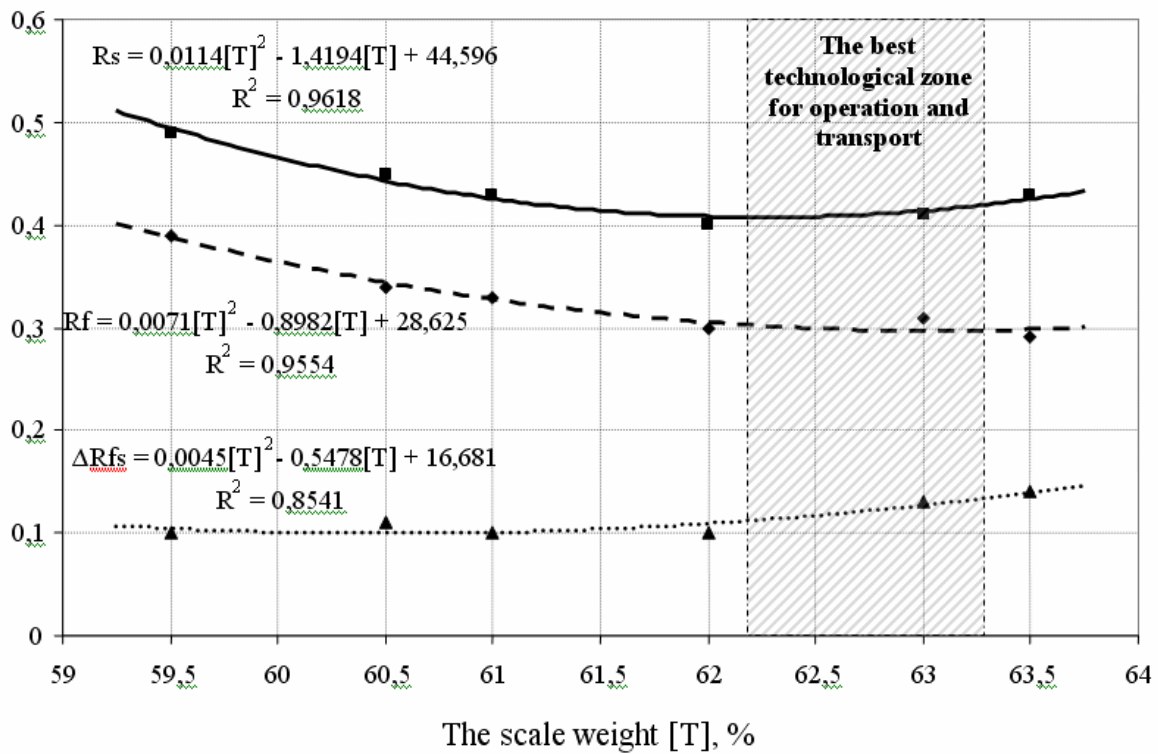


Fig.2. The weight scale influence on strength of compression

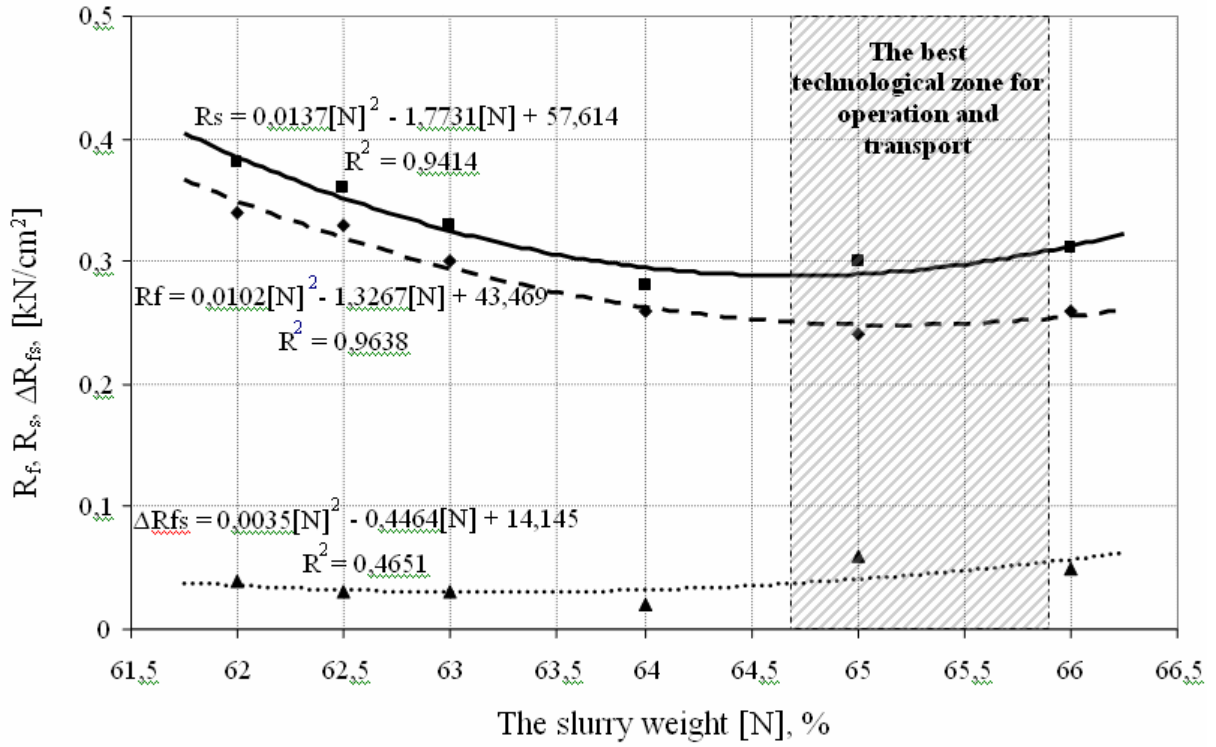


Fig. 3. The variation of strength of compression, function of slurry weight

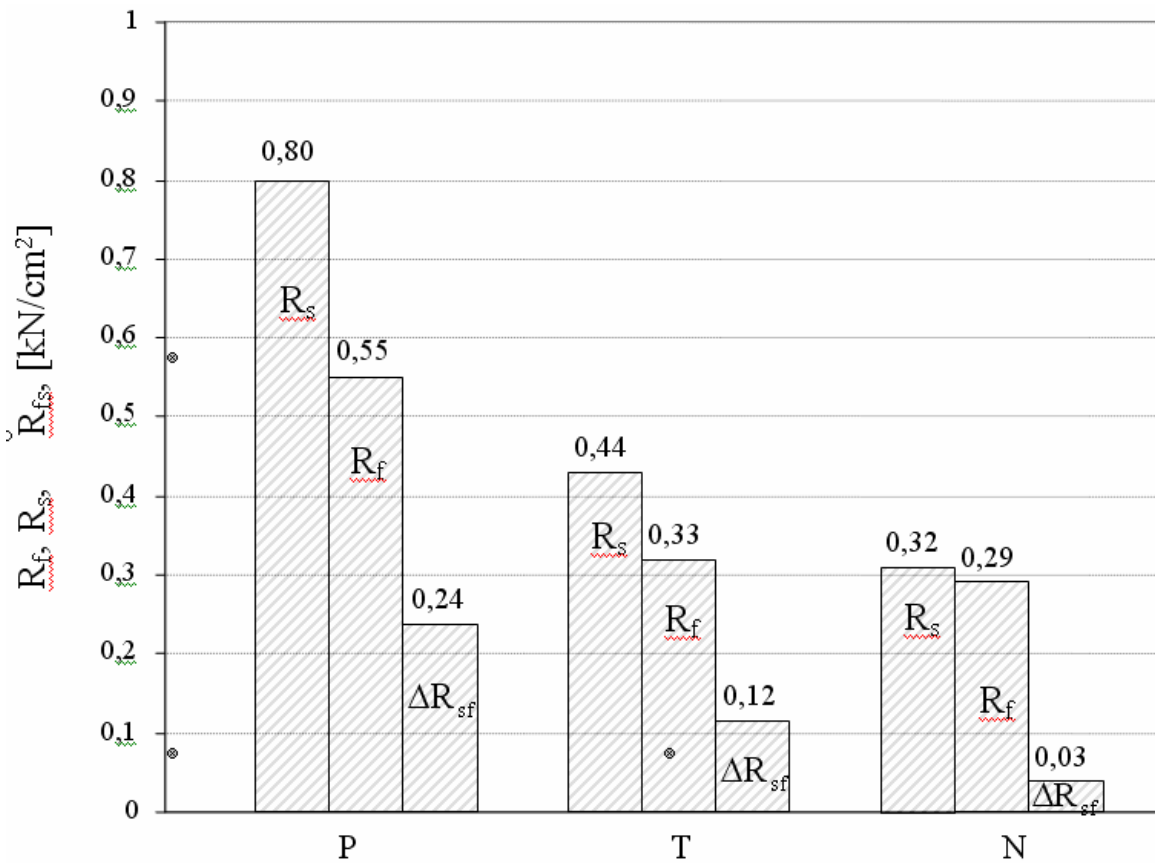


Fig. 4. Hystogram for comparison of 3 technological situations by mean value

#### 4. CONCLUSIONS

The quantitative analysis of correlation equations, which were obtained by simple regression, shows that in case of briquettes, the EAF dust content have to be 74% for providing minimum 0,48 [kN/cm<sup>2</sup>] fissuring strength.

From analysis for compression tests of EAF dust briquettes result the following conclusions:

a) The briquettes suffer a physical degradation during operation and transport; the compression strength will be influence be EAF dust content, bentonite content and lime content, too.

b) There are 2 phases in physical degradation process: I – the beginning phase of fissuring (the appearance of the first fissures) and II – the crushing phase (destruction of briquettes carcass). It is very important the crushing strength for the second phase. For the best EAF dust content, between 74-75%, the crushing content, too.

After charge of briquettes in electric furnace, the physical disintegration process of briquettes structures go on accelerated from 200<sup>0</sup>C.

*Received April 15, 2005*

*“Politehnica” University București*

#### REFERENCES

/1/. Nicolae, A., Nicolae, Maria, Sohaciu, Mirela ș.a., *Dezvoltare durabilă în siderurgie prin valorificarea materialelor secundare*, Ed. Printech, București, 2004.

#### EXEMPLU DE OPERAȚIONALIZARE A CONCEPTULUI DE DEZVOLTARE DURABILĂ LA NIVELUL UNUI SEGMENT METALURGIC

(Rezumat)

În lucrare se experimentează posibilități concrete de a aplica conceptul de dezvoltare durabilă în cazul utilizării prin reciclare a materialelor secundare pulverulente (praf, ținder, nămol) la elaborarea oțelului în cuptorul cu arc electric (EAF). Metoda de valorificare este fabricarea brichetelor. Se cercetează comportarea brichetelor la transport și manipulare prin măsurători experimentale privind rezistența la fisurare ( $R_f$ ), rezistența la sfărâmare ( $R_s$ ) și intervalul de sfărâmare ( $R_{fs}$ ). Se stabilesc domeniile optime din punct de vedere tehnologic de utilizare eficientă a brichetelor. Se fac recomandări referitoare la proporțiile optime de praf, ținder și nămol care pot fi adăugate în brichete.

## SOLUTIONS FOR A DATA ACQUISITION SYSTEM IN MATERIAL SCIENCE

BY

DOINA RĂDUCANU, TOM SAVU, MIHAI TÂRCOLEA, IONEL NEGULESCU, ION CINCA,  
VASILE DĂNUȚ COJOCARU

**Abstract.** The paper is focused on developing application-specific tools to find solutions match closely with Materials Science needs. The computer-based approach is used to develop test and measurement systems for plastic deformation procedures such as: longitudinal, transversal and helicoidally rolling, drawing, low and high temperature torsion. An adequate hardware solution is realized for each application mentioned above. The software solutions are based on LabVIEW program. The scientific parameters included in data acquisition system are: force, power, displacements, and temperature.

**Keywords:** data acquisition system, materials science

### 1. INTRODUCTION

The paper is focused on developing application-specific tools based on LabVIEW program to find solutions match closely with Materials Science needs, more specific for bodies deformation. The computer-based approach is used to develop dedicated software applications for test and measurement systems in plastic deformation procedures such as: longitudinal, transversal and helicoidally rolling, drawing, low and high temperature torsion.

The data acquisition system applies to five experimental testing-lines. Technical data for these testing-lines are presented as follows:

- Piercing helicoidally laboratory mill used to deform samples up to 30 mm diameter. One strain gauge force transducer is available.
- Cold strip rolling-mill used to deform ferrous and non-ferrous alloys. On the strip mill cylinder is available a strain gauges pressure transducer.
- Low and high temperature rolling-mill for ferrous and non-ferrous alloys. Two strain gauges force transducers are mounted on the working stand of this equipment.
- Drawing testing machine for ferrous and non-ferrous alloys wires and pipes, with three strain gauges force transducers.
- Low and high temperature torsion testing machine. For measurements of torsion moment and elongation, one strain gauge moment transducer is available.

## 2. EXPERIMENTAL LINE PRESENTATION.

Requires of this paper needs a detailed presentation only for a single experimental line: the drawing testing line as shown in figure 1.

This machine is used for experiments focused on cold drawing for ferrous and non-ferrous alloys wires and pipes, with small and medium diameter (up to 6 mm) and small wall thickness. Pipes drawing can be made using two methods, with or without internal support. The scientific parameter included in data acquisition system is the drawing force.

Three strain gauges force transducers are available. Two strain gauges force transducers are mounted: one on drawing-die holder (fig. 2) and an other on the carriage of drawing testing machine (fig. 3), both allowing measurement and recording for drawing force. The third one can be placed for more accurate measurements. Friction forces between deformed material and drawing-die can be measured (fig. 4). Also one electrical power transducer is available, connected to machine electrical engine.



Fig. 1. Experimental drawing testing line



Fig. 2. Drawing-die holder



Fig. 3. Carriage of drawing testing machine

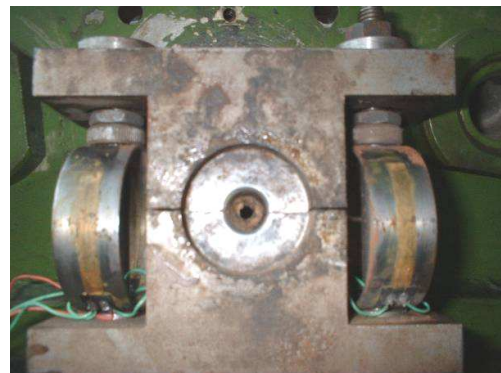


Fig. 4. Drawing-die holder for friction forces

## 3. DATA ACQUISITION SYSTEM SOLUTION.

The data acquisition system (fig. 5) is measuring the signals from:

- Three strain gauges force transducers (1.1, 1.2 and 1.3);
- One electrical power transducer (1.6);



- Two switches providing TTL boolean signals (1.4 and 1.5).

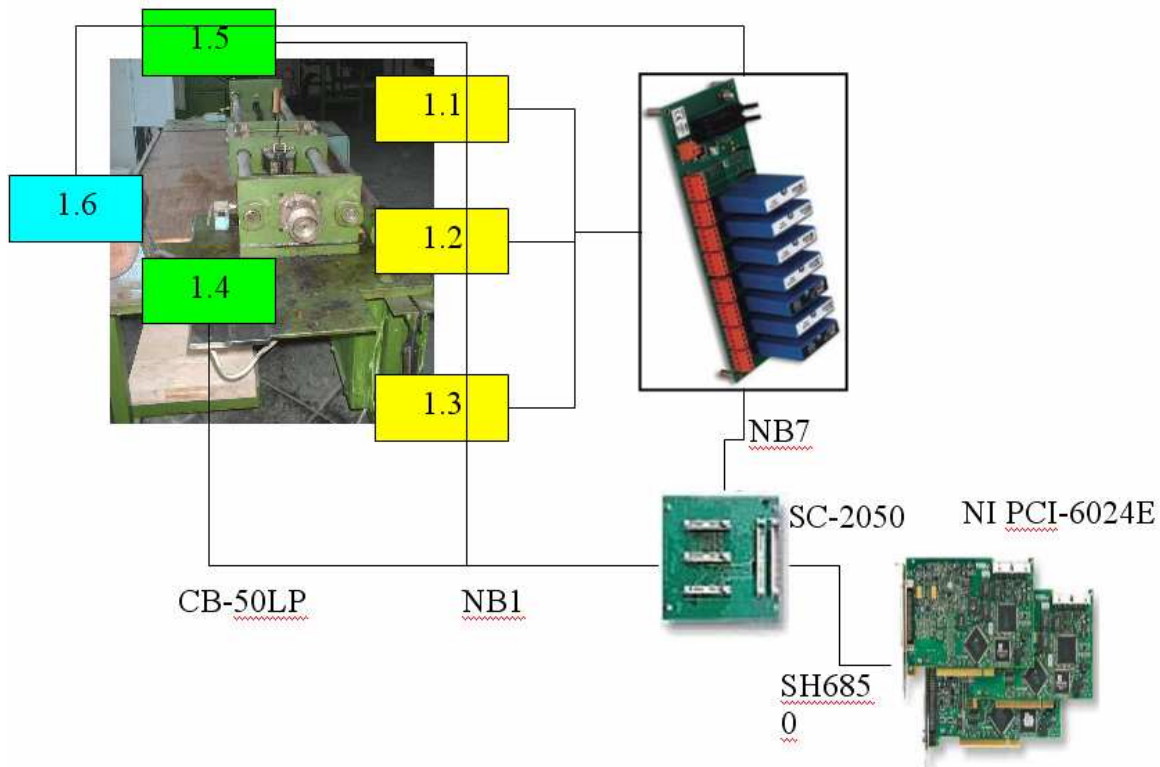


Fig. 5. Data acquisition system.

The signals from the force and electrical power transducers are first routed through a set of signal conditioning accessories:

- A set of three 5B38 full-bridge strain gauge modules (10 V excitation, 3 mV/V sensitivity, accepting transducer impedance from 300  $\Omega$  to 10 k $\Omega$ );
- One 5B41 analogue input module ( $\pm 10$  V input range, 10 kHz bandwidth).

All the 5B modules are mounted on an eight channels back-plane, powered from a +5 VDC, 1 A, supply.

The conditioned signals are routed by the back-plane, through a 26-pin connector, to a PCI-6024E multifunction data acquisition board (16 single-ended or eight differential analogue input channels, digitised on 12 bits at 200 kS/s).

For making available the pins of the data acquisition board that are not used for communication with the 5B back-plane, the connection between the two system components is split by a SC-2050 adapter.

The available pins can be accessed through a CB-50LP block connector, this being the place where the signals from the two switches are entering into the data acquisition system.

#### 4. COMMENTS.

The software application is developed in LabVIEW graphical programming environment.

Median software filters are applied to the measured values for reducing the environmental noise.

The signals from the three force transducers are measured between the true signals received from the two switches (marking the start and the end of the movement).

Transformation of the amplitude of the measured electrical signal into force units is performed using predetermined calibration constants.

Force and electrical power values are graphically and digitally represented in the user interface, being also saved to data files from which the values can be subsequently loaded for future reference.

The snapshot of the application's front panel can also be saved in a picture file.

The experimental testing line described above is useful to observe the influence of the technological parameters (deformed material, drawing-die geometry, quality of lubricants) upon process energetically balance (drawing force, necessary input power and energetically efficiency of the deformation process) in all cases described here.

With the acquired dates optimisation studies are available.

*Received April 25, 2005*

*“Politehnica” University București*

#### REFERENCES

#### SISTEM INTEGRAT DE ACHIZIȚII DE DATE ÎN ȘTIINȚA MATERIALELOR

(Rezumat)

Lucrarea prezintă o serie de dezvoltări de aplicații, utilizând soluții specifice necesare și apropiate de domeniul științei materialelor. Baza de date a calculatorului este utilizată pentru a derula teste a face măsurători de parametrii pentru diferite procedee de deformare plastică, cum ar fi: laminarea longitudinală, transversală și elicoidală, tragere, torsiune la cald sau la rece. Pentru fiecare dintre procedeele de deformare plastică menționate s-a realizat o aplicație hard. Aplicațiile soft sunt bazate pe programul Lab VIEW. Parametrii captați în achiziția de date, pentru diversele procedee menționate sunt: forță, putere, deplasări și temperatură.